

VOLUME 81

AUGUST 25, 1977

NUMBER 17

JPCHA_x

THE JOURNAL OF

PHYSICAL
CHEMISTRY



PUBLISHED BIWEEKLY BY THE AMERICAN CHEMICAL SOCIETY

THE JOURNAL OF PHYSICAL CHEMISTRY

BRYCE CRAWFORD, Jr., *Editor*
STEPHEN PRAGER, *Associate Editor*
ROBERT W. CARR, Jr., **C. ALDEN MEAD**, *Assistant Editors*

EDITORIAL BOARD: C. A. ANGELL (1973-1977), F. C. ANSON (1974-1978), V. A. BLOOMFIELD (1974-1978), J. R. BOLTON (1976-1980), L. M. DORFMAN (1974-1978), W. E. FALCONER (1977-1978), H. L. FRIEDMAN (1975-1979), H. L. FRISCH (1976-1980), W. A. GODDARD (1976-1980), E. J. HART (1975-1979), W. J. KAUZMANN (1974-1978), R. L. KAY (1977-1981), D. W. McCLURE (1974-1978), K. MYSELS (1977-1981), R. M. NOYES (1973-1977), R. G. PARR (1977-1979), W. B. PERSON (1976-1980), J. C. POLANYI (1976-1980), S. A. RICE (1976-1980), F. S. ROWLAND (1973-1977), R. L. SCOTT (1973-1977), W. A. STEELE (1976-1980), J. B. STOTHERS (1974-1978), F. A. VAN-CATLEDGE (1977-1981), B. WEINSTOCK (1977)

Published by the
AMERICAN CHEMICAL SOCIETY
BOOKS AND JOURNALS DIVISION

D. H. Michael Bowen, Director
Marjorie Laflin, Assistant to the Director

Editorial Department: Charles R. Bertsch,
Head; Marianne C. Brogan, Associate
Head; Celia B. McFarland, Joseph E.
Yurvati, Assistant Editors

Magazine and Production Department:
Bacil Guiley, Head

Research and Development Department:
Seldon W. Terrant, Head

Advertising Office: Certcom, Ltd., 25 Sylvan
Road South, Westport, Conn. 06880.

© Copyright, 1977, by the American
Chemical Society. No part of this publication
may be reproduced in any form without
permission in writing from the American
Chemical Society.

Published biweekly by the American
Chemical Society at 20th and Northampton
Sts., Easton, Pennsylvania 18042. Second
class postage paid at Washington, D.C. and
at additional mailing offices.

Editorial Information

Instructions for authors are printed in
the first issue of each volume. Please conform
to these instructions when submitting man-
uscripts.

Manuscripts for publication should be
submitted to *The Journal of Physical
Chemistry*, Department of Chemistry, Uni-
versity of Minnesota, Minneapolis, Minn.
55455. Correspondence regarding **accepted
papers and proofs** should be directed to the

Editorial Department at the ACS Easton
address.

Page charges of \$60.00 per page may be
paid for papers published in this journal.
Payment does not affect acceptance or
scheduling of papers.

Bulk reprints or photocopies of indi-
vidual articles are available. For information
write to Business Operations, Books and
Journals Division at the ACS Washington
address.

Requests for **permission to reprint**
should be directed to Permissions, Books and
Journals Division at the ACS Washington
address. The American Chemical Society and
its Editors assume no responsibility for the
statements and opinions advanced by con-
tributors.

Subscription and Business Information

1977 Subscription rates—including surface
postage

	U.S.	PUAS	Canada, Foreign
Member	\$24.00	\$33.00	\$34.00
Nonmember	96.00	105.00	106.00
Supplementary material	15.00	19.00	20.00

Air mail and air freight rates are avail-
able from Membership & Subscription Ser-
vices, at the ACS Columbus address.

New and renewal subscriptions should
be sent with payment to the Office of the
Controller at the ACS Washington address.

Changes of address must include both old
and new addresses with ZIP code and a recent
mailing label. Send all address changes to the
ACS Columbus address. Please allow six
weeks for change to become effective. **Claims
for missing numbers** will not be allowed if
loss was due to failure of notice of change of
address to be received in the time specified:

if claim is dated (a) North America—more
than 90 days beyond issue date, (b) all other
foreign—more than 1 year beyond issue date;
or if the reason given is "missing from files".
Hard copy claims are handled at the ACS
Columbus address.

Microfiche subscriptions are available
at the same rates but are mailed first class to
U.S. subscribers, air mail to the rest of the
world. Direct all inquiries to Special Issues
Sales, at the ACS Washington address or call
(202) 872-4554. **Single issues** in hard copy
and/or microfiche are available from Special
Issues Sales at the ACS Washington address.
Current year \$4.75. Back issue rates available
from Special Issues Sales. **Back volumes** are
available in hard copy and/or microform.
Write to Special Issues Sales at the ACS
Washington address for further information.
Microfilm editions of ACS periodical pub-
lications are available from volume 1 to the
present. For further information, contact
Special Issues Sales at the ACS Washington
address. **Supplementary material** men-
tioned in the journal appears in the microfilm
edition. Single copies may be ordered directly
from Business Operations, Books and Jour-
nals Division, at the ACS Washington ad-
dress.

	U.S.	PUAS, Canada	Other Foreign
Microfiche	\$2.50	\$3.00	\$3.50
Photocopy			
1-7 pages	4.00	5.50	7.00
8-20 pages	5.00	6.50	8.00

Orders over 20 pages are available only on
microfiche, 4 × 6 in., 24X, negative, silver
halide. Orders must state photocopy or mi-
crofiche if both are available. Full biblio-
graphic citation including names of all au-
thors and prepayment are required. Prices
are subject to change.

American Chemical Society
1155 16th Street, N.W.
Washington, D.C. 20036
(202) 872-4600

Member & Subscription Services
American Chemical Society
P.O. Box 3337
Columbus, Ohio 43210
(614) 291-7230

Editorial Department
American Chemical Society
20th and Northampton Sts.
Easton, Pennsylvania 18042
(215) 258-9111

Volume 81, Number 17 August 25, 1977

JPCHAx 81(17) 1607-1700 (1977)

ISSN 0022-3654

Kinetics and Mechanism of the Gas Phase Reaction of OH Radicals with Methoxybenzene and <i>o</i> -Cresol over the Temperature Range 299-435 K ... R. A. Perry, R. Atkinson,* and J. N. Pitts, Jr.	1607
Kinetics of the Base-Stacking Reaction of <i>N</i> ⁶ , <i>N</i> ⁶ -Dimethyladenosine. An Ultrasonic Absorption and Dispersion Study ... M. P. Heyn,* C. U. Nicola, and G. Schwarz	1611
The Reaction of the Precursor of the Hydrated Electron with Electron Scavengers ... Charles D. Jonah,* John R. Miller, and Max S. Matheson	1618
Reactions of Phosphate Radicals with Organic Compounds ... P. Maruthamuthu and P. Neta*	1622
Electron Scavenging in Ethanol and in Water ... Dušan Ražem and William H. Hamill*	1625
Hamaker Constants and the Principle of Corresponding States ... Melvin D. Croucher* and Michael L. Hair	1631
Modified Potentiometric Method for Measuring Micellar Uptake of Weak Acids and Bases ... E. Azaz and M. Donbrow*	1636
Structure of Some Polymer-Detergent Aggregates in Water ... B. Cabane	1639
Application of the Polanyi Adsorption Potential Theory to Adsorption from Solution on Activated Carbon. 9. Competitive Adsorption of Ternary Solid Solutes from Water Solution ... Michael R. Rosene and Milton Manes*	1646 ■
Application of the Polanyi Adsorption Potential Theory to Adsorption from Solution on Activated Carbon. 10. pH Effects and "Hydrolytic" Adsorption in Aqueous Mixtures of Organic Acids and Their Salts ... Michael R. Rosene and Milton Manes*	1651 ■
The Tammann-Tait-Gibson Model for Aqueous Electrolyte Solutions. Application to the Refractive Index ... J. V. Leyendekkers and R. J. Hunter*	1657 ■
Studies of Matrix Isolated Uranium Tetrafluoride and Its Interactions with Frozen Gases ... K. R. Kunze, R. H. Hauge, D. Hamill, and J. L. Margrave*	1664
Low Resolution Microwave Spectroscopy. 7. Conformational Isomers, Energies, and Spectral Intensity Anomalies of Neopentyl Esters ... Nancy S. True and Robert K. Bohn*	1667 ■
Low Resolution Microwave Spectroscopy. 8. Rotational Isomers of Allyl Cyanofornate, Allyl Fluorofornate, Allyl Fornate, and Allyl Chlorofornate ... Nancy S. True and Robert K. Bohn*	1671 ■
Complexation of the Cesium Cation by Macrocyclic Polyethers in Various Solvents. A Cesium-133 Nuclear Magnetic Resonance Study of the Thermodynamics and Kinetics of Exchange ... Elizabeth Mei, Alexander I. Popov, and James L. Dye*	1677
The Molecular Structure of Tetrafluoro-1,3-dithietane as Determined by Electron Diffraction ... Joseph F. Chiang* and K. C. Lu	1682 ■
Kinetics of Hydrogen Absorption by LaNi ₅ ... S. Tanaka, J. D. Clewley, and Ted B. Flanagan*	1684
Studies of Cationic Radicals in γ -Irradiated Single Crystals of α -Aminoisobutyric Acid and Related α -Amino Acids by Electron Spin Resonance and SCF MO INDO Calculation ... Atsuko Minegishi	1688

■ Supplementary and/or miniprint material for this paper is available separately (consult the masthead page for ordering information); it will also appear following the paper in the microfilm edition of this journal.

* In papers with more than one author, the asterisk indicates the name of the author to whom inquiries about the paper should be addressed.

AUTHOR INDEX

- | | | | |
|-------------------------|-----------------------|---------------------------|---------------------------|
| Atkinson, R., 1607 | Flanagan, T. B., 1684 | Leyendekkers, J. V., 1657 | Perry, R. A., 1607 |
| Azaz, E., 1636 | | Lu, K. C., 1682 | Pitts, J. N., Jr., 1607 |
| | Hair, M. L., 1631 | | Popov, A. I., 1677 |
| Bohn, R. K., 1667, 1671 | Hamill, D., 1664 | Manes, M., 1646, 1651 | |
| | Hamill, W. H., 1625 | Margrave, J. L., 1664 | Ražem, D., 1625 |
| Cabane, B., 1639 | Hauge, R. H., 1664 | Maruthamuthu, P., 1622 | Ropp, R. C., 1699 |
| Carroll, B., 1699 | Heyn, M. P., 1611 | Matheson, M. S., 1618 | Rosene, M. R., 1646, 1651 |
| Chiang, J. F., 1682 | Hunter, R. J., 1657 | Mei, E., 1677 | |
| Clewley, J. D., 1684 | | Miller, J. R., 1618 | Schwarz, G., 1611 |
| Croucher, M. D., 1631 | Jonah, C. D., 1618 | Minegishi, A., 1688 | |
| | | | Tanaka, S., 1684 |
| Donbrow, M., 1636 | | Neta, P., 1622 | True, N. S., 1667, 1671 |
| Dye, J. L., 1677 | Kunze, K. R., 1664 | Nicola, C. U., 1611 | |

THE JOURNAL OF PHYSICAL CHEMISTRY

Registered in U. S. Patent Office © Copyright, 1977, by the American Chemical Society

VOLUME 81, NUMBER 17 AUGUST 25, 1977

Kinetics and Mechanism of the Gas Phase Reaction of OH Radicals with Methoxybenzene and *o*-Cresol over the Temperature Range 299–435 K

R. A. Perry, R. Atkinson,* and J. N. Pitts, Jr.

Department of Chemistry and Statewide Air Pollution Research Center, University of California, Riverside, California 92502 (Received January 5, 1977)

Publication costs assisted by the University of California, Riverside

Absolute rate constants for the reaction of OH radicals with methoxybenzene and *o*-cresol have been determined over the temperature range 299–435 K using a flash photolysis-resonance fluorescence technique. In both cases it was observed that for temperatures between ~330 and 390 K the OH decays were nonexponential, with the decay rates decreasing with time after the flash. For the temperature regions 299 K < $T \leq 330$ K and 390 K < $T < 435$ K the OH decays were exponential, with the rate constants at 400 K being a factor of ~6 lower than those at 299 K. The observed behavior is explained by the occurrence of both OH radical addition to the aromatic ring and H atom abstraction at room temperature, with the abstraction reaction being the only reaction observed above ~390 K due to the rapid decomposition of the OH-aromatic adduct within the time scale of the observation. In the temperature region where nonexponential decays are observed it is postulated that the OH-aromatic adduct, formed by OH radical addition to the ring, is decomposing back to reactants. The overall room temperature rate constants determined were $(1.96 \pm 0.24) \times 10^{-11}$ cm³ molecule⁻¹ s⁻¹ and $(3.41 \pm 0.68) \times 10^{-11}$ cm³ molecule⁻¹ s⁻¹ for methoxybenzene and *o*-cresol, respectively.

Introduction

The gas phase reactions of the hydroxyl radical with aromatic compounds are of fundamental interest as well as being of importance in kinetic chemical models of photochemical air pollution.^{1,2} Rate constants for the reaction of OH radicals with aromatic hydrocarbons have been determined at ~300 K using discharge flow,³ flash photolysis-resonance fluorescence,⁴⁻⁶ and relative rate techniques.^{7,8} Recently absolute OH radical rate constants have been determined⁶ for benzene, toluene, toluene-*d*₈, *o*-, *m*-, and *p*-xylene, and 1,2,3-, 1,2,4-, and 1,3,5-trimethylbenzene over the temperature range 296–473 K. It was observed⁶ that for temperatures between ~325 and ~330 K the OH decays were nonexponential. For the temperature regions 380 K < $T < 473$ K and 296 K < $T \leq 325$ K the OH decays were exponential, with the rate constants at ~380 K being a factor of 4–12 lower than those at ~298 K. The observed behavior was explained⁶

by postulating the occurrence of both OH radical addition to the aromatic ring and H atom abstraction at room temperature, with the abstraction reaction being the sole reaction observed above ~380 K due to the rapid decomposition of the OH-aromatic adduct within the time scale of the observations. In the temperature region where nonexponential decays were observed it was proposed⁶ that the OH-aromatic adduct, formed by OH radical addition to the ring, was decomposing back to reactants. Rate constants for the reaction of OH radicals with toluene-*d*₈ substantiated⁶ this reaction scheme, being within 5% of that for toluene at 298 K, but being a factor of ~2.5 lower at 432 K than that for toluene.

In this work absolute rate constants for the reaction of OH radicals with methoxybenzene and *o*-cresol have been determined over the temperature range 299–435 K using a flash photolysis-resonance fluorescence technique in order to study the effects of substituent groups. Phenolic

compounds are formed from the gas phase reaction of $O(^3P)$ atoms with aromatic hydrocarbons,⁹⁻¹⁴ and are possible products from the reaction of OH radicals with aromatic hydrocarbons under polluted atmospheric conditions.¹⁵

Experimental Section

The apparatus and techniques used have been described previously,^{5,6} and hence only a brief summary will be given here. OH radicals were produced by the pulsed vacuum ultraviolet photolysis of H_2O at wavelengths longer than the LiF cutoff ($\geq 1050 \text{ \AA}$). OH radical concentrations were monitored as a function of time after the flash by resonance fluorescence using a cooled EMI 9659QA photomultiplier fitted with an interference filter transmitting the 3064-\AA band of OH ($A^2\Sigma^+, v' = 0 \rightarrow X^2\Pi, v'' = 0$). The intersection of the detection system aperture and the resonance radiation beam defined a fluorescence viewing zone at the center of the reaction vessel whose cross section was $\sim 2 \text{ cm}$ in diameter. This region was well separated from the reaction vessel walls, thus minimizing wall losses of the OH radicals. The reaction cell was enclosed in a furnace which could be held constant to better than $\pm 1 \text{ K}$ over the temperature range 295–475 K, and the gas temperature was measured by a chromel–alumel thermocouple mounted inside the reaction vessel.

The flash lamp was typically operated at discharge energies of 25–50 J per flash at repetition rates of one flash every 3 s. Signals were obtained by photon counting in conjunction with multichannel scaling. OH radical decay curves were accumulated from 30–1050 flashes, depending on the signal strengths. OH half-lives ranged from 1.83 to 113 ms, and the OH radical concentrations were followed over at least three half-lives. In all cases the flash duration ($\leq 1 \mu\text{s}$) was negligible in comparison to the OH radical half-lives encountered.

In order to avoid the accumulation of photolysis or reaction products, all experiments were carried out under flow conditions so that the gas mixture in the reaction vessel was replenished every few flashes. The partial pressure of H_2O in the reaction cell was $\sim 0.02 \text{ Torr}$. The argon used had a purity level of $\geq 99.998\%$, according to the manufacturer, while the methoxybenzene and *o*-cresol had stated purity levels of $\geq 99\%$. In addition, the *o*-cresol was distilled prior to use and stored under argon.

A known fraction of the total argon flow was saturated with the aromatic vapor at 273 K (methoxybenzene) or 293 K (*o*-cresol). Aromatic partial pressures in this fraction of the total flow were determined by their ultraviolet absorption using a 9.0 cm pathlength cell and a Cary 15 spectrophotometer. The absorption cell was calibrated using known pressures of the aromatics as measured by an MKS Baratron capacitance manometer. All flows were monitored by calibrated flowmeters, and the gases were premixed before entering the reaction vessel. Prolonged flowing of the *o*-cresol and, to a lesser extent, of methoxybenzene, was necessary in order to obtain steady-state gas phase concentrations of these aromatics during the determinations of rate data.

Results

OH radical decays were obtained for the reaction of OH radicals with methoxybenzene and *o*-cresol over the temperature range 299–435 K at a total pressure of $\sim 100 \text{ Torr}$ of argon. The experimental observations were entirely analogous to those recently reported⁶ for the aromatic hydrocarbons. Thus nonexponential OH radical decays were observed over the temperature region $\sim 330\text{--}390 \text{ K}$, with the decay rates decreasing with time after

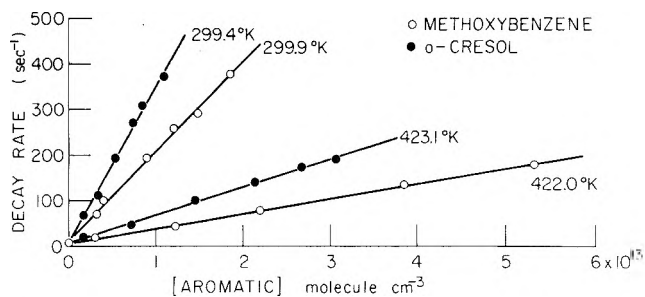


Figure 1. Plots of the OH radical decay rate against aromatic concentration for methoxybenzene at 299.9 and 422.0 K and for *o*-cresol at 299.4 and 423.1 K. Total pressure $\sim 100 \text{ Torr}$ of argon.

the flash. For the temperature regions $299 \text{ K} < T \leq 330 \text{ K}$ and $390 \text{ K} \leq T < 435 \text{ K}$ the OH decays were exponential, obeying the integrated rate expression

$$[\text{OH}]_{t_0}/[\text{OH}]_t = S_0/S_t = \exp[(k_0 + k[\text{aromatic}])(t - t_0)] \quad (\text{I})$$

where $[\text{OH}]_{t_0}$ and $[\text{OH}]_t$ are the concentrations of OH at times t_0 and t , respectively, S_0 and S_t are the corresponding resonance fluorescence intensities, k_0 is the first-order rate for removal of OH in the absence of added reactant (primarily attributed to diffusion out of the viewing zone and to reaction with impurities), and k is the rate constant for the reaction



The rate constants, k , obtained at 400 K were a factor of ~ 6 lower than those at 299 K.

As in the previous work,⁶ rate constants k were determined as a function of temperature from either (a) the dependence of the OH radical decay rate on the aromatic concentrations, as shown in Figure 1 for *o*-cresol and methoxybenzene at ~ 299 and $\sim 423 \text{ K}$, or (b) from a single OH decay rate, R , at a known aromatic concentration, using

$$R = (t - t_0)^{-1} \ln S_0/S_t = k_0 + k[\text{aromatic}] \quad (\text{II})$$

This latter method obviously has a somewhat larger degree of uncertainty, partially associated with the estimation of the OH decay rates in the absence of reactant, $R = k_0$. However, for OH decay rates $\geq 200 \text{ s}^{-1}$, any error associated with the estimation of k_0 (which was typically $10\text{--}20 \text{ s}^{-1}$) was $\sim 5\%$. Values of k_0 were estimated using values obtained by method (a) for the same aromatic at similar temperatures. The error limits given in Table I and shown in Figure 2 are the estimated overall error limits, which, for method (a), include the least-squares standard deviations (1–3%) as well as the estimated accuracy limits of other parameters such as total pressure and the aromatic concentrations in the reactant mixture. Using method (a), the experimental decay rates in the range typically used for method (b), $R \geq 200 \text{ s}^{-1}$, were within 5% of those calculated from least-squares analysis of the data. Hence this spread is indicative of the random errors associated with method (b), and is included in the overall error limits for method (b) (Table I and Figure 2). For *o*-cresol the overall error limits are estimated to be approximately $\pm 20\%$ on account of greater errors in the ultraviolet absorption calibration. However, the relative rate constants for *o*-cresol are estimated to be accurate to approximately $\pm 5\text{--}10\%$.

Table I gives the rate constants obtained at the temperature used, and Figure 2 shows the data plotted in Arrhenius form. The solid lines for $T \leq 330 \text{ K}$ and $T \geq$

TABLE I: Rate Constants, k , for the Reaction of OH Radicals with Methoxybenzene and *o*-Cresol

Methoxybenzene		<i>o</i> -Cresol	
Temp, K	$10^{12} k \text{ cm}^3 \text{ molecule}^{-1} \text{ s}^{-1}$	Temp, K	$10^{12} k \text{ cm}^3 \text{ molecule}^{-1} \text{ s}^{-1}$
299.9	19.6 ± 2.4^a	299.4	34.1 ± 6.8^a
309.0	17.3 ± 2.6^b	310.6	29.3 ± 5.9^b
309.7	17.5 ± 2.6^b	322.0	29.8 ± 6.0^b
318.5	17.5 ± 2.6^b	330.7	26.8 ± 5.4^b
321.7	17.8 ± 2.7^b	335.4	25.5 ± 5.1^b
329.5	12.7^c	344.4	18.5^c
357.4	6.7^c	356.5	15.0^c
370.4	3.0^c	385.8	6.4^c
385.5	3.33 ± 0.50^b	392.8	6.0^c
392.3	3.25 ± 0.50^b	400.6	5.6 ± 1.1^b
404.1	3.31 ± 0.50^b	407.8	5.4 ± 1.1^b
413.2	3.90 ± 0.56^b	423.1	6.2 ± 1.2^a
417.9	2.85 ± 0.43^b		
422.0	3.30 ± 0.40^a		
428.7	2.76 ± 0.41^b		
435.3	2.72 ± 0.41^b		

^a OH radical decays were observed to be exponential. The rate constants were obtained from the dependence of the OH decay rates on aromatic concentration. The indicated error limits are the estimated overall error limits which include the least-squares standard deviations, as well as the estimated accuracy limits of other parameters such as aromatic concentrations in the reactant mixture. ^b OH radical decays were observed to be exponential. The rate constants were obtained from the OH decay rate at a single aromatic concentration. The indicated error limits are the estimated overall error limits. ^c OH radical decays were observed to be nonexponential. Rate constants were obtained from the initial OH decay rate at a single aromatic concentration. No realistic error limits can be given to the nonexponential behavior of the OH decays, and, in extreme cases, the rate constants given indicate the order of magnitude only.

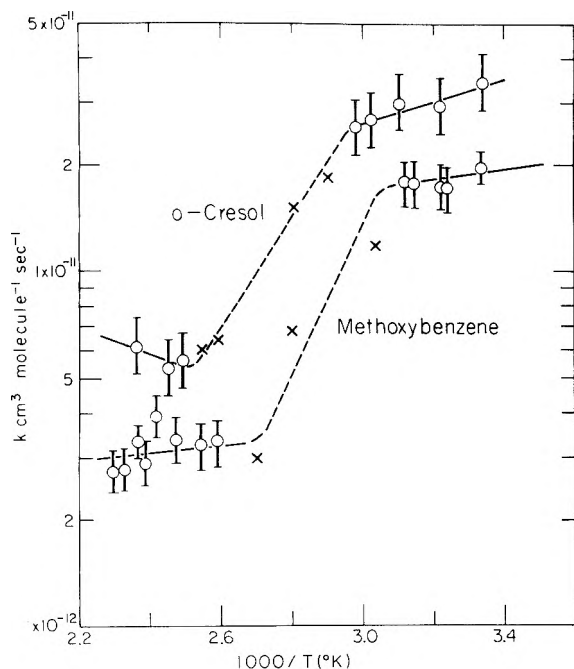


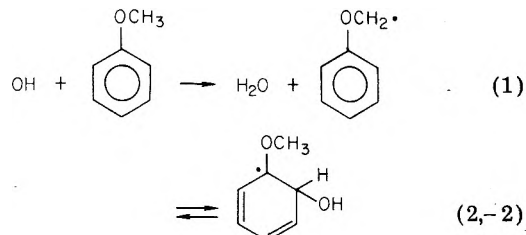
Figure 2. Arrhenius plots of $\log k$ against $1000/T(\text{K})$ for methoxybenzene and *o*-cresol: (O) exponential OH radical decays observed; (X) nonexponential OH radical decays observed. The dashed lines merely reflect the trend of the data in temperature regions where nonexponential decays are observed.

390 K were obtained from least-squares fitting of the data in these temperature regions, while the dashed lines between these temperature regions merely indicate the trend of the data.

Discussion

From the initial OH radical concentrations and the aromatic concentrations used, it can be estimated⁵ that errors in the measured rate constants due to reaction of OH radicals with reaction products would be typically <5–10%, using an assumed rate constant of $10^{-10} \text{ cm}^3 \text{ molecule}^{-1} \text{ s}^{-1}$ for the reaction of OH radicals with all reaction products.

The experimental observations are again explained (using methoxybenzene as an example) by a reaction scheme⁶ involving both abstraction (reaction 1) and addition to the aromatic ring (reaction 2). Addition of the



OH radical is shown for attack at the ortho position by analogy with the reaction of $\text{O}(^3\text{P})$ atoms with aromatic hydrocarbons;^{10,12,14} obviously addition of OH radicals may occur at any of the carbon atoms of the aromatic ring, forming a variety of OH-aromatic adducts which initially contain the excess energy due to the exothermicity of the reaction. The initially formed OH-aromatic adduct, which contains approximately 18 kcal mol^{-1} of excess energy (see later), will, as discussed previously,⁶ be readily thermalized in the presence of ~ 100 Torr of argon; hence reaction -2 refers to the decomposition of the thermalized OH-aromatic adduct back to reactants.

The experimental results are consistent with the occurrence of the above reactions with the OH-aromatic adducts being stable within the time frame of the OH radical observations (~ 1 – 30 ms) from 299 to ~ 330 K, and being unstable for temperatures ≥ 390 K. Hence at room temperature the measured rate constants are those for both addition and abstraction, $k = k_1 + k_2$, while at ≥ 390 K only k_1 , the rate constant for abstraction, is measured.

The following Arrhenius expressions for H atom abstraction (k_1) and addition to the aromatic ring (k_2) can be obtained from least-squares analysis of the data in the temperature regions $T = 299$ – 325 K and $T \geq 360$ K for methoxybenzene, and $T = 299$ – 340 K and $T \geq 400$ K for *o*-cresol (in view of the appreciable error limits the Arrhenius activation energies are quoted to the nearest $0.1 \text{ kcal mol}^{-1}$):

methoxybenzene:

$$k_1 = 1.7 \times 10^{-12} e^{500/RT} \text{ cm}^3 \text{ molecule}^{-1} \text{ s}^{-1}$$

$$k_2 = 3.7 \times 10^{-12} e^{800/RT} \text{ cm}^3 \text{ molecule}^{-1} \text{ s}^{-1}$$

o-cresol

$$k_1 = 5.0 \times 10^{-11} e^{-1800/RT} \text{ cm}^3 \text{ molecule}^{-1} \text{ s}^{-1}$$

$$k_2 = 1.6 \times 10^{-12} e^{1800/RT} \text{ cm}^3 \text{ molecule}^{-1} \text{ s}^{-1}$$

Because of the small temperature ranges in each region the error limits are large and extrapolation outside of these temperature ranges will give large uncertainties in the values obtained. Discussion of the individual values of the preexponential factors and Arrhenius activation energies has little merit in view of the large error limits, except to point out that reaction 2 has a negative temperature dependence, as previously observed⁶ for the aromatic hydrocarbons (except benzene). The overall uncertainties in E_1 and E_2 are estimated to be $\pm 2 \text{ kcal mol}^{-1}$. By ex-

TABLE II: H Atom Abstraction Rate Constants, k_1 , and the Ratio $k_1/(k_1 + k_2)$ for the Reaction of OH Radicals with Methoxybenzene and *o*-Cresol at 299 K

Aromatic	$10^{12} k_1$ cm ³ molecule ⁻¹ s ⁻¹ ^{a,b}	$k_1/(k_1 + k_2)$ ^b
Methoxybenzene	3.9	0.20
<i>o</i> -Cresol	2.6	0.08

^a Extrapolated from $T \geq 380$ K to 299 K using the Arrhenius lines in Figure 2. ^b Error limits are estimated to be approximately a factor of 2.

TABLE III: Comparison of Substituent Effects on the Rate Constants for the Reaction of OH Radicals and O(³P) Atoms at Room Temperature and of CF₃ Radicals at 338 K with Aromatics

Aromatic	Relative rate constants		
	OH ^a	O(³ P) ^b	CF ₃ ^c
Benzene	1.0	1.0	1.0
Toluene	4.6	3.1	1.43
Methoxybenzene	14.6	4.6	1.93
<i>o</i> -Xylene	10.5	7.3	3.80
<i>o</i> -Cresol	25.4	24.3	

^a References 4-8. ^b References 16 and 17. ^c Reference 18; $T = 338$ K.

trapolation of the data above ~ 390 K to room temperature, the values of k_1 and $k_1/(k_1 + k_2)$ at 299 K shown in Table II can be obtained. These values are of a similar order of magnitude as those derived for the aromatic hydrocarbons.⁶

The overall room temperature rate constants for methoxybenzene and *o*-cresol, when compared to those for benzene,⁴⁻⁶ toluene,⁴⁻⁶ and *o*-xylene⁵⁻⁷ (Table III) further demonstrate the electrophilic character of OH radical reactions. Similar substituent effects, as shown in Table III, have been observed for the reaction of O(³P) atoms^{16,17} and CF₃¹⁸ radicals with the aromatics.

The rate constant k_{-2} for the thermalized OH-aromatic adduct is given by

$$k_{-2} = A_{-2} e^{-E_{-2}/RT} \quad (\text{III})$$

As noted above, OH radicals are monitored with the present experimental system for ~ 1 -30 ms after the flash, and significant nonexponentiality of the OH decay curves was observed at temperatures from ~ 330 to 390 K. Hence the half-life of the OH-aromatic adduct must be of the order of ~ 5 -10 ms in this temperature range, corresponding to $k_{-2} \sim 100$ s⁻¹ at 360 K. For A_{-2} estimated to be $\sim 3 \times 10^{13}$ s⁻¹ (of the same order of magnitude as the A factors for decomposition of the cyclohexadienyl¹⁹ and

methylcyclohexadienyl radicals²⁰) the activation energy for reaction -2 becomes $E_{-2} \sim 18$ kcal mol⁻¹. (Individual data are given in Table IV.)

From eq III the half-lives of the OH-aromatic adducts can be estimated to be 0.33 s at 299 K, 19 ms at 330 K, 0.28 ms at 390 K, and 0.03 ms at 435 K. These values of A_{-2} and E_{-2} thus give half-lives of the OH-aromatic adducts which are totally consistent with both the reaction scheme discussed above and the experimental observations.

Knowing the activation energies for reactions 2 and -2, the heats of formation of the OH-aromatic adducts can be obtained as²¹

$$\Delta H_f(\text{OH-aromatic adduct}) = \Delta H_f(\text{aromatic}) + \Delta H_f(\text{OH}) - \Delta H_2$$

where ΔH_2 is the enthalpy of reaction 2 and

$$\Delta H_2 = E_{-2} - E_2 + RT$$

where E_{-2} and E_2 are the activation energies for reactions -2 and 2, respectively.

Table IV gives the Arrhenius activation energies E_{-2} and E_2 used together with the experimental and calculated heats of formation ΔH_f of the OH-aromatic adducts. The calculated values of $\Delta H_f(\text{OH-aromatic adduct})$ were obtained as in the previous work,⁶ except that a stabilization energy of 19.0 kcal mol⁻¹ was found to give the best fit between the experimental and calculated values of $\Delta H_f(\text{OH-aromatic adduct})$. This value is similar to, though somewhat higher than, that of 16.5 kcal mol⁻¹ previously determined for the aromatic hydrocarbons.⁶ While these two stabilization energies are equivalent within the error limits (estimated at ± 5 kcal mol⁻¹), a trend to a higher stabilization energy for the radicals produced from methoxybenzene and *o*-cresol may be expected, as the methoxy and hydroxyl substituents will stabilize the OH-aromatic adducts via interaction of the electrons on the oxygen atom with the aromatic ring.²²

Such an approach can be extended to the reaction of OH radicals with olefins, where addition has been shown to be the major reaction pathway at room temperature.²³ In the case of propylene the calculated heat of formation, ΔH_f , of the 1-hydroxypropyl radical from group additivity rules yields a value of $E_{-2} \sim 32$ kcal mol⁻¹ (using $E_2 = -1$ kcal mol⁻¹)²⁴ where E_2 and E_{-2} refer to OH radical addition to propylene and the reverse reaction, respectively. Hence the lifetime of the 1-hydroxypropyl radical would be ~ 10 ms at 650 K and nonexponential hydroxyl radical decays are predicted to be observed at around this temperature using the present experimental technique. With either the present experimental technique or with a flash photolysis-resonance absorption technique, the radical would, however, be stable at lower temperatures with respect to

TABLE IV: Arrhenius Activation Energies for Reactions 2 and -2 and Heats of Formation ΔH_f for the OH-Aromatic Adducts

Aromatic	E_2 , kcal mol ⁻¹	E_{-2} , ^a kcal mol ⁻¹	ΔH_f , kcal mol ⁻¹		
			Aromatic	OH-aromatic adduct	
				Expt ^b	Calcd ^c
Methoxybenzene	-0.8 ± 2	18.1 ± 2	-18.00^d	-28.4 ± 4	-29.5
<i>o</i> -Cresol	-1.8 ± 2	19.1 ± 2	-30.74^e	-43.1 ± 4	-42.6

^a E_{-2} obtained using $A_{-2} = 3 \times 10^{13}$ s⁻¹, $k_{-2} = 100$ s⁻¹ at the temperature corresponding to the midpoint of the dashed lines in Figure 2. Indicated error limits are equivalent to a factor of 100 in A_{-2}/k_{-2} at the temperature of the midpoint of the dashed lines of Figure 2. ^b Calculated using $\Delta H_f(\text{OH}) = 9.2 \pm 1$ kcal mol⁻¹³⁰ and $\Delta H_f(\text{OH-aromatic adduct}) = \Delta H_f(\text{aromatic}) + \Delta H_f(\text{OH}) - (E_{-2} - E_2 + RT)$. ^c Calculated from group additivity rules, using a stabilization energy for the radicals of 19.0 kcal mol⁻¹. The calculated values of ΔH_f refer to the following cyclohexadienyl radicals: for methoxybenzene, 1-methoxy-2-hydroxy and for *o*-cresol, 1-methyl-2,3-dihydroxy. These radicals were obtained by assuming that OH radical attack occurs ortho to the methoxy and hydroxy groups, respectively, analogous to O(³P) reaction.^{10,12,14} ^d Reference 21. ^e Reference 31.

decomposition over the observational times scales employed, and, in fact, "normal" Arrhenius behavior has been observed²⁴⁻²⁹ for the reaction of OH radicals with a variety of olefins over the temperature range 210–500 K.

Acknowledgment. The authors gratefully acknowledge the financial support of NSF Grant No. CHE76-10447 and Environmental Protection Agency Grant No. 800649. The contents do not necessarily reflect the view and policies of the Environmental Protection Agency, nor does mention of trade names or commercial products constitute endorsement or recommendation for use.

References and Notes

- (1) M. C. Dodge, Workshop on Mathematical Modeling of Photochemical Smog, Summary Proceedings, Report EPA-R4-73-010, Environmental Protection Agency, Washington, D.C., 1973.
- (2) B. J. Finlayson and J. N. Pitts, Jr., *Science*, **192**, 111 (1976).
- (3) E. D. Morris, Jr., and H. Niki, *J. Phys. Chem.*, **75**, 3640 (1971).
- (4) D. D. Davis, W. Bollinger, and S. Fischer, *J. Phys. Chem.*, **79**, 293 (1975).
- (5) D. A. Hansen, R. Atkinson, and J. N. Pitts, Jr., *J. Phys. Chem.*, **79**, 1763 (1975).
- (6) R. A. Perry, R. Atkinson, and J. N. Pitts, Jr., *J. Phys. Chem.*, **81**, 296 (1977).
- (7) G. J. Doyle, A. C. Lloyd, K. R. Darnall, A. M. Winer, and J. N. Pitts, Jr., *Environ. Sci. Technol.*, **9**, 237 (1975).
- (8) A. C. Lloyd, K. R. Darnall, A. M. Winer, and J. N. Pitts, Jr., *J. Phys. Chem.*, **80**, 789 (1976).
- (9) G. Boocock and R. J. Cvetanovic, *Can. J. Chem.*, **39**, 2436 (1961).
- (10) G. R. H. Jones and R. J. Cvetanovic, *Can. J. Chem.*, **39**, 2444 (1961).
- (11) I. Mani and M. C. Sauer, Jr., *Adv. Chem. Ser.*, No. **82**, 142 (1968).
- (12) E. Grovenstein, Jr., and A. J. Mosher, *J. Am. Chem. Soc.*, **92**, 3810 (1970).
- (13) R. A. Bonanno, P. Kim, J. H. Lee, and R. B. Timmons, *J. Chem. Phys.*, **57**, 1377 (1972).
- (14) J. S. Gaffney, R. Atkinson, and J. N. Pitts, Jr., *J. Am. Chem. Soc.*, **98**, 1828 (1976).
- (15) H. Akimoto, M. Hoshino, G. Inoue, M. Okuda, and N. Washida, 12th Informal Conference on Photochemistry, Gaithersburg, Md., June 28–July 1, 1976.
- (16) R. Atkinson and J. N. Pitts, Jr., *J. Phys. Chem.*, **78**, 1780 (1974); **79**, 295 (1975).
- (17) R. Atkinson and J. N. Pitts, Jr., *J. Phys. Chem.*, **79**, 541 (1975).
- (18) S. W. Charles, J. T. Pearson, and E. Whittle, *Trans. Faraday Soc.*, **59**, 1156 (1963).
- (19) D. G. L. James and R. D. Suart, *Trans. Faraday Soc.*, **64**, 2752 (1968).
- (20) A. Amano, O. Horie, and N. H. Hanh, *Int. J. Chem. Kinet.*, **8**, 321 (1976).
- (21) S. W. Benson, "Thermochemical Kinetics", Wiley, New York, N.Y., 1968.
- (22) C. K. Ingold, "Structure and Mechanism in Organic Chemistry", Cornell University Press, Ithaca, N.Y., 1953.
- (23) R. J. Cvetanovic, 12th International Symposium on Free Radicals, Laguna Beach, Calif., Jan 4–9, 1976.
- (24) R. Atkinson and J. N. Pitts, Jr., *J. Chem. Phys.*, **63**, 3591 (1975).
- (25) N. R. Greiner, *J. Chem. Phys.*, **53**, 1284 (1970).
- (26) I. W. M. Smith and R. Zellner, *J. Chem. Soc., Faraday Trans. 2*, **69**, 1617 (1973).
- (27) R. Atkinson, R. A. Perry, and J. N. Pitts, Jr., *Chem. Phys. Lett.*, **38**, 607 (1976).
- (28) R. Atkinson, R. A. Perry, and J. N. Pitts, Jr., *J. Chem. Phys.*, **66**, 1197 (1977).
- (29) R. Atkinson, R. A. Perry, and J. N. Pitts, Jr., *J. Chem. Phys.*, in press.
- (30) J. A. Kerr, M. J. Parsonage, and A. F. Trotman-Dickenson, "Strengths of Chemical Bonds", in "Handbook of Chemistry and Physics", 56th ed, The Chemical Rubber Company, Cleveland, Ohio, 1975–1976.
- (31) J. H. S. Green, *Chem. Ind.*, 1575 (1962).

Kinetics of the Base-Stacking Reaction of N^6,N^6 -Dimethyladenosine. An Ultrasonic Absorption and Dispersion Study

M. P. Heyn,* C. U. Nicola, and G. Schwarz

Department of Biophysical Chemistry, Biozentrum der Universität Basel, Klingelbergstrasse 70, CH-4056 Basel, Switzerland (Received December 28, 1976)

Publication costs assisted by the University of Basel

The kinetics of the self-association reaction of N^6,N^6 -dimethyladenosine in water was studied by means of ultrasonic absorption and dispersion in the frequency range from 0.5 to 36 MHz. The self-association is believed to occur by vertical stacking of the purine rings. A single relaxation process was observed. This observation as well as the temperature and concentration dependence of the relaxation time and amplitude are in good agreement with the predictions based on a random isodesmic association model. At 25 °C the stacking recombination rate constant equals $1.74 \times 10^9 \text{ M}^{-1} \text{ s}^{-1}$. The magnitude and the temperature dependence of the recombination rate constant are in accordance with the values expected when the reaction is diffusion controlled. From the dissociation rate constant we obtain a value of $1.96 \times 10^{-8} \text{ s}$ for the lifetime of a stacked complex at 25 °C. In the evaluation of the amplitude data both the volume and enthalpy change have to be considered. For the volume change we find $\Delta V = -8.3 \text{ mL/mol}$. The isodesmic association constant determined from the kinetic measurements is consistent with the value of 34 M^{-1} at 25 °C determined from equilibrium measurements.

Introduction

In contrast to the large number of equilibrium studies on base stacking, the kinetics has not received much attention.¹⁻³ This appears to be due to two factors. Since most of the bases and nucleosides have a low solubility and a small association constant, measurements can only be performed over a limited concentration range with small amplitudes. In the second place, the relaxation times are very short ranging from 50 to 3 ns and are thus experimentally not easily accessible. Some kinetic studies have been carried out with planar aromatic compounds, such as dyes, which in aqueous solution also self-associate by

stacking.⁴⁻⁷ The kinetics of linear self-association is furthermore of considerable importance for systems which can form hydrogen bonded aggregates⁸ and for aggregates of proteins.^{9,10}

Several theoretical treatments of the kinetics of linear self-association have recently appeared. The two most frequently discussed models are the sequential model, in which only monomers can add to or break off larger aggregates, and the two-state or random association model, in which association–dissociation reactions occur between any two aggregates. The sequential model was treated in great detail from the point of view of light-scattering

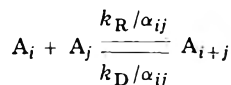
temperature-jump kinetics.^{9,10} The relaxation time spectrum and the amplitudes were calculated for a number of weighed-in monomer concentrations.^{9,10} As expected, this model led to a broad spectrum of relaxation times when the aggregation was sufficiently high. Most of the amplitude was associated with the longest relaxation time. The mean relaxation time was predicted to increase with increasing concentration and a clearly biphasic progress curve should be observed. The experimental data for the two purine derivatives investigated so far are characterized by an ultrasonic absorption spectrum which is somewhat broader than expected for a single relaxation process and by a decrease of τ with increasing weighed-in monomer concentration.¹⁻³ The sequential model appears to be inappropriate for these systems. In all of these considerations an isodesmic sequential model was assumed, in which the association constant is assumed to be independent of the length of the aggregate. In contrast to the sequential isodesmic model, which in general predicts a broad spectrum of relaxation times, the random isodesmic association model is equivalent to a dimerization model with only one relaxation time.^{1,9}

The only two studies on the base stacking kinetics of nucleic acid components were carried out with N^6,N^9 -dimethyladenine¹ and 6-methylpurine.² They were studied under conditions where base ionization reactions are negligible. In both cases ultrasonic absorption was used to determine the kinetic parameters. With the equipment presently available,^{11,12} both the ultrasonic absorption and dispersion can be measured. About 40 frequency points are obtained per spectrum. In the previous studies typically eight or nine frequency points were measured, and only the absorption was determined. We are thus in a considerably better position to answer the important question whether only one relaxation time occurs. From equilibrium measurements alone it is not possible to distinguish between a sequential isodesmic model and a random isodesmic association model. This is in principle possible from kinetic measurements by measuring the number of relaxation times and the concentration dependence of the relaxation times and amplitudes. The accuracy of the present data should allow us to make such a distinction. The appropriate expressions for the relaxation time and amplitude as a function of the weighed-in monomer concentration for the random isodesmic association model are derived in the next section. Dimer models need not be considered, since molecular weight determinations using the ultracentrifuge showed that aggregation occurs much beyond the dimer stage.¹³ In previous equilibrium measurements on the self-association of N^6,N^9 -dimethyladenosine^{13,14} we determined the association constant (34 M^{-1} at 25°C) and the enthalpy change (-6.3 kcal/mol) for the isodesmic association model. It is of interest to compare the kinetically determined association constant with the value determined from the equilibrium measurements. Hydrophobic interactions are thought to be responsible for the stacking reaction. In connection with the various theories for these interactions there is considerable interest in the sign of the volume change for the reaction. From measurements of the ultrasonic absorption amplitude the sign of this volume change could be determined. N^6,N^9 -Dimethyladenosine has the advantage of having no charged groups at neutral pH so that the contribution of protolytic reactions to the relaxation amplitude can be neglected.

Kinetics and Thermodynamics of the Random Isodesmic Association Model

In the random isodesmic association model each ag-

gregate can combine with any other aggregate and the association constant, rate constants, volume change, and enthalpy change are assumed to be independent of the size of the aggregates. These assumptions will be discussed in more detail below. We consider the following set of reactions:



A_i represents a linear aggregate consisting of i stacked monomers. i and j may assume any integer value larger or equal to 1. k_R is the common recombination rate constant, k_D is the common dissociation rate constant. When $i = j$, $\alpha_{ij} = 2$ (on symmetry grounds), otherwise $\alpha_{ij} = 1$. The equilibrium association constant equals

$$\frac{k_R/\alpha_{ij}}{k_D/\alpha_{ij}} = \frac{k_R}{k_D} = K$$

and is the same for all reactions. Let c_n be the molar concentration of the species A_n . The differential equation describing the time dependence of c_n is then ($n \neq 1$)

$$\begin{aligned} dc_n/dt = & \sum_{i=1}^{\infty} \sum_{j=1}^{\infty} (k_R/2)c_i c_j - \sum_{j=1}^{\infty} k_R c_n c_j \\ & - \sum_{i=1}^{\infty} \sum_{j=1}^{\infty} (k_D/2)c_{i+j} + \sum_{j=1}^{\infty} k_D c_{n+j} \end{aligned} \quad (1)$$

The first and fourth sum describe the formation of A_n from smaller aggregates and from larger aggregates, respectively. The second and third terms describe the decrease in c_n due to growth into larger aggregates and break up into smaller aggregates. For $n = 1$ the first and third sums are absent. The equilibrium concentrations will be denoted by \bar{c}_n . At equilibrium the left-hand side of eq 1 is zero for every n , and the solution of the set of equations is

$$\bar{c}_n = K^{n-1} \bar{c}_1^n \quad (2)$$

The equilibrium concentrations are thus the same as in the sequential isodesmic model,^{4,15} as expected. With equilibrium methods it is not possible to distinguish between the two isodesmic models. Let \bar{c}_0 be the total weighed-in monomer concentration and let \bar{c}_m be the molarity. With the help of (2) \bar{c}_0 and \bar{c}_m can be expressed in terms of \bar{c}_1 :

$$\bar{c}_0 = \sum_{i=1}^{\infty} i \bar{c}_i = \frac{\bar{c}_1}{(1 - K \bar{c}_1)^2} \quad (3)$$

and

$$\bar{c}_m = \sum_{i=1}^{\infty} \bar{c}_i = \frac{\bar{c}_1}{1 - K \bar{c}_1} \quad (4)$$

The sum in (3) converges since it represents mass conservation. Using the customary dimensionless variables $s = K \bar{c}_1$ and $L = K \bar{c}_0$

we can write (3) as

$$L = s/(1 - s)^2 \quad (5)$$

Inverting and choosing the correct root, we have

$$s = \frac{2L + 1 - (4L + 1)^{1/2}}{2L} \quad (6)$$

Substituting in (4), we find

$$K\bar{c}_m = \frac{s}{1-s} = \frac{2L+1-(4L+1)^{1/2}}{(4L+1)^{1/2}-1} = \frac{1}{2}[(1+4L)^{1/2}-1] \quad (7)$$

The variable L can be changed experimentally by varying \bar{c}_0 or the temperature. It is the natural dimensionless variable of the problem. Equations 3-7 also apply for a sequential isodesmic model. The fraction f_n of weighed-in monomers that is incorporated in aggregates of length n is given by

$$f_n = \frac{n\bar{c}_n}{\bar{c}_0} = \frac{nK^{n-1}\bar{c}_1^n}{\bar{c}_0} = n\frac{s^n}{L} = \frac{n}{L} \left[\frac{2L+1-(4L+1)^{1/2}}{2L} \right]^n \quad (8)$$

It is convenient to introduce the concept of a stacking bond. A linear aggregate consisting of i monomers contains $(i-1)$ stacking bonds. The total concentration of stacking bonds \bar{c}_{st} is thus

$$\bar{c}_{st} = \bar{c}_2 + 2\bar{c}_3 + 3\bar{c}_4 + \dots = \sum_{i=1}^{\infty} (i-1)\bar{c}_i \quad (9)$$

Clearly

$$\bar{c}_{st} + \bar{c}_m = \sum_{i=1}^{\infty} i\bar{c}_i = \bar{c}_0$$

Thus

$$K\bar{c}_{st} = K\bar{c}_0 - K\bar{c}_m = \frac{s}{(1-s)^2} - \frac{s}{(1-s)} = \frac{s^2}{(1-s)^2} = (K\bar{c}_m)^2 \quad (10)$$

or

$$\bar{c}_{st}/\bar{c}_m^2 = K \quad (11)$$

K can thus be viewed formally as the equilibrium constant for the reaction between stacking surfaces at the ends of aggregates (concentration \bar{c}_m) to form stacking bonds (concentration \bar{c}_{st}). A stacking bond can be formed by the recombination of any two aggregates. A stacking bond can be broken at any site within an aggregate. If the stacking rate constants, the volume change, and the enthalpy change are independent of the size of the stack and if the random association model is assumed, we can kinetically observe only changes in \bar{c}_{st} . Consequently the relaxation time spectrum will be completely degenerate with only one relaxation time remaining. Using eq 1 we will now derive the differential equation for \bar{c}_{st} . Multiplying (1) by $n-1$ and summing over n we obtain

$$\frac{d\bar{c}_{st}}{dt} = \frac{k_R}{2} \sum_{n=1}^{\infty} (n-1) \sum_{\substack{i=1 \\ i+j=n}} c_i c_j - k_R \sum_{n=1}^{\infty} (n-1) \sum_{j=1}^{\infty} c_n c_j - \frac{k_D}{2} \sum_{n=1}^{\infty} (n-1) \sum_{\substack{i=1 \\ i+j=n}} c_{i+j} + k_D \sum_{n=1}^{\infty} (n-1) \sum_{j=1}^{\infty} c_{n+j}$$

Taking the first two terms and the last two terms together one obtains after some manipulation

$$\frac{d\bar{c}_{st}}{dt} = \frac{k_R}{2} \sum_{i=1}^{\infty} \sum_{j=1}^{\infty} c_i c_j - \frac{k_D}{2} \sum_{i=1}^{\infty} \sum_{j=1}^{\infty} c_{i+j}$$

This result can also be written as

$$\frac{d\bar{c}_{st}}{dt} = \frac{k_R}{2} \left(\sum_{i=1}^{\infty} c_i \right)^2 - \frac{k_D}{2} \sum_{n=1}^{\infty} (n-1) c_n$$

or as

$$\frac{d\bar{c}_{st}}{dt} = \frac{k_R}{2} \bar{c}_m^2 - \frac{k_D}{2} \bar{c}_{st}$$

The rate equation for stacking bond formation is thus

$$\frac{d\bar{c}_{st}}{dt} = \frac{k_R}{2} (\bar{c}_0 - \bar{c}_{st})^2 - \frac{k_D}{2} \bar{c}_{st} \quad (12)$$

At equilibrium $d\bar{c}_{st}/dt = 0$ and we obtain the familiar result (11). By the assumption of random isodesmic association, the equilibrium and kinetic problems have been reduced formally to those of a dimerization reaction of stacking surfaces (\bar{c}_m) into stacking bonds (\bar{c}_{st}). Equation 12 can be solved and the resulting relaxation time τ is given by

$$1/\tau = k_R \bar{c}_m + (k_D/2) \quad (13)$$

Substituting for \bar{c}_m from (7), we can transform this result into a more useful and familiar form in terms of the variable L :

$$1/\tau = (k_R/2K)(4L+1)^{1/2} \quad (14)$$

Squaring we have

$$1/\tau^2 = (k_R^2/4K^2)(4L+1) = (k_D^2/4)(4K\bar{c}_0+1) = k_D k_R \bar{c}_0 + (k_D^2/4) \quad (15)$$

For a single relaxation process characterized by the relaxation time τ the ultrasonic excess absorption $\alpha\lambda$ and the ultrasonic velocity $v(\omega)$ depend on the angular frequency ω of the sound wave in the following way

$$\frac{\alpha\lambda}{\pi} = g \frac{\omega\tau}{1+(\omega\tau)^2} \quad (16)$$

$$\frac{2(v(\infty) - v(\omega))}{v(\infty)} = g \frac{1}{1+(\omega\tau)^2} \quad (17)$$

g is the amplitude of the relaxation process. $v(\infty)$ is the high frequency limit of the velocity. For the single Debye absorption curve (16), maximum absorption occurs at the angular frequency $\omega = 1/\tau$ or at the frequency $f = 1/2\pi\tau$. The amplitude g is related to the absorption maximum by

$$g = 2(\alpha\lambda)_{\max}/\pi \quad (18)$$

Alternatively g can be determined from the ultrasonic dispersion:

$$g = \frac{2(v(\infty) - v(0))}{v(\infty)} \quad (19)$$

The amplitude g is related to the reaction volume ΔV and the reaction enthalpy ΔH in the following way:

$$g = \frac{\Gamma}{RT\kappa} \left(\Delta V - \frac{\alpha_p}{\rho c_p} \Delta H \right)^2 \quad (20)$$

In (20) κ is the adiabatic compressibility, T the absolute temperature, R the gas constant, ρ the density, α_p the thermal expansion coefficient, and c_p the specific heat at constant pressure. In using this expression for the case of random association we are implicitly assuming that ΔV and ΔH are the same for all possible aggregation reactions. The factor Γ is defined by

$$\Gamma = K(\partial\bar{c}_{st}/\partial K) \quad (21)$$

and depends only on the equilibrium properties of the

system. From (10) and (5) it is easy to see that

$$\bar{c}_{st} = \bar{c}_1 L = \bar{c}_0 s$$

Using (6) we thus obtain the following expression for Γ

$$\Gamma = \bar{c}_0 L \frac{ds}{dL} = \frac{2L + 1 - (4L + 1)^{1/2}}{2K(4L + 1)^{1/2}} \quad (22)$$

Rearranging (22), we obtain

$$\Gamma = -\frac{1}{2K} + \frac{1}{2K} \frac{2L + 1}{(4L + 1)^{1/2}} \quad (23)$$

Plotting Γ vs. $(2L + 1)/(4L + 1)^{1/2}$ thus appears to be a useful way to present the amplitude data. The data at a fixed temperature and with varying \bar{c}_0 should lie on a straight line intersecting the horizontal axis at $(2L + 1)/(4L + 1)^{1/2} = 1$. The slope and the intercept with the vertical axis are equal to $1/(2K)$ and $-1/(2K)$, respectively, and depend on T via K . Since $(2L + 1)/(4L + 1)^{1/2}$ depends both on \bar{c}_0 and K , K should be known in advance. A second way to present the amplitude data is obtained by dividing eq 22 by \bar{c}_0 :

$$\frac{\Gamma}{\bar{c}_0} = \frac{2L + 1 - (4L + 1)^{1/2}}{2L(4L + 1)^{1/2}} \quad (24)$$

When the normalized dimensionless amplitude data Γ/\bar{c}_0 are plotted vs. L , all the data points both with varying \bar{c}_0 and varying T should lie on the curve (24). This function has its maximum at $L = (1 + 2^{1/2})/2 = 1.207$, is zero at $L = 0$, and decreases monotonically to zero for large L (see Figure 4). It is in principle possible to determine $K(T)$ from the \bar{c}_0 value at which Γ/\bar{c}_0 has its maximum. Since the maximum is very broad and the data are of limited accuracy, this is not an accurate way of determining K . As an order of magnitude check it is useful though. In order to determine the maximum it is necessary to collect data at L values well below 1.207.

We will now briefly discuss the assumptions made in the random isodesmic association model. The sequential model, in which only monomers can add to or break off an aggregate, may be criticized on physical grounds. It is not reasonable to exclude reactions between aggregates of various sizes since the major part of the interaction between the bases is short ranged. In the random association model this sequential restriction is removed. The isodesmic feature, namely, that the chemical parameters describing the reaction between any two aggregates are the same, is certainly a simplification. We assumed that the association constant, the rate constants, the enthalpy change, and the volume change are independent of the sizes of the two interacting aggregates. If the reaction is diffusion controlled, the recombination rate constant k_R for the self-association of two neutral aggregates A_i and A_j depends on the size of the reacting partners in the following way

$$k_R = \frac{4\pi N}{1000} (D_i + D_j)(R_i + R_j) \quad (25)$$

in which D_i is the diffusion constant and R_i is the radius of an aggregate containing i monomers. N is Avogadro's number. The diffusion constant D_i depends on the size of the particle. For a spherical particle of radius R_i we have

$$D_i = kT/6\pi\eta R_i \quad (26)$$

in which k is Boltzmann's constant, η the viscosity of the solution, and T the absolute temperature. In this case the

expression for the rate constant simplifies to

$$k_R = \frac{2NkT}{3000\eta} \frac{(R_i + R_j)^2}{R_i R_j} \quad (27)$$

With R_i proportional to i , we note that k_R is approximately independent of i and j as long as i and j do not differ too much. This is certainly the case when both i and j are small. Using (8) we can calculate the fraction of monomers incorporated in aggregates containing i monomers. With the highest L values employed in our experiments we find that more than 75% of the monomers are in aggregates with lengths less than 6. Thus in our experiments the aggregates are so small that the approximation of an i -independent rate constant appears to be justified.

Experimental Section

Materials and Methods. N^6,N^6 -dimethyladenosine (Merck-Schuchardt and Koch-Light) was found to be chromatographically pure by thin-layer chromatography. Elemental analysis confirmed this result (theoretical values in brackets): 48.88 (48.80) C, 5.73 (5.80) H. The substance was used without further purification. All solutions were prepared in twice distilled water on a weight per volume basis. Concentrations were determined spectrophotometrically using an extinction coefficient for the unstacked molecule of $18800 \text{ M}^{-1} \text{ cm}^{-1}$ at 275 nm.¹⁶

The construction of the 5-mL ultrasonic cell and the methods to determine both the absorption and dispersion have been described previously.^{11,12} For ultrasonic absorption measurements the solution densities have to be known very accurately. A minimum of four significant figures is required. The densities were determined with a digital measuring device DMA 02 C (Anton Paar KG, Graz, Austria). A NaCl solution of the same density as the N^6,N^6 -dimethyladenosine solution was used as a reference. This choice appears to be justified, since NaCl does not absorb in this frequency range and since the ultrasonic velocities in a NaCl solution and in an N^6,N^6 -dimethyladenosine solution of the same density are almost the same. Since the relaxation amplitudes are small for N^6,N^6 -dimethyladenosine, scattering from small air bubbles presented a serious problem in the 0–2 MHz range. This problem has been discussed elsewhere.¹⁷ In order to remove most of these bubbles the N^6,N^6 -dimethyladenosine solutions were heated for 1.5 h at 65 °C. The bubbles then become so large that they can be removed by gentle shaking. This treatment did not change the concentration of the solution and no hydrolysis seems to occur. To fill the cell a special syringe was used which allows a very small rate of filling.

Results

Measurements were performed for weighed-in concentrations \bar{c}_0 ranging from 3.02×10^{-2} to $17.4 \times 10^{-2} \text{ M}$ at the four temperatures 15, 25, 35, and 45 °C. The excess absorption and dispersion data for $\bar{c}_0 = 0.115 \text{ M}$ at 15 °C are shown in Figure 1. A simultaneous least-squares fit was made of both the absorption and dispersion data to eq 16 and 17 using g and τ as common parameters. Figure 1 shows that it is indeed possible to fit both sets of data assuming a single relaxation process characterized by a relaxation time τ of 14.57 ns and an amplitude g of 8.60×10^{-4} . As expected for a single Debye curve, the log–log plot of Figure 1 has a slope of +1 on the low frequency side of the maximum and of –1 on the high frequency side. The dispersion and excess absorption data can be used to construct a Cole–Cole plot. The resulting curve is circular with center on the dispersion axis, again indicating that

TABLE I: Association and Rate Constants for the Self-Association of N^6,N^6 -Dimethyladenosine in Aqueous Solution as a Function of the Temperature

T, K	$k_R, M^{-1} s^{-1}$	k_D, s^{-1}	$k_R \eta/T, \text{erg mol}^{-1} \text{deg}^{-1}$	$K,^a M^{-1}$	$K,^b M^{-1}$
288	$(1.26 \pm 0.07) \times 10^9$	$(0.28 \pm 0.01) \times 10^8$	0.50×10^5	49 ± 2.0	47 ± 2.8
298	$(1.74 \pm 0.10) \times 10^9$	$(0.51 \pm 0.02) \times 10^8$	0.52×10^5	34 ± 1.4	33 ± 2.0
308	$(2.12 \pm 0.13) \times 10^9$	$(0.89 \pm 0.04) \times 10^8$	0.50×10^5	24 ± 1.0	24 ± 1.4
318	$(2.37 \pm 0.14) \times 10^9$	$(1.33 \pm 0.05) \times 10^8$	0.45×10^5	17 ± 0.7	16 ± 1.0

^a Equilibrium measurements. ^b Amplitude measurements.

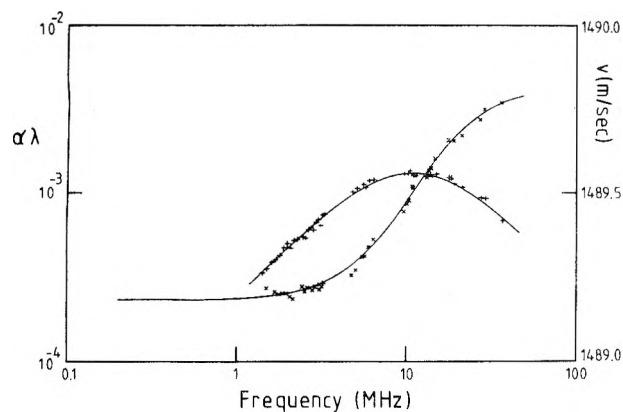


Figure 1. The sound velocity $v(x)$ and the excess sound absorption coefficient $\alpha\lambda$ (+) of a 0.115 M aqueous solution of N^6,N^6 -dimethyladenosine at 15 °C as a function of the frequency. The continuous curves are least-squares fits to eq 16 and 17 for a single relaxation process with parameters $\tau = 14.57$ ns and $g = 8.60 \times 10^{-4}$.

only a single relaxation process contributes. At each temperature and concentration the relaxation time and amplitude were determined in this way. The relaxation time data for the four temperatures are plotted according to eq 15 in Figure 2. In accordance with the theory for the random isodesmic association model the data at 15, 25, and 35 °C lie on straight lines. Although the data at 45 °C show considerable scatter they are not inconsistent with a straight line. The experimental error in τ is estimated to be $\pm 2\%$. According to eq 15 the slope of the straight line equals $k_R k_D$, the intercept on the vertical axis equals $1/4k_D^2$, and the intercept on the horizontal axis equals $-1/4K$. These three parameters are temperature dependent. The intercepts on the vertical axis are small and thus difficult to determine accurately. The slope can be determined more reliably. The data were therefore evaluated in the following way. The intercepts on the horizontal axis, $-1/4K(T)$, were fixed by using the value of the association constant obtained previously.^{13,14} The slope of the straight lines and the intercept with the vertical axis were then used to determine k_R and k_D . In this way only one kinetic constant was obtained from the kinetic data. An independent "kinetic" association constant cannot be determined in this way. Figure 2 shows, however, that the kinetic data are consistent with the values for the association constant from the equilibrium measurements, since it is possible to draw straight lines through the kinetic data and the horizontal intercepts determined by the equilibrium measurements. The values of the kinetic constants obtained in this way are collected in Table I. From the way we analyzed the data, it follows that the ratios k_R/k_D must be approximately equal to the association constants determined by equilibrium methods, as is indeed the case. The value of the recombination rate constant k_R may be compared with the prediction from eq 25 for a diffusion controlled reaction. Values for the diffusion constants of various adenine derivatives at 25 °C are available.¹⁸ A value of $4.8 \times 10^{-6} \text{ cm}^2 \text{ s}^{-1}$ appears to be reasonable for N^6,N^6 -dimethyladenosine at 25 °C. For the encounter distance $(R_i + R_j)$ we take 3.4 Å, the value

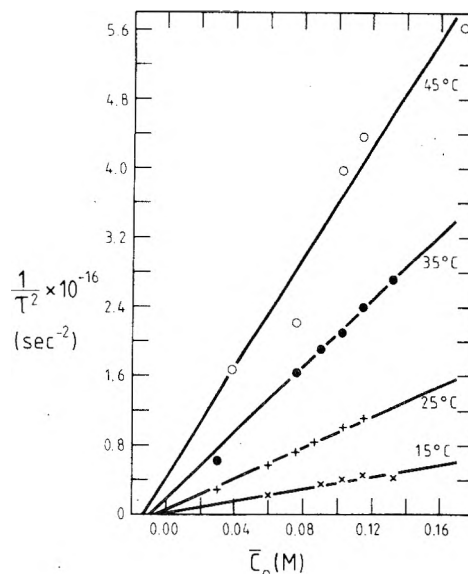


Figure 2. The square of the reciprocal relaxation time, $1/\tau^2$, plotted vs. \bar{c}_0 , the weighed-in concentration of N^6,N^6 -dimethyladenosine: (O) 45 °C; (●) 35 °C; (+) 25 °C; (X) 15 °C. The rate constants determined from the straight lines are collected in Table I.

determined from X-ray diffraction measurements for the distance between the bases in a stacked dinucleotide. Using these values we obtain a predicted recombination rate constant at 25 °C of $2.47 \times 10^9 \text{ M}^{-1} \text{ s}^{-1}$. This should be compared with the experimental value of $1.74 \times 10^9 \text{ M}^{-1} \text{ s}^{-1}$. In view of the approximations made the agreement must be considered to be satisfactory. According to eq 27, the product $k_R(T)\eta(T)/T$ must be temperature independent if the reaction is diffusion controlled. This is also the case if the particles are not spherical. The values for this product are collected in Table I. We note that these values are indeed approximately independent of the temperature. The value at 45 °C is a little lower than the others. The error in k_R at 45 °C is however quite large compared to the error in k_R at the three other temperatures. An alternative way to present these data is to plot $\ln k_R$ vs. $1/T$. In this way an approximately linear plot is obtained with an apparent activation energy of 4.1 kcal/mol. This value is in good agreement with the value of 4.4 kcal/mol at 35 °C calculated on the basis of eq 27 using the temperature dependence of the viscosity of water. We conclude that the reaction is essentially diffusion controlled.

The amplitude data were evaluated with eq 18, 19, and 20. From (20) it is apparent that at a single temperature only the absolute value of $[\Delta V - (\alpha_p/\rho c_p)\Delta H]$ can be determined. We will call this absolute value Δ . Δ was calculated from eq 20 using the experimental g values and using the Γ values calculated from (22) with the association constant K from equilibrium measurements. For a fixed temperature the Δ values so determined are approximately independent of the weighed-in monomer concentration \bar{c}_0 . Using the value of $\Delta H = -6.3$ kcal/mol previously determined from equilibrium measurements,^{13,14} the contribution of the ΔH term to Δ is about 2.7 mL/mol at 45

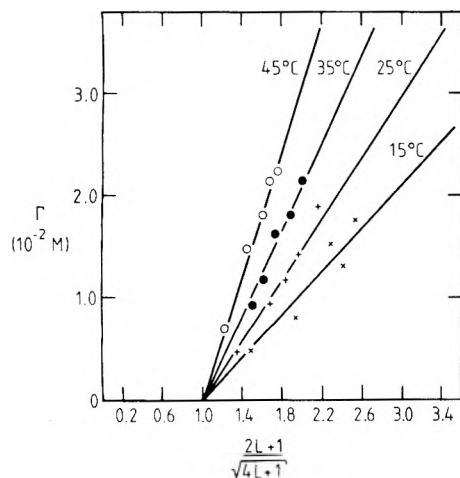


Figure 3. The amplitude of the relaxation process Γ plotted vs. $(2L + 1)/(4L + 1)^{1/2}$: (O) 45 °C; (●) 35 °C; (+) 25 °C; (X) 15 °C. For an isodesmic random self-association process the data at one temperature are predicted to lie on a straight line intersecting the horizontal axis at 1 (eq 23).

°C and cannot therefore be neglected if $|\Delta V|$ ranges between 5 and 10 mL/mol. Under such circumstances Δ is expected to be temperature dependent since the thermal expansion coefficient α_p varies considerably between 15 and 45 °C. For water α_p changes from $1.51 \times 10^{-4} \text{ deg}^{-1}$ at 15 °C to $4.23 \times 10^{-4} \text{ deg}^{-1}$ at 45 °C. We observed that Δ decreased from 7.3 mL/mol at 15 °C to 6.3 mL/mol at 45 °C. Since the contribution of the ΔH term to Δ is positive and increasing with increasing temperature, and since Δ decreases with increasing temperature, one concludes that ΔV must be negative. Correcting the Δ values at the four temperatures for the contribution of the ΔH term (using $\Delta H = -6.3 \text{ kcal/mol}^{13,14}$ and the thermal expansion coefficient of water), an approximately temperature independent ΔV value is obtained. A small temperature dependence remains, which is most likely due to experimental error. At 25 °C we find $\Delta V = -8.3 \text{ mL/mol}$. The sign of ΔV is in agreement with the concentration dependence of the apparent molar volume which can be calculated from the solution density. The apparent molar volume decreases from 205.9 mL/mol at a weighed-in monomer concentration of 0.0101 M to 202.3 mL/mol at a concentration of 0.0876 M. Making the assumption that the volume change is independent of the stack length a ΔV value of -8.2 mL/mol at 25 °C can be calculated from these data. Although the agreement with the value determined from the amplitude is fortuitous, there can be little doubt that the concentration dependence of the density is only consistent with a negative ΔV . Since we have confirmed the value of ΔV , independently of the ultrasonic absorption data, we may conversely use it together with the experimental g values to compute Γ values and to plot them according to eq 23. The results are shown in Figure 3. Equation 23 predicts that for each temperature the data at various concentrations should lie on a straight line with a slope of $1/2K(T)$ and passing through the point $(2L + 1)/(4L + 1)^{1/2} = 1$. One observes that the data are in reasonable agreement with this prediction and that the slope increases with increasing temperature as should be the case since ΔH is negative. The association constants determined from the slopes are collected in the last column of Table I. Comparing with the association constants determined from the equilibrium measurements^{13,14} (fifth column of Table I), we note that the agreement is quite good. This is not so surprising since the equilibrium association constant was used in calculating the horizontal coordinate. What the table shows

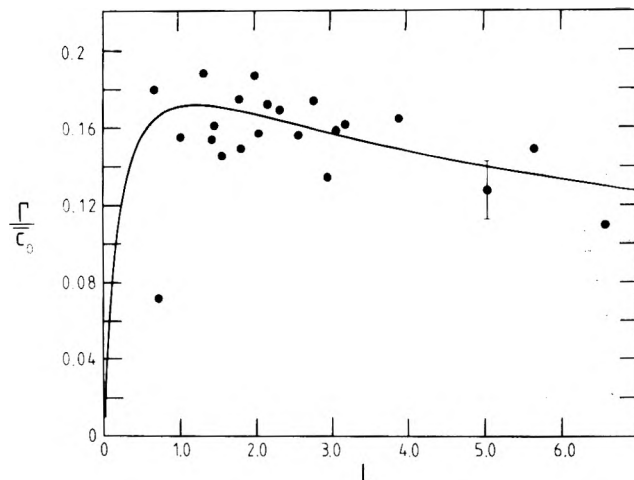


Figure 4. The amplitude Γ divided by the weighed-in monomer concentration c_0 plotted vs. $L = Kc_0$. The continuous curve is the prediction for the isodesmic random self-association model (eq 24). The error bar gives an estimate of the error in Γ/c_0 .

however is that the K values from the amplitude measurements are consistent with those from the equilibrium measurements. In principle it is possible to determine K from these amplitude data independently of the equilibrium data by fitting all the data to eq 23 using as parameters ΔH and K (25 °C). These parameters could be varied until the data at the four temperatures lie on four straight lines with slopes obeying van't Hoff's law. This was not attempted in view of the limited accuracy of the data. An alternative way to present all the amplitude data on a single curve is provided by eq 24. Such a plot of Γ/c_0 vs. L is shown in Figure 4. The continuous curve is the prediction for the isodesmic random association model (eq 24). The horizontal coordinate L was calculated using the association constant from the equilibrium measurements. Here again a least-squares fit of all the data would yield a ΔH and a K (25 °C) value. Due to the very broad maximum at $L = 1.207$ and the very considerable scatter in the experimental points, it is however not possible to determine K accurately in this way. One may conclude however that the amplitude data are at least consistent with the equilibrium association constant of 34 M^{-1} at 25 °C. An association constant which is larger or smaller by a factor of 2 is unlikely to be correct. The qualitative features predicted by the model, a decrease of the amplitude for large and small L values with a broad maximum around $L = 1.207$, are in agreement with the experimental data. Accurate data for small L values are difficult to obtain because at such concentrations the amplitude is very small. To give an idea of typical excess absorption values, α/f^2 at the resonance frequency equals $338 \times 10^{-17} \text{ s}^2/\text{cm}$ for a solution with $c_0 = 0.06 \text{ M}$ at 25 °C ($L = 2.0$). This should be compared with the value of $22 \times 10^{-17} \text{ s}^2/\text{cm}$ for water at 25 °C.

Discussion

In the previous ultrasonic absorption studies on the self-association of N^6, N^9 -dimethyladenine¹ and 6-methylpurine,² it was concluded that the absorption curves were somewhat broader than would be expected for a single relaxation process. Due to the limited accuracy, these data were not inconsistent with a random isodesmic association model,¹ which predicts only one relaxation time. They left room however for an interpretation based on models with several relaxation times. The results for 6-methylpurine for instance were explained using a sequential model with attenuated association constants,³ in which the association

constant for the formation of an aggregate consisting of n monomers equals K/n . These authors claim that their model leads to a narrow relaxation time spectrum and an absorption curve consistent with a slightly broadened Debye. The present data with typically 40 frequency points per curve, both for the absorption and the dispersion, show no broadening with respect to a single Debye curve and thus lend strong support to the random isodesmic association model. It is possible that the previously observed broadening was due to experimental inaccuracy. The sequential isodesmic association model leads under certain conditions also to a single relaxation process (complete degeneracy).⁸ These conditions are not satisfied in the present system. A simple dimerization, which would also lead to a single relaxation time, can be excluded on the basis of molecular weight determinations.¹³ In two ultrasonic absorption studies on purine nucleosides evidence was presented for absorption in the 2–4-ns range.^{19,20} The relaxation times were independent of the concentration. This fact in conjunction with other evidence led these authors to attribute the absorption to the intramolecular anti-syn conformational equilibrium of the glycosidic bond. The association constants of the nucleosides studied by these authors are so low that it is indeed likely that a contribution due to self-association could not have been observed at the concentrations employed. In our experiments we found no evidence for the presence of such a second relaxation process which should have occurred at frequencies close to the upper end of the range available to us.

The dependencies of $1/\tau^2$ and Γ on temperature and concentration are also in good agreement with the predictions from the random isodesmic association model. Although no completely independent "kinetic" association constants could be determined, the relaxation time data are consistent with the association constant from equilibrium measurements, which was also obtained using the isodesmic model. The results for k_R in Table I show that base stacking is a very fast process. From the magnitude of k_R and its temperature dependence we concluded that the reaction is diffusion controlled. At 25 °C, we obtained $k_R = 1.74 \times 10^9 \text{ M}^{-1} \text{ s}^{-1}$. This value should be compared with the corresponding values of $9.3 \times 10^8 \text{ M}^{-1} \text{ s}^{-1}$ for N^6,N^9 -dimethyladenine¹ and $1.16 \times 10^9 \text{ M}^{-1} \text{ s}^{-1}$ for 6-methylpurine.³

The amplitude data were evaluated using a bootstrap procedure. The scale of the horizontal coordinate in Figure 3 and 4 depends on K . The association constants determined from equilibrium measurements were used for this purpose. The slopes of the amplitude plots in Figure 3 can be used to determine "kinetic" association constants. The fact that these were within experimental error equal to the equilibrium values (Table I) shows the self-consistency of the equilibrium and kinetic data. From the amplitude and density data an approximately temperature independent ΔV value of -8.3 mL/mol was determined. For the closely related compound N^6,N^9 -dimethyladenine a temperature dependent volume change was found with

$\Delta V = -6.8 \text{ mL/mol}$ at 25 °C.¹ The decrease of ΔV with increasing temperature was rationalized by correlating it with a decrease in the water structure.¹ The ΔH contribution to the amplitude was neglected. In view of the fact that for N^6,N^9 -dimethyladenine $\Delta H = -8.7 \text{ kcal/mol}$,^{1,13} it is likely that at least a part of the apparent temperature dependence of ΔV can be accounted for by the contribution of the ΔH term to Δ . Using $\Delta H = -8.7 \text{ kcal/mol}$, we obtained a ΔV value of -8.9 mL/mol at 25 °C for N^6,N^9 -dimethyladenine which is about the same as the value of -8.3 mL/mol we found for N^6,N^9 -dimethyladenosine. For two other self-associating purine derivatives values are known for the volume of the reaction. For 9-methylpurine a value of -4.0 mL/mol was determined,²¹ for 6-methylpurine a value of -4.5 mL/mol was obtained.³ It is interesting to note that for these last two compounds which have rather small association constants, the ΔV values are about half of those of the two methylated adenine derivatives, which have association constants which are at least a factor of 5 larger. The sign of ΔV has also been determined for a number of purine derivatives by dilatometry.²² For all of these compounds a negative ΔV was found. It thus appears likely that the volume change for the stacking reaction of all purine derivatives is negative. This negative sign appears not to be in conflict with current thinking on the theory of hydrophobic interactions.^{21,23}

Acknowledgment. We are indebted to Dr. A. Labhardt for valuable advice. We wish to thank A. Lustig for performing the density measurements.

References and Notes

- (1) D. Pörschke, and F. Eggers, *Eur. J. Biochem.*, **28**, 490 (1972).
- (2) F. Garland and R. C. Patel, *J. Phys. Chem.*, **78**, 848 (1975).
- (3) F. Garland and S. D. Christian, *J. Phys. Chem.*, **79**, 1247 (1975).
- (4) B. H. Robinson, A. Seelig-Löffler, and G. Schwarz, *J. Chem. Soc., Faraday Trans. 1*, **71**, 815 (1975).
- (5) D. H. Turner, R. Yuan, G. W. Flynn, and N. Sutin, *Biophys. Chem.*, **2**, 385 (1974).
- (6) D. H. Turner, G. W. Flynn, S. K. Lundberg, L. D. Faller, and N. Sutin, *Nature (London)*, **239**, 215 (1972).
- (7) G. G. Hammes and C. D. Hubbard, *J. Phys. Chem.*, **70**, 1615 (1966).
- (8) J. Rassing, *Adv. Mol. Relaxation Processes*, **4**, 55 (1972).
- (9) D. Thusius, P. Dessen, and J.-M. Jallon, *J. Mol. Biol.*, **92**, 413 (1975).
- (10) D. Thusius, *J. Mol. Biol.*, **94**, 367 (1975).
- (11) A. Labhardt and G. Schwarz, *Ber. Bunsenges. Phys. Chem.*, **80**, 83 (1976).
- (12) A. Labhardt, Ph.D. Thesis, University of Basel, 1975.
- (13) R. Bretz, A. Lustig, and G. Schwarz, *Biophys. Chem.*, **1**, 237 (1974).
- (14) M. P. Heyn and R. Bretz, unpublished results.
- (15) M. P. Heyn and R. Bretz, *Biophys. Chem.*, **3**, 35 (1975).
- (16) L. B. Townsend, R. K. Robins, R. N. Loeppky, and N. J. Leonard, *J. Am. Chem. Soc.*, **86**, 5320 (1964).
- (17) E. Meyer and E.-G. Neumann, *Physikalische und Technische Akustik*, F. Vieweg und Sohn, Braunschweig, 1967, p 121.
- (18) W. J. Bowen and H. L. Martin, *Arch. Biochem. Biophys.*, **107**, 30 (1964).
- (19) L. M. Rhodes and P. R. Schimmel, *J. Am. Chem. Soc.*, **96**, 2609 (1974).
- (20) F. I. Braginskaya, *Sov. Phys. Acoust.*, **20**, 424 (1975).
- (21) U. Gaarz and H.-D. Lüdemann, *Ber. Bunsenges. Phys. Chem.*, **80**, 607 (1976).
- (22) D. D. Kasarda, *Biochem. Biophys. Acta*, **217**, 535 (1970).
- (23) P. O. P. Ts'o, in "Basic Principles in Nucleic Acid Chemistry", Vol. 1, P. O. P. Ts'o, Ed., Academic Press, New York, N.Y., 1974, p 558.

The Reaction of the Precursor of the Hydrated Electron with Electron Scavengers[†]

Charles D. Jonah,* John R. Miller, and Max S. Matheson

Chemistry Division, Argonne National Laboratory, Argonne, Illinois 60439 (Received March 4, 1977)

Publication costs assisted by Argonne National Laboratory

We show that there are several compounds whose ability to decrease the initial 50-ps yield of the hydrated electron is not correlated with the reactivity of that compound. Several mechanisms have been proposed. Explicit corrections have been included for time-dependent reaction rates. It is shown that other corrections require assumptions about the mechanism of the presolvation reaction.

Introduction

In the deposition of energy by ionizing radiation in polar media, the electrons ejected by the radiation can be solvated. A great many studies of the solvated electron in various media have been made and the properties and reactions of the solvated electron have been well catalogued.^{1,2} It has generally been assumed that an electron is ejected from the electron shell of a solvent molecule as a quasifree particle and is subsequently solvated. A great deal of information has been gained about the solvated electron but almost none about its precursor. This observation was made by Hamill 8 years ago³ and is nearly as true now as it was then.

One of the first pieces of direct evidence about the precursor came from the work of Hunt and co-workers,^{4,5} after they had improved the time resolution of pulse radiolysis experiments to 30 ps. They found that the initial yield of the solvated electron was decreased in the presence of high concentration of scavengers and the fraction of the electrons remaining, f , could be described by the expression

$$f = \exp(-[S]/C_{37}) \quad (1)$$

where $[S]$ is the concentration of the scavenger and C_{37} is a constant which depends on the solvent and the scavenger species.^{4,5} They assumed the initial yield of the electron could be determined by extrapolation of the data to zero time using the rate constants measured in the experiment.¹ It was pointed out by Schwarz⁶ that corrections are required since rate constants for fast reactions are time dependent and will affect the extrapolation.

Czapski and Peled^{7,8} pointed out that further corrections may be required because at high scavenger concentrations, some electrons may be solvated within a reaction radius of a scavenger. These initial "encounter pairs" are not accounted for by extrapolating a rate process to zero time.

The work of Hamill et al. eliminated these difficulties in interpretation by finding a system where reaction of the solvated electron is minimal.⁹ In their work, a strong decrease in the initial yield of the electron was found in ethanol when benzene was added. The rate constant of benzene is very small (less than 10^7) and so no effect of time-dependent rate constants could be expected. In alcohols, the solvation time of the electron is slower than in water so one would expect an increase in the time allowable for precursor scavenging. Qualitatively similar results were seen by Thomas using both photogeneration and radiolytic generation of electrons.¹⁰ The major difficulty with the benzene-alcohol system is that a high concentration (2 M) of benzene is required.

* Work performed under the auspices of the Division of Physical Research of the U.S. Energy Research and Development Administration.

We have attempted to find reactants with similar reactivity with the solvated electron but different reactivities with its precursor. The work of Miller shows¹¹ that in glasses, precursor and the trapped electron may have greatly different reactivities. We started by examining several compounds which had been tried in glasses. Lam and Hunt had found that except for H_{aq}^+ the reactivity of a scavenger with the precursor closely parallels the high concentration rate constant of the scavenger with the solvated electron.⁵ We have found several compounds which were considerably more, or considerably less, reactive with the precursor than one would have expected from their reactivity with the solvated electron.

Experimental Section

The picosecond pulse radiolysis equipment has been previously described in detail.¹² The Argonne microwave linear accelerator generates pulses of 20–22-MeV electrons 60 times per second. Each pulse consists of a main pulse containing greater than 90% of the charge with a width (fwhm) of 30 ps and a satellite pulse 770 ps from the main pulse. Approximately 30% of the electron beam is intercepted by a cell containing 1 atm of xenon. The Cerenkov light generated by the xenon cell is used as the analyzing light. The remainder (70%) of the electron beam is used for radiolysis of our sample. Using a focussed electron beam, approximately 1.5 krd (10^{17} eV/g) was deposited in the irradiated volume (approximately 0.25 cm³). Both the electron beam and the light beam are delayed. The delay of the light beam can be varied so that it reaches the irradiation cell before, during, or after the pulse of ionizing radiation. By varying the delay of the light beam the transmission of the sample as a function of time is determined. The light detection system used an RCA C7253A five-stage side-on photomultiplier. The photocurrent from the photomultiplier was integrated and stretched using a commercial charge sensitive FET preamplifier (Tennelec TC 162).

This system has a risetime but the risetime is not similar to the ordinary electronic risetime. The effect of the finite pulse width which causes the risetime will mask any processes occurring during the pulse and will give a smaller absorption than is actually occurring. It will not decrease the apparent rate constant measured for an exponential process. Thus, risetime affects how soon a process may be measured but not the speed at which it appears to occur.

Solutions were made using water purified by a deionizing water system which included charcoal filter and submicron final filter.¹³ Chemicals were used as received. Solutions were degassed using helium. To avoid complexes the perchlorate salts of reactive cations were used. Ferric and mercuric solutions were run in the presence of perchloric

TABLE I: Measured Values of C_{37} ^a

Compd	C_{37}	C_{37} (corr)	$r_{C_{37}}$	$k_{C_{37}}$	k_{dil}^b	k_{calcd}	k_{calc}/k_{dil}
SeO ₄ ²⁻	0.42	0.42	9.8	0.36	0.11	2.0	18.0
MoO ₄ ²⁻	0.63	0.65	8.5	0.5	0.2 ^c	1.5	5.0
OCl ⁻	0.48	0.52	9.1	1.6	0.7	2.75	4.0
Acetone	1.4 (1.4)	1.6	6.3	0.87	0.87	2.9	3.6
NO ₃ ⁻	0.42 (0.45)	0.47	9.5	2.0	1.1	2.9	2.8
Te(OH) ₆	0.075	0.09	16.0	3.7	3.2 ^c	7.3	2.3
Cu ²⁺	0.9	1.3	6.6	3.0	3.3	7.2	2.2
HgCl ₂	0.08	0.09	16.0	5.4	3-4 ^c	7.3	1.7-2.1
Ag ⁺	0.14	0.17	13.3	6.0	4.0	7.8	1.9
Cr ³⁺	0.30	0.84	7.8	7.0	6.0	10.2	1.7
CH ₃ NO ₂	0.30	0.37	10.2	4.0	3.0	4.7	1.6
Cd ²⁺	0.38 (0.35)	0.55	9.0	4.0	5.0	8.0	1.6
Fe ³⁺	1.3	> 3.5	< 5.0	5.3	6.0 ^c	9.6	1.6
Hg ²⁺	0.062	0.09	16.0	8.0	8.0	10.8	1.4
CrO ₄ ²⁻	0.2 (0.2)	0.26	11.5	4.5	2.0	2.7	1.35
IO ₄ ⁻	0.14	0.33	11.0	11.0	3.7 ^d	3.6	0.98

^a The measured values of C_{37} are defined in Eq 1 and are given in mol L⁻¹. $C_{37}(\text{corr})$ is the C_{37} corrected for time-dependent rate constants, also in units of mol L⁻¹. The values in parentheses are those measured by Hunt.⁵ $r_{C_{37}}$ is the reaction radius in angstroms necessary to explain the corrected C_{37} with a Czapski-Peled type argument.^{7,8} The $k_{C_{37}}$ rate constants are all in units of 10¹⁰ mol⁻¹ s⁻¹. k_{calcd} is the rate constant calculated using $r_{C_{37}}$ and the Smoluchowski-Debye equation. $k_{C_{37}}$ is the rate constant at concentration = C_{37} . ^b Rate constants from M. Anbar, M. Bambenek, and A. B. Ross, *Natl. Stand. Ref. Data Ser., Natl. Bur. Stand., No. 43* (1973). ^c Extrapolated from picosecond measurement. ^d Measured by J. R. Miller and B. B. Saunders, unpublished result.

acid to prevent hydrolysis. All mercuric perchlorate solutions were run equimolar in acid, and the 0.005 and 0.05 M Hg were also run in 0.025 and 0.2 M perchloric acid, respectively. The ferric perchlorate solutions were run in either 0.025 M perchloric acid or perchloric acid one-half the concentration of the ferric ion, whichever gave the higher acid concentration. Corrections were made for the reaction of the acid with the hydrated electron.

Rate constants were determined from the data using a nonlinear least-squares fitting routine. The maximum absorption and the first-order decay constant were measured. From these values the initial yield was determined from a precalculated table. The table was calculated assuming triangular light and electron pulses, of 30 and 40 ps, full width at half maximum, respectively, instantaneous formation of the electron and an exponential decay process. The table is relatively insensitive to most assumptions as long as the pseudo-first-order constant is less than a few times 10¹⁰. A larger uncertainty can come from the finite absorption at "infinite" time. This can be caused by direct effects on the solute (which is not unlikely considering the concentrations we use), absorbances from products of reactions between electrons and the solute, and transient absorbances in the cell windows. The first and third causes will affect the value one should use for the initial absorption of the electron differently than does the second. One must decide which mode causes the absorption to correctly interpret the absorption. (These absorbances are small ($\approx 0.5\%$) compared to the hydrated electron absorption ($> 30\%$) but in the presence of a scavenger which decreases the absorption of the electron to 0.1 of its initial value, a considerable error could arise).

In general, concentrations studied are under 1 M so corrections for wavelength shift of the electron should be small. Increased electron density of the solutions might increase the yields by as much as 5% (for 1 M NaNO₃), which would be within the error limits of the experiments. No corrections were made for shift in spectral absorption, and only for solutions greater than 1 M were corrections made for the change in electron density.

Results and Discussion

A typical semilogarithmic plot, from which the C_{37} is measured, is shown in Figure 1. Similar plots were done

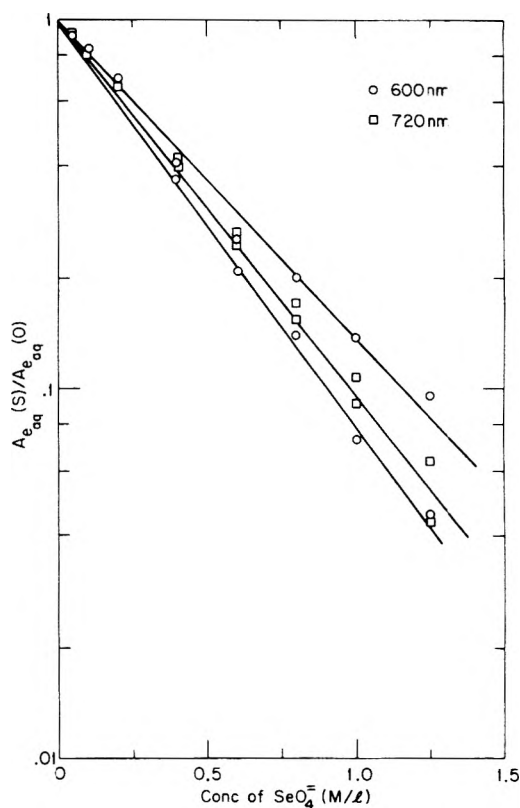


Figure 1. Plot of the fraction of electron remaining vs. the concentration of selenate. The amount of absorption of the electron relative to the final absorption in the presence of selenate is larger at 720 nm than at 600 nm. The two points at each concentration make different assumptions about the meaning of the final absorption (see text for the two assumptions). The two extreme lines were used to measure the error limits on C_{37} .

for the other species. Two wavelengths were used for the selenate experiments to eliminate effects of final product absorption. Table I summarizes the data for the compounds we have studied. C_{37} values in parentheses are those of Hunt and co-workers.⁵ The rate constants in the table are evaluated at the C_{37} concentration.

To relate these C_{37} values we must correct for any effects of time-dependent rate constants. If we take the for-

mulation of Noyes,¹⁴ the time dependent rate constant $k(t)$

$$k(t) = \frac{4\pi\rho D'}{1 + (4\pi\rho D'/k_i)} \left[1 + \frac{k_i}{4\pi\rho D} e^{-x^2} \operatorname{erfc}(x) \right]$$

$$x = \left(\frac{Dt}{\rho} \right)^{1/2} \left(1 + \frac{k_i}{4\pi\rho D} \right) \quad (2)$$

where ρ is the reaction radius, D' is the sum of the diffusion constants of the species reacting, and k_i is the intrinsic reactivity, if there were no diffusion limitations. To make a correction for time-dependent rate constants it is necessary to assume a value for k_i . The values of the time-dependent rate constants are only weakly dependent on k_i for times greater than 50 ps. (ρ and k_i can be adjusted, within reason, to match long-time behavior.) The parameter k_i will determine the maximum value of the second-order rate constant. We have calculated corrections assuming that k_i is very large (pure Smoluchowski behavior). The C_{37} values corrected for time-dependent rate constants are shown in Table I. Only for those reactions with large rate constants is the correction substantial.

As Czapski and Peled have pointed out,^{7,8} the initial yield of the electron may be decreased without invoking any new type of reaction. If an electron is solvated closer than its reaction radius from a scavenger, it will react. The kinetics one will see is a normal decay having as the initial number of electrons, not all the electrons created, but only those which are not solvated within the reaction radius of an electron. The dependence of the decrease of the initial yield of hydrated electron on scavenger concentration is the same as that which Hunt et al.^{4,5} and we have observed, a semilogarithmic plot.

To see if the effect proposed by Czapski^{7,8} is sufficient to explain the decrease of the initial yield for a particular compound, we should compare the reaction radius for that compound with the radius necessary to explain the "prediffusion" decrease in the solvated electron (C_{37}). For a positively charged ion, it is difficult to determine with any reliability the reaction radius which would explain the dilute rate constant (k_{dil}). Since it is straightforward to calculate the dilute rate constant that would be expected from a given radius and charge, we compare k_{dil} with the rate constant calculated using $r_{C_{37}}$ (k_{calcd}).

In Table I we have summarized all of the data including the ratio of k_{calcd} to k_{dil} . The table is arranged with the highest ratio k_{calcd} to k_{dil} on top. If time-dependent rate constants and the effect of Czapski and Peled were the only causes of reduced initial yields, this ratio would be one for diffusion-controlled reactions aside from small variations due to the inaccuracy of the Smoluchowski-Debye equation.¹⁵ Looking at Table I, we see that this ratio is between 1.0 and 18, and all but IO_4^- are above 1.3. Clearly there is an additional mechanism for reducing the initial yield.

In Figure 2 we have plotted the dilute concentration rate constant vs. k_{calcd}/k_{dil} . It appears as if the data points fall along two lines, one of slope $\sim 1/3$ for the positively charged and neutral species and one of slope $\sim 2/3$ for the negatively charged species. These types of plots could only have significance if the rate constant can be described by the Smoluchowski-Debye equation with a reaction radius greater than zero. This limitation is necessary since the Smoluchowski-Debye equation gives a rate constant 3.15×10^{10} for a single charged positive reacting with a hydrated electron and 6.3×10^{10} for a doubly charged positive reacting with the hydrated electron when the reaction radius is zero. Therefore the zinc ion could not possibly fall on either of the lines plotted in Figure 2. Zinc must

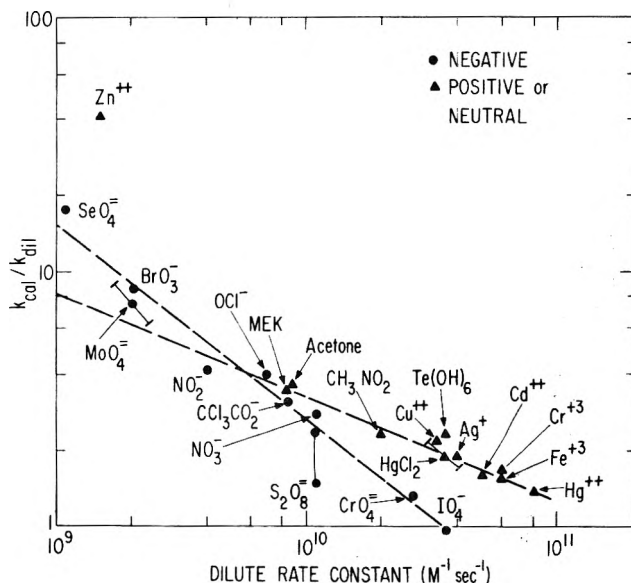


Figure 2. Plot of dilute rate constant vs. k_{calcd}/k_{dil} (Table I). The two dashed lines have slopes of $-1/3$ (goes through positive or neutral species) and $-2/3$ for the negative species.

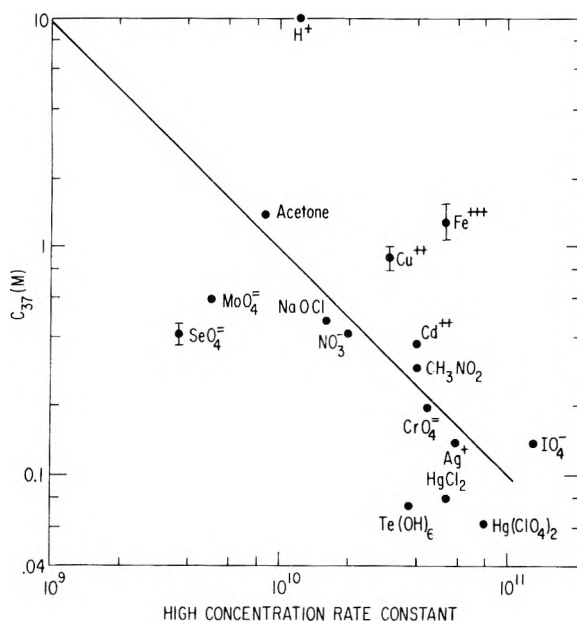


Figure 3. Plot of C_{37} for the scavenger vs. high concentration rate constant. The line is that of Lam and Hunt.⁵

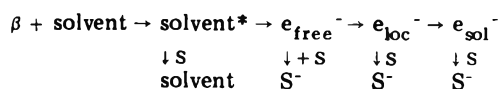
be slightly above a line with a slope of -1 originating from k_{dil} of 6.3×10^{10} . There are similar limits to $+1$ and $+3$ ions.

Lam and Hunt have proposed that measured C_{37} and high concentration rate constants could be correlated by the expression⁵

$$k_{e_{aq}}^{-1} C_{37} = (1.0 \pm 0.2) \times 10^{10} \text{ s}^{-1} \quad (3)$$

Figure 3 shows a plot of our data. The straight line is the Hunt expression. Note that these are the C_{37} values uncorrected for time-dependent rate constants to make them comparable to the work of Lam et al. We also use the high concentration rate constants. Selenate, molybdate, and telluric acid are quite a bit more efficient decreasing the initial yield than would be predicted from the relationship of Lam and Hunt while cupric and ferric are much less efficient. These data may not fairly show the ability of the Hunt expression to correlate the rate constant to C_{37} . We have consciously tried to pick compounds which

Scheme I



we felt, through studies of glasses or other data, would not fit this expression. Not all were selected that way of course. Some were run to check our technique by reproducing the data of Hunt (see Table I).

It seems clear that there is evidence of a reaction of a precursor that cannot be explained by the hypothesis of Czapski and Peled.^{7,8} For instance, selenate and chromate have C_{37} radii of 9.8 and 11.5, respectively, a difference of 15%, while their dilute reaction rates differ by a factor of 18. Physically, selenate and chromate are fairly similar so we would not expect there to be some physical characteristic which would detract from the reactions of the selenate ion but which would not interfere with the chromate ion.

To be able to correlate the ability to decrease the initial yield of an electron with the chemical properties of the scavenger, one must consider the effects of Czapski and Peled. After making necessary corrections the correlations could then give us information about the mechanisms of the reaction of the precursor of the solvated electron. Unfortunately to make the correction requires an understanding of the mechanism of reaction. To show this we consider a pathway for the formation of the solvated electron as shown in Scheme I. We use β for the irradiating fast electron S for a scavenger molecule and solvent* as an excited state solvent molecule. The e_{free}^- is a nonlocalized electron presumably losing energy on collisions and e_{loc}^- is an electron which has become localized, but is not yet fully solvated. This includes a range of states between just barely localized and fully solvated which probably occur roughly from 10^{-14} to 10^{-12} s in water. It seems clear that reaction of the scavenger with an interaction radius will give the semilogarithmic plot which has been observed.

Reaction with solvent* is probably not the major mechanism by which scavengers reduce initial solvated electron yields. The experimental data show that the initial yield decreases very close to exponentially with increasing scavenger concentration, to at least a factor of 10 reduction in initial yield. Therefore the scavenger must be reacting with a species which is the common precursor of all of the solvated electrons. Solvent* is probably not a precursor of all, or even the majority of solvated electrons. Instead, many or perhaps most are the result of direct ionization¹⁶⁻¹⁹ in which the electron is ejected with several volts of energy,¹⁷ and thus could not be considered to originate from a precursor having a lifetime longer than 10^{-15} s. Indirect, auger ionizations contribute a small fraction. These conclusions, which are based on gas phase data, are also expected to hold for condensed phases.¹⁹

There has been much consideration given to the reaction $e_{\text{free}}^- + S \rightarrow S^{\cdot-}$.^{4,20} To describe the amount of electron solvated as a function of scavenger concentration, the expression

$$\frac{e_{\text{sol}}^-(S = S_0)}{e_{\text{sol}}^-(S = 0)} = \frac{(1 - f_{\text{ps}} N_s)^m \ln P}{\ln [P(1 - f_{\text{ps}} N_s)]} \quad (4)$$

has been derived where f_{ps} is the probability of a scavenger reacting with a presolvation electron in one collision, N_s is the mole fraction of scavenger, P is the probability that the electron does not solvate in a collision, and m is the number of collisions required before the electron could possibly solvate.²⁰

We cannot say whether this type of mechanism is a reasonable explanation for our data since we do not know values for m , f_{ps} , and P . We can put conditions on the magnitude of these parameters if this equation is to fit our data. For the species that reacts most quickly with the presolvated electron, telluric acid, f_{ps} will be largest. For an f (telluric acid) and m we calculated the P necessary so that at 0.1 M $\text{Te}(\text{OH})_6$ the right-hand side of eq 4 is 0.37. One then sees if the log of the right-hand side is linear with N_s in the region of $M = 0.02$ – 0.3 M. It turns out that $m > 300/f$ (telluric acid). This limit requires about twice the error limits we see on our data. A less conservative estimate would be $m > 400/f$. Either of these values of m is much larger than 6 to 10, the range of m proposed by Freeman.²⁰

For the last step in the mechanism $e_{\text{loc}}^- + S$, it is clear that if the reaction radius for this reaction is greater than the radius for e_{sol}^- with a scavenger no Czapski–Peled type correction is necessary. If the reaction radius is less such a correction would be necessary. However, if all of the reaction was due to e_{loc}^- reaction, the data of Table I are consistent with the e_{loc}^- reaction radius being larger than the reaction radius of e_{sol}^- with the scavenger.

If we parametrize the reaction of e_{free}^- as

$$\frac{e_{\text{sol}}^-(S = S_0)}{e_{\text{sol}}^-(S = 0)} = e^{-[S_0]/C_{37}} \quad (5)$$

and e_{loc}^- as

$$\frac{e_{\text{sol}}^-(S = S_0)}{e_{\text{sol}}^-(S = 0)} = e^{-[S_0]/C_{37}^{\text{loc}}} \quad (6)$$

and the Czapski–Peled effect as

$$\frac{e_{\text{sol}}^-(S = S_0)}{e_{\text{sol}}^-(S = 0)} = e^{-[S_0]/C_{37}^{\text{CP}}} \quad (7)$$

than the fraction of the electron that remains at time just greater than 0, f if the reaction takes place with e_{loc}^- is

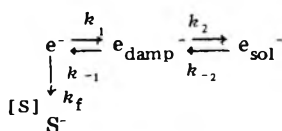
$$f = e^{-[S]/C_{37}^{\text{loc}}} \quad (8)$$

while if the reaction takes place with the free electron

$$f = e^{-[S_0]/C_{37}^{\text{free}}} e^{-[S_0]/C_{37}^{\text{CP}}} = e^{-[S]/C_{37}^{\text{meas}}} \quad (9)$$

We see then, if one wants to correlate the reactivity of a precursor of an electron with some property, the mechanism of the reaction will determine what sort of corrections should be made to measured data to obtain the number one should use to make correlations.

Another mechanism has been proposed where all reactions of the solvated electron go through a mechanism of the form²¹



where e_{damp}^- is the same stage of partial solvation. It would appear that this mechanism is ruled out by the data of chromate and selenate. Since all steps in the mechanism would be the same for chromate and selenate except the reaction step, one would expect that the ratio of $1/C_{37}$ of chromate to $1/C_{37}$ of selenate would be the same as the ratio of their rate constants. However

$$\frac{k_{\text{CrO}_4^{2-}} - 1/C_{37}^{\text{SeO}_4^{2-}}}{k_{\text{SeO}_4^{2-}} - 1/C_{37}^{\text{CrO}_4^{2-}}} = 9 \quad (10)$$

considerably different from one. It is conceivable that there could be a structure changing function of the selenate which would explain the data; however, in looking at Figure 3, we see that selenate is not unique. The data are well scattered on the graph and no slope of -1 would appear to be satisfactory. Since the data of Hunt seems to fit the line shown, it is possible we are looking at unusual species; however, the number of species differing greatly from the line argues for this not being the case.

Conclusions

We have found that for most of the species studied, the mechanism proposed by Czapski and Peled together with corrections for time-dependent rate constants is insufficient to explain the decrease of the initial yield. In addition, we find that the correlation between C_{37} and rate constant does not seem to be general but only fit a restricted class of compounds.

The mechanism that one invokes for the decrease of the initial yield of the electron determines what sort of corrections one must make to get a number which is indicative of the dry electron reactivity with a scavenger.

To correlate dry electron reactivity with other parameters one must make an assumption on the mechanism of dry electron reactions.

Acknowledgment. We acknowledge the assistance of R. M. Clarke in the running of these experiments. We are grateful to Donald Ficht, Lee Rawson, and Joe Becker for

keeping the accelerator faithful. We also are grateful for the friendly and helpful discussions with John Hunt and Gidon Czapski.

References and Notes

- (1) "The Solvated Electron in Radiation Chemistry", A. K. Pikaev, Translated by Israel Program for Scientific Translations, Ltd. IPST Cat. No. 5848, Available from U.S. Department of Commerce, National Technical Information Service, Springfield, Va., 22151.
- (2) M. S. Matheson in "Physical Chemistry", Vol. VII, Academic Press, 1975, New York, N.Y., Chapter 10.
- (3) W. H. Hamill, *J. Phys. Chem.*, **73**, 1341 (1969).
- (4) R. K. Wolfe, M. J. Bronskill, and J. W. Hunt, *J. Chem. Phys.*, **53**, 4211 (1970).
- (5) K. Y. Lam and J. W. Hunt, *Int. J. Radiat. Phys. Chem.*, **7**, 317 (1975).
- (6) H. A. Schwarz, *J. Chem. Phys.*, **55**, 3647 (1971).
- (7) G. Czapski and E. Peled, *J. Phys. Chem.*, **77**, 893 (1973).
- (8) G. Czapski and E. Peled, "Radiation Research", Proceedings of the Fifth International Congress of Radiation Research, O. F. Nygaard, H. I. Adler, and W. K. Sinclair, Ed., Academic Press, New York, N.Y., 1975, p 356.
- (9) H. Ogura and W. H. Hamill, *J. Phys. Chem.*, **78**, 504 (1974).
- (10) A. Bromberg and J. K. Thomas, *J. Chem. Phys.*, **63**, 2124 (1975).
- (11) J. R. Miller, *J. Phys. Chem.*, **79**, 1070 (1975).
- (12) C. D. Jonah, *Rev. Sci. Instrum.*, **46**, 62 (1975).
- (13) Continental Water Company, Chicago, Ill.
- (14) R. M. Noyes, *Proc. React. Kinet.*, **1**, 129 (1961).
- (15) Reference 1, p 158.
- (16) I. Santar and J. Bednar in "Proceedings of the Second Tihany Symposium on Radiation Chemistry", J. Dobo and P. Hedrig, Ed., Publishing House of the Hungarian Academy of Sciences, Budapest, 1967, p 17.
- (17) Y.-K. Kim, ref 8, p 219.
- (18) D. H. Katayama, R. E. Huffman, and C. L. O'Bryan, *J. Chem. Phys.*, **59**, 4309 (1973).
- (19) R. L. Platzman in "Radiation Research", Proceedings of the Third International Congress of Radiation Research, G. Silini, Ed., p 20.
- (20) G. L. Bolton, K. N. Jha, and G. R. Freeman, *Can. J. Chem.*, **54**, 1497 (1976).
- (21) J. W. Hunt, K. Y. Lam, and W. J. Chase, ref 8, p 345.

Reactions of Phosphate Radicals with Organic Compounds¹

P. Maruthamuthu and P. Neta*

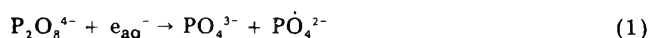
Radiation Laboratory, University of Notre Dame, Notre Dame, Indiana 46556 (Received March 8, 1977)

Publication costs assisted by the U.S. Energy Research and Development Administration

Phosphate radicals in the three acid-base forms, $\text{H}_2\text{P}\dot{\text{O}}_4$, $\text{HP}\dot{\text{O}}_4^-$, and $\text{P}\dot{\text{O}}_4^{2-}$, were produced by the reaction of hydrated electrons with peroxodiphosphate ions at pH values of 3-4, 7-9, and 12, respectively. Rate constants for the reactions of these radicals with organic compounds were determined by following the rate of decay of the phosphate radical absorption in the presence of increasing concentrations of the substrate. Rates of reaction of $\text{H}_2\text{P}\dot{\text{O}}_4$ were found to be higher than those of $\text{HP}\dot{\text{O}}_4^-$ and $\text{P}\dot{\text{O}}_4^{2-}$ by a factor of $\sim 4-10$, while the latter radicals have similar rates. The rate constants for hydrogen abstraction from aliphatic compounds ranged from $\sim 10^5 \text{ M}^{-1} \text{ s}^{-1}$ for acetic acid and 2-methyl-2-propanol to $\sim 10^8 \text{ M}^{-1} \text{ s}^{-1}$ for 2-propanol and formate. Addition to a double bond was not faster but reaction with aromatic compounds reached a rate constant $> 10^9 \text{ M}^{-1} \text{ s}^{-1}$ for the most reactive compounds. The effects of substituents were found to be similar for $\text{H}_2\text{P}\dot{\text{O}}_4$ and $\text{S}\dot{\text{O}}_4^-$ and both radicals are suggested to react with the aromatic ring by one-electron transfer to the inorganic radical. In hydrogen abstraction reactions $\text{H}_2\text{P}\dot{\text{O}}_4$ (and $\text{S}\dot{\text{O}}_4^-$) were found to react with rate constants $\sim 10-100$ times lower than those of OH and to have a selectivity about three times higher than that of OH. Radiolytic chain decomposition of peroxodiphosphate in the presence of some organic compounds was also studied.

Introduction

Phosphate radicals can be produced most efficiently by the reduction of peroxodiphosphate, e.g., with hydrated electrons:



Similar reactions take place with the protonated forms

$\text{HP}_2\text{O}_8^{3-}$ and $\text{H}_2\text{P}_2\text{O}_8^{2-}$. The rate constant for reaction of e_{aq}^- increases upon protonation from $1.8 \times 10^8 \text{ M}^{-1} \text{ s}^{-1}$ for $\text{P}_2\text{O}_8^{4-}$ to $5.3 \times 10^9 \text{ M}^{-1} \text{ s}^{-1}$ for $\text{H}_2\text{P}_2\text{O}_8^{2-}$.² The phosphate radical can also be produced by oxidation of phosphate ions with OH radicals but this reaction is very slow³ and is impractical to use as a source of these radicals. Photolysis of phosphate⁴ or peroxodiphosphate can also yield the phosphate radical by electron detachment from the

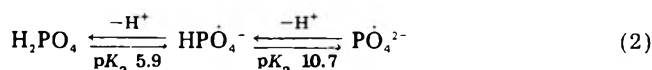
TABLE I: Rate Constants for Reactions of the Acid-Base Forms of the Phosphate Radical^a

Compound	H ₂ PÖ ₄	HPÖ ₄ ⁻	PÖ ₄ ²⁻
Methanol	4.1 × 10 ⁷	1.0 × 10 ⁷	1.0 × 10 ⁷
Ethanol	7.7 × 10 ⁷	2.0 × 10 ⁷ (4.0)	1.9 × 10 ⁷
2-Propanol	1.4 × 10 ⁸ (1.6)	2.5 × 10 ⁷ (4.0)	1.8 × 10 ⁷
2-Methyl-2-propanol	3.9 × 10 ⁶	4.5 × 10 ⁵	4.2 × 10 ⁵
Formate ion	1.5 × 10 ^{8b}	2.5 × 10 ⁷ (2.9)	2.2 × 10 ⁷
Acetic acid ^c	3.4 × 10 ⁵	8.5 × 10 ⁴	
Glycine ^d	≤ 10 ⁵		2.6 × 10 ⁷

^a Given in M⁻¹ s⁻¹. Determined at pH 12, 7, and 4 for PÖ₄²⁻, HPÖ₄⁻ and H₂PÖ₄, respectively, except as noted. The previously determined values⁵ are given in parentheses. ^b Measured at pH 4.5. ^c The rate constants are for reaction of HPÖ₄⁻ with CH₃CO₂⁻ at pH 7.1 and of H₂PÖ₄ with CH₃CO₂H at pH 3.6. ^d The reaction of PÖ₄²⁻ is with H₂NCH₂CO₂⁻ while that of H₂PÖ₄ is with H₃N⁺CH₂CO₂⁻ measured at pH 4.5.

former or rupture of the O-O bond in the latter.

The phosphate radical exists in three acid-base forms with approximate pK_a values as follows:³



These forms can react with organic compounds as do SÖ₄⁻ or OH radicals, i.e., they may abstract hydrogen, add to unsaturated compounds, or possibly oxidize by electron transfer. Several rate constants were measured⁵ which indicate a difference in the reactivity of H₂PÖ₄ and HPÖ₄⁻. Qualitative differences between HPÖ₄⁻ and SÖ₄⁻ were also indicated by ESR observation of organic intermediates.⁶

In the present study the absolute rate constants for reaction of the phosphate radical with some 20 organic compounds were measured. Radiolytic yields were also determined by chemical methods in a few systems. The behavior of the phosphate radical is compared with those of other oxidizing radicals.

Experimental Section

The peroxodiphosphate (PDP) was obtained from the FMC Corp. and was purified as described previously.⁷ Other inorganic compounds were Baker Analyzed Reagents. The alcohols, acetone, sodium formate and acetate, and propionic, malonic, succinic, and benzoic acids were also Baker Analyzed Reagents. Terephthalic and *p*-hydroxybenzoic acids were obtained from Eastman and the rest of the organic chemicals from Aldrich.

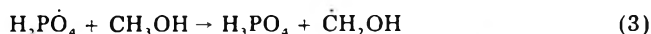
Solutions of 10–20 mM peroxodiphosphate were prepared in triply distilled water and buffered at the desired pH with sodium phosphates or tetraborate. Oxygen was removed by bubbling with pure nitrogen. The decay of the phosphate radical was monitored by kinetic spectrophotometric pulse radiolysis, mostly from observations at 520 nm, the maximum of its absorption.^{2,3} Increasing concentrations of the organic substrate were then added and the decay monitored in each case. The computerized pulse radiolysis apparatus was described previously^{8,9} and the radiation source in this case was an ARCO LP-7 linear accelerator. The electron pulses were of 5-ns duration and the currents used produced 2–3 μM of radicals as determined by thiocyanate dosimetry. Because of the low doses used and the low extinction coefficient of the phosphate radical, it was necessary to average many kinetic curves with each solution. Typically the data from ten pulses were averaged and five such averages were recorded and analyzed for each concentration. A plot of the pseudo-first-order rate constants vs. concentration gave a straight line from which the second-order rate constants were derived. The accuracy of the rate constants reported in the tables was always better than ±20% and in most cases approached ±10%.

γ-Irradiations were carried out using a ⁶⁰Co source with a dose rate of 4.7 × 10¹⁷ eV g⁻¹ min⁻¹. The concentration

of PDP before and after irradiation was determined by oxidation of excess Fe²⁺ in 1 N H₂SO₄ and spectrophotometric measurement of the Fe³⁺ formed (using ε₃₀₄ 2174 M⁻¹ cm⁻¹). This method cannot be used in the presence of organic compounds because a thermal chain reaction develops. Therefore, PDP concentrations were determined directly by spectrophotometry at 240 nm using extinction coefficient values of 58.3 at pH 3, 68.3 at pH 6.5, 46.2 at pH 10.5, and 49.3 over the range of pH 11–13. These extinction coefficients were determined by reference to the Fe²⁺ method in the pure PDP solution. G(-PDP) was determined for each solution from a yield vs. dose plot.

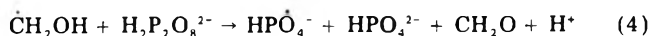
Results and Discussion

A comparison of the rate constants for the reaction of the three acid base forms of the phosphate radicals is given in Table I. Four of these values were determined previously⁵ and the two sets of results agree reasonably well. The rate constants are found to increase in this order: acetate, 2-methyl-2-propanol, methanol, ethanol, 2-propanol, and formate. This behavior is qualitatively similar to that found for reactions of OH and SÖ₄⁻ with these compounds (see below). The reactions in all these cases involve a hydrogen abstraction, e.g.



With all compounds the reaction of H₂PÖ₄ is the most rapid, that of HPÖ₄⁻ is slower by a factor of 4 to 8, while PÖ₄²⁻ reacts only slightly more slowly than HPÖ₄⁻.

Previous work indicated that the organic radicals produced by reaction 3 may reduce the peroxodiphosphate and propagate a chain reaction,² e.g.



If reaction 4 is sufficiently rapid under the conditions of the pulse experiments, the decay of the phosphate radical may level off at a plateau value corresponding to a steady-state concentration of this radical. No such phenomenon could be found in our experiments indicating that reaction 4 is not contributing to the observed kinetics.

Examination of the radiolytic decomposition of peroxodiphosphate (Table II) shows a chain reaction whose length is strongly dependent upon the organic compound used and upon the pH of the solution. No chain reaction develops with 2-methyl-2-propanol because the radical $\dot{\text{C}}\text{H}_2\text{C}(\text{CH}_3)_2\text{OH}$ does not reduce PDP. Similar results were obtained with pinacol and glycine. In experiments with formic acid G(-PDP) greater than 1000 is observed. However, the value decreased with increase in pH and no chain reaction is detected at pH ≥ 9. The reducing radical is $\dot{\text{C}}\text{O}_2^-$ at all pH values studied and the rate constant for reaction of the phosphate radical with formate does not change between pH 7 and 12. It must be concluded, therefore, that the reduction of PDP by $\dot{\text{C}}\text{O}_2^-$ is affected

TABLE II: Effect of pH on the Radiolytic Decomposition of Peroxidiphosphate in Solutions Containing Organic Compounds

Compound	pH	$G(-PDP)$
Methanol ^f	3.0	18.2
	6.5	12.7
	10.0	6.5
Ethanol ^a	10.7	10.8
	3.0	85
	6.5	51
2-Propanol ^a	10.5	24
	11.6	46
	3.0	157
2-Methyl-2-propanol ^a	6.5	50
	10.5	3.9
	13	13.6
Formic acid ^b	3.0	3.2
	6.5	3.0
	10.5	2.0
Formic acid ^b	2.8	1025
	3.7	400
	4.4	320
	5.6	93
	6.7	54
	7.8	14.2
	9.0	2.8
10.5	1.8	

^a The concentration of PDP was 0.005 M and of the alcohol 0.25 M. ^b The concentration of PDP was 0.016 M and of formic acid 0.32 M.

by pH and is the rate-determining step. The reduction rate must decrease in the order $H_2P_2O_8^{2-}$ ($pK_a = 5.2$),¹⁰ $HP_2O_8^{3-}$ ($pK_a = 7.7$),¹⁰ $P_2O_8^{4-}$, similar to the decrease observed in their rate of reaction with e_{aq}^{-2} .

Similar effects are also observed with methanol, ethanol, and 2-propanol (Table II). The chain length increases in that order in agreement with the increase expected in the rate of reduction of PDP by CH_2OH , CH_3CHOH , and $(CH_3)_2COH$.¹¹ A decrease in yield with increasing pH is again observed with each alcohol and is the result of decreasing rate of reduction of PDP upon its deprotonation. However, in more strongly alkaline solutions, where the alcohol radicals dissociate into CH_2O^- , CH_3CHO^- , and $(CH_3)_2CO^-$, the chain reaction becomes more efficient. This result is expected since the anionic forms of the alcohol radicals are known to be more strongly reducing than the neutral radicals.¹¹

All the above findings lead to the conclusion that in the chain propagation the reduction of PDP by the organic radical is the rate-determining step. Further confirmation

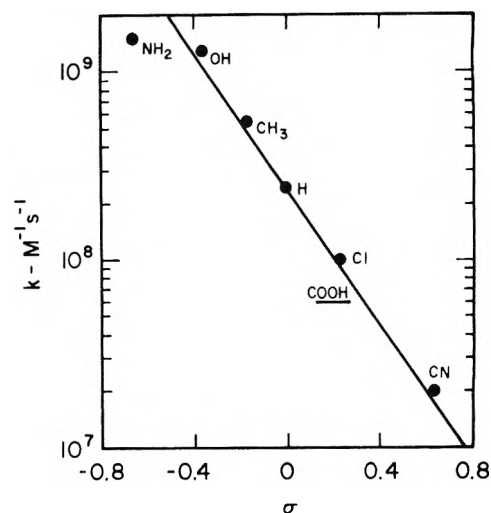


Figure 1. A correlation of rate constants for reaction of H_2PO_4 with substituted benzoic acids with the substituent constants σ . The values of σ were taken from C. D. Ritchie and W. F. Sager, *Prog. Phys. Org. Chem.*, 2, 323 (1964). The rate constant for cyanobenzoic acid was taken as twice that of cyanobenzoate ion. The bar for COOH denotes the fact that at the pH of the measurement the solution contained a mixture of the acid and the monoanion.

of this conclusion was obtained from the effect of concentrations of $G(-PDP)$. Experiments with 2-propanol at pH 6.5 showed that at 0.25 M alcohol a twofold increase in PDP concentration causes a 50% increase in $G(-PDP)$ while a threefold increase in the alcohol concentration at constant [PDP] causes only 10% increase in the yield. With 0.3 M formate ions at pH 5.6 an increase in [PDP] from 0.012 to 0.024 M resulted in increase in $G(-PDP)$ from 46 to 160, while a similar change in the concentration of formate caused an increase of only ~50%. In both experiments the yields were more strongly dependent upon the concentration of PDP than that of the organic substrate.

It should be pointed out that irradiation of aqueous solutions of PDP without organic additives does not lead to a chain decomposition, such as that observed with peroxomonophosphate.⁷ The values of $G(-PDP)$ in the absence of additives ranged from 3 to 4 in neutral and acid solution and down to 1.5 at pH 9–12, in agreement with previous measurements.² A high value of 4.9 was observed at pH 0 which may result from partial hydrolysis of PDP into peroxomonophosphoric acid which undergoes chain decomposition.⁷

TABLE III: A Comparison of the Rate Constants of H_2PO_4 with Those of SO_4^{2-} and OH^-

Compound	$H_2PO_4^a$	SO_4^{2-b}	OH^-c
Methanol	4.1×10^7	1.1×10^7	9×10^8
Ethanol	7.7×10^7	3.4×10^7	1.8×10^9
2-Propanol	1.4×10^8	8.0×10^7	2.2×10^9
2-Methyl-2-propanol	3.9×10^6	8.0×10^5	5×10^8
Formate ion	1.5×10^8	1.7×10^8	3×10^9
Acetic acid	3.4×10^5	9×10^4	2×10^7
Propionic acid	4.2×10^6	$(4.6 \times 10^6)^d$	5×10^8
Malonic acid	1.8×10^5	$(5.5 \times 10^6)^d$	2×10^7
Succinic acid	1.6×10^6	$(7.1 \times 10^6)^d$	1×10^8
Glycine	$\leq 10^5$	9×10^6	6×10^6
Alanine	$(1.6 \times 10^7)^e$	1.0×10^7	7×10^7
Acetone	3.3×10^5		9×10^7
Fumaric acid	1.5×10^7	$(1.6 \times 10^7)^d$	1×10^9
Maleic acid	3.1×10^7		5×10^8

^a Determined at pH 3.2–4.6. ^b Determined at pH 7 by J. L. Redpath and R. L. Willson, *Int. J. Radiat. Biol.*, 27, 389 (1975), except for ethanol and acetic acid which were measured by L. Dogliotti and E. Hayon, *J. Phys. Chem.*, 71, 3802 (1967), and except as noted. ^c Average literature values from the compilation by Farhatziz and A. Ross, National Bureau of Standards, Report No. NSRDS-NBS 59. ^d Determined in the present work for reaction with the anion. ^e For reaction of PO_4^{2-} at pH 12.

TABLE IV: Rate Constants for Reaction of the Phosphate Radical with Aromatic Carboxylic Acids

Compound	pH	k , $M^{-1} s^{-1}$
Reactions of $H_2PO_4^-$		
Benzoic acid	3.2	2.4×10^8
Terephthalic acid	3.4	$\sim 6.0 \times 10^7$
Terephthalate ion	5.2	3.5×10^7
<i>p</i> -Chlorobenzoic acid	3.3	1.0×10^8
<i>p</i> -Chlorobenzoate ion	5.0	4.8×10^7
<i>p</i> -Cyanobenzoate ion	4.6	1.0×10^7
<i>p</i> -Toluic acid	3.3	5.4×10^8
<i>p</i> -Hydroxybenzoic acid	3.3	1.3×10^9
<i>p</i> -Aminobenzoic acid	3.3	1.5×10^9
Reactions of $HP\dot{O}_4^-$		
Benzoate ion	7.1	$\leq 10^7$
<i>p</i> -Hydroxybenzoate ion	7.2	1.7×10^8

A comparison of the rate constants for reactions of $H_2PO_4^-$, SO_4^- , and $\dot{O}H$ with aliphatic compounds is given in Table III. It is apparent that the rates of hydrogen abstraction by the three radicals follow the same pattern although those of $\dot{O}H$ are generally higher than the others by one or two orders of magnitude. Because of this difference in the absolute rate constants, the $H_2PO_4^-$ and SO_4^- radicals are more selective than $\dot{O}H$. A logarithmic plot of the rate constants of $H_2PO_4^-$ vs. those of $\dot{O}H$ shows an approximate linear dependence with a slope of ~ 1.5 , i.e., $H_2PO_4^-$ is three times more selective than $\dot{O}H$. The rates of reaction of SO_4^- are somewhat similar to those of $H_2PO_4^-$ but higher than those of $HP\dot{O}_4^-$ and $P\dot{O}_4^{2-}$ (compare Tables III and I).

The rate constants for reaction of the phosphate radical with aromatic carboxylic acids (Table IV) are affected by the state of protonation of both the phosphate radical and the carboxyl group. From the few examples in the table it can be estimated that dissociation of the carboxyl group decreases the rate by a factor of ~ 2 while dissociation of

$H_2PO_4^-$ into $HP\dot{O}_4^-$ decreases the rate by a factor of ~ 5 –10. The effect of substituents on the rate constant is demonstrated in Figure 1. The correlation is very similar to that found for reaction of SO_4^- with aromatic compounds.¹² The value of $\sigma = -1.8$ derived from the figure is only slightly lower than that obtained for SO_4^- . It is suggested, therefore, that the mechanism of reaction is similar for both radicals, i.e., oxidation of the aromatic ring by an electron transfer, as opposed to the reaction of $\dot{O}H$ radicals which involves addition to the ring.

In conclusion, the reactions of $H_2PO_4^-$ with organic compounds are very similar to those of SO_4^- in their rate constants and mechanism. Both radicals abstract hydrogen from aliphatic compounds, add to aliphatic double bonds, and oxidize aromatic rings via electron transfer. The $HP\dot{O}_4^-$ and $P\dot{O}_4^{2-}$ radicals are less reactive. They abstract hydrogen more slowly and are also weaker oxidants. It is found, for example, that $H_2PO_4^-$ and SO_4^- oxidize Cl^- but $HP\dot{O}_4^-$ and $P\dot{O}_4^{2-}$ do not.¹³ Further studies on inorganic compounds are underway.

References and Notes

- (1) The research described herein was supported by the Division of Physical Research of the U.S. Energy Research and Development Administration. This is Radiation Laboratory Document No. NDRL-1741.
- (2) G. Levey and E. J. Hart, *J. Phys. Chem.*, **79**, 1642 (1975).
- (3) E. D. Black and E. Hayon, *J. Phys. Chem.*, **74**, 3199 (1970).
- (4) J. R. Huber and E. Hayon, *J. Phys. Chem.*, **72**, 3820 (1968).
- (5) M. Nakashima and E. Hayon, *J. Phys. Chem.*, **74**, 3290 (1970).
- (6) O. P. Chawla and R. W. Fessenden, *J. Phys. Chem.*, **79**, 2693 (1975).
- (7) P. Maruthamuthu and P. Neta, *J. Phys. Chem.*, **81**, 937 (1977).
- (8) L. K. Patterson and J. Lilie, *Int. J. Radiat. Phys. Chem.*, **6**, 129 (1974).
- (9) R. H. Schuler, P. Neta, H. Zemel, and R. W. Fessenden, *J. Am. Chem. Soc.*, **98**, 3825 (1976).
- (10) M. M. Crutchfield and J. O. Edwards, *J. Am. Chem. Soc.*, **82**, 3533 (1960).
- (11) See, e.g., P. Neta, *Adv. Phys. Org. Chem.*, **12**, 223 (1976).
- (12) P. Neta, V. Madhavan, H. Zemel, and R. W. Fessenden, *J. Am. Chem. Soc.*, **99**, 163 (1977).
- (13) P. Maruthamuthu and P. Neta, to be published.

Electron Scavenging in Ethanol and in Water

Dušan Ražem¹ and William H. Hamill²*

Department of Chemistry and the Radiation Laboratory,² University of Notre Dame, Notre Dame, Indiana 46556 (Received March 28, 1977)

Publication costs assisted by the U.S. Energy Research and Development Administration

Rate constants for scavenging solvated electrons, e_s^- , mostly in the range $k_{e_s^-} < 10^8 M^{-1} s^{-1}$, have been measured in ethanol and, as needed for comparison, in water. There is a tendency for $k_{e_s^-}$ to equal $k_{e_{aq}^-}$ over a 10^3 -fold range, but there are instances where $k_{e_s^-}$ is much greater. Inefficient scavengers for e_s^- provide relatively efficient traps for dry electrons e^- with 37% survival often at $C_{37} \approx 1 M$ scavenger but also as low as $\sim 0.2 M$. The outstanding exceptions are olefins for which $k_{e_s^-} \leq 10^7 M^{-1} s^{-1}$, but they do not measurably react with e^- . Negative ion resonances for alkenes as large as 2.2 eV have been reported and neither e^- nor e_s^- is expected to react. It is proposed that e_s^- is $C_2H_5OH^-$ and e_{aq}^- is H_2O^- . The radical anions may transfer either e^- or H to appropriate acceptors, the latter accounting for possible reaction of e_s^- with olefins and alkenols. The reaction $e_{aq}^- + e_{aq}^- = H_2$ is explained in terms of H_2O^- . Whenever e^- and e_s^- produce a common electron adduct S^- , and an equilibrium $e_s^- + S \rightleftharpoons S^-$ is approximated, then C_{37}^{-1} is proportional to $k_{e_s^-}$. This is Hunt's relation, $k_{e_s^-} C_{37} = Q$, with $Q = 1.2 \times 10^9 s^{-1}$ in ethanol.

Introduction

Bound excited states in liquids (or solids) may ionize adiabatically, as described by Franck and Platzmann.³ High energy radiation, however, forms energetic delocalized electrons, according to the Samuel and Magee model.⁴

They concluded that solvation was improbable in water and that the entire process resulting in charge recombination involves only about 10^3 collisions. This number provided an implicit basis for trapping delocalized electrons by impurities and the experimental feasibility was

demonstrated shortly by Williams and Hamill⁵ using chemically reactive scavengers in ⁶⁰Co-irradiated cyclohexane. Later work provided evidence for delocalized electrons in polar solids⁶ and liquids⁷ (dry electrons, e^-). One of the more significant observations was the marked reduction in the 100-eV yield of solvated electrons $G(e_s^-)$ observed for concentrated solutions of benzene in ethanol at the end of a 10-ns pulse, although subsequent reaction with e_s^- is very slow.⁸

Hunt and his collaborators have provided extensive evidence for reactions of electrons prior to solvation with various scavengers at <30 ps, both in aqueous and alcoholic solutions.⁹ In terms of C_{37} , the concentration of scavenger which reduces $G(e_s^-)$ to 37% of the initial value by extrapolation from 30 ps, they find that $C_{37}k_{e_s^-} = Q$ where $k_{e_s^-}$ is the conventional rate constant for scavenging solvated electrons. For water, $Q = 1.0 \times 10^{10} \text{ s}^{-1}$ and for ethanol $Q = 1.3 \times 10^9 \text{ s}^{-1}$. It should be noted, however, that these relations have been tested only in the range $k > 10^9 \text{ M}^{-1} \text{ s}^{-1}$. One of the most remarkable results, reported recently by Hunt and Chase,¹⁰ is a tenfold increase in the efficiency of dry-electron trapping by toluene in propanol at -125°C relative to $\sim 20^\circ \text{C}$. Another is the nearly proportional dependence of C_{37} for acetone and carbon tetrachloride on the concentration of bound oxygen atoms in water and several alcohols. This effect has been attributed to an efficient removal of energy from the pre-solvated electron which Wolff et al.¹¹ assumed to be hot.

In the present work and recent publications in this series, the dry electron is considered to lie near the bottom of the lowest conducting state, but strong scattering confers appreciable zero-point energy. At large scavenger concentration there must be some trapping of hot electrons, but it is not yet resolved.

This work initiates an investigation of inefficient electron scavengers in polar solvents. The objectives include: (i) measuring rate constants of e_s^- in ethanol of a number of scavengers which are known to be very inefficient; (ii) comparing $k(e_s^- + S)$ with $k(e_{aq}^- + S)$; (iii) considering possible mechanistic effects which control very slow reactions; (iv) undertaking related studies of dry electron scavenging; (v) attempting to explain $k_{e_s^-}C_{37} = Q$.

Experimental Section

A dose of approximately $1.5 \times 10^{20} \text{ eV L}^{-1}$ was delivered to the sample in each 10-ns pulse. The lifetime of the solvated electron at this dose was about $2 \mu\text{s}$ in ethanol and water. Absolute ethanol, supplied by the U.S. Industrial Chemicals Co., was used as received. Dimethyl sulfoxide (Me_2SO), Baker analyzed, was distilled under reduced pressure ($\sim 15 \text{ Torr}$) in a nitrogen atmosphere. This and other distillations were performed at 10/1 reflux ratio using a 20-plate column. Allyl alcohol, Eastman, was shaken with NaHCO_3 and subsequently distilled under nitrogen. Reagent grade cyclohexene was distilled under nitrogen from Na-K. The origin of other chemicals was the following: Research grade ethylene and butenes were from Phillips Petroleum Co; anisol, butyl chloride, allyl alcohol, allyl acetate, and allyl amine were Eastman White Label grade; the butenols and higher alkenes were freshly opened ampoules from Chemical Samples Co.; other chemicals were of chemically pure quality.

Results

Rate constants for a number of scavengers have been measured in ethanol at $\sim 20^\circ \text{C}$ in the range $>10^{-8} \text{ s}$ by measuring the optical density, OD (e_s^-). For comparison of $k_{e_s^-}$ with $k_{e_{aq}^-}$ data have been taken from the literature when they are available. A few values of $k_{e_{aq}^-}$ have been

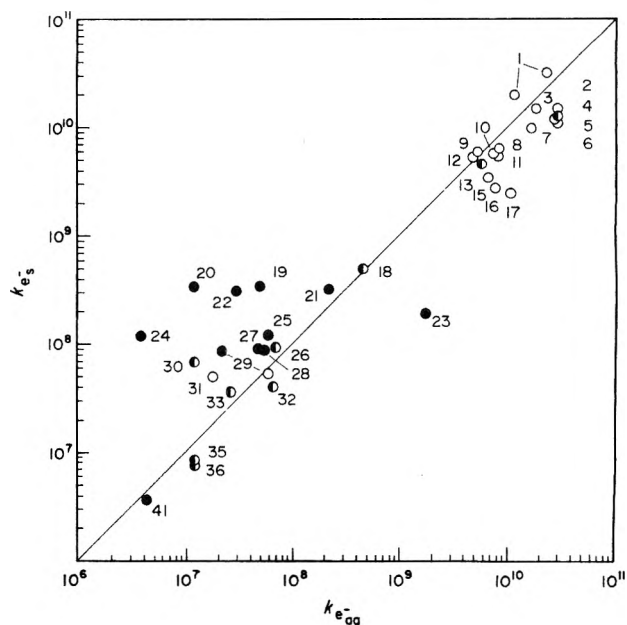


Figure 1. Comparison of rate constants for scavenging solvated electrons in ethanol, $k_{e_s^-}$, and water, $k_{e_{aq}^-}$. References to data taken from the literature, in whole (O) or in part (●), appear in Table I, together with the identification code.

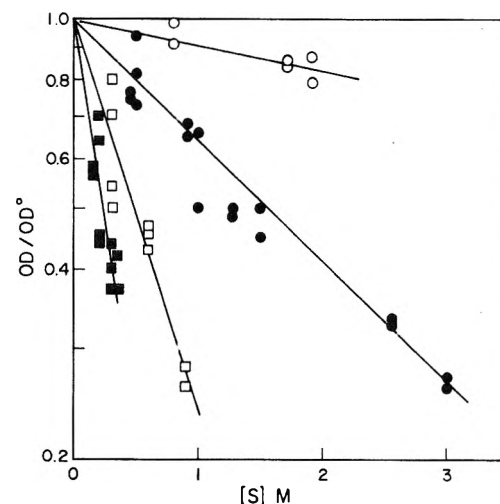


Figure 2. Extrapolated, normalized optical densities OD/OD^0 vs. $[S]$ as a result of dry-electron scavenging. Results for *c/s*-butene-2, benzene, allyl alcohol, and fluorobenzene are designated by (O), (●), (□), and (■).

measured when needed for completeness. All rate data for scavenging e_s^- and e_{aq}^- are summarized in Table I and Figure 1. The recent measurements of $k_{e_s^-}$ by Bolton and Freeman are helpful to establish the dependence of $k_{e_s^-}$ on $k_{e_{aq}^-}$ for large rate constants.¹² The narrow range of values of $k_{e_s^-}$ for the alkenes is in contrast with the wide range for the alkenols. For all systems with $k_{e_s^-} \lesssim 10^7 \text{ M}^{-1} \text{ s}^{-1}$, however, considerable caution must be used.

The evaluation of C_{37} by extrapolating $\text{OD}(e_s^-)$ to the middle of the pulse is quite satisfactory for $C_{37} \lesssim 2 \text{ M}$ and $k_{e_s^-} \lesssim 10^7 \text{ M}^{-1} \text{ s}^{-1}$.

Some evaluations of C_{37} were based on measurement of $\text{OD}(\text{Ph}_2^-)$, as well as $\text{OD}(e_s^-)$, for solutions containing a rather large concentration of an inefficient e_s^- scavenger S and $\sim 10^{-2} \text{ M}$ (C_6H_5)₂. Almost all dry-electron scavenging occurs by S. The surviving population $G(e_s^-)/G^0(e_s^-)$ is scavenged by both S and biphenyl. Since both $k_{e_s^-S}$ and $k_{e_s^-Ph_2}$ are known, the corrected yield is readily obtained.

Representative results for e^- scavenging, expressed as $\log(\text{OD}/\text{OD}^0)$ vs. $[S]$, are presented in Figure 2. Some

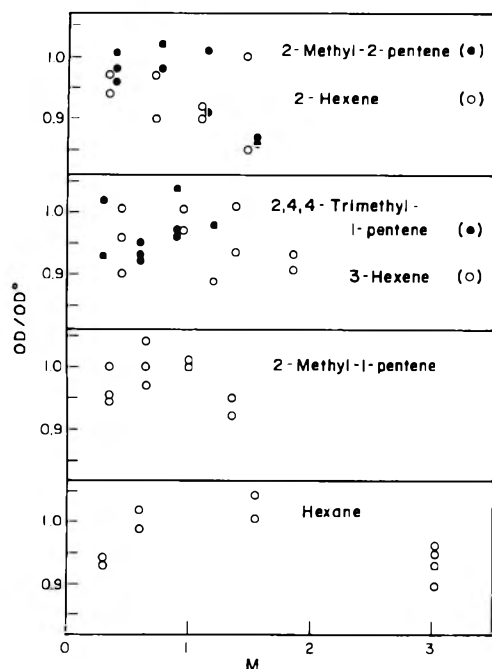


Figure 3. $OD(e_s^-)$ vs. [alkene] or [*n*-hexane].

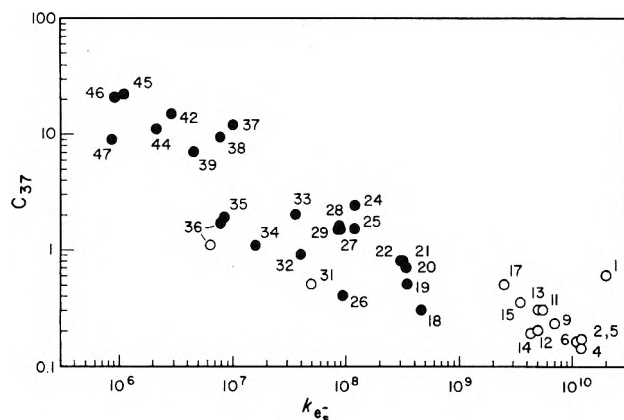


Figure 4. Concentrations C_{37} of scavenger, required to reduce the yields of dry electrons to 37% vs. $k_{e_s^-}$ for ethanol solutions. Data reported by Hunt and by Freeman are included (O). Literature references and the identification code appear in Table I.

results for olefins and for one alkane appear in Figure 3.

Values of C_{37} for solutions in ethanol appear in Table I, together with a few values for other solvents. Comparison of C_{37} and $k_{e_s^-}$ for scavengers in ethanol appears in Figure 4 which includes some of the Toronto data.

The measurement of $k_{e_s^-, Ph_2^-}$ was complicated by spectral overlap of e_s^- and Ph_2^- . Competition with CCl_4 was adopted choosing combined concentrations which limited the lifetime of e_s^- to ~ 10 ns. There was always some decay of Ph_2^- due to electron transfer to CCl_4 with a well-defined rate for which $k = 8 \times 10^9 \text{ M}^{-1} \text{ s}^{-1}$. This did not interfere with extrapolation to the initial yield of Ph_2^- . From Table I, $k_{e_s^-}$ for CCl_4 was $1.3 \times 10^{10} \text{ M}^{-1} \text{ s}^{-1}$ which agrees well with earlier measurements. From Figure 5 $k_{e_s^-, Ph_2^-} = 3.5 \times 10^9 \text{ M}^{-1} \text{ s}^{-1}$, using the average $k_{e_s^-}$ for CCl_4 .

For solutions of $(C_7H_5)_2$ alone in ethanol the rate constant for solvolytic decay of the anion was $k = 7.4 \times 10^5 \text{ s}^{-1}$ with an average deviation of 7% for 15 measurements.

Discussion

An Interpretation of $k_{e_s^-} C_{37} = Q$. Dry-electron scavenging occurs only during the very short interval τ which precedes electron localization by the solvent. When 37%

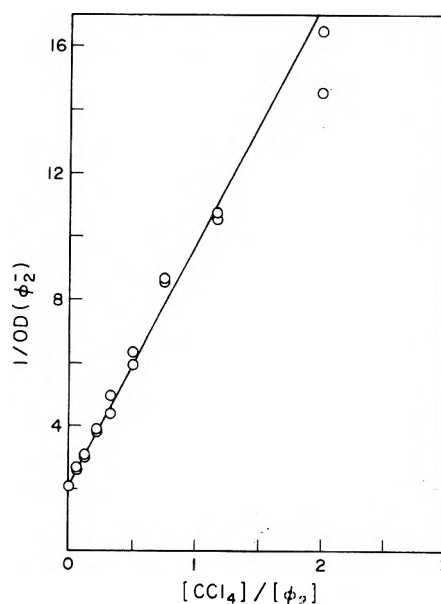


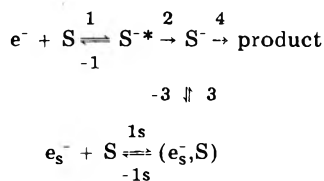
Figure 5. The rate constant $k_{e_s^-}$ for biphenyl in competition with carbon tetrachloride based on measurement of Ph_2^- at 402 nm.

of the initial electron population survives as e_s^- , then $k_{e_s^-} C_{37} \tau = 1$ from the first-order rate equation where $k_{e_s^-}$ is the "rate constant" for dry-electron trapping. Hunt's relation becomes

$$k_{e_s^-} C_{37} = k_{e_s^-} / k_{e^-} \tau = Q \quad (1)$$

The consistently lower values of C_{37} in ethanol relative to water are due to the longer lifetime of e^- .

The proportionality of $k_{e_s^-}$ and k_{e^-} in eq 1 suggests the following kinetic scheme:



where (e_s^-, S) is a collision pair. Provided S^- is in equilibrium with e_s^- , it follows that

$$K_{e_s^-} = \frac{k_1 k_2}{k_{-1} + k_2} k_{e_s^-} \quad (3)$$

This suggests, in turn, that k_1 is constant for those scavengers which satisfy eq 1 and that $k_2 \gg k_{-1}$. Substantial independence of C_{37} and $k_{e_s^-}$ can arise when $k_4 \gg k_{-3}$, no matter how small k_3 may be. Also, in the diffusion-controlled limit eq 1 is not expected to apply.

Solvent Effects. Hunt and Chase have shown that C_{37} is nearly proportional to the chemically bound oxygen concentration for water and several alcohols.¹⁰ In their model this effect is attributed to the electronegativity of oxygen (in the solvent molecule) and energy transfer from hot electrons to solvent molecules. This does not account for the isotope effect in H_2O and D_2O which suggests interaction with OH and OD vibrations involved in the localization of e^- .⁷ Localization of the electron is dominated, as proposed previously,⁷ by excitation of the OH vibration. Interaction probably involves mainly the OH proton of a strong permanent dipole since λ_{max} for the optical spectrum of e_s^- is comparably affected, unlike ethers.

These considerations are supported by a moderately strong negative ion electron resonance in thin-film solid

TABLE I: Comparisons of k_{eq} , k_{aq} , and C_{37}

No.	Scavenger	Ethanol				Water			
		This work		Lit.		This work		Lit. ^c	
		$k, \text{M}^{-1} \text{s}^{-1}$	No. of expt	C_{37}, M	$k, \text{M}^{-1} \text{s}^{-1}$	Ref	$k, \text{M}^{-1} \text{s}^{-1}$	No. of expt	$k, \text{M}^{-1} \text{s}^{-1}$
1	Perchloric acid				13	13			2.4×10^{10}
2	Nitrobenzene				9	9			1.2×10^{10}
3	Oxygen				13	13			3×10^{10}
4	Carbon tetrachloride	$(1.3 \pm 0.2) \times 10^{10}$	(5)		13	13			1.9×10^{10}
5	Acetophenone				9	9			3.0×10^{10}
6	Chloroform				9	9			2.8×10^{10}
7	Sulfur hexafluoride				13	13			3.0×10^{10}
8	Nitrous oxide				13	13			1.7×10^{10}
9	Benzyl chloride				9	9			8.7×10^9
10	Carbon dioxide				13	13			5.5×10^9
11	Methyl ethyl ketone				9	9			7.7×10^9
12	Naphthalene				9	9			8.5×10^9
13	Acetone	$(4.7 \pm 0.3) \times 10^9$	(5)		13	13			5.4×10^9
14	Biphenyl	$(3.9 \pm 0.2) \times 10^{9d}$	(7)		a	9			5.9×10^9
15	Monochloroacetic acid				9	9			6.9×10^9
16	1,3-Butadiene				13	13			8×10^9
17	Lithium nitrate				9	9			1.1×10^{10}
18	Chlorobenzene	$(4.6 \pm 0.2) \times 10^8$	(7)	0.3 ± 0.1 (11)					5×10^8
19	Benzylamine	3.4×10^8	(2)	0.5 (2)					3.4×10^7
20	Allyl alcohol	$(3.4 \pm 0.1) \times 10^8$	(6)	0.7 ± 0.3 (9)					$< 10^8$
21	Acetic acid	$(3.2 \pm 0.5) \times 10^8$	(10)	0.8 ± 0.2 (7)					$(1.2 \pm 0.2) \times 10^7$
22	Acetonitrile	$(3.1 \pm 0.4) \times 10^8$	(5)	0.8 ± 0.4 (12)	13	13			$(2.2 \pm 0.3) \times 10^8$
23	Carbon monoxide	1.9×10^8	(2)	2.4 ± 0.8 (15)					$(3.0 \pm 0.2) \times 10^7$
24	Dimethyl sulfide	$(1.2 \pm 0.2) \times 10^8$	(9)						1.8×10^8
25	3-Buten-2-ol	1.2×10^8	(4)	1.5 ± 0.5 (5)					3×10^7
26	Fluorobenzene	$(9.3 \pm 1.0) \times 10^7$	(8)	0.4 ± 0.1 (7)					1×10^9
27	1-Chlorobutane	$(9.0 \pm 0.7) \times 10^7$	(10)	1.5 ± 0.3 (5)					5×10^8
28	trans-2-Buten-1-ol	$(8.8 \pm 1.5) \times 10^7$	(5)	1.6 ± 0.4 (5)					3.4×10^7
29	Ethyl acetate	$(8.6 \pm 1.2) \times 10^7$	(10)	1.5 ± 0.3 (6)					$< 10^8$
30	Allyl amine	6.9×10^7	(2)		13	13			$(5.9 \pm 0.4) \times 10^7$
31	Phenol								7.0×10^7
32	Thiophene	$(4.0 \pm 0.5) \times 10^7$	(6)	0.9 ± 0.1 (4)					4.5×10^8
33	Aniline	$(3.6 \pm 0.3) \times 10^7$	(7)	2.0 ± 0.2 (5)					1.8×10^7
34	Anisole	$(1.1 \pm 0.2) \times 10^7$	(6)	1.6 ± 0.3 (4)					6.5×10^7
35	Toluene	$(8.5 \pm 0.9) \times 10^6$	(6)	1.9 ± 0.5 (6)					2.6×10^7
36	Benzene	$(7.9 \pm 1.0) \times 10^6$	(10)	1.7 ± 0.7 (11)	13	13			1.2×10^7
37	2-Methyl-2-pentene	$\leq 1 \times 10^7$	(9)	12	13	13			1.2×10^7
38	trans-2-Hexene	$\leq 8 \times 10^6$	(8)	9.4 (6)					

39	1-Butene	$\leq 5 \times 10^6$	(10)	7 ± 2	(8)
40	Cyclohexene	$< 1 \times 10^5$	(1)		
41	3-Buten-1-ol	3.6×10^6	(3)		(5)
42	2,4,4-Tri-methyl-1-pentene	$\leq 3 \times 10^6$	(8)	15	(6)
43	Ethylene	$\leq 2 \times 10^6$	(2)		(2)
44	trans-2-Butene	$\leq 2 \times 10^6$	(4)	11 ± 2	(5)
45	2-Methyl-1-pentene	$\leq 1 \times 10^6$	(7)	22	(3)
46	trans-3-Hexane	$\leq 9 \times 10^5$	(8)	21	(5)
47	cis-2-Butene	$\leq 9 \times 10^5$	(5)	9 ± 2	(5)

^a S. Arai and L. M. Dorfman, *J. Chem. Phys.*, **41**, 2190 (1974). ^b G. R. Freeman and G. L. Bolton, Fourth Symposium on Radiation Chemistry, Keszthely, Hungary, 1976, paper D/1.2. ^c Entries 1, 11, and 20 from ref 9; entry 13 from ref 13. All others from M. Anbar, M. Bambenek, and A. B. Ross, *Natl. Stand. Ref. Data Ser., Natl. Bur. Stand. (U.S.)*, **43** (1973). ^d Direct observation of e_s^- decay at 750 nm.

$$(4.1 \pm 0.4) \times 10^6 \quad (5)$$

$$< 3 \times 10^5 \quad (2)$$

$$< 2 \times 10^6$$

13

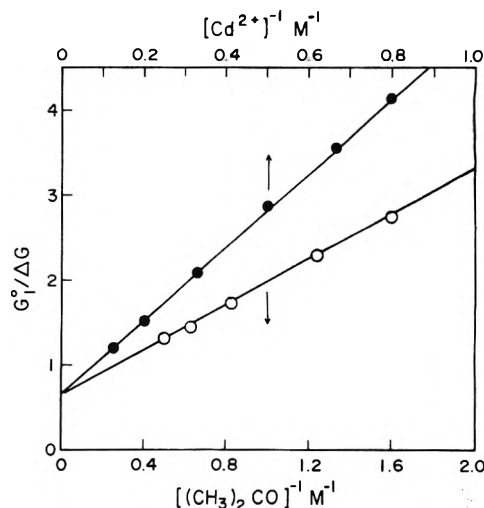


Figure 6. Examples of the interconvertibility from eq 2 to eq 3 using values of C_{37} from ref 11.

H_2O , one somewhat weaker in D_2O , and one very weak in ethanol.^{7,14} Species of the type H_2O^- may be involved.

It is somewhat relevant to observe that electron solvation by the first layer of oriented dipoles of the type ROH depends more on the electric field than on the dipole moment. Spectroscopically, the ROH-type solvents are unique for e_s^- . The electric field at the OH proton is very large because of its very small radius and the r^{-2} dependence. For partial charge q on H, $E \propto q/r^2$ or $E \propto \mu/r^2$ for field E and dipole moment μ . Although $\mu = 1.5$ D for NH_3 , the q on one H is small and the configuration is poor. The spectrum is red-shifted relative to ROH-type solvents.

Scavenging Models. Wolff et al.¹¹ reported that their results for dry-electron scavenging cannot be described by the following simple competition:

$$G^0/G_{\text{obsd}} = 1 + \nu_1[S]/\nu_2 \quad (4)$$

Their results were consistent with another model for which they obtained

$$G_{\text{obsd}}/G^0 = \exp(-[S]/C_{37}) \quad (5)$$

Measurements at this laboratory have consistently been fitted by

$$G_{\text{obsd}} = G_1^0 - G_2^0(1 + \nu_2/\nu_1[S])^{-1} \quad (6)$$

which is more general than, and includes, eq 4. When eq 6 is applied to the data for acetone of Wolff et al.¹¹ using values calculated from their C_{37} by eq 4, the fit obtained is shown in Figure 6. The same procedure was applied to results for Cd^{2+} scavenging.¹¹ From the common intercept one obtains $G_1/G_2^0 = 0.65$. It appears that evaluating C_{37} from $\log OD(e_s^-)/OD^0(e_s^-)$ vs. $[S]$ at 30 ps does not describe the scavengability of all e_s^- , but only those which survive to become e_s^- . Wolff et al.¹⁵ have shown that $G(Cd^+)$ exceeds $\Delta G(e_s^-)$ with $G^0(Cd^+) = 4.8$.

Measurements at 10 ns of Cd^+ , rather than e_s^- , in solutions containing 4 M $HClO_4$, were fit by eq 4 and gave $G^0 = 5.2$.⁷ This result agrees as well as can be expected with observations in the ns range.

Values of C_{37} in this work have been obtained from eq 5 since it is much more convenient than eq 6 and empirically yields similar results. This procedure does not entail accepting the assumption of hot electron moderation.

Most of the scavengers examined in this work were known to be inefficient in water, or in ethanol, or were expected to be. The choice was partly experimental practicality since measurements of the surviving yield of

electrons, observed as OD (e_s^-) at 10 ns, require that fast and slow scavenging be time resolved. An additional requirement was $C_{37} < 2$ M since measurements at $[S] \geq 1$ M may introduce significant errors from spectral shifts for e_s^- which would be amplified by extrapolation to large values of C_{37} .

Kinetics. Inefficient scavenging of e_s^- by S may be due in part to slow formation of S^- and in part to ionization of S^- , even when the anion is fully solvated. If the electron is more firmly bound as e_s^- than as the solvated anion, then formation of S^- via dry-electron scavenging may provide a more efficient channel. This may account in part for the greatly improved dry-electron scavenging efficiency of toluene in propanol at reduced temperature. If k_{-3} of the kinetic scheme 2 is activated, S^- is stabilized at reduced temperature.

For $k_{e_s^-}$ much less than diffusion controlled the following applies:

$$[(e_s^-, S)] = K_7[e_s^-][S] \quad (7)$$

and $k_{e_s^-}$ is given by

$$k_{e_s^-} = K_7 k_3 k_4 / (k_{-3} + k_4) \quad (8)$$

Since C_{37} is rather insensitive to $k_{e_s^-}$ in this range, small values of $k_{e_s^-}$ are due mostly to $K_7 k_3$. When S is nonpolar K_7 will be small because an inner sphere polar solvent molecule must be displaced.

Scavenging Solvated Electrons in Alcohols and Water. The results of Bolton and Freeman¹³ are summarized in Table I and Figure 1 for $k_{e_s^-}$ in the range $\geq 10^9$ M⁻¹ s⁻¹ for ethanol. There is a strong tendency for $k_{e_s^-} \simeq k_{aq^-}$. In the present work this tendency persists, but several additional scavengers are found to be relatively much more reactive in ethanol, as much as 35 times for Me₂SO and 25 times for allyl alcohol. It is surprising that the alkenols react with e_s^- at all and $k_{e_s^-}$ as large as 10^8 M⁻¹ s⁻¹ is quite unexpected. One must be concerned about impurities, particularly in the absence of support from the literature. On the other hand the alkenols also scavenge dry electrons and this result is rather insensitive to impurities. Neither do impurities account for the solvent effect of some rate constants for water and ethanol.

Dissociative attachment is conceptually the simplest mechanism for reaction of e_s^- with alkenols but the thermochemistry is not clearly favorable, the following steps being required: (i) remove ROH and electron to vacuum, $\Delta H_i \simeq 2.0$ eV (estimated); (ii) dissociate RO-H, $\Delta H_{ii} = 4.3$ eV;¹⁶ (iii) form RO⁻, $\Delta H_{iii} = -1.7$ eV; (iv) solvate RO⁻ and H. For thermoneutrality, $\Delta H_{iv} \simeq -4.6$ eV is required and this is a marginal possibility. It should be noted that ΔH_i must include the heat of evaporation of ethanol, 0.3 eV, leaving only 1.7 eV for e^- , which is minimal.¹⁷ More simply, since ethanol itself reacts only very slowly in this manner, much faster reaction with alkenols is not to be expected.

One alternative is to locate the electron density on the double bond, which is a rather implausible mechanism, although allyl amine and the olefins themselves may react very slowly with e_s^- .

Since the alkenols react rather well with dry electrons, it is necessary to reconsider the preceding thermochemistry. ΔH_i is eliminated and a small but unknown bulk electron affinity, χ , is introduced. If $\chi \simeq 0.5$ eV, then $\Delta H_{iv} = -3.1$ eV suffices and is a quite plausible single-ion solvation energy since the charge is localized on the oxygen. If the reaction proceeds adiabatically, it is fully assisted by the solvation energy. Another example is C₆H₅F for which $\Delta H = 1.5$ eV for dissociative attachment in vacuo,

but $k_{e_s^-} \sim 10^8$ M⁻¹ s⁻¹, due to the large solvation energy of F⁻.

A Model for e_s^- and e_{aq^-} . We suggest tentatively that the solvated electron e_s^- in ethanol is usefully described as C₂H₅OH⁻, the molecular radical anion. (The entity e_s^- as an electron-in-a-cavity is also quite hypothetical.) It may transfer an electron to good electron acceptors and hydrogen to good H-atom acceptors. Possibly alkenols serve as traps for e^- and as H-atom acceptors for e_s^- . In partial support of the possibility of bound C₂H₅OH⁻, there is an electron resonance at $\sim(0.6 + \chi)$ eV in the solid.¹³ Also, optical excitation of e_s^- at 77 K produces H and not e^- .¹⁸ This requires an excited dissociative state of C₂H₅OH⁻ and consequently the ground state radical anion in the solid must also exist. Whether or not C₂H₅OH⁻ is stable in vacuo it may be stabilized by the solvent. Butadiene and carbon dioxide have negative electron affinities in vacuo but they form stable radical ions, even in nonpolar liquids and solids. As the molecular electron affinity becomes sufficiently large and negative, e.g., -2.2 eV for butene,¹⁹ the solvation energy no longer suffices to bind the electron. If one accepts the evidence that e_s^- reacts with olefins, then C₄H₉ is less improbable than C₄H₈⁻. The energetics for the alkenols should be similar.

In water the well-known reaction



is diffusion controlled. Considered literally, it must be difficult to explain since no microscopic model has been reported. If e_{aq^-} is better described as H₂O⁻, then formation of H₂ can be described quite simply by the mechanism



The HO⁻-H bond is weakened by charge localization on OH and the developing electron affinity of OH is assisted by the very large hydration energy of OH⁻ with increasing H-H bonding along the adiabatic reaction coordinate.

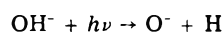
The reaction generally described by



for aqueous solutions can be described better by



This mechanism has been thoroughly demonstrated to occur analogously in OH⁻-doped KCl.²⁰ Under optical excitation the mechanism is given by



Below 120 K, H₂O⁻ is stable in the Cl⁻-vacancy although its structure is not optimal for the cubic lattice. It dissociates at higher temperature to the F center. The optical spectrum of H₂O⁻ in KCl is well resolved at 4 K in the crystal lattice and contains three components. Its envelope, however, is very similar to the asymmetric band of e_{aq^-} .

Ion-dipole interactions in water match the Madelung potentials in the KCl crystal since the heat of solution is about zero. Since the spectrum of e_{aq^-} in ice at 77 K is similar to that in water, except for the expected narrowing and blue shifting, there is only one absorbing species over the range of temperature and it may be H₂O⁻.

Since H₂O⁻ occupies a Cl⁻ vacancy in KCl it cannot have a much larger volume than Cl⁻. Consequently, H₂O⁻ is consistent with $\bar{V}_{e_{aq^-}} = 7$ mL.²¹

Thermochemical Considerations. Comparing the energy required to extract H from H₂O⁻ and C₂H₅OH⁻ involves the bond dissociation energies of the molecules, 5.17 and

TABLE II: Comparison of Alkenols

Solute	ΔH , eV	Ring size	$k_{e_s^-} \times 10^{-7}$
3-B-1	-1.87	8	0.4
	-1.46	7	
2-B-1	-1.77	7,6	9
3-B-2	-1.87	7	10
	-1.46	6	
Allyl	-1.75	7	40
	-1.52	6	

4.33 eV, and the electron affinities of the radicals, 1.86 and 1.68 eV.²² The O-H dissociation energies for the radical anions are therefore 3.31 and 2.65 eV and $C_2H_5OH^-$ is the better H-atom donor. Excepting 3-buten-1-ol, the alkenols and allyl amine react faster in ethanol (Figure 1). Also, H_2O^- is less likely to photolyze to H and OH^- .

If e_s^- reacts with butenes by formation of $C_4H_8^-$, then the thermochemistry involves: (i) transfer the electron and C_4H_8 to vacuum, $\Delta H_i \approx 2.0$ eV; (ii) addition of e^- to C_4H_8 , $\Delta H_{ii} = 2.2$ eV; (iii) solvation of $C_4H_8^-$. To achieve thermoneutrality requires $\Delta H_{iii} \approx -4.2$ eV, which is highly improbable. For dry electrons the requirement is only $\Delta H_{iii} \approx -2.0$ eV, but the evidence in Figures 2 and 3 does not support attachment. Failure to observe reaction with e^- is attributed to the negative ion resonance at 2.2 eV and very large k_{-1} .

The energy required to transfer H from $C_2H_5OH^-$ to *cis*-butene-2 is (i) raise e_s^- and C_2H_5OH to the vacuum level, $\Delta H_i \approx 2.0$ eV; remove H, $\Delta H_{ii} = 4.35$ eV; (iii) add e^- to C_2H_5O , $\Delta H_{iii} = -1.68$ eV; (iv) add H to C_4H_8 , $\Delta H_{iv} = -1.80$ eV; (v) solvate $C_2H_5O^-$, ΔH_v . For thermoneutrality, $\Delta H_v \approx -2.9$ eV is required. Since addition of alkali to ethanol converts OH^- to $C_2H_5O^-$ the solvation energy of the latter cannot be more than 0.8 eV less than the former, the difference arising from $D(HO-H)$ and $D(EtO-H)$, the electron affinities being nearly equal. Consequently, $\Delta H_v < -4$ eV is expected.

The H-atom transfer model lends itself to a consideration of the relative $k_{e_s^-}$ values of the alkenols. Why, for example, is 2-buten-1-ol 200-fold faster than 3-buten-1-ol? For thermochemical comparisons the formal process $C_2H_5OH^- \rightarrow C_2H_5O^- + H$ is common and need not be considered. The enthalpies of the alkenes and alkyl radicals will be used and the more exothermic process assumed for H-atom addition to the double bond. For

reactive proximity the alkenol will H bond to $C_2H_5O^-$ with the transferring proton close to the double bond in a ringlike structure. The various possibilities are summarized in Table II, where ΔH is that for H-atom addition. Considering both energy and ring size, 3-buten-1-ol is expected to have the smallest value of $k_{e_s^-}$.

The dry-electron adduct of the alkenols would be expected to undergo an analogous unimolecular H-atom transfer. For allyl alcohol, e.g., the product would be $H_3C-\dot{C}H-CH_2-O^-$.

Acknowledgment. We are indebted to Dr. K. P. Funabashi, Professor J. L. Magee, and Professor G. Nazarov for many helpful discussions. We are grateful to the International Atomic Energy Agency for the grant of a fellowship to one of us (D.R.).

References and Notes

- (1) International Atomic Energy Agency Fellow, on leave of absence from the "Ruder Boskovic" Institute, Zagreb, Yugoslavia.
- (2) The research described herein was supported by the Division of Physical Research of the U.S. Energy Research and Development Administration. This is Document No. NDRL-1745 from the Notre Dame Radiation Laboratory.
- (3) J. Franck and R. L. Platzmann, *Z. Phys.*, **138**, 411 (1954).
- (4) A. H. Samuel and J. L. Magee, *J. Chem. Phys.*, **21**, 1080 (1953).
- (5) R. R. Williams and W. H. Hamill, *Radiat. Res.*, **1**, 158 (1954).
- (6) T. Sawai and W. H. Hamill, *J. Phys. Chem.*, **73**, 2750 (1969).
- (7) Cz. Stradowski and W. H. Hamill, *J. Phys. Chem.*, **80**, 1054 (1976).
- (8) H. Ogura and W. H. Hamill, *J. Phys. Chem.*, **78**, 504 (1974).
- (9) J. W. Hunt, "Early Events in Radiation Chemistry", in "Advances in Radiation Chemistry", Vol. 5, M. Burton and J. L. Magee, Ed., Wiley, New York, N.Y., 1976, p 185.
- (10) J. W. Hunt and W. J. Chase, *Can. J. Chem.*, **55**, 2080 (1977).
- (11) R. K. Wolff, M. J. Bronskill, and J. W. Hunt, *J. Chem. Phys.*, **53**, 4211 (1970).
- (12) L. G. Christophorou, "Atomic and Molecular Radiation Physics", Wiley-Interscience, New York, N.Y., 1971, pp 464, 480.
- (13) G. L. Bolton and G. R. Freeman, *J. Am. Chem. Soc.*, **98**, 6825 (1976).
- (14) K. Hiraoka and W. H. Hamill, *J. Chem. Phys.*, **57**, 3870 (1972).
- (15) R. K. Wolff, J. E. Aldrich, T. L. Penner, and J. W. Hunt, *J. Phys. Chem.*, **79**, 210 (1975).
- (16) Thermochemical data used here and later are taken from J. L. Franklin, J. G. Dillard, H. M. Rosenstock, J. T. Herron, K. Draxl, and F. H. Field, *Natl. Stand. Ref. Data Ser., Natl. Bur. Stand.*, No. 26 (1969).
- (17) J. Jortner and R. M. Noyes, *J. Phys. Chem.*, **70**, 770 (1966).
- (18) T. Shida and W. H. Hamill, *J. Am. Chem. Soc.*, **88**, 3689 (1966).
- (19) K. D. Jordan, J. A. Michejda, and P. D. Burrow, *Chem. Phys. Lett.*, **42**, 227 (1976).
- (20) W. Rusch and H. Seidel, *Phys. Status Solidi*, **63**, 183 (1974).
- (21) R. R. Hentz, Farhatziz, and E. M. Hansen, *J. Chem. Phys.*, **57**, 2959 (1972).
- (22) J. M. Williams and W. H. Hamill, *J. Chem. Phys.*, **49**, 4467 (1968).

Hamaker Constants and the Principle of Corresponding States

Melvin D. Croucher* and Michael L. Halr

Xerox Research Centre of Canada Limited, Mississauga, Ontario, Canada L5L 1J9 (Received February 16, 1977)

Publication costs assisted by Xerox Research Centre of Canada Limited

A simple expression has been derived which allows the Hamaker constant of nonpolar fluids and of polymeric liquids to be calculated. This has been carried out by reformulating the well-known expression of Fowkes, using a surface free energy function derived by Patterson and Rastogi. The resulting expression, which explicitly accounts for the effect of temperature, predicts that the Hamaker constant for such materials should be a function of αT . The values obtained are in good agreement with the results of the Gregory-Tabor-Winterton type equations, in which A values are obtained from optical dispersion data.

Introduction

Coagulation of a particulate dispersion is a consequence of the attractive van der Waals forces that exist between colloidal particles. These long-range forces are also partially responsible for a wide range of structural and

energetic effects that occur in a variety of disperse systems.

The potential energy of van der Waals attraction, V_A , can be written¹ as the product of two functions, viz.

$$V_A = -A(\lambda, T) \cdot H \quad (1)$$

where $A(\lambda, T)$ is known as the Hamaker constant of the material and H is a function of the geometry of the system. Two methods have been used for calculating values of V_A : (i) a microscopic approach, which is based upon the summation of pairwise interactions between molecules that compose the system; and (ii) a macroscopic approach in which the interaction energy is calculated from the measured frequency dependent dielectric properties of the material, which implicitly accounts for all the many-body interactions which occur in condensed media.

The recent macroscopic formulations² have shown that $A(\lambda, T)$ is not a constant as predicted by the classical microscopic theories, but is a function of both the distance of separation of the colloidal bodies relative to their size (λ) and the temperature (T) of the disperse system. For nonpolar systems, retardation effects are extremely small and predictions of the attractive potential using both the macroscopic and microscopic theories are in quantitative agreement.^{3,4} A major disadvantage of the macroscopic continuum theories is that they are unwieldy to apply and often require a knowledge of experimental parameters that are not always readily available. Thus, there remains a need for a simple method of accurately evaluating Hamaker constants (and consequently V_A) which can be used in the interpretation of experimental data.

It is the purpose of this communication to derive a simple expression for the nonretarded Hamaker constant (in vacuo) for nonpolar fluids and polymeric liquids, which will enable values to be computed from readily available data. This has been carried through by reformulating the well-known expression of Fowkes,⁵ using an expression for the surface free energy derived by Patterson and Rastogi.⁶ The resulting expression for $A(\lambda, T)$, which is henceforth written as A , can be readily evaluated providing the coefficient of thermal expansion of the material is known. It is also able to explicitly account for the temperature dependence of A . The calculated values of the Hamaker constant are found to compare very favorably with those computed from optical data using the Gregory-Tabor-Winterton type equations.^{7,8} Utilizing the usual combining rules,² values of A for colloidal bodies immersed in condensed media can also be readily obtained.

Fowkes Expression for the Hamaker Constant

By assuming that the London dispersion forces between molecules were additive, Hamaker was able to derive an expression⁹ for the energy of interaction between macroscopic bodies of different geometries. Using an analogous procedure, Fowkes was able to derive an expression⁵ for the dispersion force contribution to the surface free energy, γ_d . This equation has recently been derived in a more rigorous manner¹⁰ by Mahanty and Ninham, without assuming additivity of molecular forces. Substitution of the expression for γ_d into the Hamaker expression gives the well-known Fowkes equation for the Hamaker constant:

$$A = 6\pi r^2 \gamma_d \quad (2)$$

where r is the intermolecular distance. Equation 2 has been used extensively to obtain values of A for materials in vacuo.¹¹ The required values of γ_d can be obtained from interfacial tension or contact angle data.⁵ The total surface free energy of a material can be written as

$$\gamma = \gamma_d + \sum \gamma_1 \quad (3)$$

where $\sum \gamma_1$ accounts for all other interactions acting across the interface, such as the contributions from Debye and Keesom forces. By restricting all further remarks to

nonpolar liquids we may ignore interactions other than dispersion interactions and can write $\gamma = \gamma_d$, where γ now becomes the surface tension of the fluid. A difficulty in obtaining accurate Hamaker constants lies in the choice of a value for r , since most molecules are asymmetric in shape. It will be found useful to rewrite eq 2 in the form

$$A = 6s\gamma \quad (4)$$

where s is the surface area of the molecule or segment of a polymeric molecule. Equation 4 is exact for spherical molecules and may be considered as a useful approximation for asymmetric molecules. This will be considered further in the next section.

Corresponding States Theory and Surface Tension

1. *Principle of Corresponding States.* The Prigogine corresponding states principle^{12,13} for chain and spherical molecule liquids relates the bulk molar configurational properties of the fluid to universal dimensionless reduced quantities (marked with tilde) through reduction parameters (marked with asterisk). Thus

$$\begin{aligned} V(n_i, T) &= \tilde{V}(\tilde{T}) \cdot V^*(n_i); V^* = Nr(n_i) \cdot \sigma^3 \\ U(n_i, T) &= \tilde{U}(\tilde{T}) \cdot U^*(n_i); U^* = Nq(n_i) \cdot \epsilon^* \\ S(n_i, T) &= \tilde{S}(\tilde{T}) \cdot S^*(n_i); S^* = Nc(n_i) \cdot k \end{aligned} \quad (5)$$

where $V(n, T)$, $U(n, T)$, and $S(n, T)$ are, respectively, the molar volume, molar configurational internal energy, and the molar configurational entropy; ϵ^* and σ are the intermolecular energy and distance parameters of the pair interaction potential. N is Avagadro's number, k is the Boltzmann constant, and n_i the number of atoms in the principal chain. The parameters $r(n_i)$, $q(n_i)$, and $c(n_i)$ can be considered as the effective number of segments per molecules. Only c can be ascribed an absolute significance, with $3c$ being the number of external or volume dependent degrees of freedom of the molecule. The reduced quantities \tilde{V} , \tilde{U} , and \tilde{S} depend only upon the reduced temperature \tilde{T} , which is a measure of the free volume or expansion of the liquid. It is essentially the ratio of the external energy of the $3c$ degrees of freedom to the intermolecular contact energy $q\epsilon^*$:

$$\tilde{T} = \frac{c}{q} \left(\frac{kT}{\epsilon^*} \right) = \frac{T}{T^*} \quad (6)$$

also

$$T^* = U^*/S^* \quad \text{and} \quad P^* = U^*/V^* \quad (7)$$

Numerous methods have been used to obtain the reduction parameters¹⁴ and the reduced quantities, but discussion of this is deferred until a later section.

2. *The Reduced Surface Tension.* The surface tension of nonpolar fluids and polymer liquids, i.e., materials that obey the law of corresponding states, can be written in the form¹⁵

$$\gamma(n_i, T) = \gamma^*(n_i) \cdot \tilde{\gamma}(\tilde{T}) \quad (8)$$

where $\gamma^*(n_i)$ is the reduction parameter for the surface tension, which can be put in a form⁶ analogous to that used by van der Waals, i.e.

$$\gamma^*(n_i) = k^{1/3} P^{*2/3} T^{*1/3} \quad (9)$$

Both Roe¹⁶ and Patterson and Rastogi⁶ have extended the corresponding states principle for bulk properties, to obtain an expression for the surface tension of liquids by utilizing

a cell model for the liquid state. Following Prigogine and Saraga,¹⁵ the latter authors have shown that the reduced surface tension can be written as

$$\tilde{\gamma}\tilde{V}^{2/3} = -M\tilde{U}(\tilde{V}) - \tilde{T} \ln \frac{2\tilde{V}^{1/3} - b}{2(\tilde{V}^{1/3} - b)} \quad (10)$$

where M is the fractional reduction in the number of nearest neighbors of a segment of a chain molecule due to migration from the bulk to the surface. Consequently $-M\tilde{U}(\tilde{V})$ is the corresponding increase in configurational energy of a segment, which can be identified as the reduced surface energy. The second term on the right-hand side of eq 10 is then the reduced surface entropy and b is a packing parameter.

3. *Molecular Surface Area.* In the Fowkes expression for the Hamaker constant, eq 2, the intermolecular distance r appears as one of the variables. It is evident that r could be deduced by use of a molecular model, but these usually involve assumptions which introduce unnecessary approximations. It is therefore intended to use an expression for the molecular surface area s , as in eq 4, that can be obtained from bulk corresponding states parameters which are independent of molecular models. The volume per molecule, V_m , from eq 5 can be formally written as

$$V_m = V/N = V^*\tilde{V}/N \quad (11)$$

where V is the molar volume. If we consider that each element of the segmented molecule is a length of chain having three degrees of freedom, i.e., $c = 1$, in analogy with the three external degrees of a spherical molecule, then the reduction volume V^* per mole will be given by RT^*/P^* . Therefore

$$V_m = \frac{RT^*\tilde{V}}{NP^*} = \frac{kT^*\tilde{V}}{P^*} \quad (12)$$

If we now assume that the molecular surface area is given by $f_A(V_m)^{2/3}$, where f_A is a constant of proportionality which, in the absence of more information, we set equal to unity, then

$$s = \left(\frac{kT^*\tilde{V}}{P^*}\right)^{2/3} \quad (13)$$

It should be pointed out that eq 13 is not the only expression for s that could have been used, but it does appear to be the least artificial. This subject has been discussed in more detail by Siow and Patterson.¹⁷

The Nonretarded Hamaker Constant

Substitution of eq 8–10 and 13 into eq 4 gives

$$A = 6kT \left[\frac{-M\tilde{U}(\tilde{V})}{\tilde{T}} - \ln \frac{2\tilde{V}^{1/3} - b}{2(\tilde{V}^{1/3} - b)} \right] \quad (14)$$

which is a simple expression for the so-called nonretarded Hamaker constant for nonpolar fluids where \tilde{U} , \tilde{V} , and \tilde{T} can be obtained from the *bulk thermodynamic properties* of the material in conjunction with a configurational model for the liquid state. Equation 14 also accounts explicitly for the effect of temperature upon A , which is not the case with other microscopic approximations.

The results of eq 14 can be compared with those obtained from

$$A = 3\pi^2 q^2 h\omega\beta^2/4 \quad (15)$$

which is the original expression derived by Hamaker,⁹ and is the basis of other microscopic approximations. q is the

number of interacting volume elements per cubic centimeter which is calculated from the molar volume, β is the static polarizability, h is Plank's constant, and ω is the dispersion frequency. Through a straightforward manipulation Gregory was able to transform⁷ a modified eq 15 into

$$A = \frac{27}{64} h\omega \left(\frac{\epsilon - 1}{\epsilon + 2} \right)^2 \quad (16)$$

where ϵ is taken as the square of the limiting refractive index in the visible wavelength region. Equations 15 and 16 are strictly valid only for materials having one characteristic dispersion frequency, although in practice an average value of the major dispersion frequencies is usually taken, together with the respective molecular parameters. Expressions similar to (16) have been derived by numerous workers^{7,8} and have been used extensively to calculate Hamaker constants. Equations 2, 14, 15, and 16 are compared in the Discussion section.

Models for the Configuration Properties

Two methods have been used in evaluating the configurational properties¹⁴ in corresponding states theories. The earliest method utilized experimental data. For example, the energy of vaporization was used to obtain a value for $-\tilde{U}$. Now, the most widely accepted and simplest method is through the use of a theoretical model for the liquid state. The configurational energy can be written in terms of a generalized Mie potential between point centers¹⁸

$$\tilde{U}(\tilde{V}) = \frac{1}{n-m} [-n\tilde{V}^{-m/3} + m\tilde{V}^{-n/3}] \quad (17)$$

In principle m and n can take any values and when $m = 6$ and $n = 12$ eq 17 reduces to the well-known Lennard-Jones potential in terms of a volume dependence rather than a distance dependence. The use of a cell model partition function with \tilde{U} leads to a reduced equation of state¹⁸ for the liquid of the form

$$\frac{\tilde{P}\tilde{V}}{\tilde{T}} = (1 - b\tilde{V}^{-1/3})^{-1} - \frac{mn}{3(n-m)\tilde{T}} [\tilde{V}^{-n/3} - \tilde{V}^{-m/3}] \quad (18)$$

At normal pressures $\tilde{P} = 0$, and therefore

$$\tilde{T} = \frac{mn}{3(n-m)} \tilde{V}^{-m/3} (1 - \tilde{V}^{-(n-m)/3}) (1 - b\tilde{V}^{-1/3}) \quad (19)$$

By using the thermodynamic identity for the thermal expansion coefficient α , the equation of state yields an expression for \tilde{V} in terms of α . Thus

$$(\alpha T)^{-1} = -\frac{m}{3} + \frac{n-m}{3(\tilde{V}^{(n-m)/3} - 1)} + \frac{b}{3(\tilde{V}^{1/3} - b)} \quad (20)$$

where b is a packing fraction which is given by

$$b = (m/n)^{1/(n-m)} \quad (21)$$

A knowledge of α at a temperature T allows \tilde{V} , \tilde{T} , and \tilde{U} to be obtained through eq 20, 19, and 17, respectively, which then allows a value for the Hamaker constant to be computed from eq 14.

Three intermolecular potentials have been used in the literature in conjunction with corresponding states cal-

TABLE I: Expressions Used for the Different Configurational Models

	(3-∞)	(6-∞)	(6-12)
\tilde{U}	$-\tilde{V}^{-1}$	$-\tilde{V}^{-2}$	$-2\tilde{V}^{-2} + \tilde{V}^{-4}$
\tilde{V}^a	$\left[\frac{3 + 4\alpha T}{3(1 + \alpha T)} \right]^3$	$\left[\frac{3 + 7\alpha T}{3(1 + 2\alpha T)} \right]^3$	No simple relationship ^b
\tilde{T}	$\tilde{V}^{-1}(1 - \tilde{V}^{-1/3})$	$2\tilde{V}^{-2}(1 - \tilde{V}^{-1/3})$	$4\tilde{V}^{-2}(1 - \tilde{V}^{-2})(1 - b\tilde{V}^{-1/3})$
M^c	0.29	0.53	0.35
b	1.0	1.0	0.89

^a Obtained by rearranging eq 20. ^b Because no simple relationship exists for obtaining \tilde{V} from \tilde{T} , a computer print out of \tilde{V} for different values of αT was generated, which then allowed accurate values of \tilde{V} to be calculated using an interpolation procedure. ^c These values were obtained by Patterson and Rastogi⁶ from a least-squares treatment of the dimensionless reduced surface tension vs. αT for a variety of organic liquids. On the basis of a close packed lattice, M should have a value of 0.25.

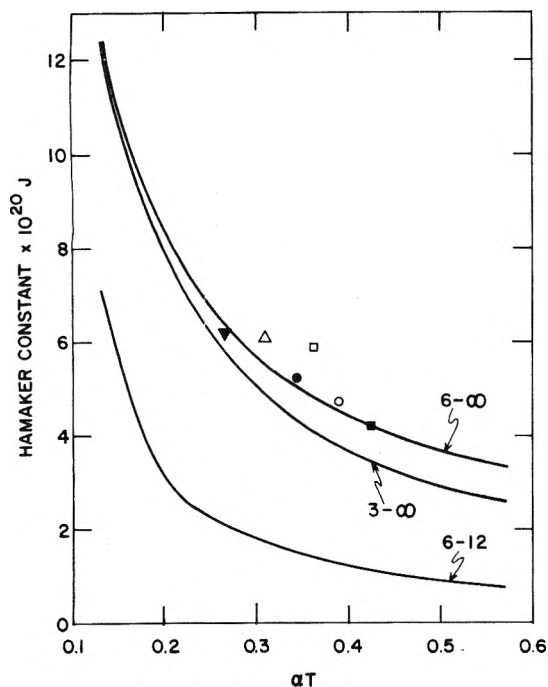


Figure 1. The Hamaker constant is shown plotted against αT for the three models of the liquid state shown in Table I. The data points refer to (∇) *n*-hexane, (Δ) toluene, (\bullet) *n*-octane, (\square) cyclohexane, (\circ) methyl ethyl ketone, (\blacksquare) acetone, and were calculated using eq 16.

culations. They are the van der Waals energy-volume relationship which was introduced by Flory,¹⁹ and can be formally obtained by putting $m = 3$, $n \rightarrow \infty$ in eq 17, the r^{-6} dispersion relationship which is obtained by putting $m = 6$, $n \rightarrow \infty$, and the Lennard-Jones relationship mentioned earlier. All three models have been used in computing A values. The actual expressions used to obtain the values of \tilde{U} , \tilde{V} , and \tilde{T} for the different models, together with the respective M and b values are listed in Table I.

Results and Discussion

The preceding discussion indicates that the nonretarded Hamaker constant for nonpolar liquids should be a universal function of αT . Figure 1 shows the Hamaker constant calculated using eq 14 plotted against αT for the various models shown in Table I. All three models show that A decreases, with a decreasingly negative slope, as αT increases. Both the (6-∞) and (3-∞) models give predictions for A which are very similar at small values of αT , but diverge as αT increases. It is of interest to note that the two curves intersect at a value of $\alpha T \approx 0.12$, although this is not shown in Figure 1. The addition of a "soft" repulsive contribution to the intermolecular pair potential, as in the Lennard-Jones (6-12) model, decreases the effective Hamaker constant by a factor of about 3 compared to the (m -∞) potentials. It is also somewhat surprising that

TABLE II: Comparison of Hamaker Constants of Organic Liquids at 25 °C

Liquid	$A/10^{-20}$ J (eq 14)	$A/10^{-20}$ J (eq 16)	$A/10^{-20}$ J (ref 22)
Chlorobenzene ^a	5.89		58.0, 76.7
Toluene ^b	5.40	6.1	10, 42
1,4-Dioxane ^c	5.26	5.9	
Cyclohexane ^d	4.82	5.9	4.64
Carbon tetrachloride ^d	4.78	6.3	37.7-57.0
Methyl ethyl ketone ^e	4.53	4.7	
Diethyl ether ^c	4.30	4.2	
Acetone ^c	4.20	4.2	
Ethyl acetate ^c	4.17	4.2	
Propylene oxide ^f	3.95		

The values of α used in this study were taken from the following. ^a P. J. Flory and H. Shih, *Macromolecules*, 5, 761 (1972). ^b S. Morimoto, *Makromol. Chem.*, 133, 197 (1970). ^c I. Timmermans, "Physico-Chemical Constants of Pure Organic Compounds", Elsevier, New York, N.Y., 1950, p 502. ^d S. E. Wood and J. A. Gray, *J. Am. Chem. Soc.*, 74, 3729 (1952). ^e P. J. Flory and H. Höcker, *Trans. Faraday Soc.*, 67, 2258 (1971). ^f J. M. G. Cowie and I. J. McEwen, *Polymer*, 16, 244 (1975).

A correlates with αT but not with an energy parameter such as the internal energy or P^* (see eq 7) since both α and P^* reflect the molecular cohesion of the substance.

Also plotted in Figure 1 are the Hamaker constants of six nonpolar liquids, which were calculated from optical data using eq 16. These values have been taken from Table II of ref 20. It can be seen that there is good agreement between the A values calculated from eq 16, and eq 14 using the (6-∞) potential. It is perhaps surprising that the (6-∞) model gives better agreement with Vincent's data than does the (3-∞) model, because in principle the configurational properties in eq 14 relate to the bulk properties of the fluid, and the Flory potential has been found to give a somewhat better representation of both the solution¹³ and surface behavior⁶ than have the other models. We are unable to offer any explanation for this, but note that the results are consistent with the original model of Fowkes.⁵ Figure 1 also shows that the Hamaker constant for cyclohexane obtained by Vincent is $\sim 20\%$ larger than the value computed using eq 14. However, van Voorst Vader²¹ has computed a value of 4.20×10^{-20} J using an expression which is identical with eq 16. This value is $\sim 10\%$ smaller than that obtained using the corresponding states formulation. These different values highlight the inherent difficulties in applying eq 16; namely, choosing the correct experimental parameters. A more detailed comparison of the Hamaker constants for nonpolar fluids, obtained from eq 14 and 16, together with other values (quoted by Visser²²) are shown in Table II. The results for A calculated from both optical and thermodynamic data are in good agreement, whereas the results obtained by other methods show an extremely wide range of values.

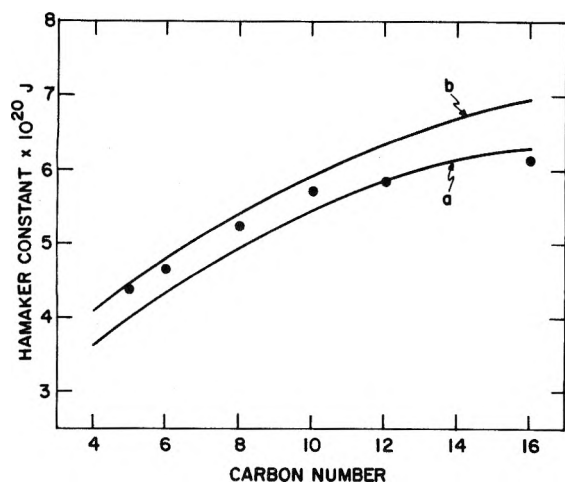


Figure 2. The Hamaker constant is shown plotted against the carbon number for the n -alkane series. Curve a has been calculated from eq 14 using a value for M of 0.53; curve b results when M is changed to 0.55. The points (●) refer to Hamaker constants calculated from eq 16.

TABLE III: Comparison of Hamaker Constants of Normal Alkanes at 25 °C

Alkane	$A/10^{-20}$ J (eq 2) ^a	$A/10^{-20}$ J (eq 15) ^a	$A/10^{-20}$ J (eq 14) ^b	$A/10^{-20}$ J (eq 16)
Pentane	3.44	3.85	3.94	4.4(5.04)
Hexane	3.80	4.19	4.32	4.7(5.48)
Octane	4.26	4.62	5.02	5.2(6.08)
Decane			5.45	5.7
Dodecane			5.84	5.9(6.75)
Hexadecane			6.31	6.2

^a Taken from F. Hauxwell and R. H. Ottewill, *J. Colloid. Interface Sci.*, 34, 473 (1970). ^b The values of α used in eq 7 were taken from R. A. Orwoll and P. J. Flory, *J. Am. Chem. Soc.*, 89, 6814 (1967).

A crucial test of eq 14 is whether it can reproduce the Hamaker constants for the model n -alkane series. Figure 2 shows a comparison of the Hamaker constants obtained using eq 14 and 16 plotted against the carbon number. Using the value of M obtained by Patterson and Rastogi,⁶ together with the (6- ∞) model in eq 14 gives curve a. Curve b results when the value of M is changed slightly to 0.55. The A values obtained from optical data are adequately encompassed when $M = 0.54$. Table III shows a comparison of the Hamaker constants obtained from eq 2, 14, 15, and 16 for several members of the n -alkane series from $n_i = 5$ -16. All of these microscopic approximations are in reasonably good agreement (which would be expected since the inherent assumptions of the original London-Hamaker equations are exemplified by these materials). The bracketed A values in Table III have been taken from a paper by Israelachvili.²³ Both sets of data in column 5 have been computed using equations which are essentially identical for these materials, but the values differ by $\sim 15\%$. This again suggests that the application of eq 16 is not an unambiguous exercise. With more complex liquids these difficulties are obviously compounded. In comparison, eq 14 is straightforward to use, the coefficient of thermal expansion being the only experimental parameter required.

It is widely recognized that adsorbed polymeric materials are important in stabilizing colloidal dispersions²⁴ (steric stabilization). The effect of this solvated polymeric sheath on the van der Waals attraction was originally studied theoretically by Vold²⁶ and more recently by Osmond, Vincent, and Waite.²⁷ In order to compute the interaction curves, the Hamaker constant of the solvated polymer

TABLE IV: Hamaker Constants of Polymers at 25 °C

Polymer	T_g , °C	$A/10^{-20}$ J (eq 14) ^b	$A/10^{-20}$ J (eq 16)
Poly(vinyl chloride)	81	10.82 ^c	10.0
Polyisobutylene	-70	10.10 ^b	
Polystyrene	100	9.80 ^b	7.8
Poly(vinyl acetate)	32	8.91 ^a	
Natural rubber	-73	8.58 ^b	
Polybutadiene	-81	8.20 ^c	
Polybutene-1	-24	8.03 ^d	
Poly(ethylene oxide) ^e	-115 to -40	7.51 ^b	6.8
Polydimethylsiloxane	-123	6.27 ^b	

^a Taken from "Polymer Handbook", J. Brandrup and E. H. Immergut, Ed., 2nd ed, Wiley, New York, N.Y., 1975. ^b The values of α used in eq 7 were taken from the reference indicated. ^c D. C. Bonner and J. M. Prausnitz, *AIChE J.*, 19, 943 (1973). ^d H. Shih and P. J. Flory, *Macromolecules*, 5, 758 (1972). ^e G. Delmas and P. de Saint-Romain, *Europ. Polym. J.*, 10, 1133 (1974). ^f G. Delmas and P. Tancrede, *Europ. Polym. J.*, 9, 199 (1973). ^g There are conflicting T_g data for this polymer.

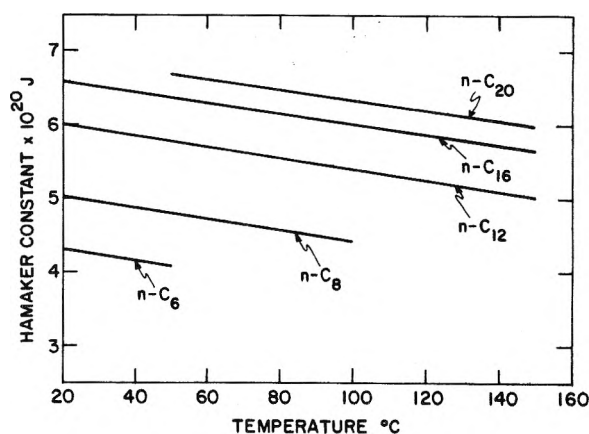


Figure 3. The Hamaker constant is shown plotted against temperature for various members of the n -alkane series. The $\alpha(T)$ data used in eq 14 were taken from R. A. Orwoll and P. J. Flory *J. Am. Chem. Soc.*, 89, 6814 (1967).

must be known. At room temperature many of the polymers of interest are glasses, for which the principle of corresponding states and hence eq 14 do not hold.²⁸ In solution, however, the polymer is in the liquid state and eq 14 is applicable, providing that the liquid state value for α is known. Values of α may be obtained by extrapolating measurements made above the glass transition temperature (T_g), to the temperature range of interest and this has now been done for a wide variety of polymers.²⁹ It would seem obvious that the Hamaker constant of a solvated polymer will differ from that of a glassy polymer but from the data shown in Table IV it is difficult to draw any specific conclusions. At present, eq 14 appears to be the only method of computing A values for solvated polymers.

Equation 14 also accounts for the temperature dependence of A provided of course that α is known as a function of temperature. Figure 3 shows the Hamaker constant (calculated using the 6- ∞ potential) plotted against temperature for various members of the n -alkane series. The figure shows that A decreases linearly with temperature, and that the relative change in the Hamaker constant decreases, as the chain length increases. This is to be expected since there is a decrease in $d\alpha/dT$ as the chain length increases so that, for the high molecular weight materials polystyrene and polydimethylsiloxane, the Hamaker constants are constant over the temperature range 25-150 °C. Unfortunately, there does not appear

to be any data in the literature with which to compare these trends.

Conclusion

It has been found that a corresponding states formulation for the Hamaker constants of nonpolar fluids gives good numerical agreement with values obtained using optical data. This microscopic formulation, which utilizes a macroscopic experimental parameter, is also able to explicitly account for the temperature dependence of the Hamaker constant.

Other surface free energy terms to be found in the literature³⁰ were investigated, along with the corresponding states formulation, but were found either to be impractical or to violate the assumptions inherent in the original derivation of the Hamaker constant. The application of the Prigogine corresponding states principle to this problem has been carried out in the same pragmatic spirit as that of the original derivation of Fowkes.

References and Notes

- (1) R. H. Ottewill, "Colloid Science", D. H. Everett, Ed., Specialist Periodical Reports, Vol. 1, The Chemical Society, London, 1973.
- (2) P. Richmond, "Colloid Science", D. H. Everett, Ed., Specialist Periodical Reports, Vol. 2, The Chemical Society, London, 1975.
- (3) E. R. Smith, D. J. Mitchell, and B. W. Ninham, *J. Colloid Interface Sci.*, **45**, 55 (1973).
- (4) R. Evans and D. H. Napper, *J. Colloid Interface Sci.*, **45**, 138 (1973).
- (5) F. M. Fowkes, *Ind. Eng. Chem.*, **56**, 40 (1964).
- (6) D. Patterson and A. K. Rastogi, *J. Phys. Chem.*, **74**, 1067 (1970).
- (7) J. Gregory, *Adv. Colloid Interface Sci.*, **2**, 396 (1969).
- (8) D. Tabor and R. H. S. Winterton, *Proc. R. Soc., London, Ser. A*, **312**, 435 (1969).
- (9) H. C. Hamaker, *Physica*, **4**, 1058 (1937).
- (10) J. Mahanty and B. W. Ninham, *J. Chem. Phys.*, **59**, 6157 (1973).
- (11) G. D. Parfitt, "Dispersion of Powders in Liquids", 2nd ed, G. D. Parfitt, Ed., Applied Science, London, 1973.
- (12) I. Prigogine (with the collaboration of A. Bellemans and V. Mathot), "The Molecular Theory of Solutions", North-Holland, Amsterdam, 1957, Chapter 9.
- (13) D. Patterson and G. Delmas, *Discuss Faraday Soc.*, **49**, 98 (1970).
- (14) D. Patterson, *Rubber Chem. Technol.*, **40**, 1 (1967).
- (15) R. Defay, I. Prigogine, A. Bellemans, and D. H. Everett, "Surface Tension and Adsorption", Longmans, London, 1966, Chapter 11.
- (16) R.-J. Roe, *Proc. Natl. Acad. Sci. U.S.A.*, **58**, 819 (1966).
- (17) K. S. Siow and D. Patterson, *Macromolecules*, **4**, 26 (1971).
- (18) D. Patterson, S. N. Bhattacharyya, and P. Picker, *Trans. Faraday Soc.*, **64** 648 (1968).
- (19) P. J. Flory, R. A. Orwoll, and A. Vrij, *J. Am. Chem. Soc.*, **86**, 3507 (1964).
- (20) B. Vincent, *J. Colloid Interface Sci.*, **42**, 270 (1973).
- (21) F. van Voorst Vader and H. Dekker, "Chemistry, Physical Chemistry and Applications of Surface Active Substances", Vol. 2, Carl Hanser Verlag, Munich, 1973, p 735.
- (22) J. Visser, *Adv. Colloid Interface Sci.*, **3**, 331 (1972).
- (23) J. N. Israelachvili, *J. Chem. Soc., Faraday Trans. 2*, **69**, 1729 (1973).
- (24) B. Vincent, *Adv. Colloid Interface Sci.*, **4**, 193 (1974).
- (25) D. H. Napper, *Ind. Eng. Chem., Prod. Res. Develop.*, **9**, 467 (1970).
- (26) M. J. Vold, *J. Colloid Sci.*, **16**, 1 (1961).
- (27) D. W. Osmond, B. Vincent, and F. A. Waite, *J. Colloid Interface Sci.*, **42**, 262 (1973).
- (28) J. G. Curro, *J. Macromol. Sci. Rev. Macromol. Chem.*, **C11**, 321 (1974).
- (29) H. Shih and P. J. Flory, *Macromolecules*, **5**, 758 (1972).
- (30) S. W. Mayer, *J. Phys. Chem.*, **67**, 2160 (1963); T. S. Ree, T. Ree, and H. Eyring, *J. Chem. Phys.*, **41**, 524 (1964); S. Wu, *J. Macromol. Sci. Rev. Macromol. Chem.*, **C10**, 1 (1974); H. Schonhon, *J. Chem. Phys.*, **43**, 2041 (1965).

Modified Potentiometric Method for Measuring Micellar Uptake of Weak Acids and Bases

E. Azaz and M. Donbrow*

School of Pharmacy, Hebrew University, Jerusalem, Israel (Received May 12, 1976; Revised Manuscript Received June 6, 1977)

The potentiometric method of measuring micellar uptake of weak acids or bases is reexamined. A modification simplifying and improving the method is proposed, based on measurement of the pH difference between paired solutions identical in degree of neutralization and concentration of the weak function, one solution containing the surfactant. The theory is presented and its application assessed in relation to typical binding equilibria. Some experimental improvements and results for benzoic acid solubilization in a hexadecyl polyethylene glycol (24) ether are given.

Introduction

The potentiometric determination of micellar binding of weak electrolytes, developed by Donbrow and Rhodes¹⁻³ and independently by Evans,⁴ is based on comparison of pH values measured during the titration of the micellar solutions to those of the acid or base in surfactant-free solution. It is applicable only if the ionized species is not micelle bound, as shown for benzoate³ and cresolate,⁵ if other micelle-interacting acids, bases, or solvents are absent¹ and if the surfactant does not influence the pK_a or ionic strength, as is probable in the case of nonionic surfactants of low cmc. Ionic strength errors are introduced in Evans' titration technique but can be avoided.⁶ The method is applicable to surfactants not fully saturated with solubilizate, a common situation for which few quantitative methods are available.⁷ The main advantage of the titration method over other methods is economy in

time. Accuracy is however limited by the measurement of concentrations of the un-ionized and ionized species from slight buret reading differences, errors being greatly magnified near the start and end of each titration and further multiplied if comparison titrations are used. Extensive calculations are required, including corrections for phase volume ratio, which changes during the titration.

The present authors have reexamined the method and found that greater accuracy, reproducibility, and speed can be achieved using a nontitration comparative technique.

Experimental Section

The pH values were measured for pairs of half-neutralized solutions identical in concentration of weak electrolyte and other respects, except for one of the pair containing the surfactant in the required concentration. The instrument and materials used were as previously

described.⁶ Cetomacrogol 1000 B.P.C. had the average formula $\text{CH}_3(\text{CH}_2)_{15}(\text{OCH}_2\text{CH}_2)_{24}\text{OH}$.^{6,7}

However, instead of using freshly decarbonated water, (and excluding CO_2) as previously, which had been found to give falling and fluctuating pH values, air-equilibrated distilled water was used, which maintained its pH value for several weeks at 6.5 ± 0.2 . It was prepared by passing air, previously washed with 10% H_2SO_4 and then with distilled water, through distilled water for about 10 h.

Theory and Discussion

Designating the concentrations originally present in the aqueous blank as c_a for the un-ionized and c_s for the ionized acid, and with Δc_a representing the amount of the un-ionized acid solubilized in the micellar phase of the solution containing the surfactant, it may be shown that under the conditions of validity of the Henderson-Hasselbach equation, the pH difference between the surfactant and aqueous solutions is given by

$$\Delta\text{pH} = -\log \frac{c_a - \Delta c_a}{c_s} + \log \frac{c_a}{c_s} \quad (1)$$

Hence

$$\Delta\text{pH} = -\log (1 - \Delta c_a/c_a) \quad (2)$$

Equation 2 is applicable at any degree of neutralization, provided the paired solutions are at the same degree of neutralization with respect to the total un-ionized acid present. Identity of the ionic species and the ionic strength in the two solutions ensures that the apparent dissociation constant remains the same, enabling it to be eliminated from the calculation, together with activity coefficient corrections.⁶

Where the micelle volume is not negligible, the ionic strength is fractionally higher in the surfactant solution, in which case

$$\Delta\text{pH} - \Delta \log \gamma = -\log (1 - \Delta c_a/c_a) \quad (2a)$$

where $\Delta \log \gamma$ is the activity coefficient correction. It is generally negligible, being of the order of 0.005 in 20% nonionic surfactant solution (cf. Figure 1).⁹

From eq 2, the unbound aqueous acid in the surfactant solution ($c_a - \Delta c_a$) is $c_a \cdot 10^{-\Delta\text{pH}}$ and the micellar acid is $c_a(1 - 10^{-\Delta\text{pH}})$, hence the fraction of the total un-ionized acid bound is given by

$$\Delta c_a/c_a = 1 - 10^{-\Delta\text{pH}} \quad (3)$$

The ratio of bound to free acid at a given concentration is thus

$$\Delta c_a/(c_a - \Delta c_a) = 10^{\Delta\text{pH}} - 1 \quad (4)$$

This may be expressed as an apparent distribution coefficient K_D' for known volumes (or weights) of the micellar and aqueous phases,¹⁰ V_m , V_w , given by

$$K_D' = V_m/V_w(10^{\Delta\text{pH}} - 1) \quad (5)$$

In the solubilization of the un-ionized form of a base, the equations corresponding to (4) and (5) are

$$\Delta c_b/(c_b - \Delta c_b) = 10^{-\Delta\text{pH}} - 1 \quad (6)$$

$$K_D' = V_m/V_w(10^{-\Delta\text{pH}} - 1) \quad (7)$$

Although half-neutralized solutions were found convenient for use in the modified method, the degree of neutralization does not control the ΔpH value, which is determined by the nature and parameters of the binding reaction. The equilibria are generally of the following types:

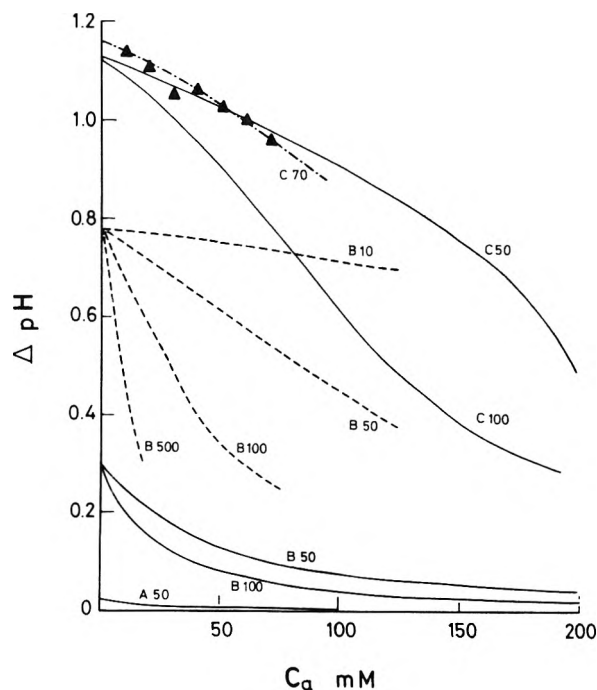


Figure 1. Relation between ΔpH and total un-ionized acid, c_a , at given K_1K_2 values and varying K_1/K_2 ratios. ΔpH is the pH difference between an aqueous solution and one which contains w grams of surfactant per liter both at identical concentration and degree of neutralization of the acid substrate. A, B, and C represent $w = 1, 20,$ and 200 , respectively. Numbers represent values of K_1 (L mol^{-1}). K_1K_2 values (L g^{-1}) are as follows: 0.05 (—), 0.25 (---), 0.058 (---). Experimental points are shown for benzoic acid at degrees of neutralization ranging between 25 and 90%, solubilized in 20% cetomacrogol (▲).

(a) K_D' is virtually constant over the concentration range measured, c_1 to c_2 . In this case, ΔpH is independent of concentration, eq 2 taking the form

$$\Delta\text{pH} = [\log (1 + K_D')]]_c^c \quad (8)$$

(b) The micelles are unsaturated and binding follows a Langmuir type equation

$$\Delta c_a = \frac{w\phi K_1 K_2 (c_a - \Delta c_a)}{1 + \phi K_1 (c_a - \Delta c_a)} \quad (9)$$

where K_1 and K_2 are the Langmuir parameters representing the binding constant and saturation concentration, respectively, w is the weight of surfactant present in micellar form, and ϕ is the volume correction factor for the aqueous acid concentration, defined by $\phi = (V_m + V_w)/V_w$. Substitution into eq 2 yields

$$\Delta\text{pH} = \log (1 - \phi K_1 \Delta c_a - w\phi K_1 K_2) \quad (10)$$

When $1 \gg \phi K_1 (c_a - \Delta c_a)$ in eq 9

$$\Delta\text{pH} = \log (1 + \phi w K_1 K_2) \quad (11)$$

This defines the limiting ΔpH value as $c_a \rightarrow 0$ and may also represent a constant value of ΔpH at higher concentration when K_1 is very low.

(c) When the micelles are saturated with substrate, Δc_a is constant ($\phi K_1 (c_a - \Delta c_a) \gg 1$ in eq 9), in which case $\Delta c_a = wK_2$, yielding

$$\Delta\text{pH} = -\log (1 - wK_2/c_a) \quad (12)$$

The forms of these $\Delta\text{pH} - c_a$ relations are shown in Figure 1 for some hypothetical parameters of similar order to the K_1 and K_2 values measured experimentally for benzoic acid and phenol solubilization.^{7,8} An actual set of experimental points and the best matching theoretical curve are also

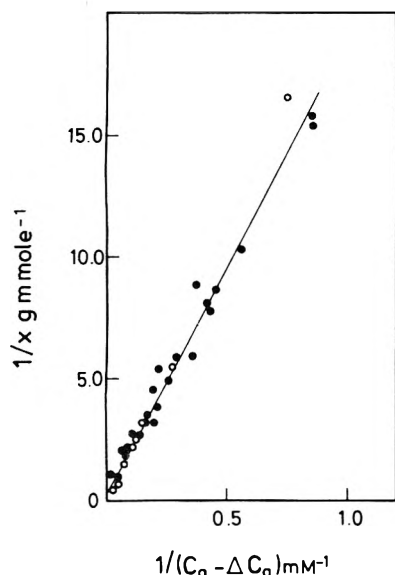


Figure 2. Binding of benzoic acid by cetomacrogol at 25 °C: (●) data obtained by different methods and laboratories;⁷ (○) present work. The plot represents a reciprocal form of Langmuir's type equation $1/x = 1/K_2 + 1/K_1K_2(c_a - \Delta c_a)$ where x is the amount of acid bound to 1 g micelles (in mmol/g), $c_a - \Delta c_a$ is the concentration of free un-ionized benzoic acid (in mM), K_1 is the binding constant (in L/mmol), and K_2 is the amount of acid bound per 1 g of micelles at monolayer saturation (in mmol/g).

included to illustrate the sensitivity. Since the experimental error resides mainly in pH measurement, error is minimized by raising the ΔpH value, which can be achieved by increasing the surfactant concentration and selecting a suitable c_s range.

The experimental error in assessment of bound substrate due to inaccuracy in pH readings may be estimated by differentiation of eq 5. Neglecting changes in the phase volume ratio, this gives

$$dK_D'/d(\Delta\text{pH}) = 2.303V_m/V_w \cdot 10^{\Delta\text{pH}} \quad (13)$$

The fractional error is conveniently expressed as

$$\Delta K_D'/K_D' = 2.303(1 - 10^{-\Delta\text{pH}})^{-1} \text{pH}_x \quad (14)$$

where pH_x is the experimental error in measurement of ΔpH . Using equipment of 0.002 pH accuracy^{6,8} with the modified method, ΔpH should be measurable to 0.005 pH or better. The corresponding errors in K_D' at this limit calculated from eq 14 are 5.6, 3.1, 1.7, and 1.3% at ΔpH values of 0.1, 0.2, 0.5, and 1.0, respectively. Experimental

results were generally measured between ΔpH 0.2 and 1.2 and their scatter about mean readings or about the best curve for a range of substrate concentrations was within the predicted values above.

Some examples of the effect of surfactant concentration are illustrated in Figure 1 for different solubilization parameters. ΔpH values are maximal at low c_a , where micellar uptake is highest, converging to the eq 11 value as $c_a \rightarrow 0$ for all $K_1:K_2$ ratios having a common K_1K_2 value. However, reproducibility may fall off at very low concentrations, due to the low buffer capacity of the solution. All curves tend toward $\Delta\text{pH} = 0$ at high enough c_a in accordance with eq 2 and 12, the ΔpH value and convergence depending on the degree of saturation of the micelles. Where the $K_1:K_2$ ratio is high, it is advantageous to work at a low c_a value.

The method has been applied to benzoic acid over a range of concentration up to 12 mM free acid (equilibrium value) in 2% cetomacrogol, yielding K_D' values close to those obtained by the titration technique and with less scatter. Since the value of K_D' varies with free acid concentration, it is difficult to make a point to point comparison of accuracy. However, linearization of the relation K_D' - free acid concentration by means of a reciprocal Langmuir equation plot⁷ led to slopes of similar values in the two methods which were also in agreement with those obtained by other methods and in other laboratories (Figure 2). From the slopes of individual titrations, K_1K_2 values ranged from 4.4 to 6.9×10^{-2} L/g,⁷ where K_1K_2 is the product of the two Langmuir equation parameters for the system benzoic acid-cetomacrogol-water. The statistical slope of the line obtained from Figure 1 gives a K_1K_2 value of 5.2×10^{-2} , while the modified method yields 4.9×10^{-2} .

References and Notes

- (1) M. Donbrow and C. T. Rhodes, *J. Pharm. Pharmacol.*, **15**, 233 (1963).
- (2) M. Donbrow and C. T. Rhodes, 23rd F.I.P. Conference, Munster, 1963, Govi-Verlag GMBH, Frankfurt am Main, 1964, pp 397-404.
- (3) M. Donbrow and C. T. Rhodes, *J. Chem. Soc. Suppl.*, **2**, 6166 (1964).
- (4) W. P. Evans, *J. Pharm. Pharmacol.*, **16**, 323 (1964).
- (5) E. Azaz and M. Donbrow, unpublished data.
- (6) M. Donbrow and C. T. Rhodes, *J. Pharm. Pharmacol.*, **17**, 258 (1965).
- (7) M. Donbrow, E. Azaz, and R. Hamburger, *J. Pharm. Sci.*, **59**, 1427 (1970).
- (8) E. Azaz and M. Donbrow, *J. Colloid Interface Sci.*, **57**, 11, 19 (1976).
- (9) Where ionic strength affects the binding equilibrium through alteration of solubility and/or micellar properties, adjustment to known ionic strength is required, as in other methods. The paired solutions of the modified method are particularly convenient for such adjustment, and no correction was needed in the mathematical treatment.^{6,8}
- (10) V_m is defined and determined as in A. T. Florence, *J. Pharm. Pharmacol.*, **18**, 384 (1966).

Structure of Some Polymer-Detergent Aggregates in Water

B. Cabane

Physique des Solides,¹ Université Paris-Sud, 91405-Orsay, France (Received November 15, 1976; Revised Manuscript Received May 31, 1977)

Publication costs assisted by CNRS

Poly(ethylene oxide) (PEO) dissolved in water associates with sodium dodecyl sulfate (SDS) to form aggregates whose thermodynamic properties are well defined. In order to determine the structure of these aggregates, some microscopic information is required. This paper presents NMR experiments on the ^{13}C , ^1H , and ^{23}Na nuclei of the detergent and polymer molecules. As a result, it is shown that a PEO-SDS aggregate can be described as a mixed micelle. The polymer is wrapped around this micelle; some of the monomers of the polymer are directly adsorbed at the hydrocarbon/water interface, but most of them form loops in the surrounding water. The NMR data also indicate that the detergent/polymer/water interface tends to retain a certain stoichiometric composition. As a result, there is a line of stoichiometric compositions for the solutions, where all the available material (detergent and polymer) is used in such mixed micelles. When the composition of the solution departs from this stoichiometry, the mixed micelles resist the change in composition, and the excess material is present as regular detergent micelles or unassociated polymer molecules.

1. Introduction

This paper discusses a certain type of association between small molecules and polymers in water solutions. In general, the nature of such associations is the result of a competition between two types of interactions: the interactions between the small molecules and the monomers of the polymer, and the interactions between the small molecules themselves. The following examples illustrate this range of situations.

(i) In the simplest case, there is no attraction between the small molecules. This is the case for molecules which are water soluble, and do not have an amphiphilic character. Then, each of them interacts individually with a few monomers of the polymer. The association of the nonionic polymer poly(vinylpyrrolidone) with a variety of cosolutes follows this pattern.¹

(ii) In the next case, there is an attraction between the small molecules, but it is smaller than their interactions with the monomers of the polymer. For example, consider detergent molecules, which normally pack their hydrocarbon chains in the core of micelles, and a polyelectrolyte with a charge opposite to that of the detergent.² In this case, one would like to know how the interactions between the detergent molecules change the system with respect to situation (i).

(iii) Finally, the interactions between the small molecules may predominate. Indeed, the motivation for this work was to investigate whether this may be the case for the association of detergent molecules with a nonionic, hydrophilic polymer. Then one must consider the interaction between an aggregate of detergent molecules, on one hand, and a number of monomers of the polymer, on the other. More precisely, one would like to know what types of aggregates are formed by the detergent molecules, and what is the topology of the association of the polymer with these aggregates.

Scope. The system discussed in this paper is composed of a nonionic, yet hydrophilic polymer, poly(ethylene oxide) (PEO), and an anionic detergent with a small counterion, sodium dodecyl sulfate (SDS). The solutions of SDS in water, above the critical micelle concentration $x_0 = 2.3 \times 10^{-3} \text{ g/cm}^3$, form well-defined micelles whose average aggregation number is on the order of 60 at cmc^3 as well as for the concentrations used here.^{4,5} The system

SDS-PEO has already been studied by surface tension measurements,^{6,7} conductivity,⁶⁻⁸ dialysis,^{9,10} viscosity,⁶ and dye solubilization.^{8,10,11} From these data, it appears that the detergent molecules aggregate with the polymer. Generally, when detergent is added to a polymer solution, the association process starts abruptly above a certain detergent concentration x_1 lower than x_0 , and saturates abruptly above another detergent concentration x_2 .⁶⁻¹² x_1 has been attributed to a process analogous to micelle formation,^{7,9,12} and x_2 to the complete coverage of the polymer by linear adsorption of detergent molecules along its chain.⁶ Necessarily, for lack of microscopic data, these models had to be vague. Therefore, it appears that this detergent-polymer system is well characterized macroscopically, but the microscopic features of the association have been uncertain.

This paper presents an attempt to determine the structure of the aggregates through NMR, which makes it possible to investigate separately various parts of the molecules. The main results consist of chemical shifts of the ^{13}C nuclei of the detergent and polymer molecules (section 3.2). The variation of these shifts with composition of the solution is used to determine the relative positions of the molecules in the aggregates (section 4.1); it will be argued that the detergent molecules form a detergent/water interface. A description of this interface is given in section 4.2, and its composition is discussed in sections 4.3 and 4.4.

2. Experimental Section

2.1. Concentrations. The systems studied in this paper are solutions whose composition can be defined by the concentrations in water x for the detergent and y for the polymer. The NMR properties of the detergent were measured at a fixed detergent concentration of $x = 2 \times 10^{-2} \text{ g/cm}^3$, as functions of the polymer concentration y . This was advantageous in three ways. First, the ionic strength of the solution remained constant; this is important because the detergent is sensitive to the presence of electric charges. Secondly, the signal-to-noise ratio remained constant. Thirdly, the measured properties turned out to be simple functions of y/x , whose measurements at constant x are easiest to interpret (section 4.3). Conversely, and for similar reasons, the NMR properties of the polymer were measured at a fixed polymer concentration of $y = 1 \times 10^{-2} \text{ g/cm}^3$, as functions

¹Laboratoire associé au CNRS.

of the detergent concentration. In fact, because the properties of the solutions turned out to be simple functions of one parameter only (y/x for the detergent properties, x/y for the polymer properties), the data plotted in one way could be plotted in the other as well.

2.2. Experiments. ^{13}C NMR spectra and relaxation times were obtained at 69 MHz with a FFT, high-resolution spectrometer built by the Groupe de biophysique, Ecole Polytechnique, 91120 Palaiseau, France. The temperature of the sample was maintained at 40 °C by a flow of cold air. The 69-MHz spectra show separate lines for most carbons of the SDS chain; these lines were assigned with the help of paramagnetic ions bound to the polar groups of the SDS molecules; the resulting assignment is indicated in Figure 8. The samples used for shift measurements were solutions in D_2O , and the field was locked on the NMR of D_2O . In the measurement of the shifts of the lines, we used as a reference the lock signal (D_2O); it is known that this resonance is not shifted by small amounts of dissolved detergent or polymer, and this was confirmed in our experiments.^{13,14} The values of the shifts were found to be reliable within an experimental uncertainty of ± 2 Hz; most of this uncertainty was associated with small variations (± 2 °C) in the temperature of the sample. Shifts to higher frequencies were counted as positive. The results of these experiments are in agreement with those of previous, unpublished experiments made at 25 MHz on a JEOL spectrometer. For the measurements of the ^{13}C relaxation rates, the temperature of the sample was 22 °C; the accuracy of the relaxation rates is 10%.

^1H chemical shifts were measured at 250 MHz with a Cameca spectrometer; TMS was used as an external shift reference; the temperature of the sample was 22 °C.

^{23}Na relaxation rates were measured with a home-made pulsed spectrometer at 22 MHz and a temperature of 25 °C.

Surface tensions were measured with a Lauda tensiometer by the ring detachment method; the measurements were made after cleaning the surface and aging it for a few minutes. As we were interested only in the shape of the tension vs. concentration curves, and not in the absolute values of the surface tensions, no corrections were applied to the data.

2.3. Materials. Poly(ethylene oxide), listed as PEG 20.000, was purchased from Prolabo, France. This polymer was analyzed by GPC; its weight average molecular weight was found to be 10^4 , with a polydispersity $M_w/M_n = 2.6$. Proton NMR spectra of this polymer showed no impurities or oligomers except for a small amount of water. Sodium dodecyl sulfate listed as "specially pure" was purchased from BDH; the maximum content of decyl and tetradecyl sulfates listed by the manufacturer is 1%. The purity of this material was checked by measurements of its surface tension in water (Figure 1). The solvent used in the NMR experiments was D_2O with a deuterium content of 99.83%, purchased from CEA. The samples were prepared by mixing and heating to 40 °C for 0.5 h; they were discarded after 1 week. A deterioration of the molecular weight of the polymer was observed in a few samples which had been stored for 3 months.

3. Experimental Results

3.1. Surface Tensions. The variations of the surface tension of detergent-water solutions with the concentration of the detergent are related to the chemical potential of the detergent molecules. In particular, the formation of aggregates of detergent molecules changes the slope of the curve of the surface tension γ plotted vs. the logarithm of the total detergent concentration x . This property has

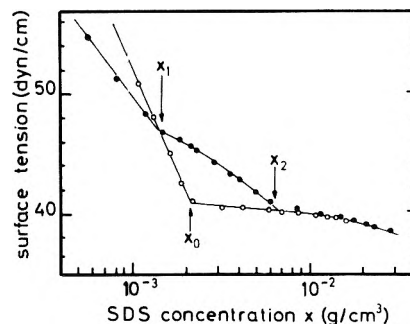


Figure 1. Effect of added PEO on the surface tension of SDS solutions, measured as a function of the logarithm of the SDS concentration x : circles, SDS only; dots, SDS with $y = 2 \times 10^{-3}$ g/cm³ PEO. The binding of SDS with PEO begins at x_1 and is completed at x_2 ; x_0 marks the CMC of pure SDS in water.

been used extensively to determine the critical micelle concentration x_0 of the detergent and to show the association of detergent with polymers.^{6,7} We have repeated and extended some of these measurements for the system PEO-SDS. A typical plot of γ vs. $\log x$ (Figure 1) shows two transition concentrations labeled x_1 and x_2 . Dialysis experiments^{9,10} show that the binding of detergent molecules with the polymer starts abruptly at x_1 and continues up to x_2 . Beyond x_2 , the surface tension of the solution is close to that of a solution containing regular detergent micelles. The known properties of the transition concentrations x_1 and x_2 are as follows:

(i) x_1 is lower than x_0 , indicating that the detergent-polymer aggregate has a lower free energy than a pure detergent micelle. The value of x_1 depends on the length of the hydrophobic chain of the detergent molecule and on the ionic strength of water in the same way as x_0 .^{10,12} For large molecular weight polymers ($M > 5000$), x_1 does not depend upon M , nor upon the concentration of the polymer.^{6,7}

(ii) $(x_2 - x_1)$ measures the amount of detergent bound to the polymer.¹² It is also independent from M ,^{6,7} and increases linearly with the concentration of the polymer (Figure 2); for concentrations in g/cm³, the upper line in Figure 2 yields $x_2 - x_1 = 2y$. In the following NMR study, the detergent concentrations will always be much larger than x_1 ; in this case, the saturation observed at x_2 for the polymer depends only on the ratio x/y .

3.2. Chemical Shifts. In order to obtain some information on the respective positions of the SDS and PEO molecules, we have studied the chemical shifts of their ^{13}C and ^1H NMR lines. Indeed, the shifts of NMR lines are sensitive to various changes in the local environment of the observed nuclei: The shifts of the ^1H nuclei of a hydrocarbon chain vary by about 0.02 ppm,¹⁴ and those of a ^{19}F nuclei on the fluorocarbon by 1 ppm,¹⁵ when the chain is transferred from water to a hydrocarbon environment. In general, the shifts of ^{13}C nuclei are not affected by this process. However, for a chain transferred from water or a hydrocarbon solvent to the interior of a micelle, the shifts of the ^{13}C nuclei located in the middle of the chain vary by 1 ppm.¹⁶ This effect is attributed to a change in the average conformation of the chain.¹⁷ Finally, a variation of the electrical charge borne by a neighboring atom can change chemical shifts by a few parts per million.¹⁸

However, it is not necessary to unravel all these effects in order to obtain some information on the relative positions of the SDS and PEO molecules. Rather, it is sufficient to assume that the variations of the chemical shifts reflect changes in the local environment of the observed nuclei, and proceed to observe which are the nuclei whose

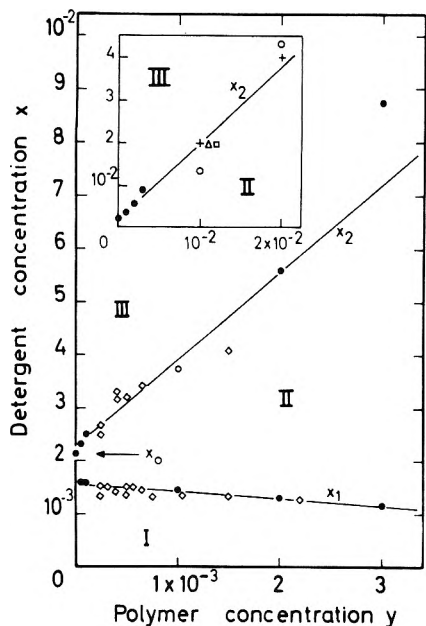


Figure 2. The concentrations x_1 and x_2 marking the beginning and the completion of the binding of SDS with PEO, as functions of the PEO concentration y (units are g/cm^3): dots, from surface tension; crosses, translational diffusion of the polymer; triangle, relaxation of the counterions; circles, ^{13}C chemical shifts of PEO; square, ^{13}C shifts of C1; lozanges, from ref 6. It is argued that region I contains only unassociated polymer and detergent molecules, region II polymer-detergent aggregates in equilibrium with excess polymer molecules, and region III polymer-detergent aggregates in equilibrium with excess detergent micelles.

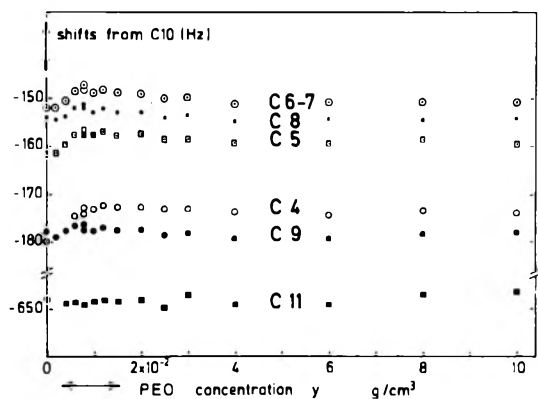


Figure 3. Effect of added PEO on the difference of chemical shifts between the carbon atoms of the SDS chain; the positions of C4, ..., C11 are plotted with respect to C10 which is used as a reference (see Figure 4 for a plot of C10). It is argued that the corresponding segments of the SDS chain are not affected by the binding with PEO.

shifts change when PEO and SDS associate.

Two basic observations can be made on the ^{13}C spectra when PEO is added to a micellar solution of SDS. First, most ^{13}C lines of the detergent are not shifted. Second, a few lines are shifted by large amounts.

(i) If the C atoms of the SDS molecule are labeled from the C closest to the polar group to the one in the methyl group as C1 through C12, the unshifted lines correspond to all C atoms beyond C3. Figure 3 shows that these lines are not shifted with respect to each other;¹⁹ Figure 4 shows that two lines are not shifted with respect to D_2O ; thus the same would be true of the other lines. Therefore the set of lines C4 to C12 can be used as a reference for the shifts of the other lines; for practical reasons, the line of C10 was chosen.²⁰

(ii) The lines of C1, C2, C3, and PEO are shifted when the composition of the solution is changed (Figures 5-7). The main features of these curves are as follows: (a) C1

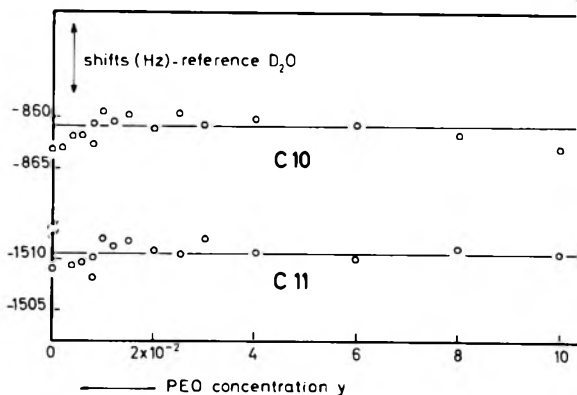


Figure 4. Effect of added PEO on the chemical shifts of the carbons C10 and C11 of the SDS chain, with the resonance of D_2O used as a shift reference.

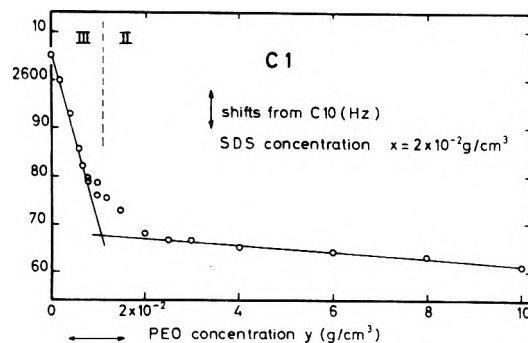


Figure 5. Effect of added PEO on the difference of chemical shifts between the carbons C1 and C10 of the SDS chain. On the left-hand side of the curve ($x > 2y$), the SDS molecules are exchanged between regular SDS micelles and PEO-SDS aggregates; on the right-hand side ($x < 2y$), they are included in PEO-SDS aggregates in equilibrium with excess PEO.

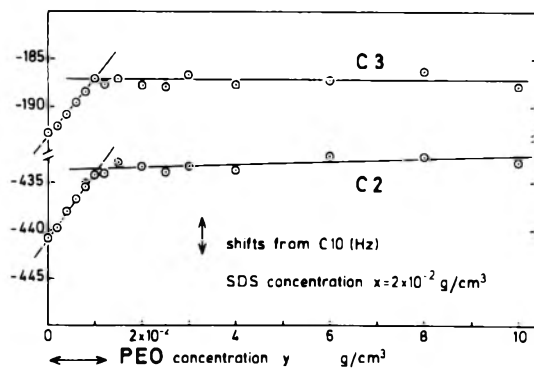


Figure 6. Difference of chemical shifts between carbons C2 and C10 of the SDS chain, and between C3 and C10.

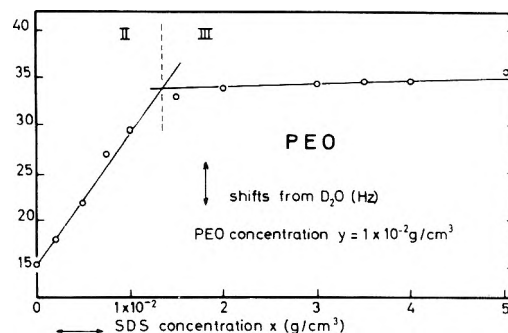


Figure 7. Effect of added SDS on the chemical shift of the ^{13}C line of PEO, with the resonance of D_2O used as a shift reference. On the right-hand side of the curve, the PEO molecules are included in PEO-SDS aggregates of fixed composition, in equilibrium with regular SDS micelles. On the left-hand side ($x < 2y$), the PEO molecules are exchanged between PEO-SDS aggregates and the excess PEO in the solution.

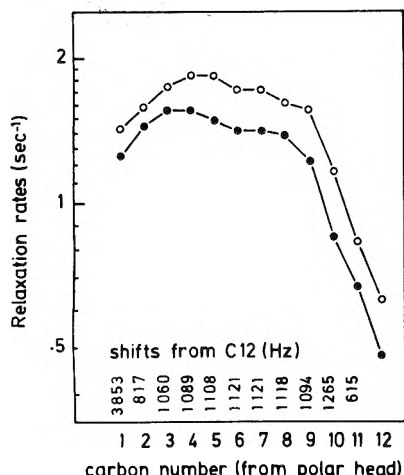


Figure 8. Relaxation rates of the ^{13}C nuclei of the SDS chains in regular SDS micelles (dots) and in PEO-SDS aggregates (circles). SDS concentration $x = 5 \times 10^{-2} \text{ g/cm}^3$, PEO concentration $y = 2.5 \times 10^{-2} \text{ g/cm}^3$. The positions of the lines of these ^{13}C in the spectrum of SDS are also listed numerically by their distance from the line of the methyl carbon.

is shifted by 50 Hz to lower frequencies when PEO is added to a SDS solution. Most of the variation occurs in the range $x > 2y$; further additions of PEO have little effect. This saturation occurs at the same composition which was observed in surface tension measurements (section 3.1). (b) C2 and C3 show the same behavior, but in the opposite direction of C1, and with a smaller amplitude. (c) There is also a shift of the PEO line when y/x is changed, but only for $x < 2y$. Beyond this point, its position remains constant. If SDS is added to a PEO solution, then the shift is toward higher frequencies.

The proton shifts show the same features, but with a much smaller amplitude. When PEO is added to a SDS solution, the lines of the protons attached to C1 and C2 are shifted by 6 and 4 Hz to lower frequencies; all the variation of the shifts occurs in the region $x > 2y$. On the other hand, the line of the main chain protons (C3 to C11) remains unshifted with respect to an external reference. Finally, the line of PEO shows a small variation of the shift in the region $x < 2y$. For the sake of brevity, these data are not shown in the figures.

3.3. ^{13}C Relaxation Rates. The ^{13}C nuclei of the SDS chain are relaxed by the reorientations of the corresponding methylene groups. We have measured these relaxation rates at a Larmor frequency of 69 MHz; they depend upon the spectral power of the reorientations at 207 and 345 MHz.²¹ In this frequency range, the reorientations of the methylene groups are associated with changes in the conformation of the SDS chain; they are controlled by internal rotation barriers and by steric constraints imposed by neighboring molecules.²² This effect of neighboring molecules on the rigidity of a hydrocarbon chain can be large: for example, the ^{13}C relaxation rates of a short detergent chain decrease by a factor of 4 when it is transferred from a micelle to water or to a hydrocarbon solvent.²³

The relaxation rates of SDS are shown in Figure 8. For SDS in PEO-SDS aggregates, they are only 1.2 times larger than for SDS in regular micelles. On the other hand, the relaxation rate of the polymer increases from 1.4 to 2 s^{-1} upon addition of SDS (with the same concentrations as those listed in Figure 8).

3.4. Nuclear Relaxation of the Counterions. The nuclear relaxation of the ^{23}Na ions is caused by the interactions of the nuclear quadrupole with the local electric field gradients. It is therefore sensitive to the binding of

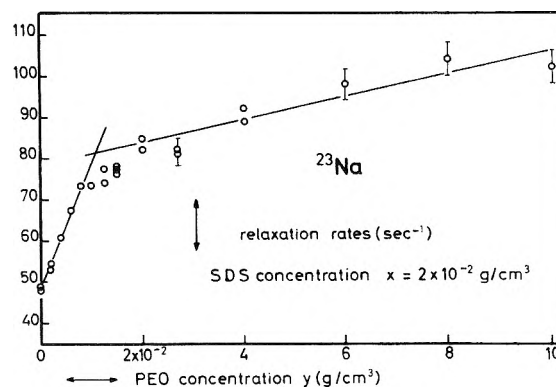


Figure 9. Effect of added PEO on the relaxation rates of the ^{23}Na counterions. The amount of polymer associated with each DS^- charge is small on the left-hand side of the figure, and large on the right-hand side.

the ^{23}Na ions to groups of negative charges, and to the configuration of these charges. This effect has been used to study the binding of ^{23}Na ions to micelles and polyelectrolytes.²⁴⁻²⁸ Usually, when the negative charges are brought closer together, the relaxation rate of the ^{23}Na ions increases for the following reasons. First, a larger number of the ions in solution will be bound to the groups of charges, because the relevant electric fields will be larger. Secondly, for simple configurations of the charges, these bound ions will also experience larger electric field gradients, and therefore have a higher relaxation rate. For example, the relaxation rate of ^{23}Na ions bound to polyacrylic acid is highest when the number of negative charges borne by the polyelectrolyte is largest.²⁵

The relaxation rates observed in this work for the ^{23}Na ions in the PEO-SDS solutions are on the order of 100 s^{-1} . They are much higher than the relaxation rates of free ^{23}Na ions; for example, in a solution of NaCl with the same molarity, the ^{23}Na relaxation rate is only 17 s^{-1} . This is caused by the binding of the Na ions to the PEO-SDS aggregates; similar increases in the relaxation rate of the counterions have been observed for ions bound to micelles²⁴ or polyelectrolytes.²⁵

The direction of the variation of the relaxation rates upon changing the composition of the solution is interesting (Figure 9). Indeed, the observed relaxation rates are highest when the solution contains mostly PEO. This means higher relaxation rates when there is a small number of DS^- charges per polymer molecule (or a large amount of polymer per charge). Finally, the precise shape of the curve shown in Figure 9 is similar to that observed for the chemical shift of C1 (Figure 5). In particular, the break in the curve is observed for the same composition of the solution.

4. Discussion

4.1. Relative Positions of the Detergent and Polymer Molecules in the Aggregates. (i) *Hydrocarbon Chains of the Detergent Molecules.* The results presented in part 3 indicate that these hydrocarbon chains experience the same environment in PEO-SDS aggregates as in regular SDS micelles. Indeed, the chemical shifts of all ^{13}C in a SDS chain, except for C1, C2, and C3, are unchanged when the SDS micelle is replaced by an aggregate of SDS with PEO, whereas they do change by 1 ppm when the chain is transferred from the micelle to water or to a hydrocarbon solvent (section 3.2). This indicates that the average conformation of a SDS chain in a PEO-SDS aggregate, as measured by ^{13}C chemical shifts, cannot be distinguished from that of a SDS chain in a regular micelle, and differs from the conformation of a SDS chain in other solvents.

Also, the relaxation rates of these ^{13}C indicate that the lifetimes of these conformations are not substantially different from those found in regular SDS micelles (section 3.3). Furthermore, the variation of x_1 with the length of the detergent chain is similar to that of x_0 (section 3.1); thus the last methylene groups of the chain must be in hydrophobic environment comparable to that of a micelle. Therefore, we conclude that a SDS chain in a PEO-SDS aggregate is surrounded by other SDS chains, as it is in a SDS micelle. A similar conclusion has been reached by Smith and Muller for the system PEO-sodium 12,12,12-trifluorododecyl sulfate on the basis of measurements of the chemical shift of the ^{19}F nuclei.¹⁵

(ii) *Head Groups and Counterions.* Although NMR provides no direct information on the polar groups ($-\text{OSO}_3^-$), the chemical shift of C1 shows that the hydrated part of the SDS molecule is bound to the polymer. Indeed, addition of PEO produces a large variation in the shift of C1 (section 3.2). This occurs probably through a modification of the distribution of electric charges around C1, or through a change in the average conformation of these segments of the SDS molecule; both explanations imply that some monomers of the polymer are replacing water molecules in the vicinity of the head of the SDS molecule.

The relaxation rates of the counterions support this description (polymer attached to the heads of clustered SDS molecules) and rule out the alternative picture of a polyelectrolyte-like aggregate (isolated detergent ions attached at various points of the polymer chain). Indeed, in this last model, the distance between two negative charges would be controlled by the length of polymer chain between two consecutive sites of adsorption. As for polyelectrolytes, this would yield higher relaxation rates when there is a large number of DS^- charges per polymer molecule; the opposite behavior is observed (section 3.4). Therefore, there must be a force which keeps the charges near each other regardless of the length of the polymer strand between two points of adsorption. This force can only be the hydrophobic attraction which clusters the chains.

(iii) *Topology of the Adsorption.* In the aggregates, the chains of the SDS molecules are packed in hydrophobic clusters (see (i) above); within these clusters, they are not mixed with PEO strands; this was obvious, because PEO is not soluble in hydrocarbons. This packing also forces the charges of the SDS molecules to be near each other (see (ii)); therefore, there must be a charged hydrocarbon/water interface, as there is in a micelle. Although the shape of the aggregates has not been determined, they will be called mixed micelles subsequently, because of the similarity between their local structure and that of regular micelles.

The variations, when PEO binds with SDS, of the chemical shift of C1 and of the ^{23}Na relaxation rate indicate that the polymer is adsorbed on the surface of the mixed micelle. This is consistent with the aptitude of micelles to preferentially solubilize various polar molecules in their surface layer.²⁹ We shall now try to specify the situation of PEO with respect to this surface.

4.2. *Situation of the Polymer on the Interface.* (i) *Adsorption Sites.* The discussion of section 4.1 indicates that PEO should interact with the SDS micelles in two ways. On one hand, some monomers of the polymer should replace water molecules in the vicinity of the carbons closest to the head of the SDS molecule. On the other, an electrostatic interaction of PEO with the polar groups is indicated by the relaxation rates of the counterions. It is necessary to examine whether these two mechanisms are

compatible with the geometry of a micelle.

A typical micelle, in a solution of SDS of $2 \times 10^{-2} \text{ g/cm}^3$, contains on the average 60 molecules³⁻⁵ whose hydrocarbon chains are clustered in a hydrophobic core; the polar heads extend outside of this core. In order to specify the nature of the hydrocarbon/water interface, it is necessary to evaluate what fraction of the core surface is covered by the polar groups. Simple geometrical considerations^{30,31} imply that the area per polar group, calculated at the core surface, is about 60 \AA^2 . This area is partially covered by the polar group, whose section is approximately 20 \AA^2 . Therefore, the area of the hydrocarbon/water interface which is not covered by the polar groups is on the order of 40 \AA^2 per molecule. In other words, a large fraction (about 2/3) of the surface of the hydrocarbon core is necessarily in contact with water. Accordingly, the first two or three methylene groups of each chain must be hydrated. This has been observed in thermodynamic experiments.³²

This description shows that there are indeed, at the surface of a typical micelle, two types of sites where PEO can replace hydration water: polar groups (area 20 \AA^2 per SDS molecule) and hydrated methylene groups (area 40 \AA^2 per SDS molecule). Both adsorption mechanisms take place. The interaction of PEO with the polar groups is demonstrated by the increase in the ^{23}Na relaxation rate upon association of PEO with the micelle (section 3.4); this effect is probably caused by a specific binding of Na^+ with SO_4^- and with the oxygen of PEO.³³ The interaction of PEO with the hydrated methylene groups is demonstrated by the variation of the shift of C1 (section 4.1).³⁴ The free energy of the detergent/water interface is lowered by this process. This can be measured by the difference between the critical concentration for the formation of mixed micelles, x_1 , and that for pure micelles, x_0 (Figure 1); it yields an adsorption free energy on the order of $0.3kT$ per SDS molecule.

(ii) *Configuration of the Polymer.* We have discussed above the situation of those monomers of the polymer which are bound directly to the interface. However, the ^{13}C relaxation rate of the polymer indicates that most monomers are not directly bound to the interface. Indeed, the correlation times for the motions of the monomers of PEO in a mixed micelle are only 50% slower than those for free PEO (section 3.3). On the other hand, for polymer strongly adsorbed on solid surfaces, with about 25% of the monomers bound directly to the surface, the motions of all the monomers are slowed down by at least one order of magnitude.³⁵ This suggests that, in our case, less than 25% of the monomers are bound directly to the interface.

The proportion of monomers of the polymer which are bound directly to the interface can also be estimated, if one assumes that the free energy of adsorption for each one of these monomers is equal to kT or larger. From the chemical potentials of the SDS molecules, the average adsorption free energy per SDS molecule was found to be about $0.3kT$ (see (i)); for a mixed micelle with a typical composition (for example, $x = x_2 = 2y$, which corresponds to the saturation observed in all the experiments) this yields an average adsorption energy of $0.1kT$ per monomer of the polymer. This indicates that about 10% of the monomers of the polymer are directly bound to the interface, while the others form loops in the surrounding water.

4.3. *Composition of the Mixed Micelles.* The chemical shifts presented in section 3.2 measure the changes in the environment of the detergent or polymer molecules as functions of the variations of the composition of the so-

lution; thus it is possible to study how the composition of the mixed micelles changes with the composition of the solution.

First, consider the work at fixed polymer concentration, with increasing detergent concentrations; this corresponds to a vertical path on Figure 2, crossing at $x = x_2$ from region II into region III. The dialysis experiments of Shirahama^{9,10} indicate that, in this process, the detergent which is added to the solution beyond $x = x_2$ does not bind to the polymer; so do the surface tension measurements (Figure 1). In this range (region III), the chemical shift of the polymer molecules remains constant, indicating that there is no change in the composition of the mixed micelles to which they belong (Figure 7). Now consider the measurements of the ¹³C chemical shift of C1 on the SDS molecules, at a fixed detergent concentration and as a function of the polymer concentration (Figure 5) (this corresponds to a horizontal path on Figure 2). Through region III, this shift varies linearly from the value of the shift for regular micelles up to the shift for mixed micelles. These data imply that, in region III, the solution contains PEO-SDS mixed micelles, whose composition does not change through the entire domain (see the polymer shift), and some detergent in excess, which forms regular SDS micelles; the SDS molecules are exchanged between the regular and mixed micelles, and the chemical shifts measure a time average over these two environments.

Then consider region II. In this region (i.e., before $x = x_2$ for a vertical path in Figure 2), dialysis and surface tension experiments indicate that some of the polymer is not saturated with detergent. For the same vertical path in region II, the chemical shift of the polymer varies linearly from the value of the shift for PEO alone to the shift of PEO in the mixed micelles found at x_2 (Figure 7). Again this is the result of an exchange process; the polymer strands are exchanged between two states: some are associated with the surface of the mixed micelles, and some are not; the chemical shifts measure a time average over these two environments.

The detailed shape of the curves in Figures 5 and 7 can actually be predicted on the basis of a simple hypothesis for the association between a PEO strand (i.e., a piece of a PEO molecule) and a SDS micelle. This hypothesis states that the association process can be described by the reaction



where the composition of the mixed micelle is fixed ($x = x_2 = 2y$) and therefore the relative molecular weights of the SDS micelle and of the PEO strand are fixed too. For large values of the equilibrium constant, the mass-action law yields the following behavior for the chemical shifts:

The variation of the chemical shift of the PEO molecules should be proportional to x/y when there is an excess of PEO, i.e., $x < 2y$ (region II). On the other side of the stoichiometric composition, i.e., for $x > 2y$ (region III), this chemical shift should retain the value which it reached at the stoichiometric composition. This is indeed the behavior observed in Figure 7; however, the transition at $x = 2y$ is not sharp; this could be caused by a dispersity in the sizes of the polymer molecules and of the micelles, or by the fact that the equilibrium constant is not infinitely large.

The variation of the chemical shift of the SDS molecules should be proportional to y/x when there is an excess of SDS, i.e., $x > 2y$ (region III). On the other side of the stoichiometric composition, i.e., for $x < 2y$ (region II), this chemical shift should retain the value which it reached at $x = 2y$. This is indeed the behavior observed in Figure

5; however, the slope of the curve in the range $x < 2y$ is not zero. This indicates that the composition of the mixed micelles varies slightly in this range, but much less than the composition of the solution. At the stoichiometric point, this composition corresponds to 3.3 monomers of the polymer for one detergent molecule; for solutions with the highest polymer concentrations (10 times larger than the stoichiometric concentration), the variation of the chemical shift in Figure 5 indicates that this ratio has risen to 4.1 monomers per detergent molecule. Alternatively, one can count the number of detergent molecules associated with one polymer molecule; for a polymer of molecular weight $M = 10^4$, there are about 70 detergent molecules in a mixed micelle. In this way, polymers of known M are used as a scale for determination of the molecular weight of the mixed micelles, and this allows a determination of their aggregation numbers.

4.4. *Origin of the Saturation at $x = x_2$.* The saturation of the binding at a well-defined composition of the solution is a remarkable phenomenon, if one takes into account the nonspecific character of the interactions between the detergent and the polymer, and also the fact that most of the polymer is in water. Of course, for the adsorption of small molecules on the surface of detergent micelles there is no such saturation; as the concentration of the detergent is increased, the small molecules distribute themselves among an increasing number of micelles. On the other hand, the monomers of a polymer molecule cannot be distributed arbitrarily among the micelles, or diluted arbitrarily on the hydrocarbon/water interface, because they are attached to a polymer chain. This could certainly impose a limit to the binding of detergent with a high molecular weight polymer.

There is however a stronger limitation to this binding. Because most of the polymer is in water, the amount of detergent bound to a polymer molecule is determined primarily by the thickness of the polymer layer coating the interface; for a given quantity of polymer, thicker polymer layers will bind less detergent than thinner ones. The thickness of the polymer layer is determined by the free energy of the polymer chain; a thinner layer has proportionally more monomers bound to the interface. On the other hand, the configurational entropy of the polymer chain is smaller for a thinner layer. In summary the saturation observed at $x = x_2$ is the result of competition between the hydrophobicity of the polymer, which tends to spread it on the interface, and the entropy of the polymer chain, which tends to preserve the thickness of the polymer layer. This explains why hydrophobic polymers bind more detergent than hydrophilic ones.³⁶

5. Conclusion

(i) *Local Structure.* The chemical shift and relaxation measurements presented in this paper give local information (environments of various nuclei). Their results imply that the detergent molecules form a detergent/water interface; as in pure detergent micelles, the chains of the detergent molecules appear to be gathered in the hydrocarbon core, while their polar groups are spread on the interface. These experiments also indicate that monomers of the polymer interact with the interface (i.e., with hydrated methylene groups and with polar groups of the detergent) but do not penetrate the hydrocarbon core. Their adsorption lowers the free energy of the interface with respect to that of a pure detergent/water interface. The average adsorption free energy per monomer of the polymer is about $0.1kT$. Accordingly, only 10% of the monomers of the polymer are directly adsorbed on the interface, while the others form loops in the surrounding

water. In summary, semidilute solutions of SDS with PEO (concentrations on the order of 2% weight/weight) form mixed micelles whose local structure is determined by the strong forces between the detergent molecules; the polymer is weakly adsorbed on the surface of these micelles.

(ii) *Composition.* The chemical shifts of the polymer and detergent NMR lines have been measured as functions of the composition of the solution. Their variations indicate that there is one composition for which the solution is stoichiometric; in such solutions, all the available molecules (polymer and detergent) are incorporated in mixed micelles. For higher detergent concentrations, pure detergent micelles are formed; for lower detergent concentrations, some molecules or strands of polymer are not associated with the detergent. One remarkable feature of these mixed micelles is that they resist changes in their composition. Indeed, whereas the overall composition of the solution can be varied arbitrarily, the composition of the interfaces where detergent and polymer are associated remains within narrow limits; for each detergent molecule in a detergent/polymer/water interface, there are at least 3.3 and at the most 4.1 monomers associated with the interface, either directly (adsorbed) or indirectly (loops). These limits are presumably imposed by the free energy of the polymer chain, which resists the deformations corresponding to changes in the composition of the detergent/polymer/water interface.

Acknowledgment. It is a pleasure to acknowledge the cooperation of F. Caron and M. Gueron, whose NMR spectrometer was used for the ^{13}C work. I also thank F. Lauprêtre for preliminary ^{13}C relaxation measurements, J. P. Vairon and M. Moreau for preliminary ^{13}C chemical shift measurements, and J. Lesec for performing GPC on the polymer.

References and Notes

- (1) P. Molyneux and G. S. Ahmed, *Kolloid Z.*, **251**, 310 (1973).
- (2) S. Saito, *Kolloid Z.*, **143**, 66 (1955).
- (3) K. J. Mysels and L. H. Princen, *J. Phys. Chem.*, **63**, 1696 (1959).
- (4) F. Reiss Husson and V. Luzzati, *J. Colloid Interface Sci.*, **21**, 534 (1966).
- (5) Y. Kubota, M. Kodama, and M. Miura, *Bull. Chem. Soc. Jpn.*, **46**, 100 (1973).
- (6) M. N. Jones, *J. Colloid Interface Sci.*, **23**, 36 (1967).
- (7) M. J. Schwuger, *J. Colloid Interface Sci.*, **43**, 491 (1973).
- (8) F. Tokiwa and K. Tsujii, *Bull. Chem. Soc. Jpn.*, **46**, 2684 (1973).
- (9) K. Shirahama, *Colloid Polym. Sci.*, **252**, 978 (1974).
- (10) K. Shirahama and N. Ide, *J. Colloid Interface Sci.*, **54**, 450 (1976).
- (11) S. Saito and H. Hirata, *Kolloid Z.*, **165**, 162 (1959).
- (12) H. Arai, M. Murata, and K. Shinoda, *J. Colloid Interface Sci.*, **37**, 223 (1971).
- (13) J. Clifford and B. A. Pethica, *Trans. Faraday Soc.*, **60**, 1483 (1964).
- (14) L. Odberg, B. Svens, and I. Danielsson, *J. Colloid Interface Sci.*, **41**, 298 (1972).
- (15) M. Smith and N. Muller, *J. Colloid Interface Sci.*, **52**, 507 (1975).
- (16) T. Drakenberg and B. Lindman, *J. Colloid Interface Sci.*, **44**, 184 (1973).
- (17) B. Persson, T. Drakenberg, and B. Lindman, *J. Phys. Chem.*, **80**, 2124 (1976).
- (18) R. Hagen and J. D. Roberts, *J. Am. Chem. Soc.*, **91**, 4504 (1969).
- (19) A close examination of the data in Figure 3 reveals that there are some systematic shifts with composition. However, these shifts are small (5 Hz) compared to those of C1 (50 Hz) and C2 (10 Hz).
- (20) The lines of the central carbons (C3 to C9) are not as well separated as those of the tail carbons (C10 to C12). On the other hand, the relaxation times of C11 and C12 are too long.
- (21) The relaxation is produced by a modulation of the dipolar ^{13}C - ^1H interaction through the reorientations of the C-H bond. The relevant frequencies are sums and differences of the Larmor frequencies of the ^{13}C and ^1H nuclei.
- (22) J. Charvolin and P. Rigny, *J. Chem. Phys.*, **58**, 3999 (1973).
- (23) U. Henriksson and L. Odberg, *Colloid Polym. Sci.*, **254**, 35 (1976).
- (24) J. Rosenholm and B. Lindman, *J. Colloid Interface Sci.*, **57**, 362 (1976).
- (25) J. J. van der Klink, L. H. Zuiderweg, and J. C. Leyte, *J. Chem. Phys.*, **60**, 2391 (1974).
- (26) In a micellar solution of SDS, about 70% of the counterions are bound at the surface of the micelles. See, for example, K. J. Mysels, and C. I. Dulin, *J. Colloid Sci.*, **10**, 461 (1955); T. Sasaki, M. Hattori, J. Sasaki, and K. Nukima, *Bull. Chem. Soc. Jpn.*, **48**, 1397 (1975). These bound ions remain hydrated;²⁷ it has been proposed that the electric field fluctuations seen by the ^{23}Na ions are produced by the distortions of the hydration sphere of the ion in the vicinity of a charged surface.²⁸
- (27) B. Lindman and P. Eckwall, *Mol. Cryst.*, **5**, 79 (1968).
- (28) I. D. Robb and R. Smith, *J. Chem. Soc., Faraday Trans. 1*, **70**, 287 (1974).
- (29) J. C. Eriksson and G. Gillberg, *Acta Chem. Scand.*, **20**, 2019 (1966).
- (30) C. Tanford, *J. Phys. Chem.*, **76**, 3020 (1972).
- (31) J. E. Leibner and J. Jacobus, *J. Phys. Chem.*, **81**, 130 (1977).
- (32) J. M. Corkill, J. F. Goodman, and T. Walker, *Trans. Faraday Soc.*, **63**, 768 (1967).
- (33) A similar enhancement of the ^{23}Na relaxation rate was also observed upon adsorption of alcohol at the surface of a micelle.²⁴ This enhancement was attributed to specific complex formation between Na^+ , COO^- , and OH.
- (34) There are two additional pieces of evidence for the hydrophobic interaction between polymers and the surface of the hydrocarbon core of micelles. First, it is known that the strength of the binding depends upon the hydrophobicity of the polymer (poly(propylene oxide) is more strongly adsorbed than PEO)⁷ and upon the length of the hydrocarbon chain of the detergent.¹⁰ Secondly, it is also known that the PEO does not interact with nonionic detergents such as poly(ethylene oxide) dodecyl ethers. This is consistent with the above discussion, as the hydrocarbon core of the nonionic detergent is covered with its own hydrophilic chains, and is therefore unavailable for hydrophobic bonding with PEO. See, for example, S. Saito, *Kolloid Z.*, **158**, 120 (1958).
- (35) T. Miyamoto and H. J. Cantow, *Makromol. Chem.*, **162**, 43 (1972).
- (36) H. Arai and S. Horin, *J. Colloid Interface Sci.*, **30**, 372 (1969).

Application of the Polanyi Adsorption Potential Theory to Adsorption from Solution on Activated Carbon. 9. Competitive Adsorption of Ternary Solid Solutes from Water Solution

Michael R. Rosene and Milton Manes*

Chemistry Department, Kent State University, Kent, Ohio 44242 (Received March 23, 1977)

Publication costs assisted by the Calgon Corporation

The adsorption on activated carbon from water solution has been investigated for the ternary systems: *p*-nitrophenol (PNP)–benzamide–glucose; PNP–benzamide–methionine; PNP–thiourea–acrylamide; and the binary system: PNP–benzamide. The adsorption data, when compared with estimates from an earlier-derived Polanyi-based model (hitherto applied only to binary systems), show good agreement with the theory, which gives the adsorption of each component in the presence of the others, given the individual adsorption isotherms and the mutual solubilities. A feature of the model is that the individual components occupy different regions of the "adsorption space"; it leads to the expectation, confirmed by experiment, of isotherms with distinct segments corresponding to the presumed distinct regions of adsorption. Another feature is the prediction of conditions under which one component may be totally excluded from adsorption.

Introduction

An earlier article¹ developed a Polanyi-based theory for multicomponent adsorption of solid solutes from solution onto heterogeneous adsorbents and reported data for adsorption onto activated carbon from water solution of a number of binary solute systems. This is an extension to ternary systems.

Theory

The Polanyi-based theory for multicomponent adsorption is given by Rosene and Manes.¹ If ϵ_i is the adsorption potential of the *i*th adsorbate in the solvent (i.e., corrected for solvent displacement) and if one for convenience assumes the solutes to form ideal solutions, then the adsorptive driving force at any point in the adsorption space is

$$-\Delta G_i = \epsilon_i - RT \ln (c_s/c)_i \quad (1)$$

where ϵ_i , the net adsorption potential per mole, varies over the adsorption space, and c_s and c are the saturation and equilibrium concentrations. Given a set of adsorbates and their equilibrium and saturation concentrations, the treatment of Rosene and Manes leads to the expectation that the component that will adsorb at any given element of volume in the adsorption space is the component with the highest adsorptive driving force per unit volume, $-\Delta G/V$. For binary solutes, if $\epsilon_2/V_2 > \epsilon_1/V_1$, the condition for adsorption of component 2 in the presence of component 1 is

$$\frac{RT}{V_2} \ln \frac{c_{2s}}{c_2} \leq \frac{\epsilon_2}{V_2} - \frac{\epsilon_1}{V_1} + \frac{RT}{V_1} \ln \frac{c_{1s}}{c_1} \quad (2)$$

(The inequalities in eq 7 and 8 in the original article¹ should be corrected.) Where the equality holds is the transition between the two components. Here the molar volumes, V , represent the volumes occupied per mole of adsorbate in the adsorption space, and may not necessarily be equal to the bulk molar volumes.

For multicomponent adsorption the same equation holds, i.e.

$$\frac{RT}{V_k} \ln \left(\frac{c_s}{c} \right)_k \leq \frac{\epsilon_k}{V_k} - \frac{\epsilon_j}{V_j} + \frac{RT}{V_j} \ln \left(\frac{c_s}{c} \right)_j \quad (3)$$

where the *k*th component is the component with the highest $-\Delta G/V$ at any element of volume in the adsorption space, and the *j*th component is the one with the next highest value of $-\Delta G/V$. For a given set of concentrations the rank of $-\Delta G/V$ may change over the adsorption space, depending on the relative values of ϵ/V .

For any set of concentrations, and given the dependence on adsorbate volume of each ϵ_i/V_i (which are not necessarily related by a single correlation curve), one may in principle examine each increment of the adsorption space, apply eq 3, and assign the appropriate adsorbate. In this fashion one may determine the volumes and locations of each individual adsorbate. The calculation becomes considerably simplified and easier to represent graphically when (as assumed earlier¹) the individual adsorption isotherms may be expressed as a single correlation curve with individual scale factors for the ϵ_i/V_i . The earlier article¹ should at this point be consulted for the treatment of binary adsorbates, which we here extend to ternaries.

The calculation, as earlier, is most conveniently illustrated by considering the concentration dependence of the adsorption of the component with the highest value of ϵ/V at fixed concentrations of the other two. (Since these fixed concentrations may be set arbitrarily, there is no loss of generality.) Let components 3, 2, and 1 have respectively the highest, middle, and lowest values of ϵ/V at equal adsorbate volumes. We may consider two separate cases: (a) $-\Delta G_2/V_2$ exceeds $-\Delta G_1/V_1$ over the entire adsorption space; (b) $-\Delta G_2/V_2$ exceeds $-\Delta G_1/V_1$ over part of the adsorption space and is smaller elsewhere.

Case a is illustrated in Figure 1. Curve 3 is the correlation curve for component 3 as a single solute adsorbing from the solvent, i.e., a plot of adsorbate volume vs. ϵ/V or (as we shall plot it later, $T/V \log c_s/c$). Curve 2 is constructed by taking the corresponding correlation curve for component 2 and shifting it to the left by a distance equal to $(RT/V_2) \ln (c_s/c)_2$; as earlier,¹ the abscissa is now equal (or proportional) to the (single-component) adsorptive driving force per unit volume, $-\Delta G_2/V_2$. Curve 1 is constructed in analogy with curve 2. The concentration ratios $(c_s/c)_2$ and $(c_s/c)_1$ have here been chosen to make $-\Delta G_2/V_2 > -\Delta G_1/V_1$ over the entire space in which either could adsorb alone. Under these circumstances there would be no adsorption of component 1; this case therefore

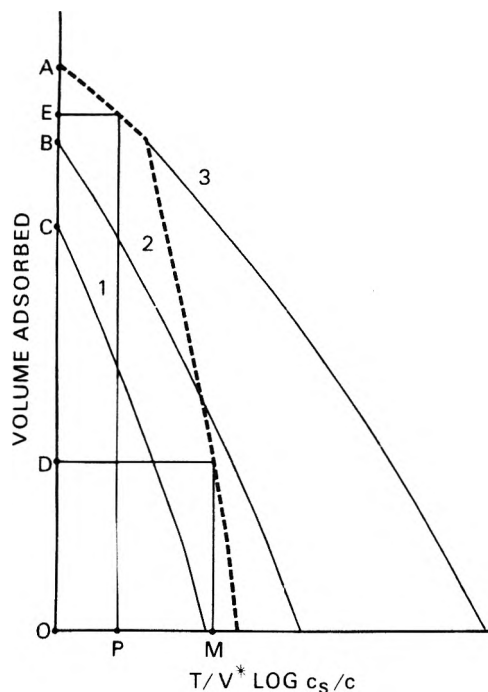


Figure 1. Schematic diagram showing construction of competitive (dotted) correlation curve for component 3 in the presence of components 2 and 1. Curve 3 is the correlation curve of pure component 3 in water; its abscissa is proportional to $\epsilon/V \ln$ in water, or $(T/V) \log (c_s/c)$. Curves 2 and 1 are similar correlation curves, shifted leftward by $(T/V) \log (c_s/c)$ for each component. Their abscissas are equal or proportional to $-\Delta G/V$, the adsorptive driving force per unit volume. The abscissa for the competitive (dotted) correlation curve is the difference between the abscissa of curve 3 and the larger of curves 2 and 1 (in this case curve 2, since curves 1 and 2 do not cross). The individual points are discussed in the text.

reduces to the competition of components 3 and 2, and is solved by the earlier treatment for binaries. The abscissa of any point on the dotted line is the difference between that of component 3 and the larger value of either of the other components; it is equal (or proportional) to the net adsorptive driving force per unit volume, and therefore (by eq 3) to $RT/V_3 \ln (c_s/c)_3$. The ordinate is equal to the volume of adsorbed component 3. The interpretation of Figure 1 is now exactly analogous to the binary system. For example, let $RT/V_3 \ln (c_s/c)_3$ be equal to the abscissa OM. The corresponding ordinate OD represents the volume of adsorption space occupied by component 3. The total occupied volume is equal to OB. The volume BD is occupied by component 2; component 1 does not adsorb anywhere in the adsorption space. If we set $(RT/V_3) \ln (c_s/c)_3$ equal to OP, then the total occupied volume in the adsorption space is equal to OE, and component 3 is the only adsorbate. As earlier, the dotted line representing the competitive adsorption shows a single kink at the ordinate B, which is the volume above which component 2 neither adsorbs nor competes.

Case b is illustrated in Figure 2 for the same components. The abscissa scale factors are identical, but the concentrations have been chosen so that component 1 is more strongly adsorbed than component 2 in part of the adsorption space. The dotted line is again constructed by subtracting from the abscissa of curve 3 the corresponding value of either curve 2 or curve 1, whichever is larger. The dotted line now has two kinks: one at C, where competition from component 1 begins; and one at D, where curves 1 and 2 cross. It is below this crossover point that component 2 becomes the dominant competitor.

We now consider the composition and volume of the overall adsorbate at different concentrations of component

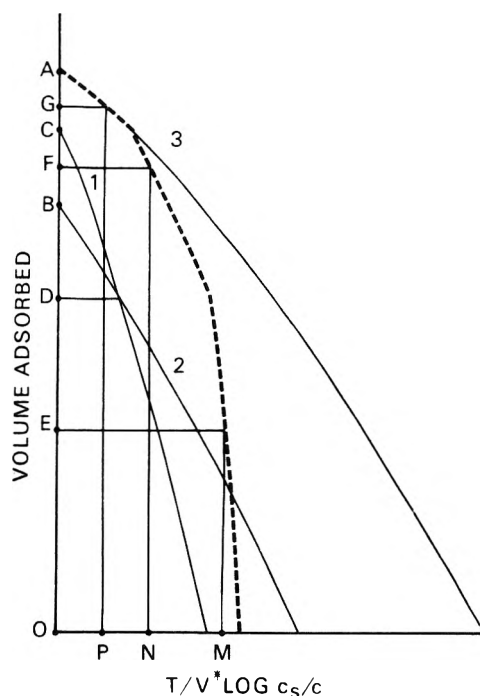


Figure 2. Schematic diagram showing construction of competitive (dotted) correlation curve for component 3 in the presence of components 2 and 1. Curve 3 is the correlation curve of pure component 3 in water; its abscissa is proportional to ϵ/V in water, or $(T/V) \log (c_s/c)$. Curves 2 and 1 are similar correlation curves, shifted leftward by $(T/V) \log (c_s/c)$ for each component. Their abscissas are equal or proportional to $-\Delta G/V$, the adsorptive driving force per unit volume. The abscissa for the competitive (dotted) correlation curve is the difference between the abscissa of curve 3 and the larger of curves 2 and 1. The individual points are discussed in the text.

3. We consider in turn the three regions of the dotted line. For example, if $(RT/V_3) \ln (c_s/c)_3$ is equal to OM, then the adsorbate space is filled to the volume OE with component 3, volume ED is occupied by component 2, and volume DC by component 1. Volume CA is occupied only by solvent. If now we enter at an abscissa equal to ON, then the volume OF is occupied by component 3 and FC by component 1; component 2 is excluded. Its higher value of ϵ/V is overridden by the higher concentration of component 1 at the higher adsorbate volumes; at lower adsorbate volumes, where component 2 would ordinarily adsorb in a binary mixture of 1 and 2, it is superseded by component 3. If we enter the plot at the abscissa OP, the total adsorbate volume is equal to OG; here the adsorbate consists entirely of component 3.

Experimental Section and Data Reduction

Materials. The activated carbon was the same as in all the studies in this series. The *p*-nitrophenol (PNP), acrylamide, thiourea, and methionine were high grade chemicals from commercial sources and were used as received. Practical grade benzamide was recrystallized from methanol-water. Glucose solutions were treated with small amounts of activated carbon to remove traces of UV absorbing impurities.

Adsorption Experiments. Competitive adsorption was determined by the shaker-bath techniques described earlier,² using UV absorption spectrophotometry for analysis. PNP and benzamide were separated by high pressure liquid chromatography on a reverse-phase ODS packing (Whatman CO: PELL), using methanol-water as the mobile phase. Other filtrates containing two UV-absorbing solutes were either directly analyzed by UV spectrophotometry where peaks were well separated

TABLE I: Solubilities of Adsorbates in Water and Competitor Solutions

Component	Medium	Solubility, g/L
Acrylamide	Water	588 ^a
Acrylamide	95% sat. thiourea	560
Benzamide	Water	13.5
Benzamide	33% sat. glucose	10.0
Coumarin	Water	2.2 ^b
Coumarin	33% sat. glucose	1.4
Glucose	Water	750 ^c
Methionine	Water	34.8
PNP	Water	16.0 ^b
PNP	5% sat. benzamide	15.0
PNP	33% sat. glucose	12.5
PNP	95% sat. thiourea and 10% sat. acrylamide	12.6
Thiourea	Water	75.7 ^a
Thiourea	10% sat. acrylamide	52

^a Reference 4. ^b Reference 3. ^c Reference 1.

(PNP-benzamide) or else separated by chloroform extraction (PNP-benzamide-methionine).

Published data were used for single-solute isotherms of PNP,³ coumarin,³ thiourea,⁴ methionine,⁴ acrylamide,⁴ and glucose.¹ The benzamide isotherm was newly determined by the earlier-described column technique.¹

Solubilities were determined as described earlier,¹ both in water and in the ternary solutions.

Reduction of Data. The adsorbate molar volumes, V^* , for the individual components, were estimated, as described earlier,⁴ by first plotting the adsorbate volume vs. $T/V \log c_s/c$ and extrapolating the adsorbate volume to saturation, i.e., to the vertical axis. The adsorbate densities were then calculated as the densities required to bring the experimental limiting adsorbate volumes to 65 cm³/100 g, the value from the hydrocarbon correlation line of Manes and Hofer;² this procedure has been used earlier.⁴ The molar adsorbate volumes V^* were calculated by use of the adjusted densities. The theoretical curves for competitive adsorption of PNP were calculated by the methods described in the theoretical section, using V^* throughout as the molar volume in calculating both the abscissas and the ordinates. The abscissas of plotted points for the competitive adsorption of PNP were $T/V^* \log c_s/c$; the ordinates were the adsorbate volumes, calculated from the adsorbate masses by use of the adjusted density of PNP, where c_s is the solubility of PNP in the equilibrium mixture of the other two solutes.

The procedure used here differs from that of Rosene, Ozcan, and Manes⁴ for single solutes, where the bulk molar volume was used in calculating the abscissas; the difference is due to the difference in the equations for calculating competitive adsorption between solutes and for single solute correlation curves where the only competition is with the solvent. The physical interpretation is that the model assumes that all presumed interstices in loosely packed solute adsorbates are occupied by solvent. The present procedure differs from that of Rosene and Manes¹ in that the limiting volume of PNP was there used as the standard limiting adsorbate volume rather than the limiting volume of the hydrocarbon correlation line. The present procedure was chosen because a number of the adsorbates showed higher limiting adsorbate volumes than PNP, which would have required the physically unsatisfying assumption of adsorbate densities higher than the bulk densities. The change, however, is purely formal; the same results are obtained for any chosen value of the limiting adsorbate volume. However, we should point out that the values of V^* for PNP are not the same in this and the earlier¹ article.

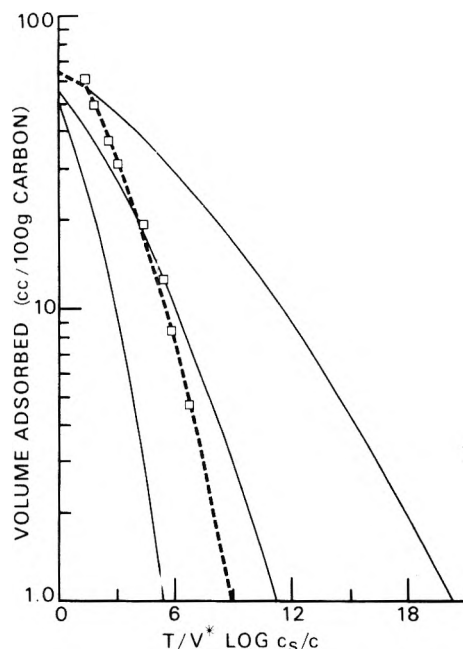


Figure 3. Comparison of experiment and theory for the system PNP-26% saturated benzamide-33% saturated glucose. The solid curves are the analogues of Figure 1 for the three individual components (reading from right to left). The dotted curve is constructed by subtracting the abscissa of the benzamide curve from the PNP curve. Its abscissa is $T/V^* \log c_s/c$, where the concentrations are the equilibrium and saturation concentrations in the multicomponent system. The points are experimental points for PNP.

Results

Table I gives the solubilities of the individual adsorbates in water and in the presence of the other components. Table II⁵ gives adsorption data for benzamide from water, both as mass loading vs. concentration and (adjusted) volume loading vs. $T/V^* \log c_s/c$. Table III⁵ gives adsorption data for PNP over the following wide concentration range: 26%-saturated benzamide and 33%-saturated glucose (I); 6%-saturated benzamide and 33%-saturated glucose (II); 20%-saturated benzamide and 3%-saturated methionine (III); 95%-saturated thiourea and 10%-saturated acrylamide (IV); 33%-saturated glucose and several concentrations of coumarin (V); and 5%-saturated benzamide (binary system) (VI). Table III also gives volume loadings (adjusted) for the following: benzamide in I, II, III, and VI; methionine in III; and coumarin in V. The adsorption of glucose, acrylamide, and thiourea were not determined.

The data for the adsorption of PNP for systems I-IV and VI are shown in Figures 3-7, which give (adjusted) adsorbate volumes for PNP vs. $T/V^* \log c_s/c$. The theoretical curves, shown as solid and dotted lines, are analogous to Figures 1 and 2. The agreement with theory may be judged by the proximity of the experimental points to the dotted line.

The observed and theoretical benzamide capacities, which are not readily plotted, are listed as follows for each system as (adjusted) cm³ adsorbed per 100 g of carbon, where the data are given in order of increasing ordinates in the corresponding figure and the theoretical values are given in parentheses: Figure 3, 46 (50), 43 (46), 39 (43), 31 (36), 20 (24), 16 (18), 8 (6), 0 (0); Figure 4, 20 (22), 14 (15), 7 (8), 2 (0), 0 (0), 0 (0), 0 (0); Figure 5, 48 (49), 45 (46), 43 (42), 37 (36), 28 (28), 20 (15), 8 (0), 0 (0); Figure 7, 32 (34), 28 (31), 21 (24), 11 (11), 0 (0). The molar volumes V^* and V (cm³/mol) were as follows: acrylamide, 87, 63; benzamide, 163, 90; coumarin, 162, 110; glucose, 205, 117; methionine, 289, 111; PNP, 146, 94; thiourea, 110, 54.

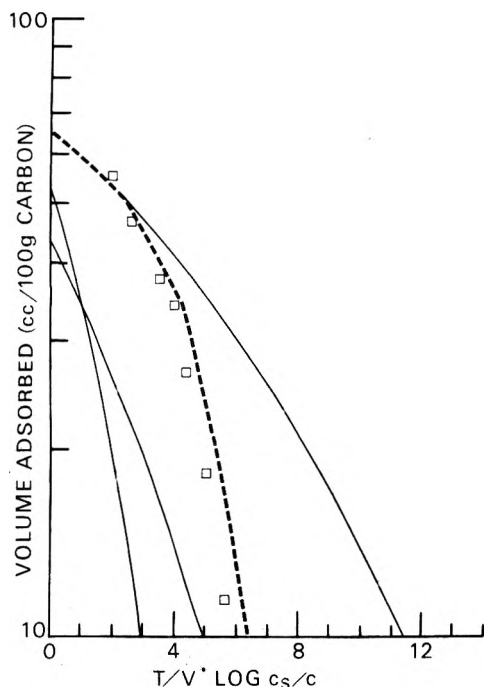


Figure 4. Comparison of experiment and theory for the system PNP-6% saturated benzamide-33% saturated glucose. The curves are constructed similar to those in Figure 2. Here again the solid PNP curve is on the right. The glucose curve is the one with the higher limiting volume. The dotted curve, to which the experimental points should fit, is constructed by subtracting from the abscissa of the PNP curve the corresponding abscissa of either the glucose or the benzamide curve, whichever is greater. This results in a doubly kinked dotted curve.

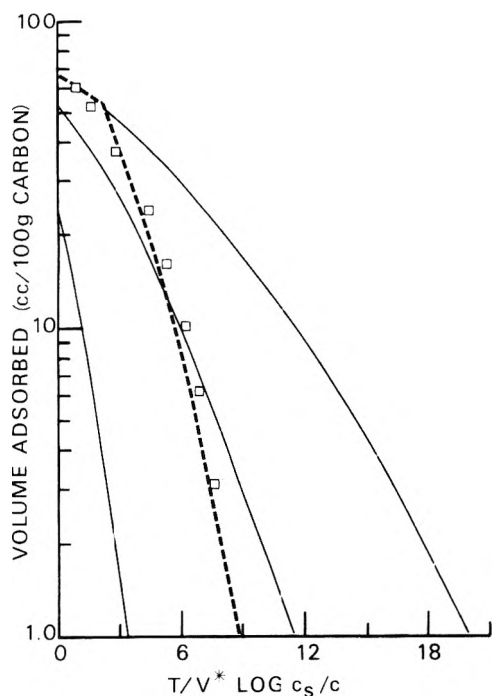


Figure 5. Comparison of experiment and theory for the system PNP-20% saturated benzamide-3% saturated methionine. The solid and dotted curves are the analogues of Figure 3, and are placed from right to left.

Discussion

We first consider the choice of components and experimental conditions. Although the calculations illustrated in Figures 1 and 2 are not restricted to any particular concentrations, it was expedient for two-dimensional plots to vary the concentration of one component (PNP) at essentially constant concentrations of the other two. The most weakly adsorbable components (glucose,

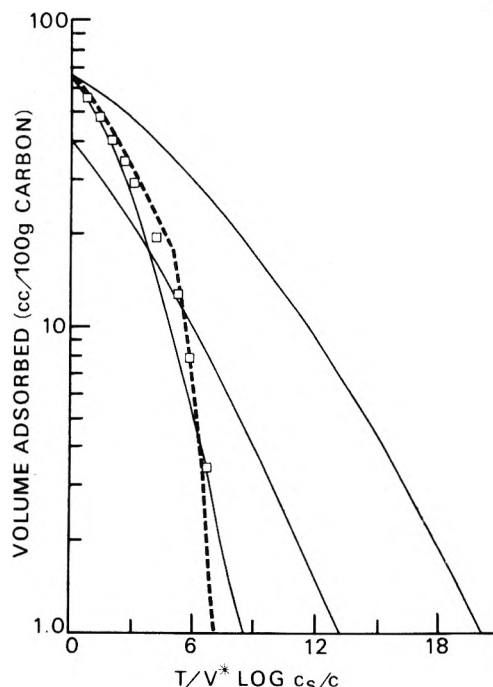


Figure 6. Comparison of experiment and theory for the system PNP-95% saturated thiourea-10% saturated acrylamide. The solid and dotted curves are the analogues of Figure 4 where the PNP curve is on the right and the thiourea curve has a higher limiting volume than the acrylamide curve (the one with the less steep slope).

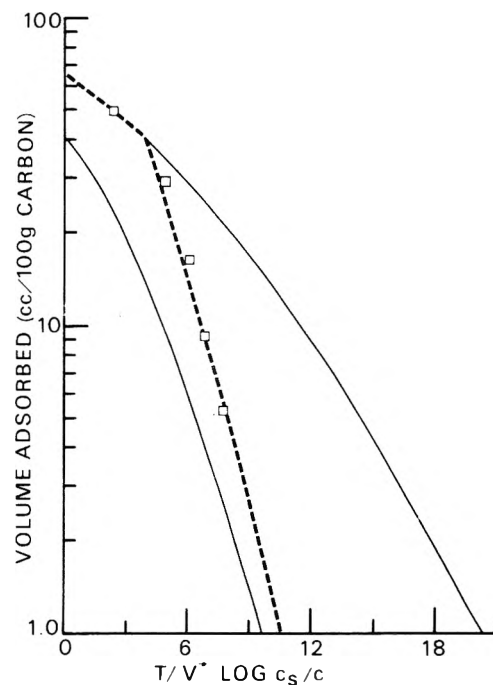


Figure 7. Comparison of experiment and theory for the binary system PNP-5% saturated benzamide. The solid curves are PNP on the right and benzamide on the left. The dotted line is the calculated competitive curve.

methionine, thiourea) were either not adsorbed at all because of competition (e.g., glucose in Figure 3 and methionine in Figure 5), or else were at relatively high concentrations that were insensitive to small amounts of adsorption (e.g., glucose in most of Figure 4 and thiourea in Figure 6). For these components it was therefore relatively easy to maintain concentration invariance. The same was true for acrylamide. For benzamide, where adsorption could significantly change the concentration, the theory was used to calculate the expected adsorption, using an iterative calculation, and the calculated amounts

of solid were added to the solutions before equilibration in order to compensate for the expected adsorption. This method worked well for the systems in Figures 3–5. It did not work nearly as well for coumarin in PNP–coumarin–glucose, because the abscissa scale factors ϵ/V^* for coumarin and PNP are quite close to each other, with the result that the competitive correlation curve of PNP, for example, approaches a vertical slope. It then becomes quite difficult to predict the adsorbate composition in the corresponding concentration range. The data for this system are therefore presented in tabular form only.

The problems illustrated by mixtures of PNP and coumarin illustrate a principal reason for the choice of the other systems for study, namely, that they should have well-separated values of ϵ/V^* . Another criterion was ease of analysis by UV in mixtures, or else easy separability for UV analysis. With one exception it was convenient to use components that had been previously studied.⁴ Benzamide, the one exception, was chosen rather than benzoic acid (which also had the desired value of ϵ/V^*) because of its higher solubility and because the dissociation of benzoic acid at low concentrations was expected to introduce complications. Some systems (e.g., PNP–acetone oxime) were excluded because they form liquid eutectic mixtures at room temperature. All of the systems that were investigated are reported here. Moreover, the capacity range for PNP was investigated down to the limits imposed by the sensitivity of our analytical method.

We now consider the experimental results. Figure 7 gives results for the binary system PNP–benzamide, which was studied as a preliminary to the study of its ternary systems. The agreement with theory is as good as in our earlier work with binary systems.¹

We now consider the ternary system PNP–benzamide–glucose in Figures 3 and 4, which illustrate the effect of concentration ratios on the competitive (dotted) correlation curve. In Figure 3, as expected, there is only one region of competitive adsorption because the benzamide excludes glucose everywhere. The region of no competition is too short to show up well here; however, an attempt to lengthen it by reducing the benzamide and glucose concentrations would have forced the lower points into an experimentally inaccessible concentration region. Figure 4 now shows two distinct regions of competition, where the PNP competes in turn with glucose and (at the lower capacities) with benzamide. The adsorption of benzamide, reported above, is also in reasonable agreement with expectations; here, however, the precision of the measurement is reduced at the relatively high slopes. Glucose adsorption was not determined because its high concentrations precluded precise measurement.

Figure 5 shows data for PNP–benzamide–methionine, where methionine should have been completely excluded by benzamide. Here the methionine was determined and its nonadsorption verified. The data are in agreement with what in effect becomes the binary system of PNP–benzamide.

Figure 6 is for PNP–thiourea–acrylamide, showing two distinct regions of competition. Here the region of no competition is not seen, as expected, because of the

near-saturation of thiourea. However, there are two quite distinct regions of competition, the transition zone is at the expected capacity, and the data show overall excellent fit to the calculated curve. As in Figure 4, the transition between the two zones of competition is at the intersection of the curves for the two individual competitors.

Having seen how the model accounts for the adsorption of ternary solute mixtures from the equilibrium concentrations, we now consider the reverse calculation of the adsorption and of the equilibrium concentrations that result when a given amount of carbon is added to a given volume of a ternary solution of specified initial composition. If the abscissa scale factors are well separated, then the adsorption and the equilibrium concentrations are calculated by successive approximations. For example, in the PNP–benzamide–glucose system it is convenient to estimate the adsorption and equilibrium concentrations of PNP at the initial concentrations of benzamide and glucose, and then to apply similar calculations to benzamide and to glucose, repeating the cycle of calculations until convergence is attained. If two components have almost identical values of ϵ/V^* , then one may assume that they adsorb in equal volumes at an approximately constant ratio of relative concentrations. For this calculation the instability of predicting the adsorption from the concentrations becomes a stability condition.

We now consider briefly the expected generality and limitations of the present approach. As noted earlier,¹ one would expect complications from chemisorption, reaction, molecular sieving effects, and the formation of solid solutions, i.e., from systems that do not conform to the assumptions of the model. One would expect the effects of relatively weak interaction of solutes in solution (as in binary systems) to appear as a change in the mutual solubilities; this is accounted for in the calculation method. We have already noted the sensitivity of adsorbate composition to equilibrium concentrations for compounds with nearly equal values of ϵ/V^* . However, except for the complication of the added component, our ternary systems have behaved pretty much like the binary systems with the same components; the calculation of multicomponent adsorption from single-component adsorption continues to be more accurate than the prediction of individual isotherms.⁴

Finally, we have not found any earlier attempt to treat ternary solute systems.

Acknowledgment. We thank the Calgon Corporation for support of this work.

Supplementary Material Available: Tables II and III containing the single solute adsorption data and the competitive adsorption data (3 pages). Ordering information is available on any current masthead page.

References and Notes

- (1) M. R. Rosene and M. Manes, *J. Phys. Chem.*, **80**, 953 (1976).
- (2) M. Manes and L. J. E. Hofer, *J. Phys. Chem.*, **73**, 584 (1969).
- (3) C. C. T. Chiou and M. Manes, *J. Phys. Chem.*, **78**, 662 (1974).
- (4) M. R. Rosene, M. Ozcan, and M. Manes, *J. Phys. Chem.*, **80**, 2586 (1976).
- (5) See paragraph at end of text regarding supplementary material.

Application of the Polanyi Adsorption Potential Theory to Adsorption from Solution on Activated Carbon. 10. pH Effects and "Hydrolytic" Adsorption in Aqueous Mixtures of Organic Acids and Their Salts

Michael R. Rosene and Milton Manes*

Chemistry Department, Kent State University, Kent, Ohio 44242 (Received March 23, 1977)

Publication costs assisted by the Calgon Corporation

The effect of pH variation on the adsorption, on activated carbon, from water solutions containing organic acids and their salts is accounted for in terms of a previously published Polanyi-based model of competitive adsorption between the acid and its salt. Since the adsorbability of each species is strongly dependent on its solubility, the competitive adsorption of the salt is not controlled solely by pH, but may also depend on the identity of the cations in solution. Experimental data on the adsorption of sodium benzoate-benzoic acid at constant total molar concentration and over a wide pH range agree well with predictions based on the individual adsorption isotherms and solubilities. At pH values below 10 there is no significant adsorption of sodium benzoate; the effect of pH on adsorption is completely accounted for by its effect on the concentration of the free acid. The competitive model also accounts successfully for the increase in pH ("hydrolytic adsorption") that results when solutions of sodium benzoate at various concentrations are treated with a neutral carbon; here, however, it becomes necessary to deal with complications in the sodium benzoate isotherm that appear to be due to chemisorption and to effects of the ash content of the carbon. The model should be equally applicable to organic bases.

Introduction

Consider the adsorption from water solution onto activated carbon of a mixture of an organic acid (or base) and one of its salts. According to our Polanyi-based model of competitive adsorption¹ we should be able to calculate the adsorption of each component at any pair of equilibrium concentrations from the solubilities and the individual adsorption isotherms of the pure components. From this point of view the effect on adsorption of, for example, acidifying a solution of the salt of an organic acid, should be accounted for solely in terms of the resultant change in concentration of the individual species in solution.

Another test of the competitive adsorption model is whether it can account quantitatively for the phenomenon of "hydrolytic adsorption", which is exemplified by an increase in pH that results when a neutral carbon is equilibrated with a solution of sodium benzoate. This phenomenon has been studied by Bartell and Miller² and by Miller,³ and has been shown to result from preferential adsorption of the organic acid and the consequent release of OH⁻ into the solution. However, in the absence of a method for dealing with competitive adsorption of acid and salt it has not been hitherto possible to make quantitative estimates of the expected pH.

We here describe a detailed study of the benzoic acid-sodium benzoate system in water solution, starting with the same activated carbon that has been used in all of the investigations in this series.^{1,4} We found at the outset that apparent anomalies in the adsorption of benzoic acid at uncontrolled pH were readily resolved by taking into account the effect of carbon ash alkalinity on the concentration of the undissociated acid. We then considered adsorption at constant total concentration and variable pH, and then hydrolytic adsorption. Although most of the data on pH variation could be accounted for solely in terms of the benzoic acid concentration, the competitive model was indispensable in accounting quantitatively for hydrolytic adsorption.

One complication was the absence of benzoic acid-water isotherm data at low capacities, where the equilibrium

concentration becomes too low to measure; it was circumvented by using benzoic acid-methanol data (which extend to lower capacities) and extrapolating the concentrations to water solution. Additional complications came in determining the adsorption and competitive effect of sodium benzoate, the first salt to be reported in this series. In addition to requiring a straightforward modification of the theoretical treatment, it also showed experimental complications arising from interaction with ash components in the carbon and some apparent chemisorption even on ash-extracted carbon. Once these complications were dealt with, the data were well accounted for by the competitive model.

The competitive model was useful not only for accounting for the data, but also to track down the sources of the originally observed deviations from theory in sodium benzoate adsorption. Thus we were led to the effects of ash and of chemisorption (both novel effects in this series) by a study of the adsorption of benzamide from sodium benzoate, which also served as a consistency check for the data on the adsorption of sodium benzoate on ash-extracted carbon. The competitive model, which was earlier used to demonstrate looseness of packing of some solid adsorbates,⁴ thus afforded additional information on the nature of adsorption.

Theory

The earlier article of Rosene and Manes¹ should be consulted for details of the treatment of competitive adsorption of binary solid mixtures. The competitive adsorption of an organic acid and its salt at given equilibrium concentrations of each (alternatively, at a fixed total concentration and pH) requires no new theoretical treatment except for plotting the correlation curve for a completely dissociated salt, which we now consider. For simplicity we shall consider 1:1 salts.

Whereas for an undissociated solute the adsorptive driving force per mole is¹

$$-\Delta G = \epsilon - RT \ln \frac{a_s}{a} \approx \epsilon - RT \ln \frac{c_s}{c} \quad (1)$$

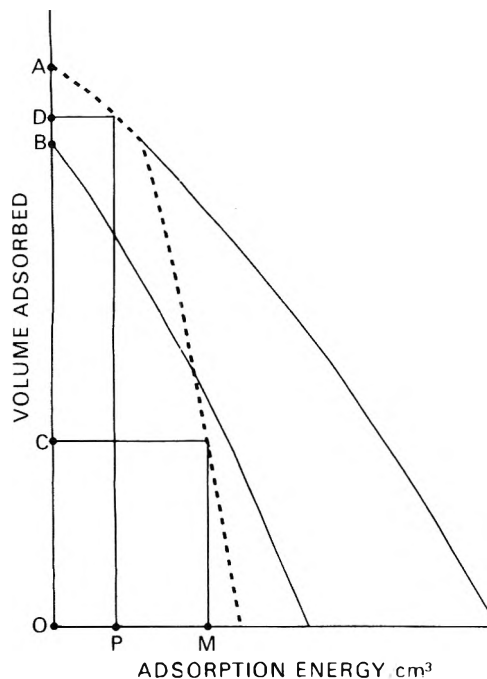


Figure 1. Schematic diagram showing construction of the competitive correlation curve of an acid and its salt. The solid curve on the right is the correlation curve for the acid. The solid curve on the left is that of the salt, shifted leftwards by $2RT/V \ln c_s/c$. The dotted curve is constructed by taking its abscissa as the difference between the abscissas of the solid curves.

where ϵ is the (location-dependent) adsorption potential, and a_s and c_s and a and c the corresponding activities and concentrations at saturation and at equilibrium. The corresponding driving force for a completely dissociated salt should be

$$-\Delta G = \epsilon - RT \ln \frac{a_s^+}{a^+} - RT \ln \frac{a_s^-}{a^-} \quad (2)$$

where a_s^+ etc. refer to the activities of the anion and cation at saturation and at equilibrium.

The criterion for the competitive adsorption of an acid from its salt becomes (in the absence of extraneous common ion)

$$\frac{RT}{V_{\text{acid}}^*} \ln \left(\frac{c_s}{c} \right)_{\text{acid}} \leq \frac{\epsilon_{\text{acid}}}{V_{\text{acid}}^*} - \frac{\epsilon_{\text{salt}}}{V_{\text{salt}}^*} + \frac{2RT}{V_{\text{salt}}^*} \ln \left(\frac{c_s}{c} \right)_{\text{salt}} + \frac{2RT}{V_{\text{salt}}^*} \ln \frac{\gamma_{\pm}(s)}{\gamma_{\pm}(e)} \quad (3)$$

where the V^* 's are the molar volumes of the individual species as adsorbates and $\gamma_{\pm}(s)$ and $\gamma_{\pm}(e)$ are the mean ionic activity coefficients of the ions at saturation and at equilibrium. In effect the competitive power of the salt is twice as sensitive to a change in concentration as an undissociated solute because two particles are involved.

The calculation of the competitive adsorption of acid and salt, illustrated in Figure 1, now becomes quite analogous to the earlier calculation of Rosene and Manes¹ for binary solutes (for simplicity the activity coefficient term has been omitted). The solid curve terminating in the ordinate A is the correlation curve for the acid, i.e., a plot of the adsorbate volume of the acid adsorbing from water as a single component vs. its $\epsilon/V_{\text{acid}}^*$, where V_{acid}^* is the molar volume of the acid as an adsorbate. The solid curve terminating in B is the single-component correlation curve for the salt, shifted toward the left by the distance $(2RT/V_{\text{salt}}^*)_{\text{salt}} \ln (c_s/c)_{\text{salt}}$, where c_s and c are the saturation and equilibrium concentrations of the salt. Its abscissa

is proportional to its adsorptive driving force $-\Delta G/V_{\text{salt}}^*$. The dotted curve is the competitive correlation curve for the acid in the presence of the salt. It is constructed by taking its abscissas as the differences between those of the two solid curves; its abscissa is therefore equal to either side of eq 3.

We now consider how to calculate the adsorption of acid and salt corresponding to a fixed total concentration and pH. Using the acid-base equilibrium equation, we calculate the individual concentrations of acid and salt; this fixes the position of curve B in Figure 1. We then calculate the term $(RT/V_{\text{acid}}^*) \log (c_s/c)_{\text{acid}}$, which becomes the abscissa value for entering the plot. If, for example, it is equal to OM, then the volume of adsorbed acid is OC and that of adsorbed salt is BC. If we enter the plot at point P, then the volume of adsorbed acid is OD and there is no salt adsorption. From the values of V^* we can readily calculate the adsorbed masses of each component.

Consider now the adsorption from a solution of a salt, MB, where the organic anion undergoes base dissociation



In the absence of adsorption one customarily estimates the equilibrium composition by use of the equilibrium equation

$$(HB)(OH^-)/(B^-) = K_b \quad (5)$$

together with the assumption of approximately equal concentrations of OH^- and the undissociated acid HB. In the presence of a neutral adsorbent that adsorbs the undissociated acid HB we have instead the stoichiometric relation

$$n_{OH^-} = n_{HB} + n_{HB}^* \quad (6)$$

where n_{OH^-} and n_{HB} are the number of moles of hydroxide ion and undissociated acid and n_{HB}^* is the number of moles of acid adsorbed from solution. If the acid is relatively strongly adsorbed, one may frequently neglect n_{HB} , in which case the number of moles of OH^- in solution is approximately equal to the number of moles of free acid adsorbed. Given this relation we can now proceed with the iterative calculation.

Given K_b and the initial concentration of MB, the initial concentration of HB is estimated from eq 5 in the customary fashion and the adsorption of acid and salt initially estimated by the calculation outlined in Figure 1. The OH^- concentration (initially too high) is then calculated from the amount of acid adsorbed and the volume of solution, and a new (lower) concentration of free acid (and, if necessary, salt) is recalculated from eq 5. The calculation is repeated until it converges. With a little practice the entire calculation can be carried out with a small hand calculator in a few minutes. For relatively high concentrations of salts the concentrations of anion and cation remain essentially equal.

Experimental Section

Materials. The benzoic acid and sodium benzoate were commercial USP grade chemicals and were used as received. Practical grade benzamide was recrystallized from water-methanol. The source of the activated carbon was the batch that was used in the previous articles in this series. For some experiments the carbon was extracted with a mixture of equal parts of 1:1 HCl:H₂O and of 25% HF to remove ash ("singly treated"). For other experiments ("doubly treated") the acid-extracted carbon was exposed to a relatively concentrated solution of sodium benzoate and washed repeatedly until the wash water was free of benzoate species.

TABLE I: Physical Properties of Adsorbates

Component	Medium	Solubility, g/L	V, cm ³ /mol	V*, cm ³ /mol
Benzoic acid	Water	3.5	96.5	149
Benzoic acid	Methanol	192	96.5	149
Benzamide	Near-sat. sodium benzoate	24	90.3	163
Sodium benzoate	Water	440	96.1	367

Adsorption Experiments. The shaker-bath techniques for equilibration in flasks and the column techniques were the same as in earlier publications.^{1,4} The shaker-bath method was used for most of the experimental points for benzoic acid–water, benzamide from sodium benzoate, and hydrolytic adsorption (sodium benzoate from water with pH determination). The column technique was used for sodium benzoate at high and low extremes of pH and several of the high capacity points for benzoic acid. Analysis was by UV spectrophotometry; for sodium benzoate–benzamide mixtures the benzamide was separated by chloroform extraction.

Sources of Data. Benzamide data were taken from Rosene and Manes,⁵ benzoic acid–methanol data (shaker bath) from Ozcan,⁶ and benzoic acid–H₂O under controlled-pH (acid) conditions from Rosene and Manes.¹

Solubility of Sodium Benzoate. The solubility of sodium benzoate (440 g/L) was determined by water addition in small increments until complete solubility was achieved.

Reduction of Data. The adjusted adsorbate volume, V^* , was determined, as in Rosene and Manes,⁵ by first plotting adsorbed volume vs. $T/V \log c_s/c$, where the molar volume V and the adsorbed volume are calculated by use of the bulk density. The adsorbate densities were then adjusted to make the (extrapolated) limiting adsorbate volume equal to 65 cm³/100 g (the limiting volume for the hydrocarbon correlation line⁹), and the ordinates adjusted accordingly. For competitive adsorption calculations the molar volume V^* was calculated by use of the adjusted adsorbate density (rather than the bulk density) and a “doubly shifted” correlation curve was plotted as the (adjusted) adsorbate volume vs. $T/V^* \log c_s/c$.

For the extrapolation of the benzoic acid–water data from methanol to water solution the abscissa scale factor in the doubly shifted benzoic acid–methanol correlation curve⁶ was adjusted by adding the difference between the empirical scale factors for methanol (Schenz and Manes⁷) and for water (Wohleber and Manes⁸). The data thus transformed coincided in the upper capacity range with the experimental benzoic acid data and were a good fit to the curve that was calculated from the hydrocarbon correlation line by use of the empirical scale factor for water³ and the theoretical factor calculated for benzoic acid from its molar refractivity.⁹ The values extrapolated by the two methods are therefore consistent with each other and also with the upper capacity data. The resulting correlation curve, i.e., a plot of adjusted adsorbate volume vs. $T/V^* \log c_s/c$ was used for both competitive and single-solute adsorption.

Since competition by salt was negligible in the adsorption of benzoic acid at uncontrolled pH, the adsorption data were correlated as a single-component correlation curve for benzoic acid in water. The benzoic acid concentration, however, was calculated from the total concentration (determined by UV spectrophotometry) and the pH. The test of theory was the fit of the resulting data points to the extrapolated correlation curve of Figure 3, with V^* as 149 cm³/mol. In calculating correlation curves for sodium benzoate the data were initially plotted as unadjusted volume adsorbed vs. $2T/V \log c_s/c$ and after

estimation of V^* as adjusted volume adsorbed vs. $2T/V^* \log c_s/c$.

In estimating the sodium benzoate correlation line from the adsorption of benzamide from near-saturated sodium benzoate, the benzamide adsorption data were plotted as (adjusted) adsorbate volume vs. $T/V^* \log c_s/c$, with V^* for benzamide at 163 cm³/mol⁵. A theoretical correlation curve for sodium benzoate (i.e., adjusted adsorbate volume vs. $2T/V^* \log c_s/c$) was constructed by taking the abscissa of each ordinate as the difference between that of the benzamide–water correlation curve⁵ and the corresponding experimental curve for benzamide–sodium benzoate. Adsorption data for sodium benzoate on doubly treated carbon were plotted as adjusted volume adsorbed vs. $2T/V^* \log c_s/c$ for sodium benzoate, with V^* as 367 cm³/mol. The fit of the resulting points to the sodium benzoate correlation line calculated from benzamide–sodium benzoate was taken as a test of theory.

In determining the pH dependence of benzoate species at constant total concentration the experimental points were calculated as millimoles of total adsorbate/100 g of carbon at a constant total (equilibrium) concentration of 21 mmol/L and variable pH. The theoretical curve in the high pH region was calculated from the calculated concentrations and the correlation curves of each species, using the calculation method illustrated in Figure 7, which gives the moles of each species adsorbed. At pH < 8 the competitive adsorption of sodium benzoate was not significant and the adsorption of benzoic acid was calculated as a single-solute system, using the benzoic acid correlation curve of Figure 2 and the concentration of undissociated benzoic acid calculated (as noted earlier) from the total concentration and pH.

In calculating hydrolytic adsorption the adsorption of each species and the equilibrium concentrations and pH were calculated, as outlined in the theoretical section above, from the individual competitive correlation curves of benzoic acid and sodium benzoate. The experimental data were the pH values and the total benzoate species adsorbed. The moles of adsorbed benzoic acid (plotted points) were taken as equal to the moles of OH⁻ in solution as calculated from the solution volumes and the pH.

Results

Table I contains solubility data as well as the molar volumes, V , and the adjusted molar volumes, V^* , for all components. Figure 2 shows adsorption data for benzoic acid–methanol and benzoic acid–water; the calculation of the curves has been described earlier. Table II¹¹ gives the data of Figure 2. Figure 3 shows experimental points for the adsorption of benzoic acid from water, calculated on the assumption that all of the solute is benzoic acid, and also with a calculation of the benzoic acid concentration based on total concentration and pH. Table III¹¹ gives the numerical data as well as the pH values. Figure 4 shows data for the adsorption of total benzoate species (essentially sodium benzoate) from the untreated carbon and two treated carbons; the bulk molar volumes are used here to avoid confusion, since the limiting adsorbate volumes (and hence V^*) are not identical. Table IV¹¹ gives the numerical data. Figure 5 shows the experimental data for benzamide

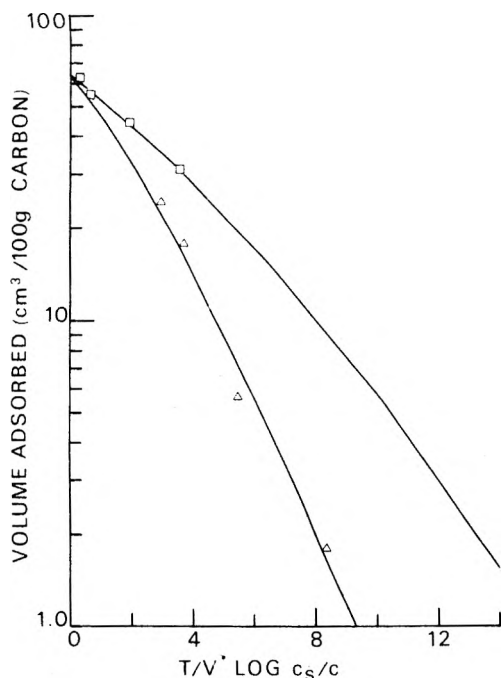


Figure 2. Extrapolation of benzoic acid adsorption data. The curve on the left is the (doubly shifted) correlation curve for benzoic acid-methanol. The curve on the right is the calculated correlation curve for benzoic acid-water. The points are experimental points from earlier publications.

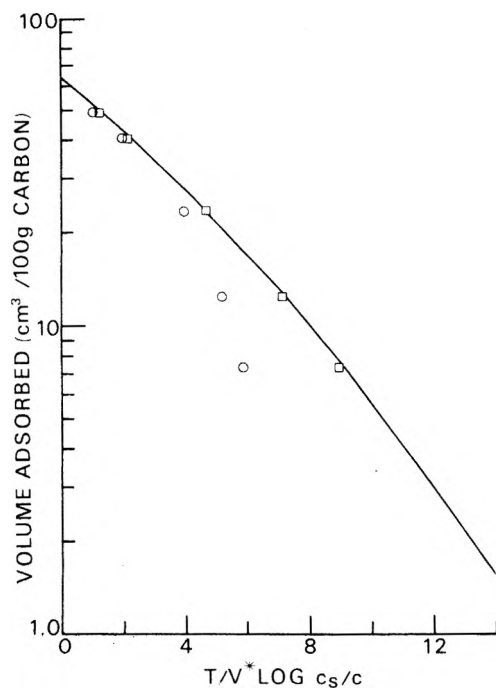


Figure 3. Adsorption of benzoic acid from water at uncontrolled pH. The curve is the calculated curve for benzoic acid-water from Figure 2. The circular points are without correction for the pH effect on benzoic acid concentration. The square points are calculated with use of the experimental pH values and calculation of the undissociated benzoic acid concentration.

in near-saturated sodium benzoate, together with the calculated correlation curve for sodium benzoate in water and the experimental points for sodium benzoate on acid extracted and sodium benzoate-treated carbon (recalculated from Table IV and Figure 4); the benzamide-water curve is from Rosene and Manes.⁵ The numerical data for benzamide-near-saturated sodium benzoate are in Table V.¹¹ Figure 6 is a plot of the total adsorption (mmol/100 g of carbon) from a 21 mM solution of total benzoate

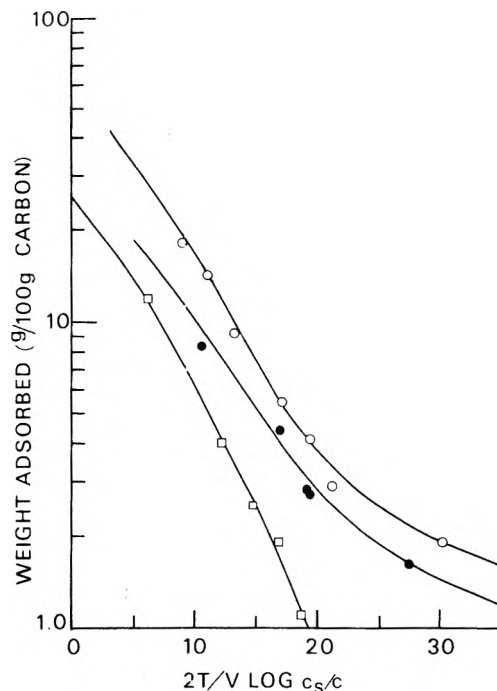


Figure 4. Adsorption of sodium benzoate on untreated (O), singly treated (●), and doubly treated (□) carbon. The curves are fitted to the data.

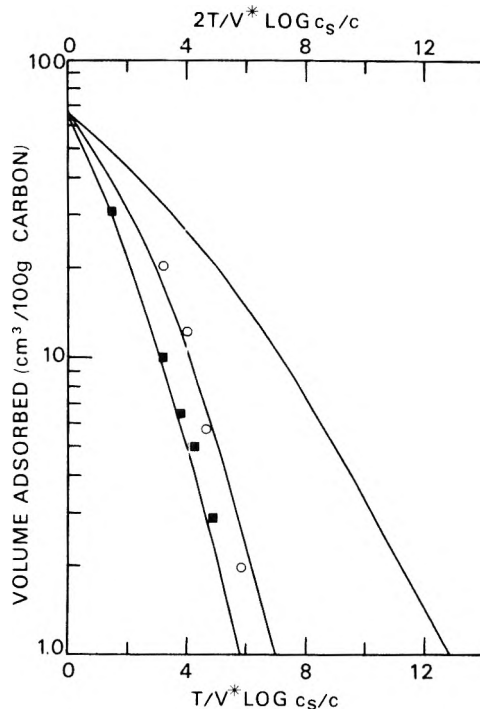


Figure 5. Estimation of the competitive correlation curve for sodium benzoate. The curve on the right is the correlation curve for benzamide-water. The middle curve is for benzamide from near-saturated sodium benzoate, showing experimental points. The curve on the left is constructed by taking each abscissa as the difference between those of the other two curves. The points are experimental for sodium benzoate on a doubly treated carbon. The upper scale applies to the left-hand curve and its points.

species (benzoic acid + benzoate ion) as a function of pH; the curve is calculated as described earlier. The data are in Table VI.¹¹ Figure 7 shows the correlation curve for benzoic acid, those for sodium benzoate at different concentrations, the competitive correlation curves, and the experimental points for benzoic acid adsorption (assumed equal to the OH^- ion in solution as measured by pH) on doubly pretreated carbon. Table VII gives numerical data on solution volume, initial sodium benzoate concentration,

TABLE VII: Hydrolytic Adsorption of Aqueous Solutions of Sodium Benzoate^a

Initial concn, g/L	Carbon added, g	Equilibrium pH		Loading of benzoic acid, cm ³ /100 g	T/V* log (c _s /c) (benzoic acid)
		Calcd	Obsd		
20.0	1.00	10.72	10.68	0.77	11.6
7.9	1.00	10.70	10.65	0.74	12.2
2.0	0.50	10.45	10.42	0.83	13.1
1.0	0.50	10.40	10.40	0.75	13.7

^a The solution volume was 100 cm³.

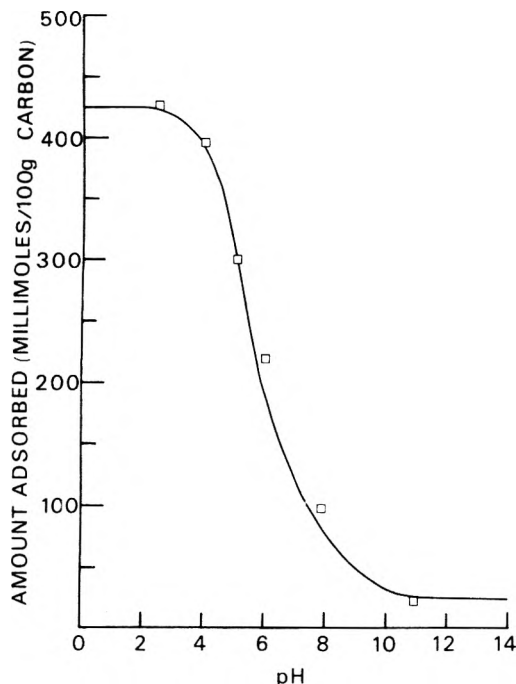


Figure 6. Adsorption from sodium benzoate–benzoic acid at constant total equilibrium concentration as a function of pH.

grams of carbon added, calculated loading of benzoic acid, $T/V^* \log c_s/c$ for benzoic acid, and predicted and observed equilibrium pH values.

Discussion

We first consider the pH dependence of adsorption or, more precisely, physical adsorption from a solution containing an organic acid and its salt. The distinction is important because the former formulation of the problem tends to gloss over the importance of the cation, which determines the solubility and therefore the adsorbability of the salt. Although the less precise formulation becomes quite adequate in the absence of significant adsorptive competition by the salt, it could fail badly in the presence of a cation that forms a salt of low solubility or, to take an extreme example, one that precipitates the salt. Such contingencies are well within the compass of the Polanyi-based model.

Turning now to the benzoic acid–sodium benzoate system, we find that the sodium benzoate is much less strongly adsorbed than benzoic acid at comparable molar concentrations because of its much higher solubility; its competitive tendency is further reduced by its relatively high value of V^* , which we continue to interpret in terms of adsorbate sponginess relative to bulk. Moreover, its adsorptive driving force is twice as sensitive to reduction in concentration as that of benzoic acid because of its dissociation in solution. For these reasons the data of Figures 3 and 6, with the exception only of the high-pH point of Figure 6 are adequately treated in terms of the single-component treatment for benzoic acid; once the true concentration of benzoic acid has been established, the

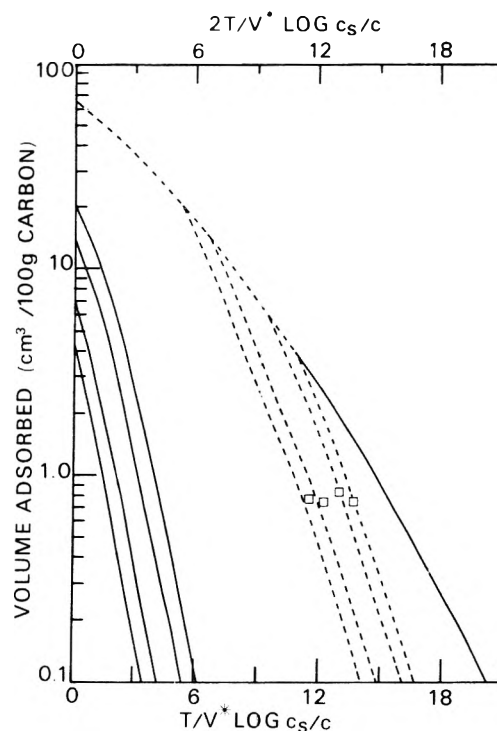


Figure 7. Hydrolytic adsorption from sodium benzoate solution on doubly-treated carbon. The solid curve on the right is for benzoic acid; the ones on the left are shifted curves for various concentrations of sodium benzoate. The dotted curves are competitive correlation curves for benzoic acid from sodium benzoate (see Figure 1). The experimental points are for benzoic acid adsorption.

sodium benzoate concentration is of no further consequence. For these points and, by extension, for relatively dilute solutions of organic acids and their much more soluble salts, the explanation of the effect of pH on adsorption becomes strikingly simple.

The pH effect has been the subject of earlier investigations. For example, Ward and Getzen¹⁰ studied the pH dependence of the adsorption of a number of organic acids, including benzoic acid, and published a curve for phenoxycetic acid that was presumably typical of their studied compounds and that is quite similar to the theoretically derived curve of Figure 6. They attributed the observed adsorption rise at low proportions of undissociated acid to interaction of the anions with protons bound to the carbon surface. Our present model, by contrast, accounts quantitatively for the effect of pH in terms of physical adsorption of the undissociated acid and, where applicable, of the salt. Moreover, Figures 3 and 6 are illustrative of the wide concentration range of our experimental data. Whereas the concentration region of pH variation in Figure 3 extends downward to the limit of our analytical method, the constant concentration in the experiments of Figure 6 approached the limit imposed by the solubility of benzoic acid at low pH. Finally, the success of the correlation of the benzoic acid data at low total concentration and relatively high pH suggests that reduction of the acid concentration by pH control should be an additional

method for downward extension of the adsorption isotherms of organic acids in water.

Although hydrolytic adsorption is a somewhat more specialized phenomenon than pH dependence, it affords a more critical test of the competitive model, at least for the benzoic acid-sodium benzoate system. Moreover, it presented more challenging problems because of the complexities of sodium benzoate adsorption, which we first consider. Initial determinations (Figure 4) had led to upward deviations from the customary shape of correlation curves, that were most pronounced at low capacities. Although they were first ascribed to the adsorption of benzoic acid resulting from hydrolysis, they could not be reconciled with quantitative estimates based on the calculated benzoic acid concentrations and the (extrapolated) benzoic acid correlation curve of Figure 3. Moreover, attempts to calculate hydrolytic adsorption of sodium benzoate by use of this data gave pH values that were too low, in keeping with excessive estimates of sodium benzoate adsorbability.

The next step was to estimate a physical adsorption correlation curve for sodium benzoate by the indirect method of determining the adsorption of benzamide from near-saturated sodium benzoate and calculating the sodium benzoate correlation curve from the difference in abscissas between benzamide-water and benzamide-sodium benzoate. (Benzamide was chosen because of its resemblance to benzoic acid and its insensitivity to pH.) The resulting correlation curve (Figure 5), when combined with that of benzoic acid, successfully accounted for hydrolytic adsorption data similar to those of Figure 7. This finding led us to look for the effects of ash impurities on the carbon.

The direct adsorption of sodium benzoate, redetermined on a neutral singly-treated (HCl-HF extracted) carbon sample, showed reduced capacity (Figure 4) at all levels, but retention of the low-capacity upward deviation. The considerably reduced capacity was ascribed to the removal of ash (e.g., aluminum salts, which could combine with considerably more than their weight of benzoate ion), and the remaining low-capacity "tail" to chemisorption, presumably on different sites than the high-energy physical adsorption sites. To get rid of this residual adsorption, the singly-treated carbon was "doubly treated", i.e., exposed to rather concentrated sodium benzoate and exhaustively washed with water. The sodium benzoate adsorption data on this doubly treated carbon are shown in Figure 4. These data had the shape of a correlation curve; moreover, when it was calculated as a competitive correlation curve it agreed (Figure 5) with the curve calculated from the benzamide-sodium benzoate curve on an untreated carbon. Finally, the correlation curve calculated from the direct adsorption data, when used to calculate hydrolytic adsorption on doubly treated carbon, gave the consistent results of Figure 7. We now have consistency between hydrolytic adsorption, (physical) adsorption of sodium benzoate, and competitive adsorption between benzamide and sodium benzoate.

The principal effect of the ash extraction was to reduce considerably the limiting volume of sodium benzoate and hence to increase its V^* . This change in V^* made the principal difference in calculating the competition of sodium benzoate in hydrolytic adsorption. Since the ash content was estimated as about 2% by weight, its removal had negligible effect on its (physical) adsorption capacity per gram.

Continuing with Figure 7 and Table VII, we note that the moles of adsorbed benzoic acid (equivalent, as noted

earlier, to the moles of released OH^-) are quite insensitive to a 30-fold change in the sodium benzoate concentration. We can identify as stabilizing factors: (a) the reduction of the equilibrium benzoic acid concentration by release of OH^- to the solution; and (b) the increased competition of sodium benzoate with the concomitant reduction of the benzoic acid concentration. This stability follows in quite straightforward fashion from the calculation method.

One may now question whether sodium benzoate chemisorption would be expected to affect the data of Figure 3, which were determined on an untreated carbon. Since the lower limit of the capacity range is well above the capacity limit for chemisorption, one would expect minimal complications from this effect.

We should note, furthermore, that our experiments on pH dependence of adsorption (Figure 6) are reported for a doubly treated carbon, in order to achieve accurate prediction of any competitive effects in the high-pH region. The curve for untreated carbon is quite similar, except for somewhat higher adsorption of sodium benzoate.

We now draw attention to a change in the method of extrapolating adsorption data to lower capacities. One method used here for benzoic acid was to find the abscissa scale factor that would fit the experimental data to the hydrocarbon correlation line and to use this scale factor to calculate low capacity data from this line. In earlier work¹ we used the same method, but with the glucose correlation line. It now appears that the glucose line deviates downward somewhat and that the hydrocarbon line gives more accurate results. The use of the hydrocarbon line to correlate the benzoic acid-glucose data of Figure 8 of Rosene and Manes¹ would have shown a slight downward deviation of the benzoic acid points at low concentrations similar to those in Figure 3, owing to the lack of pH control in those experiments. To some extent, therefore, the close fit of the points to the theoretical line represents cancellation of errors which, however, are readily corrected.

The use of adsorption from a nonaqueous solvent and of competitive adsorption to extend downward the accessible range of adsorption capacities and to distinguish physical adsorption from other complicating phenomena are probably examples of generally applicable methods. Thus we could in all likelihood have used other solvents than methanol in extrapolating the benzoic acid data, and we could also have used solutions of saturated competing solids, such as urea, for the same purpose. Similarly, benzamide was almost certainly not a unique adsorbent for distinguishing physical adsorption of sodium benzoate from complicating phenomena. Addition of these methods to the earlier use of competitive adsorption as a probe⁴ to determine the occupied volume of adsorption space suggests that the competitive model has considerable potential utility in addition to its applicability to predicting competitive adsorption. Finally, we have here treated the adsorption of mixtures of acids (or bases) and their salts as special cases of potentially competitive solutes distinguished only by their pH-mediated interconvertibility and frequently characterized by large differences in solubility; this treatment may be expected to have fairly general applicability.

Acknowledgment. We thank the Calgon Corporation for support of this work.

Supplementary Material Available: Table II, adsorption of benzoic acid from methanol; Table III, adsorption of benzoic acid from water; Table IV, adsorption of sodium benzoate from water; Table V, competitive

adsorption of benzamide from near-saturated sodium benzoate; Table VI, adsorption of benzoate species as a function of pH (2 pages). Ordering information is available on any current masthead page.

References and Notes

- (1) M. R. Rosene and M. Manes, *J. Phys. Chem.*, **80**, 953 (1976). This article gives references to the earlier literature.
- (2) F. E. Bartell and E. J. Miller, *J. Am. Chem. Soc.*, **44**, 1866 (1922); **45**, 1106 (1923); *J. Phys. Chem.*, **28**, 992 (1924).

- (3) E. J. Miller, *J. Am. Chem. Soc.*, **46**, 1150 (1924); **47**, 1270 (1925); *J. Phys. Chem.*, **30**, 1162 (1926).
- (4) M. R. Rosene, M. Ozcan, and M. Manes, *J. Phys. Chem.*, **80**, 2586 (1976).
- (5) M. R. Rosene and M. Manes, *J. Phys. Chem.*, preceding article in this issue.
- (6) M. Ozcan, Ph.D. Dissertation, Kent State University, 1972.
- (7) T. W. Schenz and M. Manes, *J. Phys. Chem.*, **79**, 804 (1975).
- (8) D. A. Wohleber and M. Manes, *J. Phys. Chem.*, **75**, 81 (1971).
- (9) M. Manes and L. J. E. Hofer, *J. Phys. Chem.*, **73**, 584 (1969).
- (10) T. M. Ward and F. W. Getzen, *Environ. Sci. Technol.*, **4**, 64 (1970).
- (11) See paragraph at end of text regarding supplementary material.

The Tammann–Tait–Gibson Model for Aqueous Electrolyte Solutions. Application to the Refractive Index

J. V. Leyendekkers and R. J. Hunter*

Department of Physical Chemistry, University of Sydney, Sydney, 2006, Australia (Received November 1, 1976; Revised Manuscript Received April 20, 1977)

An outline is given of the Tammann–Tait–Gibson model for aqueous electrolyte solutions. The parameters of the basic equations of this model are derived for a range of electrolytes (chlorides, bromides, sulfates, carbonates, bicarbonates, and chromates) at 20 °C. These parameters are then used to develop an equation for the refractive index of the solutions. An important feature of this equation is that it enables prediction of the refractive index up to about 1000 bars. In addition, the equation is simply extended to cover multicomponent electrolyte solutions. The refractive index of sea water predicted from the binary data agreed with the direct measurements within the experimental errors.

1. Introduction

The Tammann–Tait–Gibson (TTG) model, as it may be called, was developed during the 1930's by Gibson but has had very restricted application since then. Fortunately, the ideas have remained readily accessible via the excellent summary given by Harned and Owen.¹ Recently,² the work of Gibson has been reassessed and the TTG model applied to the analysis of many sea water properties. The model is particularly suited to aqueous systems under pressure and is able to cover the important structural properties of water in a simple way. However, its use should not be restricted only to sea water. Water generally comprises 90% or so of most aqueous solutions studied, and the fact that this model ascribes a major role to water (that is, its properties in the liquid phase in the presence of the ionized solute) has obvious advantages. Not the least is the high accuracy of data on water, the properties of which have been intensively studied and measured over the last century. The purpose of the present paper is to outline the TTG model, and give examples of its potential usefulness for predicting aqueous solution properties. In this way it is hoped to stimulate interest in the model.

Aside from its usefulness as an empirical correlator, evidence will be presented to show that the parameters which arise in the model (section 2) can be related to the fundamental thermodynamic, crystallographic, and other properties of the solutes involved. In section 3, estimates derived from the model of the mean separation between a cation and a water molecule are compared with those from another source; in section 4 the TTG molar volume of the solute is related to its crystallographic properties. Then, in sections 5–7 the refractive index of binary electrolyte solutions is considered. It is shown that the derived parameters of the TTG equations for refractive index are directly correlated with the oscillator properties

and hence are not simply empirical quantities. This justifies a simple extension to multicomponent solutions (section 8) which is substantiated by good agreement with experimental data.

It should be stressed that other properties of aqueous solutions could be treated in a similar way. The refractive index was simply chosen as an interesting example of how the TTG model can be applied. Other aspects of the TTG model have been given by Harned and Owen¹ and Leyendekkers.²

2. Basic Equations of the Tammann–Tait–Gibson Model

The underlying assumption of the TTG model is that the change in volume, or density, of water associated with the solution of an electrolyte is due to compression of the water rather than to any alteration in the properties of the solute (as a liquid). Tammann's hypothesis¹ states that, in the presence of an ionized solute, the water in an aqueous solution behaves as though it were subjected to a constant effective pressure, p_e , in addition to the atmospheric. Gibson³ expressed these changes in a quantitative way by extending the Tait equation for pure liquids in the following way. A full account of this has been given previously² so that only a summary is given here.

The Tait equation (the commonly used form) for water may be written²

$$v_w^p = v_w^{(p_0)} \left(1 - 0.315 \log \frac{(B_T + p)}{(B_T + p_0)} \right) \quad (1)$$

where the initial pressure $p_0 = 1$ bar and

$$B_T = 2671.8 + 19.454t - 0.27028t^2 + 0.0009798t^3 \text{ bars} \quad (1a)$$

where t is the temperature in °C, v_w is the specific volume

of pure water at the pressure indicated by the superscript. The specific volume of the water in the solution, ψ_w , is thus given by

$$\psi_w^{(p)} = v_w^{(p_0)} \left(1 - 0.315 \log \frac{(B_T + p_e + p)}{(B_T + p_0)} \right) \quad (2)$$

and the specific volume of the pure solute (as a liquid), ψ_s , is given by

$$\psi_s = (v - x_w \psi_w) / x_s \quad (3)$$

where v is the specific volume of the solution, and x_w , x_s are, respectively, the weight of water and solute per gram of solution. The effective pressure, p_e , is obtained from compressibility data via the relationship^{1,2}

$$(\beta v)^{(p)} = 0.4343 x_w C_T / (B_T + p_e + p) - x_s \frac{\partial \psi_s^{(p)}}{\partial p} \quad (4)$$

The last term is negligible at moderate pressures and concentrations (for $x_s \leq 0.25$ and $p \leq 1000$ bars). The value of C_T is $0.315 v_w$, i.e., it is a function of temperature but independent of pressure. β is the isothermal compressibility coefficient ($-(1/V)(\partial V/\partial p)$). It will be shown below (section 4) that $M\psi_s$ (where M is the molecular weight of the salt) can be identified with the "intrinsic volume" of the solute derived from other models, e.g., the hard sphere model⁴ and the "critical disruptive volume" of Scott.⁵

Equations can be derived that relate $M\psi_s$ and $(B_T + p_e)$, or B^* , to all the familiar thermodynamic properties of the solution. For example, the partial molal volume of the solute is given by^{1,2,6}

$$\bar{v}_s^{(p)} = M\psi_s - (\partial B^*/\partial m)D / (B^* + p) \quad (5)$$

where $D = 434.3 C_T$.

Thus, the change in the volume of the solution with respect to the solute depends on the "crystal" volume (melted) and the compressional effect of the solute on the solvent, water.

3. Mean Separation between Cation and Associated Water

The value of $M\psi_s$ is independent of concentration,^{1,2} from which it follows that the compressibility of the solute in solution, $\beta(\text{sol})$, is three times as great as in the solid state.¹ On the basis of the TTG model, then, $\beta(\text{sol}) = 3\beta(\text{cryst})$ and we can estimate a value for a_0 , the equilibrium separation of univalent cations and water molecules, using this equality. From the Born-Landé equation⁷

$$a_0^3 = -n u_0 \beta / 18 \quad (6)$$

where u_0 is the minimum potential energy, n is an integer, and β is the isothermal compressibility. Comparing the values for the solid, and the solid in solution with β increased threefold

$$a_0(\text{sol}) = a_0(\text{cryst}) \left[\frac{3u_0(\text{sol})}{u_0(\text{cryst})} \right]^{1/3} \quad (7)$$

The end of the water molecule facing a cation closely resembles the fluoride ion⁷ so that the fluoride-cation crystal energies and the corresponding $a_0(\text{cryst})$ values are used. The value of $u_0(\text{sol})$ is taken as the experimental value of the increase in heat content for transfer of the cation from solution to gas phase. Moelwyn-Hughes⁷ also used these last two assumptions and calculated the

TABLE I: Equilibrium Separation of Univalent Cations and Water Molecules

Cation M ⁺	$a_0(\text{M}^+) - a_0(\text{H}^+)$, ^a Å		Crystal radius, Å
	Inter- molecular force theory	TTG model	
Li ⁺	0.55	0.75	0.68
Na ⁺	0.75	1.00	0.97
K ⁺	1.42	1.30	1.33
Rb ⁺	1.58	1.42	1.47
Cs ⁺	1.73	1.54	1.67

^a $a_0(\text{H}^+)$ is 1.545 Å, this value and data for u_0 and a_0 (cryst) for the fluoride salts were taken from the compilation of Moelwyn-Hughes.⁷

equilibrium separation of cation and water molecule, a_0 , from the equation

$$(9u_0/c)a_0^4 + 7C_w a_0^2 + 5B_w = 0 \quad (8)$$

where C_w and B_w are functions of the properties of the water molecule (polarizability and dipole moment). The coordination number, c , for the given cation was estimated using the crystal repulsion constants for fluoride salts. The calculated values of $a_0(\text{sol})$ from eq 7 and 8 are compared in Table I. The values of a_0 , via both approaches, are approximately equal to $a_0(\text{H}^+)$ plus the crystal radius of the cation, which seems a very reasonable result. This is just one example of how the TTG model can be used to interpret solution properties. Other aspects of the TTG model have been given by Harned and Owen¹ and Leyendekkers.²

4. The Specific Volume of the Solute (as a Liquid) in an Aqueous Solution

Values of ψ_s and $M\psi_s$ (the molar volume) for a range of electrolytes are given in Table II. These were calculated from the compressibility data of Gibson,³ using the equations given in section 2. The average value of $M\psi_s$ over the concentration range and the standard deviation are shown. As can be seen, the volume is effectively insensitive to concentration. The value for the salt can be split into suitable conventional ionic values and correlated with certain ionic properties, the data for which are readily available. For example, we have split the values of $M\psi_s$ in Table II to give the best fit to the standard ionic entropies at 25 °C. The equation

$$M\psi(\text{ion})/z = a_0 + a_1 \bar{s}_{\text{ion}}^0 + a_2 \bar{s}_{\text{ion}}^0{}^2 \quad (9)$$

with $a_0 = 10.85$, $a_1 = 0.3557$, and $a_2 = 8.15 \times 10^{-3}$, standard deviation = $\pm 1.6 \text{ cm}^3$, and z the charge on the ion, can be used to give an estimate of $M\psi_s$ when no data are available (see Table III); values of \bar{s}_{ion}^0 are available for a large number of ions.^{8,9}

As will be shown later (section 7) errors of 2 or 3 cm^3 in $M\psi_s$ are not very critical in the calculation of the corresponding RI term, at least at moderate concentrations.

For the alkali halides with the same crystalline structure (rock-salt type lattice), the values of $M\psi_s$ are very close to those of v_{in} , the intrinsic volume of Padova⁴ and Φ_v^* , the minimum apparent molal volume of Scott.⁵ Experimental values of $M\psi_s$ and calculated values based on eq 9 are shown in Table III, together with the corresponding values of v_{in} and Φ_v^* . The value of v_{in} is given by⁴

$$v_{\text{in}} = \phi_v^0 + (-\phi_k^0) s_v / s_k \quad (10)$$

where ϕ_v^0 and ϕ_k^0 are the apparent molal volume and compressibility, respectively, at infinite dilution and s_v and

TABLE II: Specific Volume and Molal Volume of Ionized Solutes (Liquid) in Aqueous Solutions at 25 °C^a

Salt	ψ_s	$M\psi_s$	Exptl concn range, g/g solution	No. measurements
BaCl ₂	0.272 ± 0.001	56.8 ± 0.2	0.05–0.25	7
BeSO ₄	0.381 ± 0.011	40.0 ± 1	0.05–0.25	5
CdSO ₄	0.230 ± 0.017	47.9 ± 3	0.10–0.40	5
Cs ₂ SO ₄	0.263 ± 0.003	95.1 ± 1	0.10–0.50	5
KBr	0.357 ± 0.003	42.5 ± 0.3	0.08–0.40	6
KCl	0.515 ± 0.013	38.4 ± 1.0	0.06–0.26	7
K ₂ CrO ₄	0.402 ± 0.002	78.0 ± 0.4	0.14–0.38	5
LiCl	0.665 ± 0.005	28.2 ± 0.4	0.04–0.39	10
Li ₂ SO ₄	0.499 ± 0.002	54.8 ± 0.2	0.05–0.25	5
MgSO ₄	0.368 ± 0.015	44.3 ± 1.8	0.05–0.25	5
NaBr	0.336 ± 0.004	34.6 ± 0.4	0.05–0.45	5
NaCl	0.522 ± 0.004	30.6 ± 0.5	0.04–0.28	8
Na ₂ CO ₃	0.425 ± 0.018	45.1 ± 1.9	0.04–0.20	6
Na ₂ SO ₄	0.418 ± 0.009	59.4 ± 1.2	0.05–0.24	6
(NH ₄) ₂ SO ₄	0.599 ± 0.005	79.1 ± 0.6	0.06–0.40	11
ZnSO ₄	0.252 ± 0.020	40.7 ± 3	0.05–0.27	5

^a Derived from experimental compressibility data.³TABLE III: Comparison of the Molal Volume of the Pure Solute (as a Liquid), $M\psi_s$, and Other Molal Volumes

Salt	$M\psi_s$	v_{in}	Φ^*	Ψ^*
LiCl	28.3	22.7	25.3	0.64 ^a
LiBr	32.3	29.3	30.0	0.64 ^a
LiI	(38.9)	39.1	39.2	0.64 ^a
NaCl	30.6	27.1	26.9	0.65
NaBr	34.6	33.7	31.5	0.64
NaI	(41.2)	43.5	40.6	0.66
KCl	38.4	36.0	36.3	0.64
KBr	42.5	42.6	41.3	0.64
KI	(49.0)	52.4	51.0	0.65
RbCl	(43.7)	40.1	40.7	0.64
RbBr	(47.8)	46.7	46.3	0.64
RbI	(54.3)	56.5	55.9	0.64
CsCl	48.5	46.2	48.0	0.77
			47.2 ^b	0.64
CsBr	52.6	52.8	53.4	0.76
			52.8 ^b	0.64
CsI	(59.1)	62.6	63.2	0.76
			62.7 ^b	0.64

^a Using only high concentration data for ϕ_v^0 and s_v .¹^b Assuming a rock-salt type lattice structure, bracketed values were estimated on the basis of eq 9.

s_k the corresponding slopes of the linear concentration functions (i.e., $c^{1/2}$ with c in mol/L: the Masson equation). Padova⁴ derived this relationship on the basis of the hard-sphere model of a solvated ion (the ion-solvent complex is assumed incompressible).

The value of Φ_v^* is given by¹

$$\Phi_v^* = \phi_v^0 + 10^{3/2} s_v / V^{*1/2} \quad (11)$$

where V^* is the "critical disruptive volume" of the solid.⁵ The cohesive forces reach a maximum when the crystal

TABLE IV: Comparison of Molal Volumes for Nonrock-Salt Type Lattice Structures

Salt	$M\psi_s^b$	v_{in}	Ψ^*		Crystal ^a type
			$\Phi_v^* =$	$\Phi_v^* =$	
Na ₂ SO ₄	59	38.4	0.90	0.55	Orthorhombic
K ₂ CrO ₄	78		0.95		Rhombohedral
Na ₂ CO ₃	45.1		0.95		Rhombohedral
BaCl ₂	56.8		1.3		Cubic
	52.6 ^c		0.95		
HCl	(26.0)	20.7	2.26	0.19	Orthorhombic to cubic at 98.9 K
	23.5 ^c		0.96		
NaOH	(25.5)	12.8	1.15	0.21	Rhombohedral
	23.8 ^c		0.96		
KNO ₃	(56.6)	47.3	3.6	0.74	Rhombohedral or trigonal
	48.4 ^c		0.95		

^a Reference 1. ^b Bracketed values estimated on the basis of eq 9. ^c Calculated on the assumption that Ψ^* is 0.95–0.96.

expands from its normal equilibrium volume to V^* . These forces then decrease on further expansion. The use of V^* , rather than the molal volume of the pure crystalline salt, ensures that the properties of the solid state are included in the interpretation of the hypothetical upper limit to the concentration of the solution. Thus V^* is assumed to correspond to the hypothetical maximum concentration attainable in a "supersaturated" solution of a given salt, and marks the transition from rigid crystalline structure to the more mobile liquid structure. The ratio Φ_v^*/V^* or Ψ^* is of special interest as it is related to the crystal structure. Crystals with the rock-salt type lattice have a value of Ψ^* of 0.64 (Table III). The cesium salts have a different lattice structure (body-centered cubic) and Ψ^* is around 0.77 for these salts. The value of Ψ^* can be calculated from eq 11, viz.

$$\Psi^* = \Phi_v^* (\Phi_v^* - \phi_v^0)^2 / (10^3 s_v^2) \quad (12)$$

provided the data from which s_v is derived is not confined to dilute solutions (ca. <0.5 m) only.¹

The agreement between v_{in} , Φ_v^* , and $M\psi_s$ indicates the compatibility between the three "models" on which each calculation is based. However, this only applies for the alkali halides. Comparison between $M\psi_s$ and v_{in} for more complex salts, such as sodium sulfate, indicates poor agreement.

Using eq 12 and equating Φ_v^* with $M\psi_s$ and v_{in} , in turn, we calculated the corresponding Ψ^* for a number of salts (Table IV). Although the data are somewhat restricted, the trends suggest that $M\psi_s$ gives consistent results, on the basis of what might be expected for Φ_v^* . The value of $M\psi_s$ predicted from eq 9 for NO₃⁻ appears far too high; a check on the eq 9 results, via eq 12, should therefore be made as a useful guide. The hard sphere model generally gives values that appear too low. This could be expected for nonspherical ions such as OH⁻ (which is cylindrical) or CO₃²⁻ (which is planar). Since $M\psi_s$ can, apparently, be equated to Φ_v^* it is of interest to note a few points concerning this latter quantity.

From the above relationships

$$s_v = (\Psi^* V^* - \phi_v^0) V^{*1/2} / 10^{3/2} \quad (13)$$

which indicates that s_v can be described in terms of data on the crystal lattice and on ion-solvent interactions without recourse to the concept of an ionic atmosphere. This is not so very unusual since many properties of ions in solution may be derived in terms of intermolecular forces, without recourse to concepts such as electrical

charging or ionic radii. For example, as shown by Moelwyn-Hughes⁷ the energy of interaction between an ion and the solvent molecules which surround it can be given in terms of the polarizability and the dipole moment of the solvent molecule, and crystal force constants. Since Ψ^* appears to be a function of the lattice structure the above results suggest that a replacement of the concept of the ionic atmosphere by a statistical lattice structure, except at high dilutions, is quite valid.¹ These points are noted since it is felt that they help to put the TTG model in better perspective in relation to other solution theories.

Finally, the value of Ψ^* is independent of temperature, and this property will be found useful in section 9.

Application of the model to the dispersion of light is now considered.

5. Dispersion Equations

(i) *General Functions.* Two commonly used classical dispersion functions are the Drude, D, function

$$f(n) = n^2 - 1 \quad (14)$$

and the Lorentz-Lorenz, LL, function

$$f(n) = (n^2 - 1)/(n^2 + 2) \quad (15)$$

where n is the refractive index. The different functions arise from the different assumptions concerning the effective field polarizing each molecule or ion of the medium.^{7,10,11}

As far as the dispersion of light is concerned the classical and quantal theories do not differ significantly. The classical theory attributes the refraction of light to individual electrons and is thus able to explain the approximately additive nature of molecular refraction. Both the D and LL functions can be interpreted as representing the sum of the polarizabilities of the dispersion electrons. In turn, the polarizabilities are functions of the vibration frequencies of the electrons, ν_i , and of the incident light, ν_L . The Kramers-Heisenberg quantal equation takes the same form as the Drude equation but ν_i represents the transition frequency between electronic states, in this case. The LL equation will be used here to conform with the equation of Eisenberg¹⁰ for water which is used as a basis to analyze the aqueous salt solutions.

(ii) *Dispersion by Pure Solids.* Herzfeld and Wolf¹¹ used the equation

$$(n^2 - 1)/(n^2 + 2) = A' \sum N_i p_i / (\nu_{v,i}^2 - \nu_L^2) \quad (16)$$

to analyze data on solid NaCl and KCl. N_i and p_i represent, respectively, the number of oscillators (dispersion electrons) per unit volume, and the oscillator strengths. $\nu_{v,i}$ is the frequency of vibration of the electrical oscillator and ν_L is the frequency of vibration of the light. The constant A' is given by $e^2/3\pi m$, with e and m representing the charge and rest mass of the electron, respectively. For both salts, the sum of eq 16 was shown to consist of three terms, one relating to the cation, the other two to the anion. The frequencies $\nu_{v,i}$ were estimated from the absorption spectrum of the salts. It was found that oscillator strength could be chosen to give the correct dispersion according to eq 16 over the whole range of frequencies, ν_L .

(iii) *Dispersion by Water.* Eisenberg's¹⁰ equation for water gives the LL form for n as a function of the density of water, d_w , and the temperature, viz.

$$f(n) = (n^2 - 1)/(n^2 + 2) = A(d_w)^B \exp(-Ct) \quad (17)$$

where the constants A , B , and C are functions of the wavelength but independent of temperature or pressure. This equation fitted the experimental data to a high degree

of accuracy (to within a few digits in the seventh decimal place). The constant A corresponds to the specific refraction (LL type) in the limiting case where B is unity and C is zero. The value of C is zero, and B is close to unity, for methanol and other pure liquids that do not show the density anomaly associated with water and heavy water.¹⁰ The constant C , $(-\partial \ln f(n)/\partial t)_v$, reflects the change in the structure of water at different temperatures. Leyendekkers² fitted the values of A , B , and C to a polynomial in the wavelength, λ (4047-7065 Å). Equation 17 was used to calculate the refractive index of water at pressures up to 1380 bars.² Comparison with the experimental data gave deviations that were generally less than the experimental error for pressures below 1000 bars. This substantiated Eisenberg's¹⁰ observation that A , B , and C were independent of pressure up to about 1000 bars.

Eisenberg¹⁰ was able to interpret his results in terms of a two-state model for water, using the relationship

$$f(n) = 4\pi N \sum_i^k F_i \alpha_i \quad (18)$$

where N represents the number of oscillators per unit volume and F and α are the mole fraction and polarizability, respectively, of the oscillator of type i . This form of equation is the same as eq 16.

The additive nature of the component refractivities, for both crystals and water, justifies a form of equation for aqueous solutions, that will incorporate eq 17 using the Tammann principle. The residual refractivity will then relate to the ionized solute (as a solution) and can be expected to be simply related to relevant crystal properties and be independent of pressure. Such a treatment can be simply extended to multicomponent electrolyte solutions.

(iv) *Dispersion by Aqueous Electrolyte Solutions.* The density and refractive index (to 0.0001) are available¹² for electrolytes of diverse type (halides, sulfates, chromates, carbonates, and bicarbonates) only at 20 °C, and the analysis will largely be confined to this temperature.

For the model to be used here, the volume of water in 1 g of an aqueous solution is given by ψ_w of eq 2, so that the LL refractivity for the water is, from eq 17

$$f(n)_w = A(1/\psi_w)^B \exp(-Ct) \quad (19)$$

The values of B^* at 25 °C are available for many electrolytes, especially sulfates and chlorides,^{3,6} hence the values of ψ_w and ψ_s are available at this temperature. In order to estimate ψ_w at 20 °C the corresponding value of ψ_s at 25 °C was used, since this quantity is not very sensitive to temperature, and errors of estimates are less critical than they are for the other quantities. In addition ψ_s is correlated with ionic properties and hence more easily predicted for those salts for which no compressibility data are available. The value of ψ_w in eq 19 was therefore estimated from eq 3, viz.

$$\psi_w = (v - x_s \psi_s)/x_w \quad (20)$$

$f(n)_w$ could then be calculated from eq 19 and compared with the experimental $f(n)$ for the solution. This gave the refractivity contribution of the ionized solute, $\Delta f(n)$, the solute being treated as a liquid in the model used here (section 2). Thus

$$\Delta f(n) = f(n) - f(n)_w \quad (21)$$

The value of $\Delta f(n)$ could be expected to be a simple function of $(1/\psi_s)$ and of x_s , and be independent of pressure. The functional coefficients for different salts could be expected to be related to some property of the crystal such as the standard entropy.

TABLE V: Coefficients for the Equations $\Delta f(n) = b_1(x/\psi_s) + b_2(x/\psi_s)^2$ and $\Delta f(n) = c_1x + c_2x^2$

Salt	10^2b_1 10^2c_1	10^2b_2 10^2c_2	Max exptl concn, mol/kg water	\pm std dev \times 10^4
BaCl ₂	1.55748	0.245635	1.692	0.09
	5.71087	3.30253		
CaCl ₂	3.79841	0.542320	3.02	0.09
	8.43172	2.67229		
CuSO ₄	1.31940	0.353526	1.387	0.17
	5.06226	5.20421		
KBr	1.90391	0.428290	2.902	0.02
	5.33140	3.35836		
KCl	2.49926	0.389825	4.55	0.17
	4.85715	1.47234		
K ₂ CO ₃	1.63049	-0.151613	2.44	0.24
	3.70007	-0.780759		
K ₂ CrO ₄	3.46206	0.558322	1.8	0.28
	8.62297	3.46361		
K ₂ SO ₄	1.29542	-0.352574	0.713	0.008
	3.00187	-1.89326		
LiCl	4.98533	-0.479057	5.704	0.05
	7.49390	-1.08247		
MgCl ₂	4.31943		3.5	0.71
	8.84600			
MgSO ₄	1.70942	-0.0971275	2.79	0.14
	4.64554	-0.717324		
NaBr	1.93139	0.445008	3.26	0.09
	5.74449	3.93669		
NaCl	2.97724	0.0011842	5.7	0.065
	5.69338	0.0043305		
Na ₂ CO ₃	1.80291	-0.109780	1.69	0.20
	4.23744	-0.606434		
NaHCO ₃	2.35966		0.806	0.28
	5.10559			0.22
Na ₂ SO ₄	1.29029	-0.393016	2.00	0.17
	3.08583	-2.24792		
(NH ₄) ₂ SO ₄	3.36674	0.505724	2.56	0.048
	5.62216	1.41026		
SrCl ₂	1.97279	0.487152	2.115	0.14
	6.38298	5.09976		
ZnSO ₄	1.24576	0.220055	1.19	0.065
	4.94143	3.46230		

6. Calculation of the Refractivities (LL) of Water (under a Pressure p_e) and the Ionized Solute (as a Liquid)

Values of ψ_w were calculated using eq 20 and the density data¹² at 20 °C for the concentration ranges shown in Tables V and VI. Values of $f(n)_w$ and hence $\Delta f(n)$ were

calculated from eq 19 and 21 and the experimental¹² values of n , the RI. (Actually, interpolated experimental values were used, calculated from least-squares polynomials fitted to the data.) The values of A , B , and C (for λ 5892.6 Å) were 0.2064709, 0.88538, and 6.2037×10^{-5} , respectively.

The values of $\Delta f(n)$ were fitted to x_s and to x_s/ψ_s . For many of the simple electrolytes, e.g., NaCl, $\Delta f(n)$ was effectively proportional to x_s/ψ_s . However, in order to compare the coefficients for the different electrolytes we have taken the equation

$$\Delta f(n) = b_1x_s/\psi_s + b_2(x_s/\psi_s)^2 \quad (22)$$

as a basis. The values of the coefficients are listed in Table V and corresponding values for the x_s function are also shown. This latter function can be used to estimate the refractivities in multicomponent solutions. (See Section 8.)

Values of p_e and $(B^* - B_T)$ were also calculated for the different salts from eq 1a and 2, and fitted to x_s to degree 3. The values of these coefficients are listed in Table VI.

7. Correlations of the $\Delta f(n)$ Coefficients

On the model used here, it can be envisaged that the coefficients b_1 and b_2 of eq 22 can be related to composite sums of the type given in eq 16. That is, the relative values of the different electrolytes should be related to the corresponding oscillator properties.

On the basis of quantal considerations, that is, the relationship of thermodynamic properties and molecular energy levels,⁸ assuming harmonic vibration, the standard entropy of the crystal, $s^0(\text{cryst})$, could be expected to be simply related to $\nu_{v,i}$ in the composite sense. Therefore, we have fitted the values of $1/b_1^{1/2}$ (Table V) to the crystal entropy (at 25 °C). This gives

$$(1/(10^2b_1)^{1/2}) = 0.07258 + 5.96868 \times 10^{-2} s^0(\text{cryst}) \quad (23)$$

with a standard deviation of ± 0.046 .

Our model has taken the ionized solute as being in the liquid form and the second term of eq 22 might be interpreted as arising from differences in the properties of the oscillators in the different phases. For instance, it might be expected that anharmonicity is more dominant in the liquid phase. The specific heats of the salts could be expected to reflect relative deviations in this respect. The average value per atom of the specific heat of the

TABLE VI: Effective Pressure as a Function of Concentration at 20 °C^a

Salt	h_0	h_1	h_2	h_3	Max concn ^b	\pm std dev
BaCl ₂	2.96	2952.72	3574.70	1784.46	0.26	1.3
CaCl ₂	2.56	5868.61	2427.07	14839.50	0.25	1.0
CuSO ₄	-3.95	6698.97	-6107.14	38950.00	0.18	1.5
KBr	0.31	1575.34	-705.833	2558.21	0.25	0.11
KCl	0.51	3276.21	-1549.34	6344.26	0.25	0.10
K ₂ CO ₃	1.71	7288.34	3207.34	10414.30	0.25	0.72
K ₂ CrO ₄	2.40	4193.61	-1556.98	13098.50	0.26	3.2
K ₂ SO ₄	-0.47	5025.00	605.618	-5883.02	0.11	0.00
LiCl	1.74	5416.45	-1126.33	21474.60	0.20	0.26
MgCl ₂	-10.55	6873.06	2247.60	20154.40	0.25	6.5
MgSO ₄	2.36	8111.63	5725.17	10671.70	0.25	0.21
NaBr	1.48	2299.68	527.243	2845.31	0.25	0.12
NaCl	-0.03	5078.65	2.022	11206.30	0.25	0.29
Na ₂ CO ₃	0.04	10162.70	-160.132	35413.10	0.15	0.22
NaHCO ₃	2.16	3091.26	-6189.10	-7555.55	0.063	0.00
Na ₂ SO ₄	10.82	5779.68	16284.00	-38797.80	0.22	5.4
(NH ₄) ₂ SO ₄	-0.95	4259.34	-1570.25	-5161.24	0.25	0.06
SrCl ₂	2.80	3946.14	5525.44	-8084.03	0.25	0.57
ZnSO ₄	-4.02	6406.27	-5025.18	37898.20	0.16	0.67

^a Coefficients for the equation (with $B_T = 2960.61$ bars) $B^* - B_T = p_e = h_0 + h_1x + h_2x^2 + h_3x^3$ (bars). ^b g/g of solution, see Table V for concentration in mol/kg water.

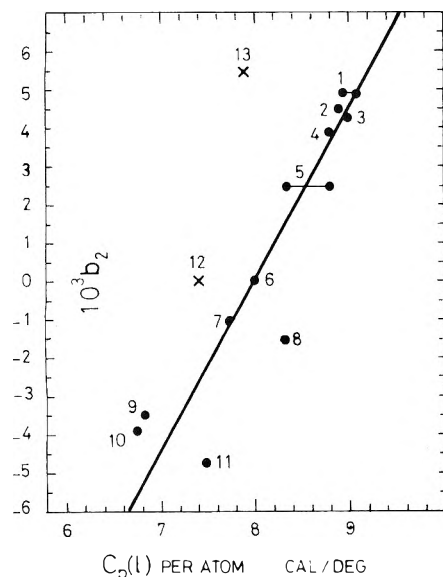


Figure 1. The coefficient b_2 of eq 22 as a function of the specific heat (average per atom) of the liquid solute. X indicates less reliable data: (1) SrCl_2 ; (2) NaBr ; (3) KBr ; (4) KCl ; (5) BaCl_2 ; (6) NaCl ; (7) Na_2CO_3 ; (8) K_2CO_3 ; (9) K_2SO_4 ; (10) Na_2SO_4 ; (11) LiCl ; (12) MgCl_2 ; (13) CaCl_2 .

molten salts ($C_p(l)$ per atom) was found to be closely correlated with the values of b_2 as shown in Figure 1. An exception was CaCl_2 . However, the value of $M\psi_s$ for this salt (and for MgCl_2) was estimated from eq 9 and, unlike b_1 , b_2 is quite sensitive to changes in this quantity. Errors in $C_p(l)$ may also be a factor. The data are from Lumsden¹³ and Janz.¹⁴ Two independent values are available each for BaCl_2 and SrCl_2 , which indicate the possible errors, in a restricted way (Figure 1).

We have also correlated b_1 with the specific refractivity of the crystal ($R_c'(D) = (n^2 - 1)/(n^2 + 2)d_c = f(n)_c/d_c$) using the experimental values for n^{12} (sodium D light), and for the density, d_c , of the crystal.⁹ This gave a linear fit with a standard deviation of $\pm 0.28 \times 10^{-2}$ for b_1 , viz.

$$10^2 b_1 = -2.5843 + 34.5894 R_c'(D) \quad (24)$$

When ν_L in eq 16 is zero, the specific refractivity, R_0' , then represents the system in the absence of an externally applied field. Since eq 16 fits the crystal data for all wavelengths, extrapolation to light of infinite wavelength (i.e., $\nu_L = 0$) gives the limiting specific refractivity, R_0' . The partial molal refraction, pmr, of salts in aqueous solution, as a function of wavelength, can be similarly treated. Heydweiller¹⁵ obtained R_0 , the pmr of many salts toward light of infinite wavelength, by extrapolation. Since these refractivities are additive, they are conveniently given as the ionic values. Ionic refractivities have also been computed from the refraction of the inert elements using Pauling's quantal treatment, and the results are in good agreement with the extrapolated pmr values.⁷ We have fitted b_1 to the limiting specific refractivities (calculated from the pmr's divided by the corresponding molecular weights) using the data of Heydweiller¹⁵ and the pmr's (for infinitely dilute solution) given by Parsons.⁹ The standard deviation of linear fit was $\pm 0.35 \times 10^{-2}$ for the former set and $\pm 0.23 \times 10^{-2}$ for the latter. The equation based on Parson's⁹ data is

$$10^2 b_1 = -2.773 + 37.6375 R_1'(D) \quad (25)$$

with $R_1'(D) = R_1(D)/M$, M is the molecular weight, $R_1(D)$ the pmr (limiting solution) of the salt, for the Na D line.

The calculated values of b_1 are compared with the original in Table VII (supplementary material, see paragraph

at end of text regarding supplementary material). The limiting specific refractivities, R_0' and $R_1'(D)$, are also listed and compared with $R_c'(D)$. The effect of changing ν_L on the specific refractivities and hence on $\Delta f(n)$ is seen to be quite small.

These relationships should be useful for estimating b_1 and b_2 for other salts. At moderate concentrations (to 1 or 1.5 m) the value of $\Delta f(n)$ can be estimated fairly closely from b_1 alone. The various equations (23, 24, and 25) given above for b_1 give errors around 0.2×10^{-2} which represent corresponding errors in $\Delta f(n)$, at these concentrations, of about 2×10^{-4} . Thus, together with the estimate for $M\psi_s$ (when no compressibility data are available) the value of $f(n)$ can be estimated from the density. The general equation is

$$f(n) = A(1/\psi_w)^B \exp(-Ct) + \Delta f(n) \quad (26)$$

and $n = [(1 + 2f(n))/(1 - f(n))]^{1/2}$ with ψ_w given by eq 2 or 20 and $\Delta f(n)$ by eq 22 or estimated from eq 23, 24, or 25.

Values of n calculated from eq 26, using the B^* values given in Table VI, and c_1 and c_2 from Table V, are compared with the experimental values in Table VIII (supplementary material). Values of the effective pressure are also listed for interest, to show the relative effects of the different solutes. It should be noted that the experimental values of n have been converted to absolute values by multiplying by 1.00029.¹⁶

The ratios b_1/b_2 for the different salts appear to fall into groups (with values 2-7 and -3 to -18). It is not clear what significance, if any, the groups have.

The above relationships can be used to predict the dispersion and other characteristics of multicomponent electrolyte solutions.

8. Multicomponent Electrolyte Solutions

When a number of different solutes are present in water, assuming that the effective pressures exerted by the individual salts are the same as in the binary solution, the value of P_e is given by

$$P_e = \sum_i p_{e,i} \quad (27)$$

with $p_{e,i}$ being a function of x_i , the concentration of the solute i in the solution. We can calculate P_e for a multicomponent solution at 20 °C from eq 27 using the values for each x_i , viz.

$$P_e = \sum_i (h_{0,i} + h_{1,i}x_i + h_{2,i}x_i^2 + h_{3,i}x_i^3) \quad (28)$$

using the coefficients given in Table VI.

Values of P_e for sea water were calculated in this way.¹⁷ The agreement between the experimental and calculated values was excellent (maximum differences was 1.7 bars at the highest concentration of ca. 0.8 m).

Similarly, the values of $\Delta f(n)$ obtained for the binary solutions can be summed according to the relative compositions, viz.

$$\Delta f(n)_{\text{mix}} = \sum_i \Delta f(n)_i \quad (29)$$

with $\Delta f(n)_i$ being calculated from Table V using the appropriate concentrations of each component. For sea water, the agreement with the direct experimental data was good, the maximum difference, at a 4% solute concentration, being 4×10^{-5} .¹⁷ Values of the refractive index calculated from the summed binary data and from the sea water data were, consequently, also in good agreement. At the highest concentration the difference in n was 1×10^{-4} . These results indicate that the equation outlined above

should be useful for estimating the refractive index of mixtures of salts. The relative insensitivity of the parameters of eq 17, 28, and 29^{2,10,18} to pressure is of particular note. This means that refractive index values can be predicted for the mixed salt solutions at pressures up to 1000 bars along the lines given in this section, the only change being that eq 2, with p equal to the total applied pressure instead of 1 bar, should be used.

It should be pointed out that B^* features in all the equations for density (or specific volume) and its derivatives, as developed from the TTG model (section 2). Since B^* for multicomponent systems can be estimated from the binary solution data, it follows that many other properties of the system, apart from n , can be estimated in this way.

9. Changes with Temperature

Finally, the effect of temperature will be discussed briefly. As noted in section 4, the value of ψ^* appears to be independent of temperature over the range 0–70 °C.¹ Since the values of ϕ_v^0 and s_v are available for most of the alkali halides at 0 °C, the corresponding values of $M\psi_s$ can be estimated from eq 12 taking the value of Ψ as 0.64. The estimated values are shown in Table IX (supplementary material). The variation with temperature is small (generally less than 1 cm³). A general quantitative indication of the effect can be gauged by noting some ionic results for sea water.^{2,18} The effective pressure exerted by the solute in sea water increases by 56 bars for the range 20–0 °C. This change is reflected largely in ψ_w (since ψ_s changes little). Temperature effects therefore are largely absorbed into the $f(n)_w$ term. For sea water, the value of $\Delta f(n)$ decreases by only 3.8×10^{-4} in going from 20 to 0 °C (n increases by 15.3×10^{-4}).

The value of $\Delta f(n)$ is also relatively insensitive to changes in the wavelength. For sea water (3.5% solute) there is a decrease in $\Delta f(n)$ of 1.5×10^{-4} in going from λ 4050 to 7070 Å. The change in $f(n)_w$ with wavelength is given by eq 19, using the appropriate values of A , B , and C .^{2,18}

10. Conclusions

The above analysis of the refractive index of binary solutions serves to illustrate the usefulness of the Tait-Gibson equation. Other properties of solutions can be treated in a similar way.² The TTG model may be most closely compared with a model that interprets solution behavior in terms of the properties of the solvent molecule (in the solution) and crystal data for the solute⁷ (see section 2).

The data presented in Tables V and VI should be useful for estimating the refractive index of mixed salt solutions at moderate concentrations. These data refer to a wavelength of 5893 Å (Na D line); however, $\Delta f(n)$ is relatively insensitive to changes in wavelength, while changes in $f(n)_w$ are accounted for by the changes in the parameters A , B , and C .²

Since A , B , C , and $\Delta f(n)$ are insensitive to pressure changes up to 1000 bars or so, and changes in ψ_w with pressure are given in eq 2, the refractive index can be estimated for this pressure range, without any additional assumptions.

The results for sea water¹⁷ indicate that the Tait-Gibson parameter, B^* , can be estimated from binary solution data and the mixing effect appears negligible. The latter result may, however, not be generally true. Further studies on multicomponent systems would be useful since B^* can be used to predict many solution properties on the basis of the TTG model.

Acknowledgment. We thank the Australian Research Grants Committee for financial assistance.

Supplementary Material Available: Calculated values of b_1 (Table VII), calculated values of n (Table VIII), and estimated values of $M\psi_s$ (Table IX) (4 pages). Ordering information is available on any current masthead page.

References and Notes

- (1) H. S. Harned and B. B. Owen, "The Physical Chemistry of Electrolytic Solutions", Reinhold, New York, N.Y., 1958.
- (2) J. V. Leyendekkers, "Thermodynamics of Seawater as a Multicomponent Electrolyte Solution", Part I, Marcel Dekker, New York, N.Y., 1976.
- (3) R. E. Gibson, *J. Am. Chem. Soc.*, **56**, 4 (1934); **57**, 284 (1935).
- (4) J. Padova, *J. Chem. Phys.*, **40**, 691 (1964).
- (5) A. F. Scott, *J. Phys. Chem.*, **35**, 3379 (1931).
- (6) R. E. Gibson, *Am. J. Sci.*, [5], **35A**, 49 (1938).
- (7) E. A. Moelwyn-Hughes, "Physical Chemistry", Pergamon Press, London, 1961.
- (8) G. N. Lewis and M. Randall, "Thermodynamics", revised by K. S. Pitzer and L. Brewer, McGraw-Hill, New York, N.Y., 1961.
- (9) R. G. Parsons, "Handbook of Electrochemical Constants", Butterworths, London, 1959.
- (10) H. Eisenberg, *J. Chem. Phys.*, **43**, 3887 (1965).
- (11) K. F. Herzfeld and K. L. Wolf, *Ann. Phys.*, [4], **78**, 35, 195 (1925).
- (12) "Handbook of Chemistry and Physics", Chemical Rubber Publishing Co., Cleveland, Ohio, 1971–1972.
- (13) J. Lumsden, "Thermodynamics of Molten Salt Mixtures", Academic Press, London, 1966.
- (14) G. J. Janz, "Molten Salts Handbook", Academic Press, New York, N.Y., 1967.
- (15) A. Heydweiller, *Phys. Z.*, **26**, 526 (1925).
- (16) L. W. Tilton, *J. Res. Natl. Bur. Stand.*, **14**, 393 (1935).
- (17) J. V. Leyendekkers and R. J. Hunter, *Mar. Chem.*, submitted for publication.
- (18) J. V. Leyendekkers, *Mar. Chem.*, **5**, 32 (1977).

Studies of Matrix Isolated Uranium Tetrafluoride and Its Interactions with Frozen Gases

K. R. Kunze, R. H. Hauge, D. Hamill, and J. L. Margrave*

Chemistry Department, Rice University, Houston, Texas 77001 (Received June 25, 1976; Revised Manuscript Received September 16, 1976)

Publication costs assisted by the National Science Foundation and the Robert A. Welch Foundation

The infrared spectra of UF_4 were recorded in matrices of neon, argon, krypton, xenon, oxygen, nitrogen, nitric oxide, and carbon monoxide. These data support a tetrahedral structure for UF_4 in the gas phase. Nitrogen and carbon monoxide doped argon matrices were studied as well as a fluorine doped nitrogen matrix.

Introduction

The infrared spectra of uranium tetrafluoride have been recorded in several different frozen gas matrices for the purpose of examining matrix interactions and collecting data relevant to a structure discussion. UF_4 , though considerably less volatile than UF_6 , can be sublimed in sufficient quantity at 500–1000 °C to give observable amounts in the matrix. The vapor pressure of UF_4 as a function of temperature is given by the following expression which holds in the range of 555–1007 °C:¹

$$\log P_{\text{mm}} = 28.539 - (16504.9/T) - 4.876 \log T$$

In addition, the reactivity of UF_4 toward fluorine which has been previously examined in argon matrices is shown to be quite different in nitrogen matrices.

Experimental Section

The matrix isolation apparatus used has been previously described.² Depleted UF_4 of 98% reported purity was used as obtained from Research Organic/Inorganic Chemical Corp. Research grade neon, argon, krypton, xenon, oxygen, nitrogen, carbon monoxide, and nitric oxide obtained from Matheson were used as matrix materials. Technical grade fluorine was obtained from Air Products Corp.

UF_4 was vaporized from a resistively heated tantalum furnace with a graphite liner and directed toward a cold copper surface where condensation occurred. Furnace temperatures were monitored using platinum–platinum–10% rhodium or chromel–alumel thermocouples; matrix temperatures were determined by using a carbon resistor. Matrix gas pressures were controlled using needle valves. The following conditions were used for trappings in unmixed matrices: neon, UF_4 temperature 638 °C, pressure $\sim 10^{-5}$ mmHg, 1 h; argon, UF_4 640 °C, pressure 2.5×10^{-5} mmHg, 1 h; krypton, UF_4 670 °C, pressure 3.0×10^{-5} mmHg, 1 h; xenon, UF_4 655 °C, pressure 3.5×10^{-5} mmHg, 1 h; oxygen, UF_4 647 °C, pressure 0.9×10^{-5} mmHg; nitrogen, UF_4 638 °C, pressure 1.2×10^{-5} mmHg, 1 h; carbon monoxide, UF_4 635 °C, pressure 1.5×10^{-5} mmHg, 1 h; nitric oxide, UF_4 651 °C, pressure $\sim 10^{-5}$ mmHg, 1 h. Mixtures of 1/50 N_2/Ar and CO/Ar were condensed for 1 h at 2.5×10^{-5} mmHg with UF_4 which was vaporized at 728 °C. All of the above procedures were followed by infrared scanning and annealing cycles. Each annealing was done at 30 K for periods of 4–6 min.

Experiments with UF_4 in F_2/N_2 matrices were performed using premixed F_2/N_2 ratios of 1/100, 1/10, and 1/1 which were introduced to the matrix chamber at a pressure of 2.0×10^{-5} mmHg. To eliminate the possibility of F_2 dissociation on the hot furnace surfaces, an exterior tube furnace with a hot surface more remote to the matrix chamber was used. UF_4 temperatures were kept at 835 °C

to ensure a sufficient supply of material to the matrix. After no difference was noted, the interior UF_4 furnace was again used for F_2/N_2 photolysis and annealing experiments in which 1/100 F_2/N_2 matrices were deposited at 2.0×10^{-5} mmHg with UF_4 vaporized at 755 °C. Photolysis after deposition was carried out using broad band radiation from a Hanovia xenon lamp. A filter of water in a container with quartz windows removed the infrared component of the radiation and prevented uncontrollable heating of the matrix.

The matrix gases were passed through a liquid nitrogen trap in all experiments except those in which pure NO and xenon matrices were used, in which cases a dry ice–acetone trap was substituted. All trappings were done at 12 K except the one in which neon was the matrix material, when a temperature of 5.2 K was maintained.

Results and Discussion

To date, the structure of the isolated UF_4 molecule has not been conclusively resolved. Gas phase electron diffraction studies³ have failed to establish a structure for UF_4 unambiguously while similar methods have shown the gas phase UBr_4 structure to be a distorted tetrahedron of C_{2v} symmetry.⁴ Previous workers have reported the infrared and Raman spectra of crystalline UF_4 and have suggested a tetrahedral structure based on their data.⁵ However, the broadness of their bands reflects lattice interactions of UF_4 in a structure in which uranium is eightfold coordinated⁶ and not present as isolated molecules. The possibility of concealed bands must also be considered.

The matrix spectra of UF_4 at various stages of annealing in neon, argon, krypton, oxygen, and nitrogen are shown in Figures 1a–c and 2a,b. A multiplicity of bands can be seen in each matrix which appears to suggest a nontetrahedral structure. However, careful examination of the spectra recorded upon successive annealing indicates that all of the bands exhibit independent behavior and probably owe their appearance to a variety of matrix sites. Annealing each matrix had the following effects: Neon; a prominent band at 544.5 cm^{-1} disappears while one grows in at 525.5 cm^{-1} . Those at 538.5 , 536.5 , and 532.2 cm^{-1} intensify. The 548.0 cm^{-1} band develops a shoulder. Argon; a band at 524.9 cm^{-1} grows in while those at 526.8 , 532.3 , and 537.5 cm^{-1} shrink. Krypton; bands at 522.7 and 529.5 cm^{-1} grow. Xenon; 519.9 , 523.3 , and 528.8 cm^{-1} disappear, 518.4 and 525.3 cm^{-1} appear. Oxygen; 522.4 , 527.9 , and 536.5 cm^{-1} grow as one at 540.5 cm^{-1} appears. Nitrogen; 506.3 , 509.6 , and 522.6 cm^{-1} grow, 511.3 and 518.8 cm^{-1} shrink. Deposition of UF_4 in a carbon monoxide matrix followed by alternate scanning and annealing produced the spectra of Figure 2c. Annealing caused the growth of a second band at 500.9 cm^{-1} , while a third at 488 cm^{-1} is believed to reflect either polymeric UF_4 or crys-

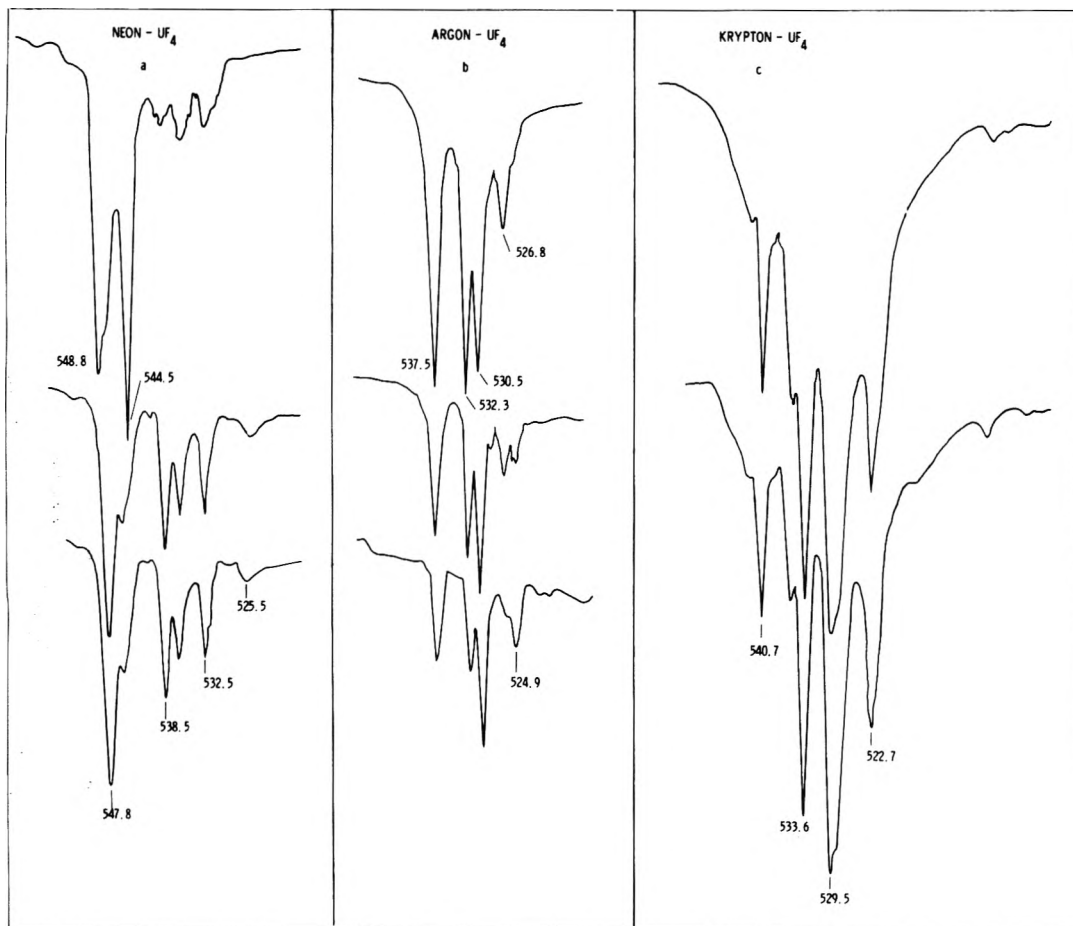


Figure 1. Infrared spectra of UF_4 in neon, argon, and krypton matrices, before and after annealing (top to bottom).

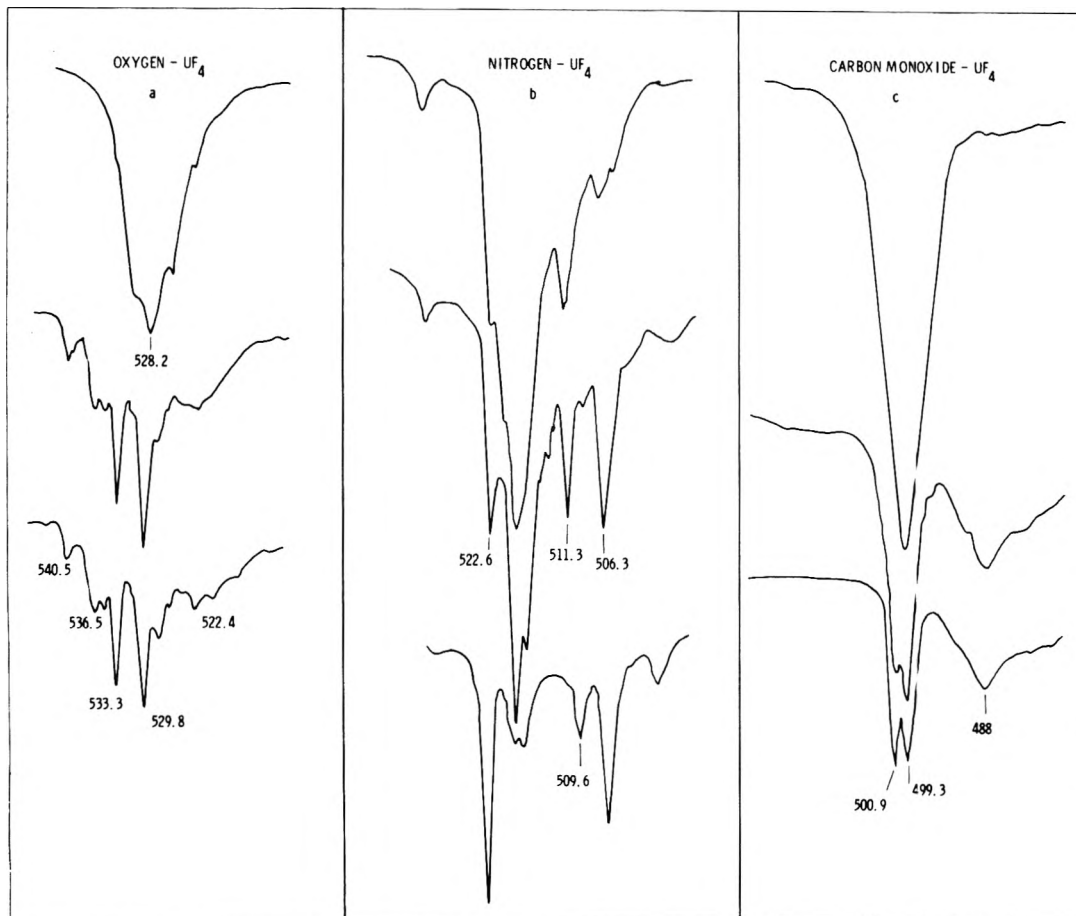


Figure 2. Infrared spectra of UF_4 in oxygen, nitrogen, and carbon monoxide matrices before and after annealing (top to bottom).

TABLE I: Correlation of UF_4 Bands (cm^{-1}) in Rare Gas Matrices

Neon	Argon	Krypton	Xenon
		540.7	536.3
548.8	537.5	533.6	528.8
544.5			
538.5	532.3	529.5	523.3
536.5	530.5	522.7	519.9
532.5	526.8		512.9
	524.9		

talline UF_4 . The presence of only two sites in this matrix contrasts to the greater variety found in the aforementioned matrices and may be attributable to a greater interaction of CO such that a smaller number of sites are energetically allowed. Evidence of a greater interaction was observed in dilute CO/Ar matrices and will be discussed below. UF_4 in NO shows a very broad band at 492 cm^{-1} which does not appreciably sharpen upon annealing. The fact that this frequency is lower than that found in a CO matrix may be due to the free radical nature of NO.

These observations lend support to either a tetrahedral (T_d) or square planar (D_{4h}) structure for gas phase UF_4 , the former being favored for steric reasons and by analogy to UBr_4 .^{4,7} As an aside, satisfactory interpretation of the gas phase UCl_4 electronic spectrum⁸ and the infrared and electronic spectra of matrix isolated UCl_4 and UBr_4 ⁷ suggest that a negligible error is incurred by disregarding deviation from tetrahedral symmetry. Thermodynamic functions of UF_4 calculated from an assumed tetrahedral model are estimated to have an error on the order of 1% by analogy to calculations on SF_4 .⁹

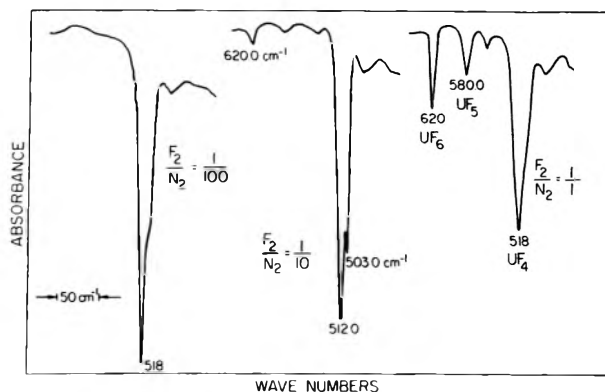
On the basis of their similar appearance, a correlation of bands in the rare gas matrices is suggested in Table I in which the correlated bands may correspond to UF_4 molecules in similar sites. The matrix red shifts follow the expected order, with neon as the least interactive medium causing the least shift, and nitrogen causing the greatest. Whereas solid state UF_4 spectra have half-widths of $50\text{--}100\text{ cm}^{-1}$, matrix isolated spectral bands measure 1.5 cm^{-1} half-width at half-height.

UF_4 in a $1/50\text{ N}_2/\text{Ar}$ doped matrix gave rise to new bands at $509.6, 515.3, 518.5, 523.0, 529.3,$ and 535.0 cm^{-1} and possibly some concealed or too weak to detect. Those at $509.6, 518.5,$ and 523.0 cm^{-1} apparently correspond to bands located at nearly the same positions in pure N_2 . Annealing changes the spectrum in a manner which suggests the stepwise introduction of N_2 into the UF_4 coordination sphere, although specific assignments are difficult. It can be suggested that the band at 535.0 cm^{-1} is one of those attributable to coordination of one molecule of N_2 to UF_4 with a resulting red shift of 2.5 cm^{-1} of the absorption at 537.5 cm^{-1} . This is a smaller shift than might be expected on the basis of the large shift seen in a pure nitrogen matrix. The band at 535.0 cm^{-1} may arise from activation of an argon band which correlates with those in krypton and xenon at 540.7 and 536.3 cm^{-1} , respectively, and would lie higher than 537.5 cm^{-1} . A proposed correlation of bands representing similar sites is given in Table II, in which correlated bands would have shifted by $8\text{--}10\text{ cm}^{-1}$. This would then put the original position of the activated band near 544 cm^{-1} .

An independent intensification of the $1/50\text{ CO/Ar}$ peaks upon annealing suggests behavior analogous to that displayed in pure argon matrices. The proposed correlation of bands in Table II for the CO doped system has the shifts from the argon positions ranging from 14 to 18 cm^{-1} , greater than those for the N_2 systems, indicating a greater interaction. If the unusual intensity of the 526.8 cm^{-1} band

TABLE II: Correlation of Matrix Site Bands (cm^{-1}) for $1/50\text{ N}_2$ and CO Doped Argon Matrices

Argon	N_2/Ar	CO/Ar
544 (postulated)	535.0	526
537.5	529.3	520.0
532.3		
530.5	520.5	517.0
526.8	516.0	510.8

Figure 3. Trappings of UF_4 with various mole fractions of F_2/N_2 in N_2 .

is attributed to a hidden adsorption of an activated argon site, as was proposed for the N_2 case, the activated band would again have shifted from the 544 cm^{-1} region, on the basis of the above shifts. A broad band at 499.8 cm^{-1} which grows in corresponds to one found at 500.3 cm^{-1} in the pure CO matrix and is assigned to UF_4 coordinatively saturated by CO. A peak at 534.5 cm^{-1} which appears upon annealing resembles the one found in the nitrogen doped matrix and is probably due to contamination by nitrogen.

Corresponding to the red-shifted UF_4 bands a blue-shifted CO band or band envelope appears centered at 2184.2 cm^{-1} prior to annealing and 2181.8 cm^{-1} following annealing. An interaction of CO consisting primarily of σ electron donation can be expected to show this type of behavior. Removal of electrons from the slightly antibonding 5σ orbital has the effect of increasing the bond strength and hence the frequency.¹⁰ The corresponding partial reduction of the metal results in a decrease in the U-F frequencies. This effect can be seen in CO adducts of PbF_2 and SnF_2 ^{10,11} and is believed to occur as a result of electron withdrawal from the metal by X groups. The opposite effect of a red shift is observed from the condensation of metal vapors with CO,¹² where π back-bonding is considerably more important. This effect has been reported for the complexation of U metal vapors by CO.¹³ π back-bonding into the CO orbitals would have the effect of shifting the CO bands to lower frequency. The observed shift of 45.2 cm^{-1} in this work is within the range reported for NiF_x ¹¹ and $PbCl_2$ ¹⁰ adducts, 62 and 36 cm^{-1} , respectively. These results can be interpreted as arising from a σ interaction, with any π interactions negligible or nonexistent.

Although conclusive evidence concerning the mode of coordination of the CO is not available, it is felt that the carbon side of the CO molecule coordinates to the metal. As has been previously pointed out,¹⁰ donation is more likely to occur from the less electronegative portion of the molecule.

The reaction of UF_4 with fluorine in argon has been reported previously¹⁴ and found to occur with essentially zero activation energy. Further experiments with matrices of fluorine in nitrogen indicate that coordination of UF_4 by nitrogen provides a significant barrier to matrix fluorination of UF_4 . Reaction of the UF_4 is essentially

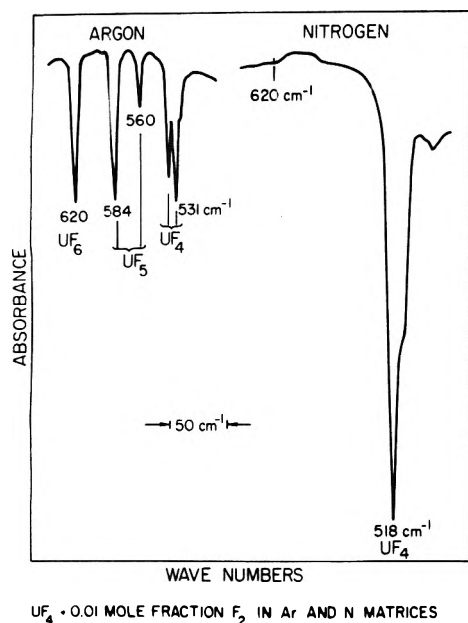


Figure 4. Reactivity of UF_4 in F_2/Ar and F_2/N_2 matrices.

quenched at 1/100 F_2/N_2 concentrations. Extent of reaction increases, as evidenced by growth of UF_6 and UF_5 bands at 620, 584, and 560 cm^{-1} , as the concentration is increased at 50% fluorine (Figure 3). Figure 4 dramatizes the inhibiting effect of nitrogen as compared to argon, for a 0.01 mole fraction matrix concentration of fluorine, where extensive reaction has occurred in the argon matrix, and none in the nitrogen matrix.

Successive annealing of UF_4 in a 0.01 F_2/N_2 matrix failed to promote reaction. However, photolysis of an identical

matrix using broad band radiation from a xenon lamp caused reaction of the UF_4 to UF_5 and UF_6 as evidenced by growth of bands characteristic of these species. Activation of UF_4 and cleavage of fluorine molecules to yield radicals is probably responsible for the observed reaction. The inhibiting action shown by the nitrogen matrix reflects the more interactive nature of this matrix. CO , which is more interactive, probably would inhibit reaction to an even greater extent.

Acknowledgment. This work has been financially supported by the National Science Foundation and by the Robert A. Welch Foundation. Helium was provided by the U.S. Office of Naval Research.

References and Notes

- (1) E. G. Chudinov and D. Ya. Choporov, *Zh. Fiz. Khim.*, **44**, 1955 (1970).
- (2) J. W. Hastie, R. H. Hauge, and J. L. Margrave, *High Temp. Sci.*, **1**, 76 (1969).
- (3) Yu. S. Ezhov, P. A. Akishin, and N. G. Rambidi, *Zh. Struct. Khim.*, **10**, 571 (1969).
- (4) N. G. Rambidi, R. A. Akishin, and E. G. Zazorin, *Russ. J. Phys. Chem.*, **35**, 575 (1961).
- (5) W. Krasser and H. W. Nunnberg, *Spectrochim. Acta, Part A*, **26**, 1059 (1970).
- (6) A. C. Lanson, R. B. Roof, Jr., and D. T. Cromer, *Acta Crystallogr.*, **17**, 555 (1964).
- (7) J. R. Clifton, D. M. Gruen, and A. Ron, *J. Chem. Phys.*, **51**, 224 (1969).
- (8) J. B. Gruber and H. G. Hecht, *J. Chem. Phys.*, **59**, 1713 (1973).
- (9) Y. N. Tumanov, *Russ. J. Inorg. Chem.*, **13**, 782 (1968).
- (10) D. Tevault and K. Nakamoto, *Inorg. Chem.*, **15**, 1282 (1976).
- (11) C. W. DeKock and D. A. VanLeirsburg, *J. Am. Chem. Soc.*, **94**, 3235 (1972).
- (12) G. A. Ozin and A. VanderVoet, *Prog. Inorg. Chem.*, **19** (1975).
- (13) J. L. Slater, R. K. Shelline, K. C. Lin, and W. Weltner, Jr., *J. Chem. Phys.*, **55**, 5129 (1971).
- (14) K. R. Kunze, R. H. Hauge, D. Hamill, and J. L. Margrave, *J. Chem. Phys.*, **65**, 2026 (1976).
- (15) R. T. Paine, R. S. McDowell, L. B. Asprey, and L. H. Jones, *J. Chem. Phys.*, **64**, 3081 (1976).

Low Resolution Microwave Spectroscopy. 7. Conformational Isomers, Energies, and Spectral Intensity Anomalies of Neopentyl Esters

Nancy S. True and Rober K. Bohn*

Department of Chemistry and Institute of Materials Science, The University of Connecticut, Storrs, Connecticut 06268 (Received March 4, 1977)

Publication costs assisted by the University of Connecticut Research Foundation

Low resolution microwave spectra of neopentyl formate, cyanofornate, fluorofornate, and chlorofornate display band series from two conformational forms designated extended and intermediate. The extended forms are characterized by $B + C$ values of 2195.1(5), 1293.4(3), 1625.0(5), and 1250(2) (^{35}Cl) MHz for the formate, cyanofornate, fluorofornate, and chlorofornate, respectively. At $\sim -63^\circ C$, the intermediate forms are characterized by $B + C$ values of 2327.4(5), 1337.1(2), 1703.0(6), and 1308.2(2) (1282.2(3) (^{37}Cl) MHz for the formate, cyanofornate, fluorofornate, and chlorofornate, respectively. For each compound the extended species is consistent with a syn-anti [$\tau_1(OCOC) = 0^\circ$, $\tau_2(COCC) = 180^\circ$] heavy atom planar structure and the intermediate species is consistent with a gauche-gauche [$\tau_1(OCOC) \sim 80^\circ$, $\tau_2(COCC) \sim 210^\circ$] structure. In each case, the bands of the higher energy (~ 1.5 to 3 kcal/mol) intermediate conformer are anomalously intense, paralleling previous findings for ethyl, propargyl, and n -propyl esters.

Introduction

Low resolution microwave (LRMW) spectra of primary esters¹⁻³ have demonstrated three stable rotamers in the conformation space defined by the carbonyl carbon to ether oxygen torsion [$\tau_1(OCOC)$] and the ether oxygen to alkyl carbon torsion [$\tau_2(COCC)$]. Observed conformers are

displayed and torsional angles are defined in Figure 1. Table I summarizes results of LRMW studies of ethyl, propargyl, and n -propyl esters. Extended (E: $\tau_1 = 0^\circ$, $\tau_2 = 180^\circ$) and compact (C: $\tau_1 = 0^\circ$, $\tau_2 \sim 90^\circ$) conformers have been observed in every ethyl, propargyl, and n -propyl ester studied except the formates. The compact forms of

TABLE I: Observed Conformers of Primary Esters, XCO₂R

R =	Ethyl	Propargyl	<i>n</i> -Propyl ^a
Formate (X = H)	E, C ^b	E ^c	EA, EG
Fluoroformate (X = F)	E, C ^d	E, C ^e	EA, EG, CA, CG
Chloroformate (X = Cl)	E, C, I ^f	E, C ^e	EA, EG, CA
Cyanoformate (X = CN)	E, C, I ^f	E, C, I ^e	EA, EG, CA, IA, IG
Trifluoroacetate (X = CF ₃)	E, C, I ^f	E, C, I ^e	EA, EG, CA, CG, IA

^a Reference 1. The second letter of the label refers to an anti (A) or gauche (G) configuration about $\tau_3(\text{OCCC})$. ^b Reference 6. ^c G. I. L. Jones, D. G. Lister, and N. L. Owen, *J. Chem. Soc., Faraday Trans. 2*, 71, 1330 (1975). Two conformers are reported for the liquid phase. ^d Reference 7. ^e Reference 2. ^f Reference 3.

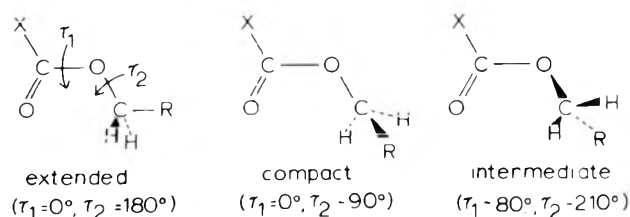


Figure 1. Conformers of neopentyl (R = C(CH₃)₃), ethyl (R = CH₃), propargyl (R = C≡CH), and *n*-propyl (R = CH₂CH₃) esters.

propargyl and *n*-propyl formates are predicted to have a axis dipole moment components which are too small to display LRMW band spectra. Ethyl chloroformate, cyanoformate, and trifluoroacetate additionally display intermediate (I: $\tau_1 \sim 45^\circ, \tau_2 \sim 240^\circ$) conformers. Intermediate conformers are also present in propargyl (R = C≡CH, Figure 1) cyanoformate and trifluoroacetate ($\tau_1 \sim 60^\circ, \tau_2 \sim 230^\circ$). The extended and compact conformers of each ester have approximately equal stability and the intermediate conformer is ca. 1.5–2 kcal/mol higher in energy. The LRMW band spectra of esters displaying the intermediate conformer show amazing intensity anomalies. In trifluoroacetate esters, the E:C:I intensity ratio at 25 °C is 1:0.8:20 for ethyl trifluoroacetate and 1:2:7 for propargyl trifluoroacetate. Similarly, bands of the intermediate conformer of *n*-propyl trifluoroacetate dominate the spectrum at room temperature. In contrast, the expected E:C:I intensity ratio at 25 °C is about 1:2:0.07 for each trifluoroacetate ester based on the relative energies: 0, 0, and 2 kcal/mol, respectively. Thus the band spectrum of the intermediate conformer of ethyl trifluoroacetate is 280 times as intense as expected. Similar but less dramatic results were obtained for ethyl, propargyl, and *n*-propyl cyanoformate.

This study of neopentyl (2,2-dimethylpropyl) cyanoformate, formate, fluoroformate, chloroformate, and trifluoroacetate was undertaken to identify and characterize the conformational isomers of neopentyl esters, determine their relative energies, and further explore the intensity anomalies observed in LRMW spectra of esters.

Experimental Section

All microwave measurements were made on Hewlett-Packard Model 8460 A microwave spectrometers. K band spectra (18–26.5 GHz) of neopentyl fluoroformate and cyanoformate and R band spectra (26.5–40 GHz) of neopentyl formate and chloroformate were recorded at both 25 and ~ -63 °C. R band spectra of neopentyl cyanoformate and fluoroformate were recorded at ~ -63 °C. A K band spectrum of neopentyl trifluoroacetate was recorded at 25 °C. In all cases the scan rate was 10 MHz/s with a time constant of 1 s. The detector crystal current was 150 μ A and the Stark voltage was 3200 V/cm. Samples were distilled into the waveguide to pressures of 30–70 mTorr. Frequency measurements are frequencies of the band maxima averaged over forward and reverse scans. Frequency accuracy is dependent on the shape and

width of the bands and ranges from about 50 to 5 MHz for the samples studied.

Neopentyl esters were synthesized using previously reported methods.^{1,4,5} They were characterized by their infrared and ¹H NMR spectra. The purity of each was estimated to be in excess of 98% by gas-liquid chromatography on a 6 ft SE-30 column with 5–10-min retention times.

Results

Neopentyl Cyanoformate. Condensed survey low resolution microwave K-band spectra of neopentyl cyanoformate at 25 and ~ -63 °C are shown in Figure 2. One a-type band series is present at 25 °C. When the sample is cooled to ~ -63 °C a second a-type series appears. Values of *B* + *C* at ~ -63 °C are 1292.4(3) and 1337.1(2) MHz for the weak and strong series, respectively. The band frequencies of the strong series shift slightly with temperature and *B* + *C* is 1338.8(2) MHz for this series at 25 °C. Based on the similarity to ethyl and propargyl esters the weak and strong series are designated extended and intermediate, respectively.

The relative intensity of the extended series increases with decreasing temperature and is therefore the more stable form of the molecule even though the relative intensity ratio E:I is 1:15 at ~ -63 °C. The energy of the intermediate species is estimated to be at least 2 kcal/mol higher than that of the extended species, assuming the intensity of the extended conformer is equal to the spectral noise level at 25 °C. Bands of the intermediate conformer are smooth, structureless, and approximately 300 MHz wide. Bands of the extended conformer are approximately 150 MHz wide.

Neopentyl Formate. Two a-type band series are present in the R-band spectra of neopentyl formate at 25 and ~ -63 °C. The LRMW rotational constant, *B* + *C*, for the extended form is 2195.1(5) MHz and for the intermediate form it is 2329.5(5) MHz at 25 °C and 2327.4(5) MHz at ~ -63 °C, respectively. The intermediate form of the molecule is 3(1) kcal/mol higher in energy than the extended form.

Figure 3 shows the *J* + 1 \leftarrow *J*, 14 \leftarrow 13, and 13 \leftarrow 12 pileups for the extended and intermediate species at ~ -63 °C. The extended series displays repeating resolvable fine structure on the high frequency side of each main band which we interpret as vibrational satellite bands. *B* + *C* values for the *v* = 1 to *v* = 4 vibrational levels are 2203.9(5), 2210.3(5), 2218.1(5), and 2228.4(5) MHz, respectively. The nearly linear dependence of *B* + *C* on the vibrational quantum number indicates that these satellite bands arise from a single vibrational mode. Most likely, this mode is the *O*-alkyl [$\tau_2(\text{COCC})$] torsion, based on analogy with the corresponding satellite patterns of the extended conformers of ethyl formate⁶ and ethyl fluoroformate.⁷ No estimate of the torsional frequency from intensity ratios can be made due to severe Stark lobe interference.

Bands of the intermediate conformer of neopentyl formate are approximately 250 MHz wide in contrast to

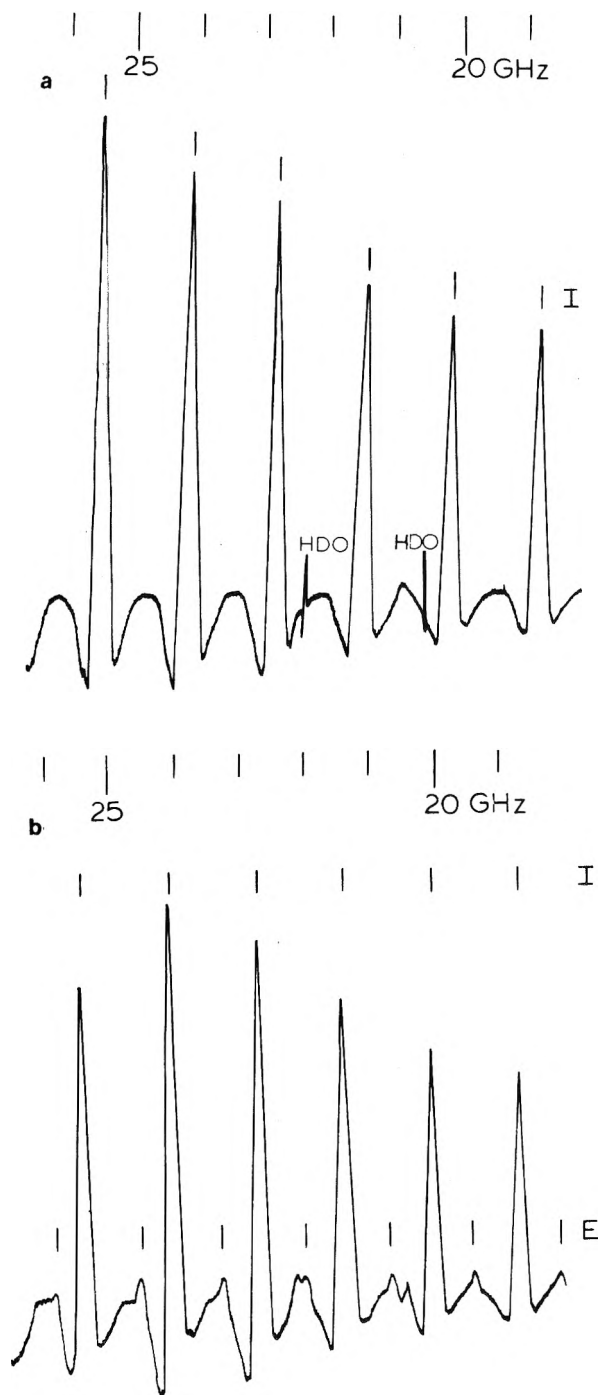


Figure 2. Condensed survey LRMW spectra of neopentyl cyanoformate. (a) K band spectrum from 18 to 28.5 GHz at 25 °C scanned at 10 MHz/s with a 1-s time constant. The band markers are calculated from $(J + 1)(B + C) = 1292.4$ and 1338.8 for the extended (E) and intermediate (I) species, respectively. (b) same as (a) except temperature is ca. -63 °C.

those of the extended species which are approximately 100 MHz wide.

Neopentyl Fluoroformate. LRMW K band spectra of neopentyl fluoroformate display a-type band series of two conformational forms. One band series with a $B + C$ value of 1704.5(3) MHz (1703.0(6) at ~ -63 °C) designated I dominates the spectrum at both 25 and ~ -63 °C. A much weaker series with a $B + C$ value of 1624.9(4), designated E, is also present at both temperatures. At 25 °C the relative intensity ratio, E:I, is 1:15 and at ~ -63 °C it is 1:5 indicating that the extended conformer is the more stable form of the molecule. Bands of the intermediate conformer are broad (approximately 200 MHz) and

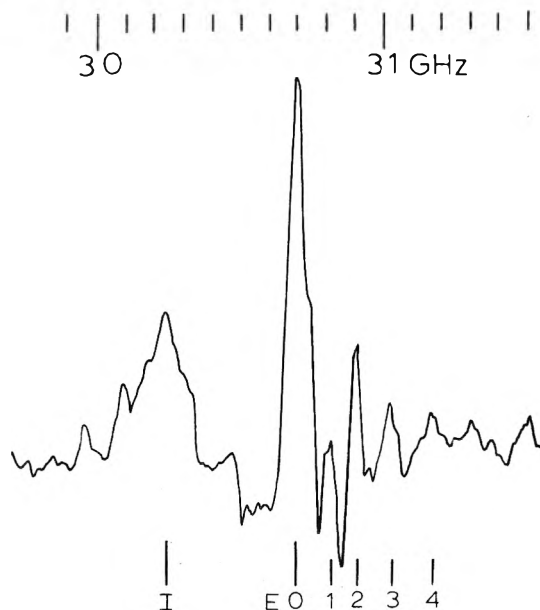


Figure 3. Condensed survey LRMW spectrum of neopentyl formate from 30 to 31.5 GHz recorded at -63 °C. The bands correspond to the $J + 1 \leftarrow J$, $14 \leftarrow 13$, and $13 \leftarrow 12$ transitions of the extended (E) and intermediate (I) conformers. Vibrational quantum numbers label the satellites of the compact band.

TABLE II: Summary of LRMW Spectral Data of Neopentyl Esters, $XCO_2CH_2C(CH_3)_3$

X	B + C, MHz	
	Extended form (E)	Intermediate form (I)
H $\nu = 0$	2195.1(5)	2327.4(5)
$\nu = 1$	2203.9(5)	
$\nu = 2$	2210.3(5)	
$\nu = 3$	2218.1(5)	
$\nu = 4$	2228.4(5)	
F	1625.0(5)	1703.0(6)
$^{35}Cl/^{37}Cl$	1250(2)/	1208.2(2)/1282.2(3)
CN	1292.4(3)	1337.1(2)
CF ₃		884(2)

structureless in contrast to those of the extended conformer which are narrow (approximately 100 MHz) and structured.

Neopentyl Chloroformate. Neopentyl chloroformate produces two LRMW band series at 25 °C with $B + C$ values of 1309.6(2) and 1283.6(2) MHz. These series are consistent with one conformational form displaying resolved isotopic species. At ~ -63 °C the $B + C$ values are 1308.2(2) and 1282.2(3) MHz for the ^{35}Cl and ^{37}Cl species, respectively. The bands are wide (~ 300 MHz) and structureless. Based on analogy with neopentyl formate, cyanoformate, and fluoroformate the corresponding conformer is designated intermediate. A few narrow, weak bands consistent with a series having a $B + C$ value of 1250(2) MHz appear at ~ -63 °C. This series is designated extended. Most bands in this series are calculated to be overlapped by bands of the more intense intermediate form. The E:I intensity ratio at ~ -63 °C is 1:15.

Neopentyl Trifluoroacetate. A LRMW K band spectrum of neopentyl trifluoroacetate at 25 °C displayed one series of extremely wide (400–500 MHz) structureless bands consistent with a $B + C$ value of 884(2) MHz. The spectrum was not recorded at ~ -63 °C as the large band widths, the poor signal/noise ratio, and the small value of $B + C$ make observation of weak series with even smaller $B + C$ values unlikely.

A summary of LRMW spectral data of neopentyl esters is presented in Table II.

TABLE III: Intensity Ratios of LRMW Band Spectra of Esters, XCO_2R , Intermediate/Extended at Room Temperature

X	R = $-CH_2CH_3$	$-CH_2C\equiv CH$	$-CH_2CH_2CH_3^a$	$-CH_2C(CH_3)_3$
H	0		0	6
F	0	0	0	15
Cl	0.8	0	0	> 25
CN	3	3.6	7	> 30
CF ₃	20	7	~ 10	Large

^a The conformers with an anti configuration about $\tau_3(OCCC)$ are used in this table.

Discussion

For each molecule, values of $B + C$ were calculated as a function of $\tau_1(OCCO)$ and $\tau_2(COCC)$, defined in Figure 1, using geometrical parameters reported for the corresponding ethyl formates.^{3,6} A C-C distance of 1.538 Å and tetrahedral bond angles for the *tert*-butyl group were used in these calculations. This geometry reproduces the experimental $B + C$ values of the extended syn-anti form of each neopentyl ester when $\tau_1(OCCO) = 0^\circ$ and $\tau_2(COCC) = 180^\circ$. To characterize the conformation of the intermediate form, $B + C$ values were calculated as a function of $\tau_1(OCCO)$ and $\tau_2(COCC)$. For neopentyl cyanofornate, results of these calculations are displayed in the contour diagram shown in Figure 4a. The calculated values of $B + C$ are indicated by the contours shown at 100-MHz intervals as function of the two torsional angles. The calculated values are accurate to about 2% due to uncertainties in the assumed structural parameters excepting torsional angles. This uncertainty has been arbitrarily assigned to the observed values for easy visualization and models consistent with 1293 ± 26 and 1338 ± 27 MHz are these lying within the hatched areas. The blank regions correspond to conformers calculated to be too asymmetric to be observable by LRMW spectroscopy.⁸

Similar surfaces were calculated for neopentyl fluoroformate, formate, chloroformate, and trifluoroacetate. The syn-anti [$\tau_1(OCCO) = 0^\circ$, $\tau_2(COCC) = 180^\circ$] structure has the smallest calculated value of $B + C$ and represents a minimum in the contour diagrams for neopentyl cyanofornate, fluoroformate, chloroformate, and trifluoroacetate. Surfaces for these four molecules have similar topography and the extended and intermediate conformers have $B + C$ values which are compatible with the same range of $\tau_1(OCCO)$ and $\tau_2(COCC)$. The minimum in the contour diagram of $B - C$ values of neopentyl formate, shown in Figure 4b, occurs at the anti-anti [$\tau_1(OCCO) = 180^\circ$, $\tau_2(COCC) = 180^\circ$] structure. The surface is qualitatively similar to that of the other neopentyl esters, but displaced 180° out of phase in the $\tau_1(OCCO)$ coordinate. Accordingly, the extended and intermediate conformers of neopentyl formate are compatible with a range of $\tau_1(OCCO)$ and $\tau_2(COCC)$ values very different from the other neopentyl esters studied. If we assume that the configuration of the intermediate conformer of each neopentyl ester is identical, one can superimpose Figure 4a for the cyanofornate and Figure 4b for the formate to determine points in τ_1 , τ_2 space which simultaneously match the observed $B + C$ values of the intermediate conformers of both compounds. These points are $\tau_1 \sim 0^\circ$, $\tau_2 \sim 140^\circ$ (or 220°) and $\tau_1 \sim 80^\circ$, $\tau_2 \sim 210^\circ$. The syn-gauche (0° , 140°) structure is not reasonable because it requires the potential energy as a function of τ_2 to have minima at 140 and 180° which are 2-3 kcal/mol different in energy. Such a wild undulation of the potential energy function is unreasonable. Therefore, as in the case of ethyl, propargyl, and *n*-propyl esters, the structure of the intermediate conformer is believed to be that which is farthest removed from the syn-anti form in the space of τ_1 and τ_2 and still has compatible $B + C$ values. The $\tau_1 \sim 80^\circ$, $\tau_2 \sim 210^\circ$

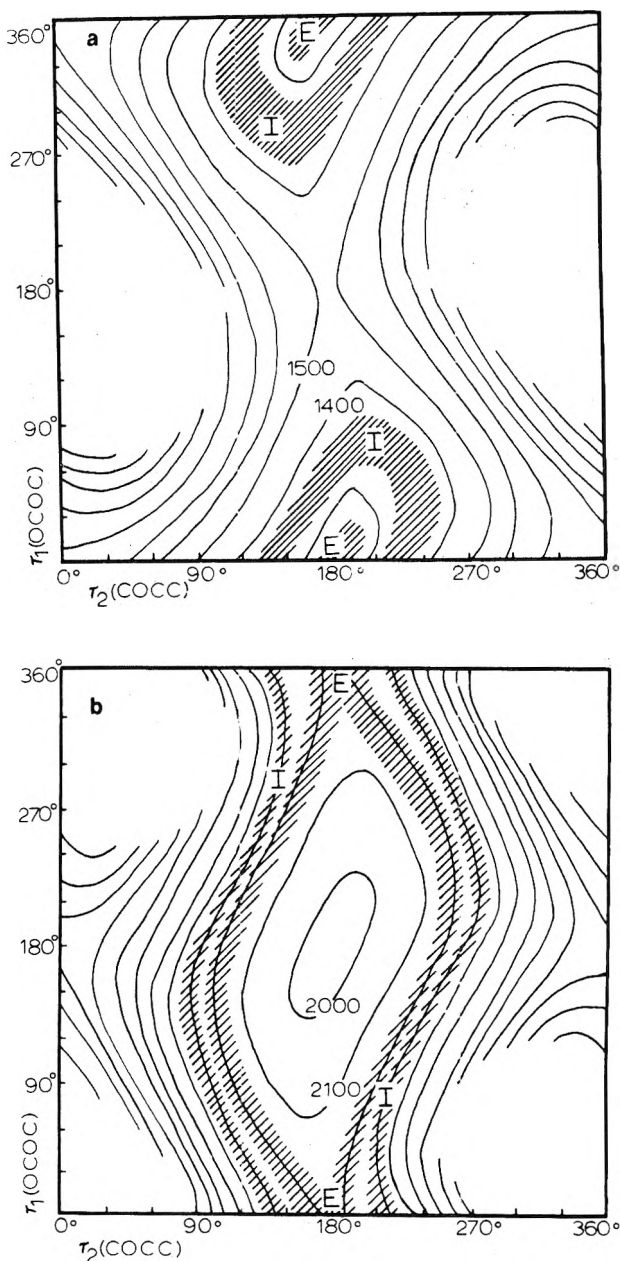


Figure 4. Contour diagrams of $B + C$ for neopentyl esters as a function of the torsional angles, $\tau_1(OCCO)$ and $\tau_2(COCC)$. The diagrams have centers of symmetry. The hatched regions cover those conformations consistent with the observed $B + C$ values. The labels E and I locate the most probable configurations of the extended and intermediate species, respectively. The blank regions correspond to models too asymmetric or nonpolar to produce LRMW band spectra and therefore unobservable by this technique: (a) neopentyl cyanofornate; (b) neopentyl formate.

structure is consistent with this argument.

Compact ($\tau_1 = 0$, $\tau_2 \sim 90^\circ$) conformers of neopentyl esters have not been observed indicating that the potential function around τ_2 in neopentyl esters is different from those of ethyl, propargyl, and *n*-propyl esters. This is reasonable since the *tert*-butyl group in neopentyl esters

is bulkier than the methyl, ethynyl, and ethyl groups occurring in comparable positions in the other esters which have been studied.

The anomalously high intensities of the LRMW spectral bands of intermediate conformers of neopentyl esters is a striking result of this study. Only the fluoroformate and formate spectra display detectable amounts of the more stable extended conformer at 25 °C. The extended form is ca. 1.5 and 3 kcal/mol lower in energy than the intermediate conformer for the fluoroformate and formate, respectively. The cyanofornate and chlorofornate spectra do not display detectable quantities of the more stable extended conformer at room temperature and even at ~-63 °C intermediate bands dominate the LRMW spectra of these molecules. For the extended and intermediate conformer of each neopentyl ester dipole moment and asymmetry differences are small and cannot account for the large intensity anomalies observed.

The intensity anomalies associated with the intermediate conformer of ethyl, propargyl, *n*-propyl, and neopentyl esters we have studied are summarized in Table III. The ratio of the room temperature LRMW band intensities of the intermediate to the extended form is shown for each ester studied. If the partition functions of each form were identical the intensity ratios would be approximately $2 \exp(-\Delta E/RT)$ or 0.16 to 0.01 for the ΔE range of 1.5 to 3 kcal/mol typical of these compounds. The intensity anomalies are largest for those esters with the more massive and complex acid and alcohol groups. We believe that the intensity of the intermediate bands arises from a large population due to a dense manifold of low-

lying excited vibrational states associated with a broad, shallow potential energy surface minimum at that configuration. Alternatively stated, the vibrational partition function of the intermediate conformer is much larger than that of the lower energy extended form. It is interesting to note that the only secondary esters characterized by LRMW spectroscopy, isopropyl esters,⁹ do not exhibit intermediate forms.

Acknowledgment. LRMW spectra were run on spectrometers at the University of Kansas, courtesy of Professor Marlin D. Harmony and NSF Grant MPS 74-22178, and Harvard University, courtesy of Professor E. Bright Wilson and NSF Grant GP-37066X. Support from The University of Connecticut Research Foundation is gratefully acknowledged.

Supplementary Material Available: Tables IV-VIII listing the band frequencies, $J + 1$ values, and $B + C$ values (6 pages). Ordering information is available on any current masthead page.

References and Notes

- (1) N. S. True and R. K. Bohn, submitted for publication.
- (2) N. S. True and R. K. Bohn, *J. Am. Chem. Soc.*, **99**, 3575 (1977).
- (3) N. S. True and R. K. Bohn, *J. Am. Chem. Soc.*, **98**, 1188 (1976).
- (4) S. Nakanishi, T. C. Meyers, and E. V. Jensen, *J. Am. Chem. Soc.*, **77**, 3099 (1955).
- (5) W. Glud, W. W. Nussler, and K. Keller, *Patentschrift*, 592539 (1934).
- (6) J. M. Riveros and E. B. Wilson, *J. Chem. Phys.*, **46**, 4605 (1967).
- (7) N. S. True and R. K. Bohn, 31st Symposium on Molecular Structure and Spectroscopy, Columbus Ohio, 1976, Abstract WB'1.
- (8) M. S. Farag and R. K. Bohn, *J. Chem. Phys.*, **62**, 3946 (1975).
- (9) N. S. True and R. K. Bohn, *J. Mol. Struct.*, **38**, 173 (1977).

Low Resolution Microwave Spectroscopy. 8. Rotational Isomers of Allyl Cyanofornate, Allyl Fluoroformate, Allyl Formate, and Allyl Chlorofornate

Nancy S. True and Robert K. Bohn*

Department of Chemistry and Institute of Materials Science, The University of Connecticut, Storrs, Connecticut 06268 (Received March 4, 1977)

Publication costs assisted by the University of Connecticut Research Foundation

Low resolution microwave spectra of allyl cyanofornate and chlorofornate display a-type band series associated with four conformational forms designated EG, CG, CG', and IG. The band series are characterized by $B + C$ values of 1838.1(3), 2019.8(3), 2188.0(7), and 2069(2) MHz, respectively, for allyl cyanofornate and 1834.5(3) (1799.5(5), ³⁷Cl), 2015(1) (1988 (1), ³⁷Cl), 2213(2), and 2081(2) MHz, respectively, for allyl chlorofornate. Allyl fluoroformate displays band series from four rotamers designated EG, ES, CG, and IG having $B + C$ values of 2406(1), 2764(1), 3075(5), and 2815(5) MHz, respectively. Allyl formate displays one band series having a $B + C$ value of 3298(3) MHz attributed to an EG conformer. Each E conformer is consistent with a syn-anti [$\tau_1(\text{OCOC}) = \text{C}^\circ$, $\tau_2(\text{COCC}) = 180^\circ$] heavy atom planar structure and each C species is consistent with a syn-gauche [$\tau_1(\text{OCOC}) = 0^\circ$, $\tau_2(\text{COCC}) \sim 90^\circ$] structure. The I conformers are consistent with a gauche-gauche [$\tau_1(\text{OCOC}) \sim 90^\circ$, $\tau_2(\text{COCC}) \sim 240^\circ$] structure. The ES conformer of allyl fluoroformate has the vinyl group syn-eclipsed with the C-O bond [$\tau_3(\text{OCCC}) = 0^\circ$]. Rotational constants of all other conformers are consistent with structures having the vinyl group eclipsed with a methylene C-H bond [$\tau_3(\text{OCCC}) = 120^\circ$]. E and C conformers are of nearly equal energy in each case. I conformers are approximately 2-3 kcal/mol higher in energy. These results parallel previous findings for ethyl, propargyl, and *n*-propyl esters demonstrating that the potential functions for internal rotation of primary esters are similar.

Introduction

Eight stable conformers of allyl esters can reasonably be postulated. Rotational isomerism involving three bonds can occur in allyl formates and acetates. Low resolution microwave (LRMW) spectroscopic studies of primary esters¹⁻⁴ have demonstrated the existence of three stable

rotamers in the conformational space defined by the carbonyl carbon to ether oxygen ($\tau_1(\text{OCOC})$) torsion and the ether oxygen to alkyl carbon ($\tau_2(\text{COCC})$) torsion. Observed conformers are displayed and torsional angles are defined in Figure 1a. Extended [$\tau_1(\text{OCOC}) = 0^\circ$, $\tau_2(\text{COCC}) = 180^\circ$] and compact [$\tau_1(\text{OCOC}) = 0^\circ$, τ_2 -

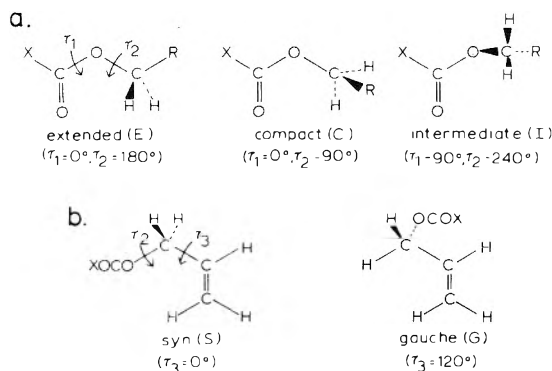


Figure 1. Conformations of allyl esters.

(COCC) $\sim 90^\circ$] conformers of nearly equal energy have been observed in ethyl,² propargyl,³ and *n*-propyl esters.^{4,5} Intermediate [$\tau_1(\text{OCOC}) \sim 45\text{--}80^\circ$, $\tau_2(\text{COCC}) \sim 230\text{--}270^\circ$] conformers have been observed in several ethyl,² propargyl,³ *n*-propyl,⁴ and neopentyl¹ esters. In each case the intermediate conformer is 1.5–3 kcal/mol higher in energy than the extended and compact forms and its spectrum is anomalously intense.

Rotational isomerism of allylic compounds has been extensively studied by high resolution microwave spectroscopy. Syn ($\tau_3(\text{OCCC}) = 0^\circ$) and gauche ($\tau_3(\text{OCCC}) = 120^\circ$) conformers, defined in Figure 1b, have been observed in butene-1,⁶ allyl chloride,⁷ allyl fluoride,⁸ allyl cyanide,⁹ and allylamine.^{10–12} The syn conformer of allyl fluoride is 166 ± 67 cal/mol lower in energy than the gauche form. The syn conformer of allyl cyanide is estimated to be the more stable. In contrast, the gauche form of butene-1 is estimated to be lower in energy. Only the spectra of the gauche isomers of allyl alcohol¹³ and allyl mercaptan¹⁴ have been assigned although the presence of other species could not be ruled out on the basis of microwave spectral data.

No structural studies of allyl esters in the gas phase have been reported. A wealth of conformational forms of allyl esters can be predicted, reflecting the previous results obtained for primary esters and allylic compounds. Combining the conformations depicted in Figures 1a and 1b, the eight reasonable conformers of allyl esters are designated ES, EG, CS, CG, CG', IS, IG, and IG'. The first letter refers to the extended (E), compact (C), or intermediate (I) configuration about $\tau_1(\text{OCOC})$ and $\tau_2(\text{COCC})$; the second letter refers to syn (S) or gauche (G) configurations about $\tau_3(\text{OCCC})$.

Elucidation and characterization of very complex mixtures of rotational isomers is possible using LRMW spectroscopy. Polar prolate molecules such as allyl formates are ideally suited to analysis by this technique. This study determines the conformational species present and their relative stabilities in gaseous samples of allyl formate, fluoroformate, chloroformate, and cyanoformate.

Experimental Section

All microwave measurements were made on Hewlett-Packard Model 8460 A microwave spectrometers. Spectra of allyl fluoroformate, allyl chloroformate, and allyl cyanoformate were obtained from 18 to 39 GHz. Spectra of allyl formate were obtained from 26.5 to 39 GHz. All spectra were recorded at room temperature and with the sample cells packed in dry ice. In all cases the Stark voltage was 3200 V/cm and the scan rate was 10 MHz/s with a 1-s detector time constant.

Samples were distilled into the waveguide to pressures of 30–70 mTorr. In order to minimize errors in intensity measurements, the sample pressure and detector crystal current were kept constant while each spectrum was being

recorded. Frequency measurements are frequencies of the band maxima averaged over forward and reverse scans. Frequency accuracy, which is dependent on the shape and width of the bands, ranges from about 5 to 50 MHz for the samples studied.

Allyl formate was prepared in low yield from allyl alcohol and formic acid. Sulfuric acid was used as a catalyst. Allyl chloroformate was prepared from allyl alcohol and phosgene by the method of Strain et al.¹⁵ The reaction was performed at 0°C . The product was washed with sodium bicarbonate and fractionally distilled at reduced pressure. Allyl fluoroformate was prepared by direct exchange between allyl chloroformate and thallous fluoride using the procedure of Nakanishi et al.¹⁶ Allyl cyanoformate was synthesized from allyl chloroformate and sodium cyanide using the method of Giuud et al.¹⁷ All samples were fractionally distilled under reduced pressure prior to use. They were characterized by their ^1H NMR and infrared spectra and their purity was established to be in excess of 98% by gas-liquid chromatography on a 6 ft SE-30 column with 5–10-min retention times.

Results

Allyl Cyanoformate. Condensed survey LRMW spectra of allyl cyanoformate at 25 and at $\sim -63^\circ\text{C}$ are shown in Figures 2a and 2b, respectively. R branch a-type band series associated with four conformational species have been assigned. *B* + *C* values are 1838.1(3), 2019(3), 2188.0(7), and 2069(2) MHz for these series. Spectral data of allyl cyanoformate appear in Tables I and II.

Conformation assignment of LRMW band series involves matching observed *B* + *C* values with those calculated from models. Also, band shape, band width, vibrational satellite patterns, and relative stability data will be compared with results of previous LRMW studies of esters to support the assignments.

Reasonable assumed geometrical parameters for allyl cyanoformate were obtained by combining appropriate fragments of the geometry suggested for ethyl cyanoformate¹⁸ with the r_s structure of propylene.¹⁹ Using these parameters, *B* + *C* was calculated at 30° intervals in the conformational space defined by $\tau_1(\text{OCOC})$ and $\tau_2(\text{COCC})$, holding $\tau_3(\text{OCCC})$ fixed at 0° (syn) and 120° (gauche) values. Only torsional angles were varied.

A calculated *B* + *C* value of 1848 MHz was obtained for the EG conformation of allyl cyanoformate and the series spaced at 1838.1(3) MHz intervals was assigned to this form. Calculations of *B* + *C* as a function of $\tau_2(\text{COCC})$, holding $\tau_1(\text{OCOC})$ fixed at the 0° syn structure and holding τ_3 at 0 and 120° , are displayed graphically in Figure 3a. *B* + *C* values of the four observed conformers are indicated by horizontal lines. Error bars correspond to an estimated 2% uncertainty in calculated *B* + *C* values due to uncertainties in the assumed structural parameters excepting the torsional angles. This uncertainty has been arbitrarily assigned to the observed values for easy visualization. Closed circles indicate assignments. Band series spaced at 2019.8(3) and 2188.0(7) MHz are compatible with the two nonequivalent compact-gauche [CG ($\tau_1 = 0^\circ$, $\tau_2 \sim 90^\circ$, $\tau_3 = 120^\circ$) and CG' ($\tau_1 = 0^\circ$, $\tau_2 \sim 270^\circ$, $\tau_3 = 120^\circ$)] conformations. The remaining a-type series, having a *B* + *C* value of 2069(2) MHz, is compatible with a gauche configuration about τ_3 . Assigning this series to a model with $\tau_1 = 0^\circ$ (and hence $\tau_2 \sim 75$ or 255°) imposes unrealistic constraints on the potential function for internal rotation about τ_2 . Based on analogy with primary esters which have been previously characterized this series is assigned to an IG conformation having a nonplanar value of $\tau_1(\text{OCOC})$. To characterize the τ_1 , τ_2 coordinates of the IG conformer,

TABLE I: $B + C$ values (MHz) of the Conformers of Allyl Cyanofornate, Fluorofornate, Fornate, and Chlorofornate

	EG	ES	CG	CG'	IG
Allyl cyanofornate					
$\nu_1, \nu_2 = 0, 0$	1838.1(3)	...	2019.8(3)	2188.0(7)	2069(2)
1, 0	1840.8(4)		2014.6(5)	2179.8(2)	
2, 0	1844.3(2)		2008.7(5)		
3, 0	1847.8(4)		...		
0, 1			2024.9(3)		
1, 1			2017.4(5)		
Allyl fluorofornate					
$\nu = 0$	2406(1)	2764(1)	...	3075(5)	2815(5)
1	2410(1)	2773(1)			
2	2415(1)				
Allyl fornate					
$\nu = 0$	3298(3)
1	3301(3)				
2	3304(3)				
3	3307(3)				
4	3313(3)				
Allyl chlorofornate (35/37)					
$\nu = 0$	1834.5(3)/1799.5(6)	...	2213(2)/...	2015(1)/1988(1)	2081(2)/2042(10)
1	1837.9(3)/1802.9(5)				
2	1841.1(3)/1806.2(5)				
3	1844.4(5)/1809.9(5)				
4	1847.9(5)/1813.7(5)				

TABLE II: Relative Intensities and Relative Energies of the Conformational Isomers of Allyl Esters

	EG	ES	CG	CG'	IG
Allyl Cyanofornate					
Relative intensity, 25 °C	1		0.7	0.8	8
Relative intensity, ~-63 °C	1		0.6	0.8	0.9
Relative energy, kcal/mol	0		~0	~0	~3
Allyl Fluorofornate					
Relative intensity, 25 °C	1	0.8		0.2	1
Relative intensity, ~-63 °C	1	0.8		0.2	0.1
Relative energy, kcal/mol	0	~0		~0	~3
Allyl Chlorofornate					
Relative intensity, 25 °C	1		0.5	0.5	1
Relative intensity, ~-63 °C	1		0.5	0.5	0.2
Relative energy, kcal/mol	0		~0	~0	~2

$B + C$ was calculated in the space defined by τ_1 and τ_2 holding τ_3 constant at the 120° gauche configuration. Results of this calculation are displayed in the asymmetric contour diagram shown in Figure 3b. Contours are spaced at 100-MHz intervals. Models consistent with the EG, CG, CG', and IG series are those consistent with the labeled, dashed contours. Continuing the analogy with previous esters displaying intermediate conformers, the IG conformer of allyl cyanofornate is tentatively assigned to the structure having a compatible $B + C$ value which is farthest removed in $\tau_1\tau_2$ space from the EG, CG, and CG' conformers. That structure has coordinates, $\tau_1(\text{OCOC}) \sim 90^\circ$, $\tau_2(\text{COCC}) \sim 240^\circ$. Since the contour diagram of $B + C$ as a function of τ_1 and τ_2 for the gauche ($\tau_3 = 120^\circ$) configuration of the allyl group is asymmetric, two non-equivalent IG conformers are expected. Only one is observed. An IG' conformation ($\tau_1 \sim 270^\circ$, $\tau_2 \sim 120^\circ$, $\tau_3 = 120^\circ$) is predicted to have $B + C = 1990$ MHz.

Relative intensity and relative energy data further support these assignments. At 25 °C the relative intensity ratio EG:CG:CG':IG is 1:0.8:0.7:8.0, respectively, and at ~-63 °C it is 1:0.8:0.6:0.7. The EG, CG, and CG' conformers are of approximately equal stability, the IG conformer is ~3 kcal/mol higher in energy. These results parallel previous findings for ethyl, propargyl, *n*-propyl, and neopentyl esters.

At low J values, bands of the EG conformer are broad and ragged. At higher J values and greater resolution than is shown in Figures 2a and 2b the ragged bands of the EG

conformer of allyl cyanofornate reveal a partially resolved cluster of narrow bands whose pattern is reproduced for each J value. Frequencies of the corresponding narrow bands in each cluster index to integral multiples of constant $B + C$ values indicating that these structures are resolved vibrational satellite band spectra. The smooth variation in $B + C$ as a function of vibrational quantum number suggests that these satellites correspond to successive states in one vibrational mode. Severe Stark lobe interference and the high degree of overlapping within the clumps of satellites precludes an unambiguous assignment of the ground state band series. The series with the smallest $B + C$ value is arbitrarily assigned to the ground state, based on analogy with the extended-gauche conformer of *n*-propyl fornate.⁴ The calculated value of Ray's asymmetry parameter, κ , is -0.96(1) for the EG conformer of allyl cyanofornate. The narrow (~50 MHz) band widths of the resolved vibrational satellite bands support this near prolate structure. Both compact-gauche conformers, CG and CG', display vibrational satellite spectra displaced to lower frequencies from the ground state bands. The rich fine structure of the CG bands which is resolved in the R band spectra is not apparent in the condensed K band spectra shown in Figures 2a and 2b. Large rotational constant variations and low frequency disposition of vibrational satellite bands is characteristic of excited states of the O-R torsional mode of compact conformers of esters.

The IG conformer of allyl cyanofornate does not display resolved vibrational satellite spectra. Bands of this conformer are smooth, broad (~400 MHz), and structureless. These features are again analogous to previous findings for intermediate conformers of primary esters.

Virtually all the absorbances in the spectra are assigned to the EG, CG, CG', and IG conformers and their satellites with the exception of a broad band centered at 23 455 MHz. This feature is more prominent at ~-63 °C and may be part of the b-type spectrum of one of the more stable conformers. LRMW spectra of allyl cyanofornate are not consistent with significant concentrations of conformational species having a syn configuration about τ_3 .

These assignments are reasonable and consistent with previous assignments of other esters but are clearly neither rigorous nor necessarily unique. This makes study of a

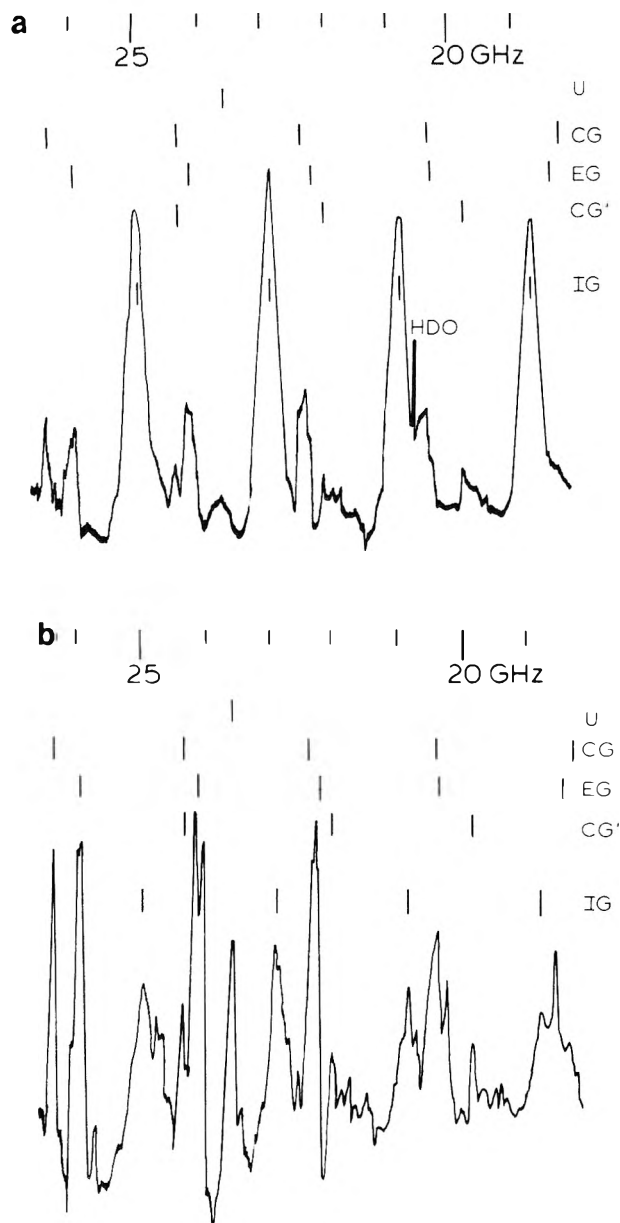


Figure 2. Condensed survey LRMW spectra of allyl cyanofornate. (a) K band spectrum from 18 to 26.5 GHz at 25 °C scanned at 10 MHz/s with a 1-s time constant. The band markers are calculated from $(J + 1)(B + C)$ with $B + C = 1838.1, 2188.0, 2019.8,$ and 2069 MHz for the EG, CG, CG', and IG conformers, respectively. (b) Same as (a) except the temperature is ca. -63 °C.

family of similar compounds absolutely essential in order to test predictions based on these assignments. Therefore, other allyl esters were synthesized and studied in order to test the assignments made above.

Allyl Fluoroformate. Condensed survey LRMW K band spectra of allyl fluoroformate at 25 and at ~ -63 °C are shown in Figures 4a and 4b, respectively. Three a-type band series having $B + C$ values of 2406(1), 2764(1), and 2815(5) MHz are present in both spectra. Corresponding conformers are designated EG, ES, and IG, respectively. Rotational constants of allyl fluoroformate were calculated using geometrical parameters suggested for ethyl fluoroformate²⁰ combined with the r_s propylene structure.¹⁹ Figure 5 displays $B + C$ calculated as a function of τ_2 . The lower asymmetric curve corresponds to a calculation holding $\tau_1 = 0^\circ$ and $\tau_3 = 120^\circ$. The upper symmetric curve has $\tau_1 = 0^\circ$ and $\tau_3 = 0^\circ$.

Error bars correspond to a 2% uncertainty in calculated $B + C$ values excepting uncertainties due to torsional

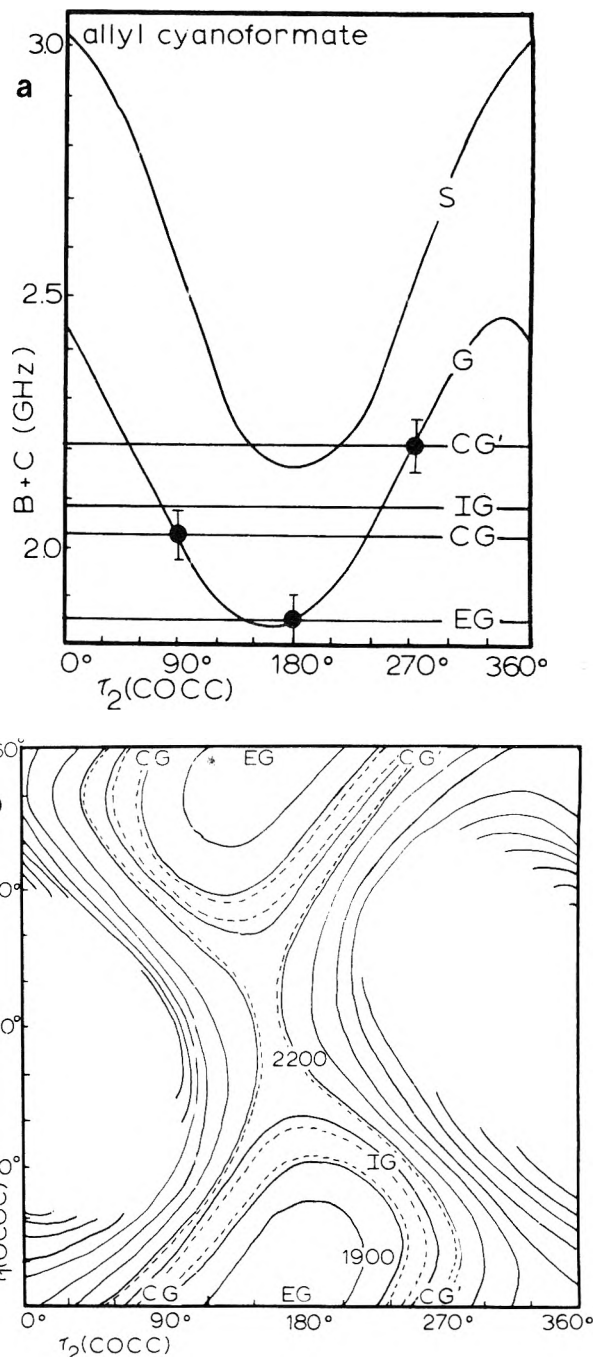


Figure 3. (a) Observed and calculated $B + C$ values of allyl cyanofornate. The horizontal lines correspond to observed $B + C$ values. The two curves display calculated $B + C$ values as a function of the torsional angle $\tau_2(\text{COCC})$ for $\tau_1(\text{O}=\text{COC}) = 0^\circ, \tau_3(\text{OCCC}) = 0^\circ$, S, (upper curve) and for $\tau_1(\text{O}=\text{COC}) = 0^\circ, \tau_3(\text{OCCC}) = 120^\circ$, G (lower curve). The closed circles indicate the assigned configurations. The error bars correspond to an estimated 2% uncertainties in the assumed structural parameters excepting torsional angles. (b) Contour diagram of $B + C$ for allyl cyanofornate as a function of the torsional angles, $\tau_1(\text{O}=\text{COC})$ and $\tau_2(\text{COCC})$ with $\tau_3(\text{OCCC}) = 120^\circ$. The dashed contours indicate the observed $B + C$ values of the species observed. The labels EG, CG, CG', and IG locate the most probable configurations of those species. The blank regions correspond to models too asymmetric to produce LRMW band spectra and therefore unobservable by this technique.

angles. The assignments of the EG and ES structures are indicated by circles. A few weak absorbances observed in R band are attributed to an a-type band spectrum with a $B + C$ value of 3075(5) MHz. This series is assigned to the CG conformer of allyl fluoroformate. To characterize the conformation of the IG rotamer $B + C$ was calculated as a function of τ_1 and τ_2 for the gauche configuration

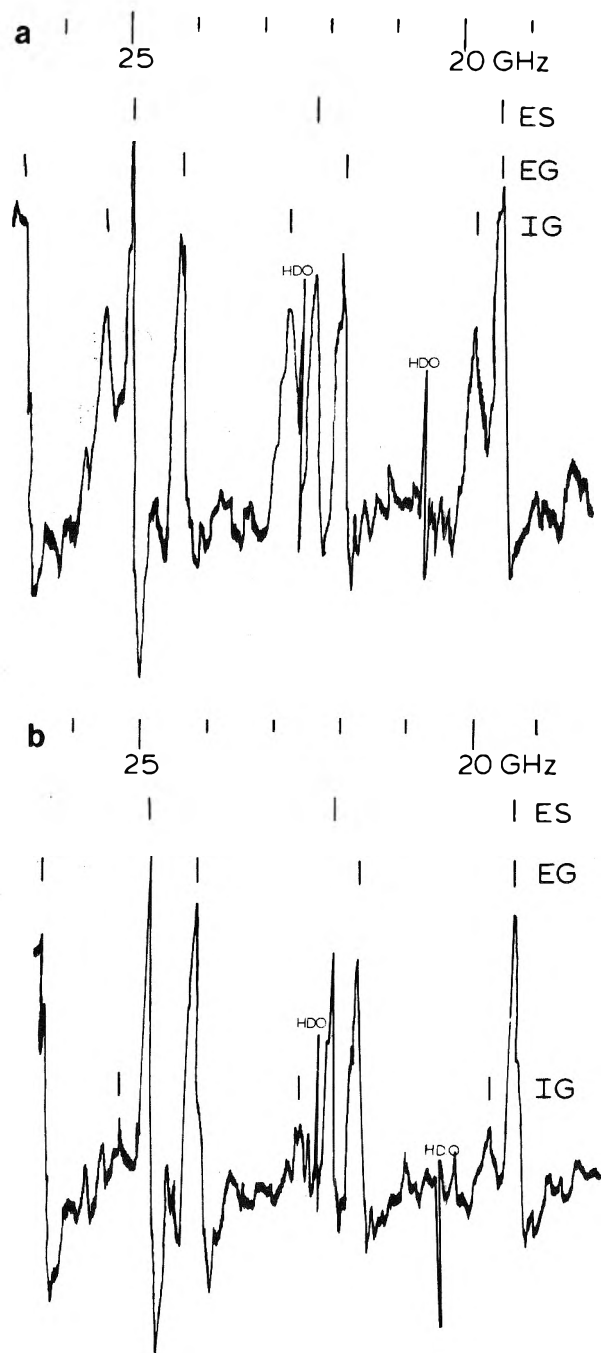


Figure 4. Condensed survey LRMW spectra of allyl fluoroformate. (a) K band spectrum from 18 to 26.5 MHz at 25 °C swept at 10 MHz/s with a 1-s time constant. The band markers are calculated from $(J + 1)(B + C)$ with $B + C = 2406, 2764, 3075,$ and 2815 for the EG, ES, CG, and IG conformers, respectively. (b) Same as above except the temperature is ~ -63 °C.

about τ_3 ($\tau_3 = 120^\circ$). Calculated values of $B + C$ for allyl fluoroformate are relatively insensitive to the value of τ_1 due to the similarity in masses of fluorine and oxygen. The observed value of $B + C$ for the IG conformer is compatible with τ_2 values of either ~ 80 or $\sim 240^\circ$ for any τ_1 value. The latter structure is consistent with the $\tau_1(\text{OCOC}) \sim 90^\circ$, $\tau_2(\text{COCC}) \sim 240^\circ$ structure suggested for the IG conformer of allyl cyanoformate.

The EG:ES:CG:IG relative intensity ratio is 1:0.8:0.2:1 at 25 °C and 1:0.8:0.2:0.1 at ~ -63 °C. The EG, ES, and CG conformers are approximately equally stable and the IG conformer is ~ 3 kcal/mol higher in energy. Spectral complexity precludes a more quantitative determination of the relative intensities and energies of the observed conformers.

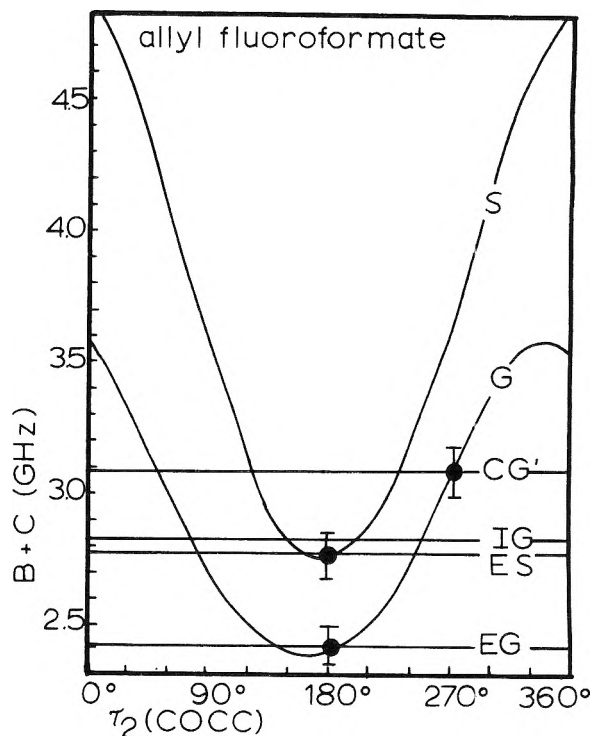


Figure 5. Observed and calculated values of $B + C$ for allyl fluoroformate. The horizontal lines correspond to observed $B + C$ values. The upper curve displays $B + C$ as a function of $\tau_2(\text{COCC})$ with $\tau_1 = 0^\circ$ and $\tau_3 = 0^\circ$. The lower curve is similar except $\tau_3 = 120^\circ$. The closed circles indicate the assigned configuration. The error bars correspond to an estimated 2% uncertainty in the calculated values due to uncertainties in the assumed structural parameters excepting torsional angles.

Fine structure of the EG bands of allyl fluoroformate is similar to that observed on the EG bands of allyl cyanoformate. Again the EG band series with the smallest $B + C$ value has been arbitrarily assigned to the ground state. Two EG vibrational satellite series have been assigned. The calculated κ value for the EG structure is -0.97 , consistent with the band widths and degree of band resolution observed. Vibrational satellites of the ES conformer are displaced to the high frequency side of the main bands. These observations are consistent with results obtained for extended forms of other primary esters.

Unlike the ES and EG conformers, bands of the IG form do not display resolvable vibrational satellite bands. Bands of the IG conformer having $J + 1 \leftarrow J$ values of $7 \leftarrow 6, 8 \leftarrow 7,$ and $9 \leftarrow 8$ are broad and featureless. For the transitions $10 \leftarrow 9$ and $11 \leftarrow 10$, the IG bands are much wider and more diffuse. IG bands for the $12 \leftarrow 11$ and $13 \leftarrow 12$ transitions were not located, although broad absorbances were present in the predicted spectral regions. This behavior has not been observed for intermediate conformers of other esters. LRMW spectral data of allyl fluoroformate are summarized in Tables I and II.

Allyl Formate. One a-type band series displaying resolved vibrational satellite spectra can be unambiguously assigned in the LRMW spectrum of allyl formate. The corresponding conformer designated EG has a $B + C$ value of 3298(3) MHz. Four series of satellite bands occurring at regular intervals on the high frequency side of the main band have been assigned. The regular change in $B + C$ as a function of vibrational quantum number indicates that these satellites belong to successively excited states in a single vibrational mode. Severe Stark lobe interference precludes an estimate of the associated torsional frequency.

A nonrepeating pattern of weak unassigned structured absorbances in the spectrum suggests that conformers

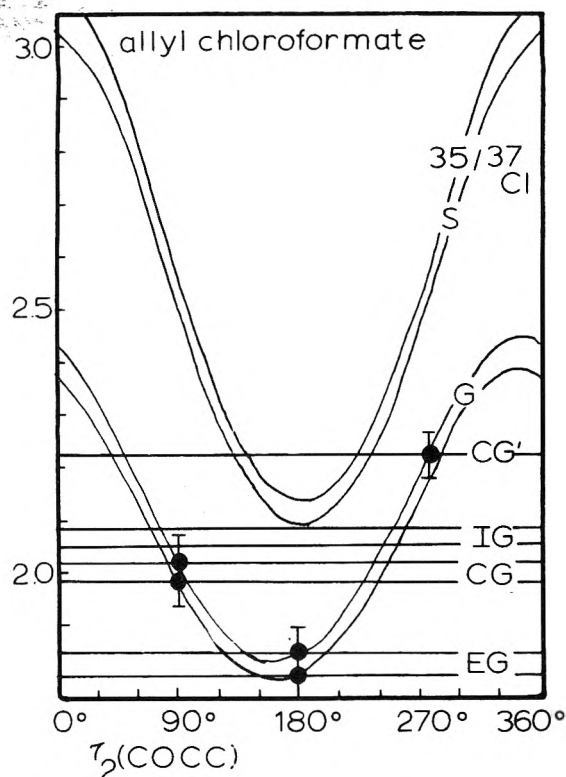


Figure 6. Observed and calculated values of $B + C$ for $^{35/37}\text{Cl}$ isotopic species of allyl chloroformate. The horizontal lines correspond to observed $B + C$ values. The upper curves display $B + C$ as a function of $\tau_2(\text{COCC})$ with $\tau_1 = 0^\circ$ and $\tau_3 = 0^\circ$. The lower curves are similar except $\tau_3 = 120^\circ$. The closed circles indicate the assigned configurations. The error bars correspond to an estimated 2% uncertainty in the calculated values due to uncertainties in the assumed structural parameters excepting torsional angles.

which do not produce a-type band spectra may be present in the sample. The temperature dependence of the relative intensities of these absorbances indicates that they are not due to background irregularities.

The observed $B + C$ value for the EG series of allyl formate is consistent with that calculated for the EG structure. Reported geometrical parameters of ethyl formate²¹ and propylene¹⁹ were used in the calculation. LRMW spectral data of allyl formate appear in Table I.

Allyl Chloroformate. Allyl chloroformate produces extremely complex LRMW band spectra at both 25 and $\sim -63^\circ\text{C}$. Fifteen R branch a-type band series have been assigned. They are consistent with four conformational forms displaying resolved chlorine isotopic species and resolved vibrational satellite species. Series having $B + C$ values of 1834.5(3), 2015(1), 2213(2), and 2081(2) MHz are assigned to vibrational ground state ^{35}Cl isotopic forms of the EG, CG, CG', and IG conformers. Series having $B + C$ values of 1799.5(5), 1988(1), and 2042(10) MHz are consistent with vibrational ground state ^{37}Cl isotopic forms of the EG, CG, and IG conformers. Figure 6 displays the assignments of these seven series. $B + C$ was calculated as a function of τ_2 while τ_1 was held fixed at 0° and τ_3 was held fixed at 0° (upper pair of curves) and 120° (lower pair of curves) for both chlorine isotopes. The parameters of propylene¹⁹ and ethyl chloroformate² were used in these calculations. Graphing conventions are identical with those of Figures 3a and 5. As was the case for allyl fluoroformate and allyl cyanoformate, the IG conformer does not fit a reasonable structure when τ_1 is constrained to zero. $B + C$ values as a function of τ_2 for nonplanar values of τ_1 were calculated. The IG conformer of allyl chloroformate is consistent with the $\tau_1(\text{OCOC}) \sim 90^\circ$, $\tau_2(\text{COCC}) \sim 240^\circ$

structure suggested for allyl cyanoformate and allyl fluoroformate.

Spectral complexity precludes a quantitative estimate of relative intensities and relative stabilities of the conformers of allyl chloroformate. Approximate relative intensity ratios are 1:0.5:0.5:1 at 25°C and 1:0.5:0.5:0.2 at $\sim -63^\circ\text{C}$ for the EG:CG:CG':IG conformers, respectively. The IG conformer is about 2 kcal/mol higher in energy than the EG, CG, and CG' forms. Bands of the EG conformer display repeating resolvable fine structure for both the ^{35}Cl and ^{37}Cl series. This fine structure is analogous to that observed for the EG conformers of allyl cyanoformate, fluoroformate, and chloroformate. Four satellite series have been assigned. Bands of the IG conformer are smooth and broad. LRMW spectral data of allyl chloroformate appear in Tables I and II.

Discussion

There are striking similarities between the conformational preferences of allyl esters and those of other primary esters which have been characterized. For each allyl ester extended and compact conformers of nearly equal energy have been observed, indicating the potential functions for internal rotation about τ_1 and τ_2 in allyl esters are similar to those of other primary esters. Intermediate conformers have been observed in every allyl ester except allyl formate. In all cases this conformer produces wide, structureless, and anomalously intense bands. For example, the relative energy of the IG form of allyl cyanoformate is about 3 kcal/mol higher than the EG conformer. According to Boltzmann's distribution, the ratio of the populations of the IG and EG forms should be ~ 0.007 at 25°C . The ratio of the corresponding band intensities is ~ 8 , i.e., the intermediate form's bands are ~ 1000 -fold more intense than expected. We have proposed in other primary esters¹⁻⁴ that this anomaly is probably due to an unusually dense population of low-lying vibrationally excited states of the intermediate conformer. Alternatively expressed, the entropy difference between the intermediate and extended forms of a primary ester is huge, $\sim 9\text{ cal deg}^{-1}\text{ mol}^{-1}$ in the case of allyl cyanoformate.

The relative energies (2–3 kcal mol⁻¹) and geometries ($\tau_1 \sim 90^\circ$, $\tau_2 \sim 240^\circ$) of intermediate forms are similar for each allyl ester studied and again parallel results obtained for other primary esters. These results demonstrate that the potential surfaces near the intermediate minima for a variety of primary esters are similar.

The gauche conformation about $\tau_3(\text{OCCC})$ places a methylene CH bond coplanar with the vinyl group. This conformation about τ_3 is the only one found in allyl cyanoformate and chloroformate. Curiously, allyl fluoroformate, in addition to three gauche conformers, displays a band series consistent with an extended-syn [$\tau_1 = 0^\circ$, $\tau_2 = 180^\circ$, $\tau_3 = 0^\circ$] structure in which the allyl and ester groups are coplanar. For every ester studied the ES conformer is calculated to be nearly prolate and have large a-axis dipole moments necessary to produce LRMW spectra.²² ES conformers, if present in significant quantities, perhaps 20%, would have been observed in LRMW spectra of the other allyl esters.

The conformations observed in the four allyl esters studied here have been assigned to five of the eight configurations suggested as reasonable (Figure 1). No more than four have been observed in a single allyl ester. The unobserved forms are CS (compact-syn), IS (intermediate-syn), and IG' (intermediate-gauche'). Only one compound displays a conformer with a syn configuration about τ_3 (C–O syn-eclipsed with C=C), allyl fluoroformate. Thus it appears that a C–H bond eclipses more favorably

with a C=C double bond than does a C-O bond. In allyl fluoroformate, there is no marked energy difference between the C-O eclipsed (syn) and C-H eclipsed (gauche) forms, however.

We do not know why IG' forms have not been observed. The more significant question, which also has no answer at present, is why is there a potential energy minimum at the intermediate configuration? This configuration ($\tau_1 \sim 45-90^\circ$, $\tau_2 \sim 210-270^\circ$) has been observed in ethyl,² *n*-propyl,⁴ allyl, propargyl,³ and neopentyl¹ esters (esters of primary alcohols) but not in isopropyl esters.²³ No theoretical model has been able to rationalize this configuration.

Acknowledgment. The authors are grateful to Professors E. Bright Wilson of Harvard University and Marlin D. Harmony of the University of Kansas for allowing the use of the microwave spectrometers supported by NSF Grants No. GP-37066X and MPS 74-22178, respectively. Calculations were carried out at the University of Connecticut Computer Center.

Supplementary Material Available: Tables III-VI listing band frequencies, $J + 1$ values, and $B + C$ values for each of the compounds and their conformers, isotopic species, and vibrational satellites species (7 pages). Ordering information is available on any current masthead page.

References and Notes

- (1) Paper 7 of this series: N. S. True and R. K. Bohn, *J. Phys. Chem.*, preceding paper in this issue.
- (2) N. S. True and R. K. Bohn, *J. Am. Chem. Soc.*, **98**, 1188 (1976).
- (3) N. S. True and R. K. Bohn, *J. Am. Chem. Soc.*, **99**, 3575 (1977).
- (4) N. S. True and R. K. Bohn, submitted for publication.
- (5) Compact conformers of formic acid esters (X = H) have insufficient *a*-axis dipole moments to be observable by LRMW spectroscopy.
- (6) S. Kondo, E. Hirota, and Y. Morino, *J. Mol. Spectrosc.*, **28**, 471 (1968).
- (7) E. Hirota, *J. Mol. Spectrosc.*, **35**, 9 (1970).
- (8) E. Hirota, *J. Chem. Phys.*, **42**, 2071 (1965).
- (9) K. V. L. N. Sastry, V. M. Rao, and S. C. Dass, *Can. J. Phys.*, **46**, 959 (1968).
- (10) G. Roussy, J. Demaison, I. Botskor, and H. D. Rudolph, *J. Mol. Spectrosc.*, **38**, 535 (1971).
- (11) I. Botskor, H. D. Rudolph, and G. Roussy, *J. Mol. Spectrosc.*, **53**, 15 (1974).
- (12) I. Botskor, H. D. Rudolph, and G. Roussy, *J. Mol. Spectrosc.*, **52**, 457 (1974).
- (13) A. N. Murty and R. F. Curl, Jr., *J. Chem. Phys.*, **46**, 4176 (1967).
- (14) K. V. L. N. Sastry, S. C. Dass, W. V. G. Brooks, and A. Bhaumik, *J. Mol. Spectrosc.*, **31**, 54 (1969).
- (15) F. Strain, W. E. Bissinger, W. R. Dial, H. Rudoff, B. J. DeWitt, H. C. Stevens, and J. H. Langsten, *J. Am. Chem. Soc.*, **72**, 1254 (1950).
- (16) S. Nakanishi, T. C. Meyers, and E. V. Jensen, *J. Am. Chem. Soc.*, **77**, 3099 (1955).
- (17) W. Glud, W. W. Nussler, and K. Keller, Patentschrift, 592539 (1934).
- (18) R. D. Suenram, N. S. True, and R. K. Bohn, submitted for publication.
- (19) D. R. Lide and D. Christensen, *J. Chem. Phys.*, **35**, 1374 (1961).
- (20) N. S. True and R. K. Bohn, 31st Symposium on Molecular Structure and Spectroscopy, Columbus, Ohio, 1976, Abstract WB'1.
- (21) J. M. Riveros and E. B. Wilson, *J. Chem. Phys.*, **46**, 4605 (1967).
- (22) M. S. Farag and R. K. Bohn, *J. Chem. Phys.*, **62**, 3946 (1975).
- (23) N. S. True and R. K. Bohn, *J. Mol. Struct.*, **36**, 173 (1977).

Complexation of the Cesium Cation by Macrocyclic Polyethers in Various Solvents. A Cesium-133 Nuclear Magnetic Resonance Study of the Thermodynamics and Kinetics of Exchange

Elizabeth Mel, Alexander I. Popov, and James L. Dye*

Department of Chemistry, Michigan State University, East Lansing, Michigan 48824 (Received March 18, 1977)

Publication costs assisted by the U.S. Energy Research and Development Administration

The formation constants for the complexation of Cs⁺ in six solvents by three crown ethers, 18-crown-6, dibenzo-18-crown-6, and dicyclohexyl-18-crown-6, were studied at 25 °C by cesium-133 NMR techniques. The solvents used, in the approximate order of decreasing first complexation constant for all crown ethers, were pyridine, acetone, propylene carbonate, acetonitrile, *N,N*-dimethylformamide, and dimethyl sulfoxide. In all solvents, 18-crown-6 formed both 1:1 and 2:1 (ligand to metal) complexes with enough difference between the complexation constants that the second constant could be determined. The formation of 2:1 complexes by the other two crown ethers was also indicated in most solvents but the second complexation constant could only be measured for the dibenzo-18-crown-6 complex in pyridine. In many cases the first complexation constant was too large to measure by the NMR technique so that only lower bounds could be established. The rate of loss of the Cs⁺ ion from dicyclohexyl-18-crown-6 and from monobenzo-2,2,2-cryptand in propylene carbonate was measured as a function of temperature. The activation energy for the latter case (15 kcal mol⁻¹) is substantially larger than for the crown ether complex (8.5 kcal mol⁻¹). Although the chemical shifts of both Cs⁺ and its 1:1 complex with 18-crown-6 are strongly solvent dependent, the chemical shift of the 2:1 complex is independent of solvent, indicating that in the "sandwich" complex the cesium ion is effectively shielded from the solvent.

Introduction

Since Pedersen's synthesis of macrocyclic polyethers,¹ the ability of these "crown ethers" to complex alkali cations has been extensively investigated.^{2,3} Most of the studies have been carried out in aqueous or methanolic solutions. In this paper we describe the ability of three crown ethers, 18-crown-6 (18C6), dibenzo-18-crown-6 (DBC), and dicyclohexyl-18-crown-6 (DCC), to form 1:1 and 2:1 complexes in a wide variety of nonaqueous solvents. Six solvents were chosen to span a range of both dielectric

constant and donicity as shown in Table I. Cesium NMR spectroscopy is an appropriate technique for such a study because of the wide range of chemical shifts and the generally narrow lines which are observed for ¹³³Cs resonance. Because of the low solubility of cesium salts, the sensitivity provided by narrow NMR lines is particularly important. Large chemical shift differences between the free and the complexed ion, together with low concentrations, permit the quantitative determination of complexation constants from <10 to ~10⁵ M⁻¹ by examining

TABLE I: Dielectric Constants and Donicities of the Solvents Used in This Study

Solvent	Dielectric constant (25 °C)	Gutmann donor no.
Acetonitrile (MeCN)	37.5	14.1
Propylene Carbonate (PC)	65.0	15.1
Acetone	20.7	17.0
<i>N,N</i> -Dimethylformamide (DMF)	36.71	26.6
Dimethyl sulfoxide (Me ₂ SO)	46.68	29.8
Pyridine (Py)	12.40	33.1

the variation of the chemical shift with mole ratio (crown/Cs⁺).⁴ By comparing these results with those obtained with cryptands⁵ a general overview of the effect of complexing agent and solvent can be made.

Experimental Section

Cesium tetraphenylborate (CsTPB) was synthesized and dried as described previously.⁶ The complexing agent 18C6 (PCR, Inc.) was recrystallized twice from acetonitrile and vacuum dried. Dicyclohexyl-18-crown-6 (E. I. duPont de Nemours, Inc.) was obtained as a mixture of isomers A and B. For studies of the chemical shift vs. mole ratio, the mixture was used as obtained. For the kinetics study, only isomer A was used after separation by the technique described by Frensdorff.² The structure and the source of cryptand C222B (and of C222) are given in a previous publication.⁷ Pyridine (Fisher) was purified under vacuum as previously described⁸ and distilled on a vacuum line to the sample tube as needed; DMF was dried over anthracene radical anions which were prepared by the reaction of anthracene with potassium in tetrahydrofuran. All other solvents were dried over freshly activated molecular sieves and transferred under a nitrogen atmosphere. Each solvent was tested for water content either by a Karl Fischer titration or with an appropriate GLC column. The water content was always below 100 ppm.

All of the chemical shift measurements were made by the pulsed Fourier transform technique at 7.87 MHz as previously described⁷ with reference to an infinitely dilute aqueous Cs⁺ solution. The shifts were corrected for the difference in the bulk diamagnetic susceptibility of the solvent and the aqueous reference solution. A positive value represents an upfield (diamagnetic) shift.

The variation of the chemical shift with mole ratio (L/Cs⁺) was used as described previously⁹ to obtain the complexation constants by means of a nonlinear least-squares curve-fitting program, KINFIT.¹⁰ When only a single complex forms, the procedure is straightforward. However, when both 1:1 and 2:1 complexes form, one of the two procedures described below was used depending upon the magnitude of the first complexation constant.⁹ When this constant was less than about 10⁵ and the second constant was large enough to give reasonable curvature of the chemical shift vs. mole ratio plot, it was possible to fit the entire curve by adjusting four constants, the two formation constants, K_1 and K_2 , and the chemical shifts for Cs⁺·(crown) and Cs⁺·(crown)₂. If this procedure failed because of the large value of K_1 , a simulation method was used to estimate a lower bound for K_1 and then only the data above a mole ratio of one were used to evaluate K_2 . In many cases, the curvature beyond a mole ratio of one was so slight (presumably because K_2 is small) that the data could not be satisfactorily fitted by the equations.

Results

The variation of the cesium-133 chemical shift as a function of the 18C6/Cs⁺ mole ratio in various solvents

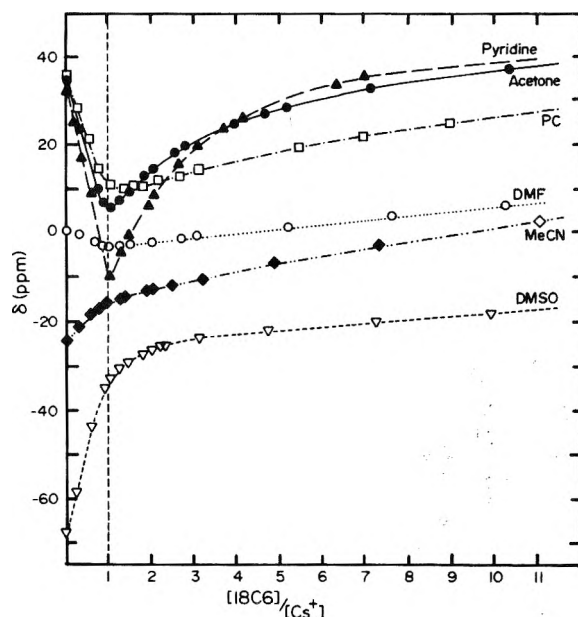


Figure 1. Cesium-133 chemical shifts vs. 18C6/Cs⁺ mole ratio in various solvents. The solutions contained 0.01 M cesium tetraphenylborate.

is shown in Figure 1. It is obvious that the solvent plays an important role in the complexation process. The behavior in pyridine, acetone, propylene carbonate, and DMF solutions shows clearly that at least two complexes are formed. A downfield shift followed by a relatively sharp break and an upfield shift which gradually approaches a limiting value can be explained by the formation of a strong 1:1 complex followed by the addition of a second molecule of the ligand to form a "sandwich" complex.^{11,12} The quantitative fit of the data when formation of a 2:1 complex is included and also the temperature dependence of the chemical shift⁴ clearly show that the second complex has a 2:1 stoichiometry. It is obvious from changes in the "sharpness" of the break shown in Figure 1 that the stability of the 1:1 complex decreases in the order pyridine > acetone > PC. However, in the first two solvents the variation of the chemical shift at mole ratios < 1.0 is so nearly linear that only lower limits can be determined for the values of K_1 . Simulation of the curve shape in this region indicates that $K_1 > 5 \times 10^5$ in pyridine and $> 2 \times 10^5$ in acetone. In PC the curvature is just large enough to permit calculation of both K_1 and K_2 . The value of $1.5 \pm 0.6 \times 10^5$ obtained for K_1 represents an approximate upper limit to the size of K_1 which can be determined by this technique. The small shift between Cs⁺ and the 1:1 complex in DMF makes determination of K_1 difficult. However, a fit of all of the data yield the values of K_1 and K_2 given in Table II.

In MeCN and Me₂SO solutions, the cesium-133 resonance shifts only upfield with increasing ligand concentration. There is some indication of a weak "break" in the curve at the 1:1 mole ratio. If we assume that only a 1:1 complex is formed, the best-fit of the data (dashed line, Figure 2) is poor. On the other hand, the inclusion of a 2:1 complex in the model as well as the 1:1 complex gives a much better fit to the data (solid line, Figure 2) and permits the determination of both K_1 and K_2 in Me₂SO solutions and an estimate of these two constants in MeCN solutions.

The attachment of two benzo groups to 18C6 to form DBC decreases both the basicity of the oxygen atoms¹ and the cavity size.¹³ In addition, the rigidity of the polyether ring is expected to be larger than that of 18C6. These factors should lead to weaker 1:1 complexes. The variation

TABLE II: Formation Constants of 1:1 and 2:1 (C/Cs⁺) Complexes of Cs⁺ with Three Crown Ethers in Various Solvents at 25 °C

Solvent	18C6	DBC	DCC (mixture)
Pyridine	$K_1 > 5 \times 10^5$ $K_2 = 74 \pm 2^c$	$(7 \pm 2) \times 10^3$ 230 ± 20	$> 10^5$ a
Propylene carbonate	$K_1 = (1.5 \pm 0.6) \times 10^4$ $K_2 = 10.9 \pm 4$	$\sim 10^3$ a	$\sim 10^4$ a
Acetone	$K_1 > 2 \times 10^5$ $K_2 = 34.0 \pm 0.5$	$> 10^3$ a	$> 10^4$ a
Dimethylformamide	$K_1 = (9 \pm 3) \times 10^3$ $K_2 = 2.44 \pm 0.05$	$K_1 = 30 \pm 3^b$	$K_1 = (2.8 \pm 0.9) \times 10^3$
Dimethyl sulfoxide	$K_1 = (1.1 \pm 0.1) \times 10^3$ $K_2 = 1.0 \pm 0.4$	$K_1 = 22 \pm 3^b$	$K_1 = (1.6 \pm 0.1) \times 10^2$
Acetonitrile	$K_1 > 10^4$ $K_2 = 3.7 \pm 0.6$	$K_1 = 35 \pm 2^b$	$K_1 > 10^4$ a

^a The variation of the chemical shift suggests formation of the 2:1 (C/Cs⁺) complex but K_2 cannot be determined. ^b It is possible that both 1:1 and 2:1 complexes form with DBC in these solvents. However a good fit of the data is obtained by assuming formation of only the 1:1 complex. ^c Uncertainties are estimated standard deviation.

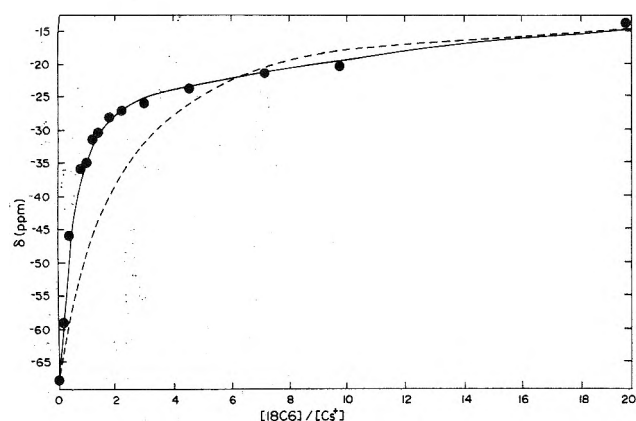


Figure 2. Least-squares fits of the calculated to the observed (●) cesium-133 chemical shifts in Me₂SO at 25 °C. Calculations were based upon the formation of only 1:1 complexes (dashed line) and upon the formation of both 1:1 and 2:1 (18C6/Cs⁺) complexes (solid line).

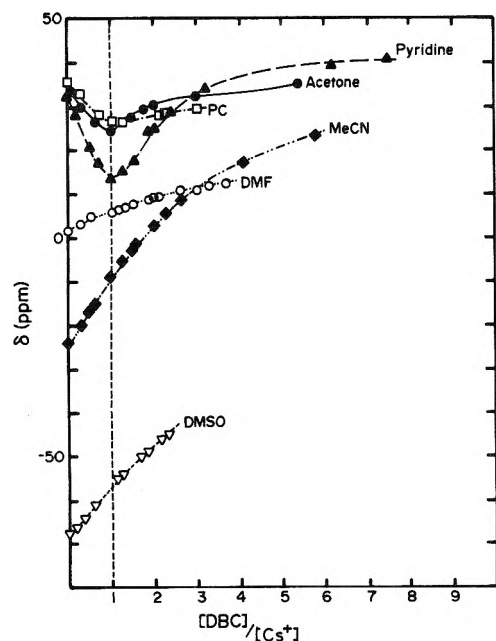


Figure 3. Cesium-133 chemical shifts vs. DBC/Cs⁺ mole ratio in various solvents. The solutions contained 0.01 M cesium tetraphenylborate.

of the chemical shift with the mole ratio (DBC/Cs⁺) is shown in Figure 3. The limited solubility of DBC restricted the ratios which could be studied. Clearly, the results, while qualitatively similar to those for 18C6 indicate a substantial decrease in the 1:1 formation constant. Even in pyridine, which shows a sharp "break" at the 1:1

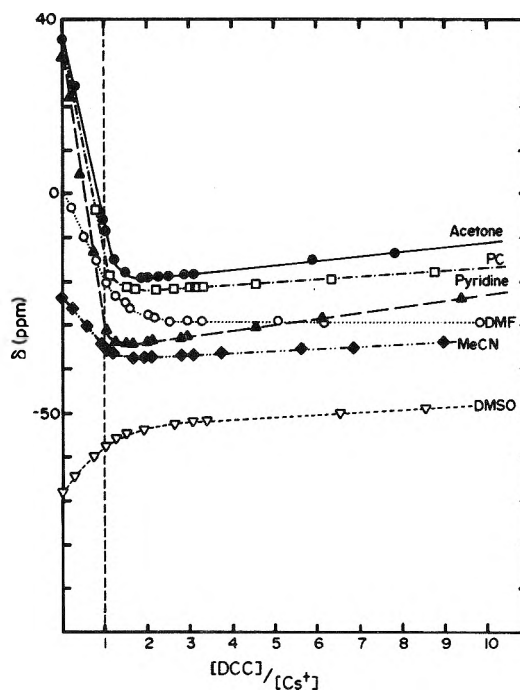


Figure 4. Cesium-133 chemical shifts vs. DCC/Cs⁺ mole ratio in various solvents. The solutions contained 0.01 M cesium tetraphenylborate.

mole ratio when 18C6 is used, there is considerable "rounding" with DBC and the value of K_1 (7×10^3) is at least two orders of magnitude smaller. It is interesting to note, however, that K_2 (2.3×10^2) is three times larger than the value obtained with 18C6. The data in all solvents are given in Table II. In acetone and PC solutions the variation of the chemical shift with increasing ligand/Cs⁺ mole ratio is too small to permit evaluation of K_1 and the solubility of DBC is too low to permit evaluation of K_2 .

For solutions in DMF, MeCN, and Me₂SO there is no perceptible change in slope at or near the 1:1 mole ratio. Therefore, it is not possible to tell whether or not sandwich complexes are formed in these solvents. If we assume that $K_1 > K_2$ (as is true for all cases in which both values can be determined) and that changes in K_1 with the solvent are similar to those for 18C6 complexes, then it seems reasonable to assume the formation of only the 1:1 complex in the concentration range studied. The values given in Table II are based upon this assumption.

The variation of the chemical shift with mole ratio for complexation by dicyclohexyl-18-crown-6 (DCC) is shown in Figure 4. The most obvious difference in its behavior from that of the other two crown ethers is the absence of an abrupt change in direction of the shift. The K_1 values

TABLE III: Rate Parameters for the Release of Cs⁺ from Some Macrocyclic Complexes in Several Solvents

Solvent	Ligand	10 ⁻³ k, s ⁻¹ (25 °C)	ΔH [‡] , kcal mol ⁻¹	ΔS [‡] , cal mol ⁻¹ deg ⁻¹	ΔG [‡] , kcal mol ⁻¹ (25 °C)
PC	DCC(A)	11 ± 1 ^a	7.9 ± 0.5	-14 ± 2	11.94 ± 0.05
PC	C222B	344 ± 38	14.3 ± 0.6	+15 ± 2	9.90 ± 0.07
PY	18C6 ^b	9.5 ± 0.2	7.8 ± 0.1	-14.2 ± 0.4	12.03 ± 0.02
DMF	C222 ^c	(9.0 ± 0.9) × 10 ³	12.9 ± 0.3	+16.5 ± 1.0	7.97 ± 0.06

^a Standard deviation estimates. ^b Reference 4. ^c Reference 5.

TABLE IV: Limiting Chemical Shifts^a of Cs⁺, Cs⁺ · (18C6), and Cs⁺ · (18C6)₂ in Various Solvents at 25 °C

Solvent	Cs ⁺	Cs ⁺ · (18C6)	Cs ⁺ · (18C6) ₂
PC	36.5	8.1 ± 0.2 ^b	44.5 ± 0.3
Acetone	35.8	6.4	47 ± 9
Py	32.4	-10.2 ± 0.2	48.0 ± 0.2
Me ₂ SO	-68.0	-23.6 ± 0.4	49 ± 24
DMF	0.8	-3.37 ± 0.05	48.2 ± 0.7
MeCN	-24.1	-14.8 ± 0.2	53 ± 7

^a In ppm from Cs⁺(aq) at infinite dilution. A positive shift is upfield (diamagnetic). ^b Standard deviation estimates.

are larger than those for DBC and are comparable to those for 18C6. However, the complexation constants for the formation of 2:1 complexes are much smaller than those for either DBC or 18C6. Indeed, only the slight upward "drift" of most of the chemical shifts beyond the 1:1 mole ratio can be used as evidence for 2:1 complex formation and certainly the data do not permit determination of K_2 . The complexation by DCC in pyridine, acetone, PC, and MeCN is so strong that only lower bounds for K_1 can be determined. An additional problem may have resulted from the use of a mixture of isomers of DCC. If the complexation constants are substantially different for the two isomers, then the fit of the data by a model which assumes only one type of complex would be poor. Even if this were the case, however, the general behavior of DCC complexes found in this study would be valid. For solutions in DMF and PC the values of K_1 are slightly smaller than for 18C6 in these solvents (see Table II).

The exchange rate and the activation parameters for the release of Cs⁺ from DCC and from monobenzo-2,2,2-cryptand (C222B) in PC were determined from a temperature-dependent study of the spectra. Characteristic two-line patterns were observed at -60 °C which merged into a single exchange-narrowed line at higher temperatures. The entire line shape was fitted by the Bloch equations as modified for exchange.¹⁴⁻¹⁶ The resulting exchange times (together with data for 18C6 in pyridine⁴ and C222 cryptand in DMF⁵ are plotted in Figure 5. The activation parameters are given in Table III.

Discussion

In all solvents used, the chemical shift of the 1:1 complex becomes more paramagnetic in the order DBC, 18C6, DCC, while the chemical shift of the 2:1 complex with 18C6 is independent of solvent and is much higher than that of any of the 1:1 complexes (see Table IV). All of the shifts, including those of the solvated cation, are strongly paramagnetic (200–300 ppm) when compared with the gaseous cation.¹⁷ The magnitude of this paramagnetic shift is determined by the overlap of donor lone-pair electrons with p and d orbitals of the cation.¹⁸ Therefore, we expect a correlation between the donating ability of the solvent or the complexing agent and the magnitude of the paramagnetic shift. Indeed, a correlation exists between the Gutmann donor number¹⁹ of the solvent and the ²³Na

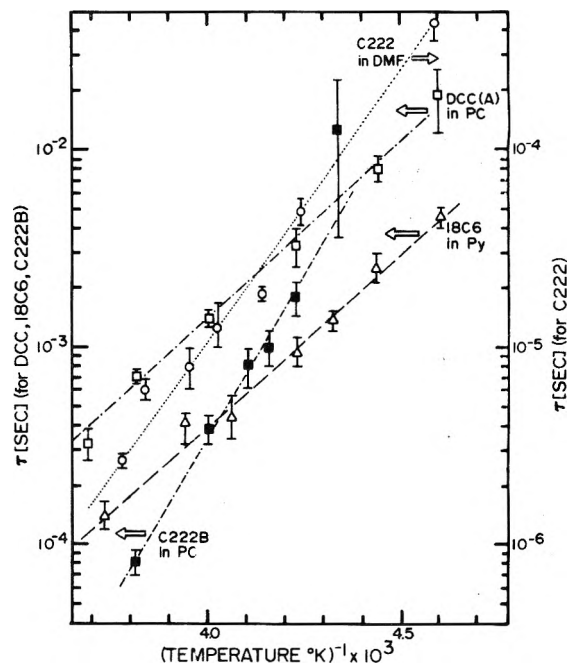


Figure 5. Arrhenius plots of exchange times of Cs⁺ in several solvents with various macrocyclic polyethers. (Data for 18C6 in PY and C222 in DMF are taken from ref 4 and 5 respectively.)

chemical shift^{20,21} and to a lesser extent for ¹³³Cs chemical shifts.⁶ However, other factors than lone-pair overlap determine the net binding of solvent or ligand to the ion. Steric factors will be particularly important for complexes between the Cs⁺ ion and crown ethers or cryptands. Thus, although DCC gives the greatest paramagnetic shift, it does not form stronger complexes than 18C6. This effect is particularly striking for the inclusive Cs⁺-C222 cryptand complexes⁵ which have relatively small formation constants in many solvents but show very large paramagnetic shifts. In this case the lone-pair interactions with the Cs⁺ ion are probably very large because the normal cavity size is too small to easily accommodate the Cs⁺ ion. According to this view, the formation of the inclusive complex would introduce considerable steric strain but give rise to strong overlap between the oxygen lone-pair electrons and the cesium cation. Conversely, the 2:1 crown complexes have much decreased paramagnetic shifts, probably because the individual lone-pair interactions with the cation are weakened when 12 ether oxygens act as donors to Cs⁺. It is interesting that the chemical shift of the 2:1 complex of Cs⁺ with 18C6 is essentially independent of solvent (Table IV). This observation indicates that in the sandwich-type complex the two ligand molecules effectively shield the Cs⁺ ion from interaction with the solvent. By contrast, the chemical shifts of the 1:1 complexes are strongly solvent dependent.

The results given in Table II and shown in Figures 1, 3, and 4 demonstrate clearly that the first complexation constant decreases in all solvents in the order 18C6 ≳ DCC ≫ DBC while the second complexation constant follows the order DBC ≳ 18C6 ≫ DCC. The variation in K_1 may

simply reflect changes in the cavity size and in the donor ability of the ether oxygens. However, the ability to form sandwich complexes must also be related to the stereochemistry of the ligands. Space-filling models suggest that the bulky benzo groups of DBC can easily avoid one another in the 2:1 complex but that the cyclohexyl groups cannot. It is also likely that the relatively weak 1:1 complex formed by DBC does not have the Cs⁺ ion located centrally in the cavity but rather that Cs⁺ forms an "exclusive" type of complex which is displaced from the center of the cavity. This would make it easier to add a second molecule of DBC and it would also lead to a smaller paramagnetic shift than if the Cs⁺ ion were "squeezed" into a small cavity.

Table I shows that there is no simple relationship between K_1 values and either the dielectric constant or the donicity of the solvent. In pyridine, which has the highest donor number, all of the crown ethers form the strongest complexes while in PC, which has the highest dielectric constant but a low donor number, intermediate values of the complexation constants are observed. It has been pointed out, however, that pyridine, being a nitrogen donor, or a "soft base" does not solvate strongly a "hard acid" such as an alkali ion.²² The combination of relatively high dielectric constant and high donicity provided by DMF and Me₂SO apparently yields a large enough solvation energy that only relatively weak complexes of the Cs⁺ ion can be formed by the crown ethers.

Recently, Matsuura et al.²³ have reported a conductometric study of the complexation constants of the alkali metal perchlorates with DBC in Me₂SO, DMF, and PC. Their concentrations were low enough so that formation of the 2:1 complex would not be expected. The K_1 value obtained for solutions in PC (3.5×10^3) is comparable to the value obtained in the present work. However, their values for solutions in DMF and Me₂SO (3×10^3 and 2×10^3 , respectively) are two orders of magnitude larger than those which we obtain by assuming formation of only the 1:1 complex. If we accept their values for K_1 then we must assume not only that a 2:1 complex also forms in these solvents but also that in DMF and Me₂SO DBC forms complexes with the Cs⁺ ion of about equal strength to those formed by 18C6 and DCC. The latter requirement is not consistent with the behavior of these complexes in other solvents.

The exchange rates obtained from NMR line shape analysis at various temperatures for DCC and C222B in PC, 18C6 in pyridine,⁴ and C222 in DMF⁵ yield essentially the same activation energies for release of Cs⁺ from the crown ethers (~ 8 kcal mol⁻¹) but a substantially higher activation energy for release of Cs⁺ from cryptands (~ 15 kcal mol⁻¹). In spite of the much larger activation energy for release from the cryptand than from the crowns, the absolute rates are not very different. Differences in the activation entropies account for this fact. While the ac-

tivation entropy for the release of Cs⁺ from DCC in PC and from 18C6 in pyridine⁴ is -14 cal mol⁻¹ deg⁻¹, it is $+15$ cal mol⁻¹ deg⁻¹ for the release of Cs⁺ from C222B and $+17$ cal mol⁻¹ deg⁻¹ from C222 in DMF.⁵ By contrast, except for the release into water, the activation entropies for release of Li⁺ from C211 and C221¹⁵ and of Na⁺ from C222¹⁶ are all negative. There are few data available on the overall entropy change, ΔS° , for the release of these ions from their crown or cryptate complexes. The entropy change for the release of Cs⁺ from an inclusive complex with C222 in DMF is $+19$ cal mol⁻¹ deg⁻¹ which is not very different from ΔS^\ddagger . This suggests that the transition state for the release of the ion resembles the final state of the solvated ion and cryptand, a suggestion which has been made previously.^{15,16} It would be of interest to have more information about the overall entropy change for both crown ether and cryptate complexation in order to assign the entropy changes to the various factors (solvation changes, configurational changes, etc.) which are operative.

Acknowledgment. The authors gratefully acknowledge the support of this work by the National Science Foundation Grant CHE73-08418 (A.I.P.) and the U.S. Energy Research and Development Administration Contract EY-76-S-02-0958 (J.L.D.).

References and Notes

- (1) C. J. Pedersen, *J. Am. Chem. Soc.*, **89**, 7017 (1967).
- (2) H. K. Frensdorff, *J. Am. Chem. Soc.*, **93**, 4684 (1971).
- (3) J. J. Christensen, D. J. Eatough, and R. M. Izatt, *Chem. Rev.*, **74**, 351 (1974).
- (4) E. Mei, J. L. Dye, and A. I. Popov, to be published.
- (5) E. Mei, A. I. Popov, and J. L. Dye, to be published.
- (6) W. J. DeWitte, L. Liu, E. Mei, J. L. Dye, and A. I. Popov, *J. Solution Chem.*, **6**, 337 (1977).
- (7) E. Mei, J. L. Dye, and A. I. Popov, *J. Am. Chem. Soc.*, **98**, 1619 (1976).
- (8) J. B. Kinsinger, M. M. Tannahill, M. S. Greenberg, and A. I. Popov, *J. Phys. Chem.*, **77**, 2444 (1973).
- (9) E. T. Roach, P. R. Handy, and A. I. Popov, *Inorg. Nucl. Chem. Lett.*, **9**, 359 (1973).
- (10) V. A. Nicely and J. L. Dye, *J. Chem. Educ.*, **48**, 443 (1971).
- (11) C. J. Pedersen, *J. Am. Chem. Soc.*, **92**, 386 (1970).
- (12) H. K. Frensdorff, *J. Am. Chem. Soc.*, **93**, 600 (1971).
- (13) J.-M. Lehn, *Struct. Bonding (Berlin)*, **16**, 1 (1973).
- (14) J. M. Ceraso and J. L. Dye, *J. Am. Chem. Soc.*, **95**, 4432 (1973).
- (15) Y. M. Cahen, J. L. Dye, and A. I. Popov, *J. Phys. Chem.*, **79**, 1292 (1975).
- (16) J. M. Ceraso, P. B. Smith, J. S. Landers, and J. L. Dye, *J. Phys. Chem.*, **81**, 760 (1977).
- (17) J. L. Dye, C. W. Andrews, and J. M. Ceraso, *J. Phys. Chem.*, **79**, 3076 (1975).
- (18) C. Deverell, *Prog. Nucl. Magn. Reson. Spectrosc.*, **4**, 278 (1969).
- (19) V. Gutmann and E. Wychera, *Inorg. Nucl. Chem. Lett.*, **2**, 257 (1966).
- (20) E. G. Bloor and R. G. Kidd, *Can. J. Chem.*, **46**, 3425 (1968).
- (21) (a) R. H. Erlich, E. Roach, and A. I. Popov, *J. Am. Chem. Soc.*, **92**, 4989 (1970); (b) R. H. Erlich and A. I. Popov, *ibid.*, **93**, 5620 (1971); (c) M. Herlem and A. I. Popov, *ibid.*, **94**, 1431 (1972); (d) M. S. Greenberg, R. L. Bodner, and A. I. Popov, *J. Phys. Chem.*, **77**, 2449 (1973).
- (22) (a) A. Hourdakos and A. I. Popov, *J. Solution Chem.*, **6**, 299 (1977); (b) N. Ahmad and M. C. Day, *J. Am. Chem. Soc.*, **99**, 941 (1977).
- (23) N. Matsuura, K. Umemoto, Y. Takeda, and A. Sasaki, *Bull. Chem. Soc. Jpn.*, **49**, 1246 (1976).

The Molecular Structure of Tetrafluoro-1,3-dithietane as Determined by Electron Diffraction[†]

Joseph F. Chiang* and K. C. Lu

Department of Chemistry, State University of New York at Oneonta, Oneonta, New York 13820 (Received November 30, 1976; Revised Manuscript Received June 6, 1977)

Publication costs assisted by the National Institutes of Health

The molecular structure of tetrafluoro-1,3-dithietane has been determined by gas phase electron diffraction. The structural parameters were obtained by a least-squares fitting of the calculated molecular intensity functions to the observed intensities. A D_{2h} symmetry was assumed for tetrafluoro-1,3-dithietane. The deduced structural parameters are C-S = 1.785 ± 0.002 Å, C-F = 1.314 ± 0.002 Å, $\angle CSC = 83.2 \pm 0.3^\circ$, $\angle FCS = 113.7 \pm 0.2^\circ$, $l_{C-S} = 0.062 \pm 0.002$ Å, and $l_{C-F} = 0.053 \pm 0.003$ Å.

Introduction

Due to the high electronegativity and small size of the fluorine atom, the substitution of fluorine into various compounds leads to significant structure changes. These changes in structural parameters are anticipated because introduction of a fluorine atom substantially alters the electron distribution within molecule.¹ One of the changes in molecular structure is the shortening of the valence bond length adjacent to the F-substitution site. For example, in F_3C-X , $F_2C=X$, or $FC\equiv X$, where X is N, C, or O, substitution of fluorine for hydrogen decreases the C-X bond length.² The effect of fluorine substitution on carbon-carbon single and double bond lengths in open chain systems has been intensively investigated,³ while little work has been done on ring compounds with C-S single bonds. Tetrafluoro-1,3-dithietane, a dimer of thiocarbonyl fluoride, is of interest because the molecule contains a four-membered ring with high symmetry which is suitable for ED investigation.

Experimental Section

A sample of tetrafluoro-1,3-dithietane was purchased from PCR, Inc. It was purified by preparative GC and was analyzed to be 99.5% pure. Two sets of sectored electron diffraction patterns with two plates of each were taken with the Cornell ED apparatus,⁴ under the following conditions at room temperature: low energy, long sample-plate distance (47 kV, 282.2 mm, $q = 13-46 \text{ \AA}^{-1}$); high energy, short sample-plate distance (67 kV, 127.0 mm, $q = 31-100 \text{ \AA}^{-1}$). MgO diffraction patterns were also recorded concurrently to calibrate the sample-plate distances. The photographic plates were traced with a double beam Jarrell-Ash microdensitometer interfaced with a digital recorder. The procedure for data reduction and structure analysis has been described in several previous publications.⁵ The elastic and inelastic form factors of Tavad et al.⁶ were used in conjunction with the Ibers and Hoerni⁷ phase-shift approximation in the intensity calculation.

Analysis and Results

The total experimental intensity curves for the two sets of data along with the refined background are plotted in Figure 1. Numerical values for the intensities at interval q 's ($= (40/\lambda) \sin \theta/2$), the error, and correlation matrices are available as supplementary material. (See paragraph

TABLE I: Bond Lengths and Angles for Tetrafluoro-1,3-dithietane

	$r, \text{ \AA}$	$l_{ij}, \text{ \AA}$
Independent Parameters		
C-S	1.735 ± 0.002	0.062 ± 0.002
C-F	1.314 ± 0.002	0.053 ± 0.003
$\angle CSC$	$83.2 \pm 0.3^\circ$	
$\angle FCS$	$113.7 \pm 0.2^\circ$	
Dependent Parameters		
$F_1 \cdots F_2$	2.090	0.049 ^a
$S_2 \cdots F_1$	2.608	0.074 ^a
$C_1 \cdots C_3$	2.371	0.093 ^a
$S_2 \cdots S_4$	2.669	0.152 ^a
$C_1 \cdots F_3$	3.336	0.103 ^a
$F_1 \cdots F_3$	3.965	0.190 ^a
$F_1 \cdots F_4$	4.482	0.113 ^a

^a The l_{ij} 's were obtained by manual adjustments to agree with the radial distribution curve.

at end of text regarding supplemental material.) These are the averaged values obtained by two tracings each of the two plates for each set of data. The reduced experimental molecular intensity curve (dotted curve) and that calculated for the best model (smooth curve) as derived from the least-squares analysis are shown in Figure 2. Figure 3 consists of the refined radial distribution curves and the difference curve between the experimental function and the curve calculated for the best model. The well-resolved peaks in the radial distribution curve are as follows: C-F = 1.314 Å, C-S = 1.785 Å, $F_1 \cdots F_2 = 2.090$ Å, $C_1 \cdots C_3 = 2.371$ Å, $S_2 \cdots F_1 = 2.608$ Å, $S_2 \cdots S_4 = 2.669$ Å, $C_1 \cdots F_3 = 3.336$ Å, $F_1 \cdots F_3 = 3.965$ Å, and $F_1 \cdots F_4 = 4.482$ Å.

A D_{2h} symmetry was assumed for tetrafluoro-1,3-dithietane. The following parameters were used in the least-squares analysis: C-F, C-S, $\angle CSC$, $\angle FCS$, l_{C-F} , l_{C-S} . All other mean amplitudes of vibration were estimated from the final radial distribution function. The structure was refined with geometrical constraints imposed on it using r 's as they appear in the argument of the intensity function without any corrections for shrinkage or anharmonicity. The final values of the parameters r_a are listed in Table I. The error limits cited in Table I are three times the diagonal elements of the error matrix. The resolution factor R_f is 0.042.

Discussion

Comparison of the structures of tetrafluoro-1,3-dithietane (TFD) and tetrachloro-1,3-dithietane⁸ is shown in Table II. The bond angles in tetrafluoro-1,3-dithietane are seen to differ very little from those in tetrachloro-

[†] Presented at the 172nd National Meeting of the American Chemical Society, San Francisco, Calif., Aug. 29-Sept. 3, 1976.

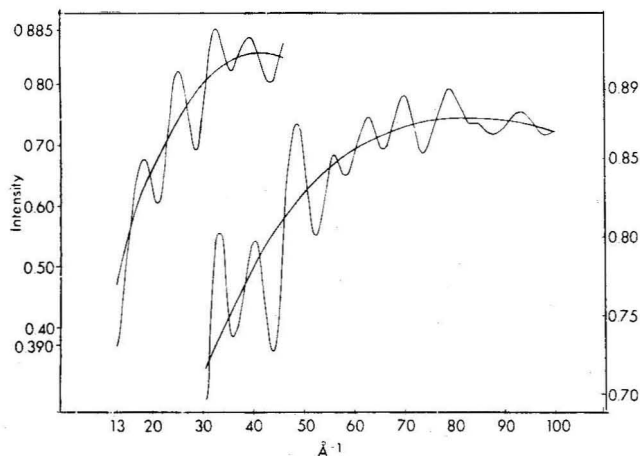


Figure 1. Total experimental intensity curve and the refined background for tetrafluoro-1,3-dithietane.

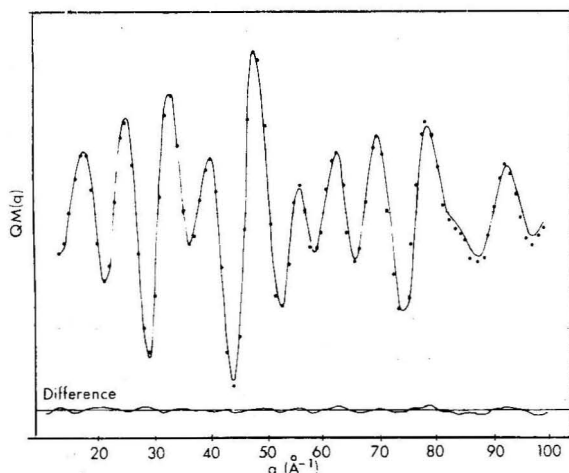


Figure 2. The theoretical (smooth curve) and the reduced experimental (dotted curve) molecular intensity curve for tetrafluoro-1,3-dithietane; the lower oscillating curve is the difference between the theoretical and experimental curves.

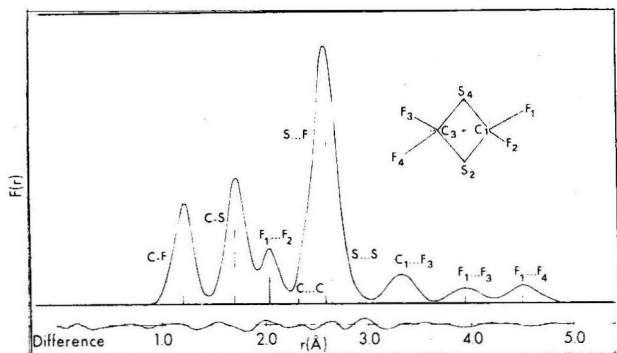


Figure 3. The refined experimental radial distribution curve. The lower oscillating curve is the difference between the experimental curve and the curve calculated from the best model.

1,3-dithietane: $\angle(\text{CSC})_{\text{F}} = 83.2^\circ$, $\angle(\text{CSC})_{\text{Cl}} = 83.9^\circ$, $\angle(\text{SCS})_{\text{F}} = 96.8^\circ$, $\angle(\text{SCS})_{\text{Cl}} = 96.1^\circ$, $\angle\text{FCS} = 113.7^\circ$, $\angle\text{ClCS} = 113.4^\circ$. The agreement can be anticipated since both molecules belong to the same symmetry group with skeletons consisting of the same atoms. The C-S bond lengths are 1.785 Å in tetrafluoro-1,3-dithietane and 1.804 Å in tetrachloro-1,3-dithietane. Both are shorter than the normal $\text{C}_{(\text{sp}^3)}\text{-S}$ length (1.819 Å) in $\text{CH}_3\text{-SH}$,⁹ but longer than the $\text{C}_{(\text{sp}^2)}\text{-S}$ length (1.748 Å) in methyl vinyl sulfide.¹⁰ The C-S bond in TFD is also longer than that in 1,2-bis(tri-

TABLE II: Comparison of Structures between $\text{C}_2\text{S}_2\text{F}_4$ and $\text{C}_2\text{S}_2\text{Cl}_4$

	$\begin{array}{c} \text{F} \quad \text{S} \quad \text{F} \\ \diagdown \quad \diagup \\ \text{C} \quad \text{C} \\ \diagup \quad \diagdown \\ \text{F} \quad \text{S} \quad \text{F} \end{array}$	$\begin{array}{c} \text{Cl} \quad \text{S} \quad \text{Cl} \\ \diagdown \quad \diagup \\ \text{C} \quad \text{C} \\ \diagup \quad \diagdown \\ \text{Cl} \quad \text{S} \quad \text{Cl} \end{array}$
C-X	1.314 Å	1.769 Å
C-S	1.785 Å	1.804 Å
C...C	2.371 Å	2.413 Å
S...S	2.669 Å	2.684 Å
$\angle\text{SCS}$	96.8°	96.1°
$\angle\text{CSC}$	83.2°	83.9°
$\angle\text{XCX}$	105.3°	107.1°
$\angle\text{XCS}$	113.7°	113.4°

fluoromethyl)dithietane (C-S = 1.73 Å).¹¹ The C-F bond length in TFD (C-F = 1.314 Å) is similar to that in perfluorocyclopropane (C-F = 1.314 Å),¹² but shorter than that in perfluorocyclobutane (C-F = 1.333 Å).¹³ This might indicate that the four-membered ring in TFD is a strained one as that in perfluorocyclopropane which also has a shorter C-F bond. The shortening of C-S bond in TFD is probably due to "fluorine substitution effects". The effects have been observed in many experimental results. For example, the C-C bond distance is 1.532 Å¹⁴ in CH_3CH_3 , and 1.514 Å¹⁵ in CF_3CH_3 ; the C=C bond length is 1.337 Å¹⁶ in $\text{CH}_2=\text{CH}_2$, 1.333 Å¹⁷ in $\text{CFH}=\text{CH}_2$, 1.316 Å¹⁷ in $\text{CF}_2=\text{CH}_2$, and 1.309 Å¹⁷ in $\text{CF}_2=\text{CFH}$; the C≡C bond distance is 1.212 Å¹⁸ in $\text{CH}=\text{CH}$ and 1.198 Å¹⁹ in $\text{CF}=\text{CH}$. Therefore, it seems reasonable to conclude that the geometry of TFD is influenced by the fluorine substitution effects and it possesses a ring strain in the gaseous phase.

Acknowledgment. This work was supported by the Research Foundation of State University of New York in the form of a grant-in-aid and NIH Grant No. CA11537. The authors wish to thank Professor S. H. Bauer for the use of his electron diffraction equipment.

Supplementary Material Available: Appendices I and II contain numerical values for the averaged intensities at integral q , and error and correlation matrices (2 pages). Ordering information is given on any current masthead page.

References and Notes

- (1) L. Pauling, "The Nature of the Chemical Bond". 3rd ed, Cornell University Press, Ithaca, N.Y., 1960.
- (2) R. L. Hilderbrandt, A. L. Andreassen, and S. H. Bauer, *J. Phys. Chem.*, **74**, 1586 (1970).
- (3) A. Yokozeki and S. H. Bauer, "Topics in Current Chemistry", Springer-Verlag, New York, N.Y., 1975.
- (4) S. H. Bauer and K. Kimura, *J. Phys. Soc. Jpn.*, **17**, 300 (1962).
- (5) (a) J. L. Hencher and S. H. Bauer, *J. Am. Chem. Soc.*, **89**, 5527 (1967); (b) J. F. Chiang, *J. Chem. Phys.*, **61**, 1280 (1974).
- (6) C. Tavard, D. Nicolas, and M. Rouault, *J. Chim. Physicochim. Biol.*, **64**, 540 (1967).
- (7) J. A. Ibers and J. A. Hoerni, *Acta Crystallogr.*, **7**, 405 (1954).
- (8) V. B. Krebs and H. Beyer, *Z. Anorg. Allg. Chem.*, **369**, 199 (1969).
- (9) T. Kojima and T. Nishikawcz, *J. Phys. Soc. Jpn.*, **12**, 680 (1957).
- (10) H. M. Seip and S. Samdal, *Acta Chem. Scand.*, **25**, 1903 (1971).
- (11) J. L. Hencher, Q. Shen, and D. G. Tuck, *J. Am. Chem. Soc.*, **98**, 899 (1976).
- (12) J. F. Chiang and W. A. Bennett, *Tetrahedron*, **27**, 975 (1971).
- (13) C. H. Chang, R. F. Porter, and S. H. Bauer, *J. Mol. Struct.*, **7**, 89 (1971).
- (14) K. Kuchitsu, *J. Chem. Phys.*, **49**, 4456 (1968).
- (15) R. H. Schwendeman, *Diss. Abstr.*, **18**, 1645 (1958).
- (16) K. Kuchitsu, *J. Chem. Phys.*, **44**, 906 (1966).
- (17) J. L. Carlos, R. R. Karl, and S. H. Bauer, *J. Chem. Soc., Faraday Trans. 2*, **70**, 177 (1974).
- (18) M. Tanimoto, K. Kuchitsu, and Y. Morino, *Bull. Chem. Soc. Jpn.*, **42**, 2519 (1969).
- (19) J. K. Tyler and J. Sheridan, *Trans. Faraday Soc.*, **59**, 2661 (1963).

Kinetics of Hydrogen Absorption by LaNi₅

S. Tanaka, J. D. Clewley, and Ted B. Flanagan*

Chemistry Department, University of Vermont, Burlington, Vermont 05401 (Received September 20, 1976; Revised Manuscript Received May 11, 1977)

The rate of hydrogen absorption by massive (unactivated) LaNi₅ was investigated in the primary solubility range in a mercury- and grease-free vacuum system. The absorption rate was reproducible with the same sample after evacuation of hydrogen and also from sample to sample. The rate of absorption was dependent upon the square root of both the hydrogen pressure and time. The rate-limiting step is believed to be bulk diffusion. This conclusion was verified by comparing the exact diffusion equation solution for hydrogen diffusion into a sphere with the experimental data obtained with a single sphere of LaNi₅ at a nearly constant boundary condition of constant hydrogen concentration (constant pressure). This slow step explains the good reproducibility of absorption rates, especially since special care was not employed to clean the surfaces. At 423 K the diffusion constant in the infinitely dilute region is $D^* = 3 \times 10^{-7}$ cm²/s.

Introduction

LaNi₅ is a remarkable absorber of hydrogen both from the standpoints of the amounts of hydrogen which can be absorbed, e.g., values of H-to-LaNi₅ (moles) can approach 7, and the rapidity of absorption and desorption.^{1,2} Furthermore, the rates are relatively insensitive to traces of impurities. Generally equilibrium¹⁻³ and kinetic data⁴ have been obtained with "activated" samples of LaNi₅. Activation consists of exposing a massive sample of LaNi₅ to hydrogen at pressures of 30–50 atm (298 to 323 K). This converts the massive sample to the hydride phase and the concomitant lattice expansion results in disintegration of the massive sample into a large surface area, "activated" sample.^{1,2} This activated sample is very active toward hydrogen absorption and desorption.

Neumann⁵ is the only investigator who did not employ activated samples. Although he did not investigate the kinetics of absorption, he noted that 12 to 15 days were needed to obtain equilibrium at room temperature. By contrast, the time for equilibrium is extremely short for the "activated" samples. For instance, Boser⁴ noted that at 298 K only 2.5 s are required for one-half of the absorption to occur in the two-phase region of this system. Boser⁴ investigated the kinetics of absorption and desorption in the two-phase region. He found that the kinetics of both processes were apparently identical. The rate law which he employed was empirical and the energy of activation which was derived from it was 31.8 kJ/mol of H₂. Boser argued that the slow step is the phase transformation. Earlier Raichlan and Doremus⁶ investigated the desorption of hydrogen from the hydride of the related intermetallic compound, SmCo₅. They also concluded that the slow step was the phase change.

There are not many detailed investigations of the kinetics of hydrogen absorption or desorption into or from metals. One of the most detailed investigations is that by Auer and Grabke⁷ who followed the rate of absorption of hydrogen by palladium sheets at small hydrogen contents (α phase). They concluded that the rate-controlling step was at the surface. Recent investigations of the uptake of hydrogen by finely divided palladium in the α phase confirm that the slow step is surface controlled.⁸

Experimental Section

The uptake of hydrogen was followed by changes of pressure measured by a diaphragm gauge (M.K.S. Instruments), displayed on a digital voltmeter, and recorded on a strip-chart recorder. The volume of the reaction chamber was approximately 25 cm³ and the dosing volume

was ~ 300 cm³. The apparatus was grease- and mercury-free and before a run was initiated the vacuum was generally 2×10^{-7} mmHg.

LaNi₅ was prepared by arc-melting the pure substituents. The stoichiometry was estimated by the starting weights and the weight loss after arc-melting. Buschow and van Mal⁹ have reported that the hydrogen pressure in equilibrium with the two solid phases, H-saturated LaNi₅ and the hydride phase, depends upon the stoichiometry of the LaNi₅. When the LaNi₅ prepared here was activated and the pressure over the two-phase region determined at 313 K, its value corresponded quite well with the value for stoichiometric LaNi₅ reported by Buschow and van Mal.⁹

Two different sample geometries were employed. Type I samples were prepared by shattering an arc-melted button into a spectrum of particle sizes; most particles were roughly parallelepipeds of sides $2 \times 2 \times 4$ mm and the total sample weight employed was approximately 9.5 g. The other type (II) was a single arc-melted sample of nearly spherical shape which weighed 0.6 g.

Hydrogen absorption was followed by changes of pressure that were quite small but still accurately measurable. For example, the total pressure for a run at 423 K with the LaNi₅ sphere fell from 92.25 mmHg to the equilibrium pressure 88.98 mmHg. This is only a 3.5% decrease. The pressure was therefore nearly constant during the absorption. If lower initial pressures were employed, e.g., 8.764 mmHg, the decrease was larger ($\sim 23\%$). The rate of absorption depended upon the square root of pressure and this dependence reduced the effect of the pressure decrease; furthermore most absorption runs were not carried to completion so the pressure did not decrease to the full calculated value.

Results and Discussion

Absorption by Multiparticle Samples. Figure 1 shows a plot of the increase of hydrogen content of a series of samples (type I) plotted as n (the ratio of H (g atom) to LaNi₅ (formula weights)) against time t at 463 K. The initial pressure was 1.80 mmHg for each run. The pressure fell considerably during these particular early runs but these serve to illustrate the reproducibility of the absorption. Two represent different preparations of LaNi₅ with similar particle sizes. One of these preparations was then annealed and quenched to 195 K. The equilibrium pressure-composition-temperature (p - c - T) data are the same for the annealed sample as for freshly arc-melted sample,¹⁰ yet the rate of absorption by this sample was

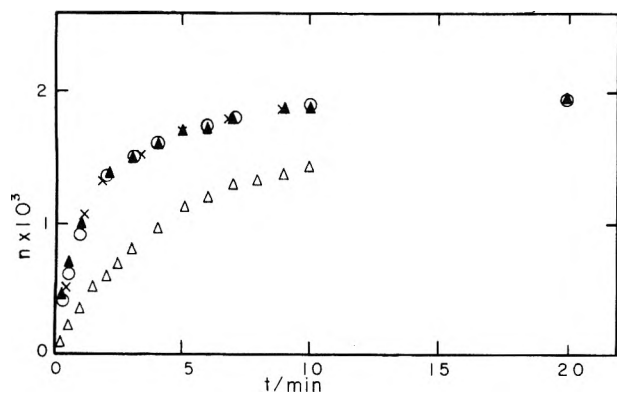


Figure 1. H-to-LaNi₅, n , plotted against time for several type I samples (463 K): O, sample 1 after arc-melting; Δ , sample 1 after annealing (>1000 K in argon); \blacktriangle , sample 1 after rearc-melting; X, different sample after preparation by arc-melting.

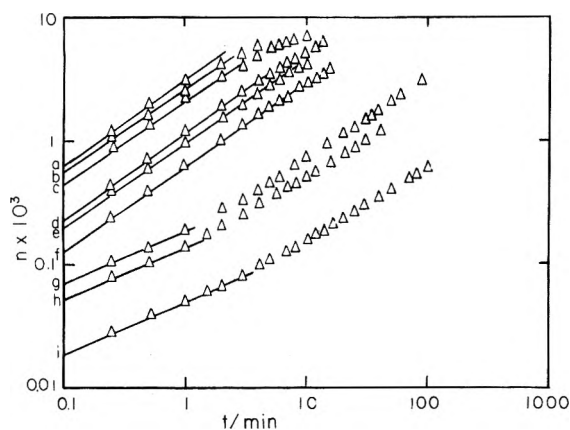


Figure 2. $\log n$ plotted against \log time for sample (type I) at several temperatures and an initial pressure of 8.5 mmHg: a, 463 K; b, 423 K; c, 383 K; d, 328 K; e, 303 K; f, 273 K; g, 238 K; h, 222 K; i, 195 K.

slower than for the other samples. If it was again arc-melted and broken up into the usual size of particles, the rate was equal to the rates of the other samples. Thus the rate of this gas/metal reaction is surprisingly reproducible for comparable sizes of samples (type I).

Time Dependence of the Rate of Absorption. The rates of absorption were followed in detail on a given sample of LaNi₅ (unactivated, type I) from 195 to 463 K. Surprisingly, absorption occurred measurably even at 195 K with these massive samples. Typical data are shown in Figure 2. In these runs the initial pressure was 8.5 mmHg and the sample was evacuated to $\sim 10^{-7}$ mmHg between each run. For times up to 4 min the pressures are reasonably constant, e.g., the pressures after $t = 4$ min were 6.0 mmHg at 463 K and 8.4 mmHg at 195 K.

The initial slopes, b on a log-log plot, defined by $n = at^b$, are found to be 0.65 (273–463 K) and 0.43 (195–273 K). The slopes of the data at the higher temperatures, >273 K, decrease with time as expected because of the pressure fall. Below 273 K the pressure fall with time is quite small and the slopes can be seen to increase with time to become nearly equal to the slopes of the higher temperature runs at small times. The reason for the change of slope at the lower temperatures is unknown but it occurs at very small values of n and small times. Similar data have been obtained with the same sample at an initial pressure of 85 mmHg in the temperature range 238–463 K. The slopes, b , were 0.42 (238–273 K) and 0.61 (383–463 K). These slopes are close enough to $1/2$ to suggest that the reaction may be diffusion controlled. Diffusion into simple geometrical shapes from a constant concentration

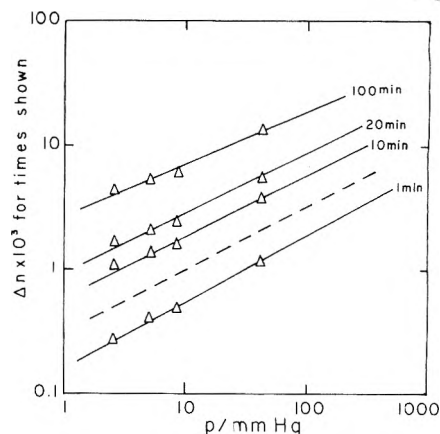


Figure 3. $\log n$ plotted against $\log p_{H_2}$ for several times of reaction (195 K). Dashed curve represents a slope of one-half.

boundary condition reduces at small times to a dependence of fraction absorbed upon $t^{1/2}$, e.g., for a sphere $n_t/n_\infty = 6(Dt/\pi r_0^2)^{1/2}$.¹¹ The reasons for deviations from the square-root dependence upon time will not be explored here but the problem of the time dependence will be reexamined with greater precision below.

Pressure Dependence of the Rate of Absorption. The pressure dependence of the rate of absorption was examined at 195 and 273 K for type I samples. Figure 3 shows data obtained at 195 K where amounts of hydrogen absorbed, Δn_t , after various times, Δt , e.g., 1, 10 min, have been plotted as a function of pressure. Since the absorption is very slow at 195 K, these all represent initial rates of absorption. The slopes, c , determine the pressure dependence

$$\log(\Delta n/\Delta t) = \log K + c \log p \quad (1)$$

where K is a constant. The slopes are seen to be very close to $1/2$ over a pressure change from 2.5 to 31 mmHg.

A further test of the pressure dependence at a different temperature was made as follows: hydrogen was introduced (273 K) at a relatively large pressure (215 mmHg) and after a given time period had elapsed (before equilibrium had been established), a small amount of hydrogen was removed from the gas phase. After this removal, the pressure over the sample at first increased slightly, due to desorption from near the surface where the chemical potential of dissolved hydrogen, μ_H (near surface) $>$ μ_H (gas phase), and thereafter decreased as absorption proceeded since μ_H (gas) $>$ $\bar{\mu}_H$ (bulk). Since the absorption took place at a very slow rate at 273 K, it occurred at a nominally constant n . The rate could be followed at nearly constant values of n and over a large pressure range by repeatedly removing increments of hydrogen. The rate was again closely proportional to $p_{H_2}^{1/2}$ over a pressure range from 4 to 130 mmHg (Figure 4). It is seen from this figure that the rate is lower at the greater value of n . This is expected if the absorption is diffusion controlled. The application of pressures in the range 4–130 mmHg results in concentrations of hydrogen adjacent to the surface related to these pressures. The resulting concentration gradient will be larger at a given pressure, the smaller is the initial concentration within the sample (Figure 4). The initial desorption of hydrogen which has been noted, following the evacuation of an increment from the gas phase, illustrates the dynamic character of the equilibrium between the gas phase, surface, and bulk.

The dependence of the rate of absorption upon $p_{H_2}^{1/2}$ is consistent with, but does not prove, diffusion control since an interface controlled reaction could also depend upon $p_{H_2}^{1/2}$. However, if the rate were surface controlled,

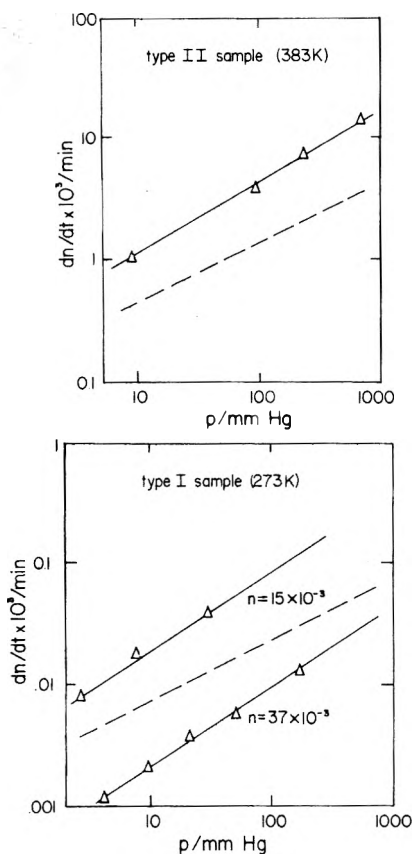


Figure 4. Plot of the log (rate of hydrogen absorption) against log p_{H_2} for type I sample at 273 K and type II sample at 383 K. The dashed lines represent slopes of one-half.

the most usual circumstance in metal/gas reactions, the rate of hydrogen absorption at small hydrogen contents should be proportional to the first power of the pressure under the initial conditions where the reverse reaction can be neglected. The pressure dependence is apparently independent of n from e.g., 0.46×10^{-3} (195 K) to 37×10^{-3} (273 K). It has been shown that Sieverts' law, i.e., $n = K_s p_{H_2}^{1/2}$, is obeyed only over a very limited range of n values in this system.^{5,10} Unfortunately equilibrium solubility data are not available at either 195 or 273 K with which to compare the pressure dependence. In any case, the initial rates (Figure 3) also have an approximate square-root dependence upon the hydrogen pressure.

Effect of Stoichiometry on the Rate of Absorption. The rate of absorption was determined for various stoichiometries of $LaNi_{5+x}$. The initial rates are plotted against x in Figure 5 (423 K) where the starting pressure was 1.8 mmHg. The rate varied with stoichiometry, attaining a maximum value at the stoichiometric compound.

Absorption by a Single Sphere. The evidence cited above with the multisized particles (type I) suggests that diffusion is the slow step in the absorption process in the hydrogen solubility region before formation of the hydride phase. In order to verify that the slow step is indeed bulk diffusion of hydrogen and to determine diffusion constants, a well-defined geometry is needed. For this purpose a sample of $LaNi_5$ closely approximating a sphere ($r_0 = 0.27$ cm) was prepared by arc-melting within a small hemisphere. The nearly spherical sample was small enough (0.6 g) so that the pressure fall during the absorption could be kept quite small so that the boundary condition at $r = r_0$ could be assumed constant. (The fact that the rate of absorption depends on $p_{H_2}^{1/2}$ rather than p_{H_2} helps to decrease the effect of a small change of pressure upon the rate.)

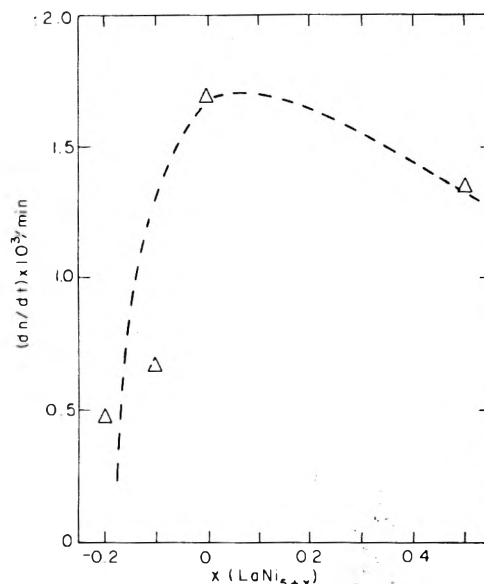


Figure 5. Plot of initial rate of hydrogen absorption against x where x is defined by $LaNi_{5+x}$. The initial pressure is 1.79 mmHg (423 K).

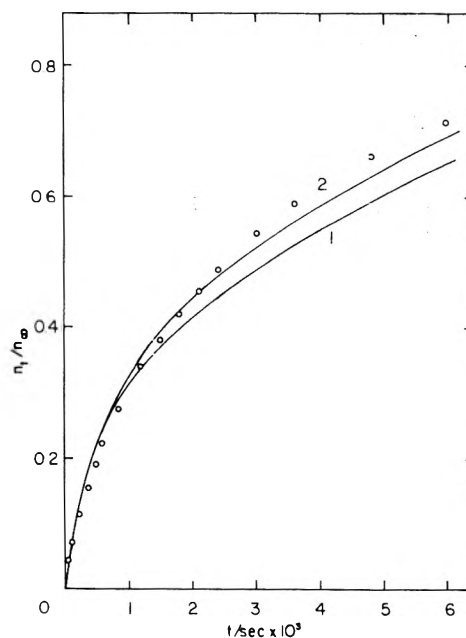


Figure 6. Plot of n_t/n_∞ against time for the sphere of $LaNi_5$ (type II sample, 423 K) where n_t and n_∞ are the H-to- $LaNi_5$ g atom to formula weight ratios at any time and at infinite time: O, experimental data; curve 1 is calculated from eq 2 with $D^* = 7 \times 10^{-7}$ cm²/s and curve 2 is calculated using eq 6 and eq 2 with $W_{H+} = 14.2$ kJ/g atom of H.

The first several runs with the sphere gave somewhat slow absorption rates but thereafter the rates were very reproducible. A typical absorption run is shown in Figure 6 (423 K), where n_t/n_∞ is plotted against t where n_t is the value of n at any time t and n_∞ is the value at equilibrium. The values of n_∞ can be determined from the p - c - T data established elsewhere.¹⁰ The calculated absorption data are determined from the solution for diffusion into a sphere at the constant boundary condition of n_∞ at $r = r_0$ and at $t = 0$, $n_t = 0$, i.e.

$$n_t/n_\infty = 1 - \frac{6}{\pi^2} \sum_{m=1}^{\infty} \frac{1}{m^2} \exp[-(m^2 \pi^2 Dt/r_0^2)] \quad (2)$$

where the value of D has been selected for best fit and $D = 7 \times 10^{-7}$ cm²/s (423 K). It can be seen that the general agreement is good enough to support the notion that the

slow step is diffusion. The details of the agreement are not good, however, mainly because the experimental amount absorbed exceeds that predicted at large times. If a larger value of D had been selected, the agreement at large times would be improved but the agreement at small times would suffer.

If the absorption isotherms are examined,¹⁰ it is clear that the system is very nonideal, i.e., Sieverts' law is followed only over a very small range. It would be expected, therefore, that D will not be independent of concentration. The relationship between the concentration-dependent diffusion constant, Fick's diffusion constant, $D(c)$, and the concentration-independent constant, Einstein's, D^* , is given by

$$D(c) = D^* \frac{c}{RT} (d\mu_H/dc) \quad (3)$$

where c represents moles of H per cm³ and $c \sim n/\bar{V}_{\text{LaNi}_5}$ and \bar{V}_{LaNi_5} is the molar volume of LaNi₅. $d\mu_H/dc$ can be derived directly from the pressure-composition-temperature data,¹⁰ since $\mu_H = \frac{1}{2} \mu_{\text{H}_2}^\circ + RT \ln p_{\text{H}_2}^{1/2}$. Alternatively $RT \ln p_{\text{H}_2}^{1/2}$ can be represented by the following equation:

$$RT \ln p_{\text{H}_2}^{1/2} = \mu_{\text{H}_2}^\circ - \frac{1}{2} \mu_{\text{H}_2}^\circ + RT \ln n/(1-n) + 2W_{\text{HH}} n \quad (4)$$

where W_{HH} is positive and represents an apparent H/H repulsive interaction, the nonideal term, the remaining terms correspond to the ideal partial configurational entropy and the standard terms. Therefore $d\mu_H/dc$ can be given in analytical form as

$$\frac{d\mu_H(n)}{dn} \frac{dn}{dc} = \frac{d\mu_H}{dc} = \left[\frac{RT}{n(1-n)} + 2W_{\text{HH}} \right] \bar{V}_{\text{LaNi}_5} \quad (5)$$

where it has been assumed that $c \approx n/\bar{V}_{\text{LaNi}_5}$ which is a good approximation in the low content region, where \bar{V}_{LaNi_5} is the molar volume of LaNi₅. Insertion of eq 5 into eq 3 gives

$$D(\bar{n}) = D(1 + 2W_{\text{HH}} \bar{n}/RT) \quad (6)$$

where $(1 - \bar{n}) \approx 1$ and \bar{n} represents the average concentration within the sphere at any time. The solution of the diffusion equation with concentration-dependent diffusion constants is shown in Figure 6 where it can be seen that much better agreement results. In order to obtain this agreement, a value of $W_{\text{HH}} = 14.2$ kJ/H was taken, which is somewhat larger than obtained earlier¹⁰ but corresponds to that obtained by Neumann.⁵ An error, of course, arises from using average values of n to calculate $D(n)$ since the diffusion constant is radially dependent at any time. This may partially account for the need of a larger nonideal term. Evidence that nonideality causes the deviation from the calculated curve with constant D can also be seen from data at 353 K where the deviation is greater than at 423 K (Figure 7). This is expected because the nonideality is greater at lower temperatures.¹⁰ Again the correction as derived from ref 5 gives good agreement.

The pressure dependence can also be determined from the variation of the initial rate of absorption by the sphere at various pressures. This is useful because this dependence can be established under conditions where p - c - T data are available. The pressure dependence was determined at small hydrogen contents where Sieverts' law should be a reasonable approximation. In these experiments the temperatures were high (353–463 K) compared to those in which the pressure dependence was established for the type I samples. The exponent of the pressure

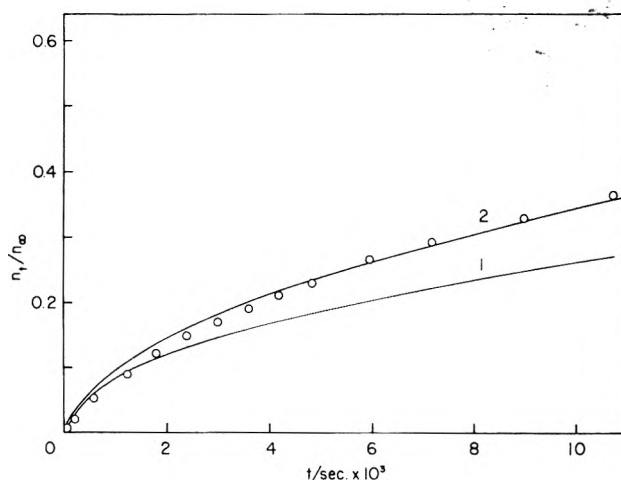


Figure 7. Plot of n_t/n_∞ for the sphere of LaNi₅ (type II sample, 353 K): O, experiment; curve 1 is calculated from eq 2 with $D^* = 5 \times 10^{-8}$ cm²/s and curve 2 is calculated with the same value of D^* and the correction for nonideality (eq 6) with $W_{\text{HH}} = 31.3$ kJ/H.

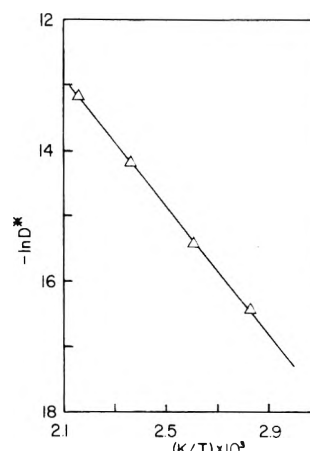


Figure 8. Plot of $\ln D^*$ against $1/T$ for the sphere of LaNi₅ (type II sample). The slope gives $E_{\text{diff}} = 40$ kJ/g atom of H.

dependence was established with two pressures (8.8 and 92.9 mmHg) at 353, 423, and 463 K, and was 0.56 ± 0.04 . At 383 K the exponent was determined at four pressures (Figure 4) and was 0.59. These results are in substantial agreement with those obtained for the type I samples.

The difficulty in obtaining accurate values of D at each temperature arises from the concentration dependence of D , which is different at each temperature. If the concentration-independent diffusion constants, which have been corrected for nonideality to give best fits to the experimental data, are employed, $E_{\text{diff}} = 40$ kJ/g atom of H (Figure 8). One difficulty with this procedure is that the lower temperature data do not cover as large a range of values of n_t/n_∞ as the high temperature data. Therefore the fit of the calculated and experimental data is not over a uniform range and the value of D^* may reflect this. It is desirable therefore to determine E_d by some other procedures. One method to eliminate the concentration dependence is to extrapolate the values of D at each temperature to $n \rightarrow 0$. The values near $n = 0$ are somewhat uncertain, however, because of the finite time lag necessary for the initiation of the reaction. These methods have been used at two different initial pressures (8.8 and 92 mmHg) and they give an energy of activation of 40 ± 4 kJ/g atom of H. The value of D^* is then

$$D^* = 3 \times 10^{-2} \exp\{-[(40000 \pm 4000 \text{ J})/RT]\}$$

It has been observed that there is a tendency for E_d to decrease with \bar{n} , e.g., there is an approximate decrease of

6 kJ/g atom of H in passing from $\bar{n} = 5 \times 10^{-3}$ to 30×10^{-3} .

Conclusions

It has been shown by the use of a sphere of LaNi₅ that the computed rates of absorption, assuming a concentration-dependent diffusion constant, agree well with experimental data. A diffusion-limited slow step rationalizes the observation that the rate of absorption is remarkably reproducible whereas for a surface-controlled absorption such reproducibility would not be expected in the absence of extreme care for surface cleanliness. The H₂ → 2H dissociation reaction at the surface of LaNi₅ must be rapid and not readily subject to poisoning by, e.g., oxygen.

Acknowledgment. The authors wish to thank the National Science Foundation for financial support of this

research. We thank B. Bowerman for help in computer programming of the diffusion equation.

References and Notes

- (1) F. A. Kuijpers, "Hydrogen in Metals", Vol. II, Julich, 1972, p 679.
- (2) F. A. Kuijpers, *Philips Res. Rep. Suppl.*, No. 2, 1 (1973).
- (3) A. Biris, R. V. Bucur, P. Ghete, E. Indrea, and D. Lupu, *J. Less-Common Met.*, **49**, 477 (1976).
- (4) O. Boser, *J. Less-Common Met.*, **46**, 91 (1976).
- (5) H. -H. Neumann, Ph.D. Thesis, Darmstadt, 1969.
- (6) J. S. Raichlen and R. H. Doremus, *J. Appl. Phys.*, **42**, 3166 (1971).
- (7) W. Auer and H. J. Grabke, *Ber. Bunsenges Phys. Chem.*, **78**, 58 (1974).
- (8) R. V. Bucur, V. Mœcca, and T. B. Flanagan, *Surf. Sci.*, **54**, 477 (1976).
- (9) K. H. J. Buschow and H. H. van Mal, *J. Less-Common Met.*, **29**, 203 (1972).
- (10) S. Tanaka and T. B. Flanagan, *J. Less-Common Met.*, **51**, 79 (1976).
- (11) R. Barrer and B. E. Fender, *J. Phys. Chem. Solids*, **21**, 12 (1961).
- (12) J. Völkl and G. Alefeld in "Diffusion in Solids", A. S. Nowick and J. J. Burton, Ed., Academic Press, New York, N.Y., 1975, p 232.

Studies of Cationic Radicals in γ -Irradiated Single Crystals of α -Aminoisobutyric Acid and Related α -Amino Acids by Electron Spin Resonance and SCF MO INDO Calculation[†]

Atsuko Minegishi

Radiation Chemistry Laboratory, Tokyo Metropolitan Isotope Research Center, 2-11-1, Fukazawa-cho, Setagaya, Tokyo, Japan
(Received October 20, 1976; Revised Manuscript Received May 31, 1977)

The cationic radical of the single crystal of α -aminoisobutyric acid γ irradiated at 77 K was identified as the deprotonated cation radical, NH₂C(CH₃)₂COO[•], by X- and Q-band ESR including photobleaching measurement. The eigenvalues of the *g* tensor were determined to be 2.0052, 2.0021, and 2.0013. The eigenvector of *g*_{max}(2.0052) is perpendicular to the molecular plane and the density axis of the unpaired electron orbital, i.e., the eigenvector of *g*_{int}(2.0021), is parallel to the molecular axis (Y axis). The eigenvector of *g*_{min}(2.0013) is on the molecular plane and perpendicular to the molecular axis. In addition to the hyperfine coupling by methyl protons, the hyperfine coupling by N was estimated, which is axially symmetric to the molecular axis and gives the unpaired electron density on N as 0.1 for 2p, and 0.01 for 2s. These features were supported by SCF MO INDO calculations. The deprotonated cation radical and the hydrogen bonded cation radical, the precursor of the former, show similar unpaired electron orbitals consisting of 2p_s of the skeleton atoms, but the *g* anisotropy of the deprotonated cation radical is smaller compared with that of the cation radical. The cationic radicals of L- α -alanine and glycine were also similarly investigated and assigned to the deprotonated cation radicals as mentioned above.

1. Introduction

At the initial stage of the radiolysis of solid sulfurless α -amino acids, it is known that an electron ejected from a parent molecule by γ - or X-irradiation is captured by a carboxyl group of the molecule and produces an anion radical, [•]NH₃CR₁R₂COO²⁻, or further [•]NH₃CR₁R₂COOH⁻ by proton abstraction from the neighboring molecule, where R₁ and R₂ represent a H atom or an alkyl group.¹⁻⁷

In contrast with the general agreement on the structure of anion radicals no definite information concerning the cationic radicals have so far been obtained.

Recently, a few papers have been published discussing the initial damage centers formed in α -aminoisobutyric acid (α -AIBA, [•]NH₃C(CH₃)₂COO⁻) by both γ - and X-

irradiation. Box and Freund⁸ reported that the ESR spectra of X-irradiated single crystal of α -AIBA at 77 K consisted of a strong central line due to the radical [•]NH₃C(CH₃)₂COO²⁻ and a satellite line signal which corresponds to the cation radical itself or its decomposed radical. While, Fujimoto, Seddon, and Smith⁹ in a more recent publication assigned the satellite line species to [•]NH₂C(CH₃)₂COO⁻, and interpreted that the hyperfine splittings were induced from the interaction of the unpaired electron with the nitrogen and the two hydrogen nuclei. Cadena, Linder, and Rowlands¹⁰ argued against the assignment by Fujimoto et al. and assigned the species as a planar conformation of the radical (CH₃)₂CCOOH, in which the hyperfine splittings by six protons of two CH₃ were considered.

Recently, the author and co-workers¹¹ studied the ESR spectra of γ -irradiated single crystals of α -AIBA and partially deuterated α -aminoisobutyric acid (part-d- α -AIBA, [•]ND₃C(CH₃)₂COO⁻) including photobleaching experiment, and assigned the satellite line species to the

[†]This study has been presented at the 15th Discussion Meeting of ESR in Japan (October 1976), Abstract p 119, and the conclusions have been supported by the ENDOR study of H. Muto, M. Iwasaki, and Y. Takahashi, simultaneously presented at the meeting, Abstract p 122.

cation radicals $^+\text{NH}_3\text{C}(\text{CH}_3)_2\text{COO}^-$ and $^+\text{ND}_3\text{C}(\text{CH}_3)_2\text{COO}^-$, respectively, assuming that the hyperfine splittings may be caused by the interaction between the unpaired electron orbital on the oxygen atom and six protons in the neighboring two methyl groups.

However, very recently, Box, Freund, Lilga, and Budzinski¹² measured the ENDOR spectra of X-irradiated part-d- α -AIBA at 4.2 K and determined the hyperfine coupling tensors for four protons. They state in an additional note to their Table I that two other weak proton couplings associated with the satellite line species could not be completely characterized by ENDOR.

These ENDOR study results, which contained some differences in the isotropic hyperfine coupling values from ours, made it necessary for this author to reexamine the analysis of the satellite line species.

In this paper, the satellite line species was further investigated in more detail by X- and Q-band spectroscopies, including correction of the g tensor and photobleaching experiment, and assigned as the deprotonated cation radical $\text{NH}_2\text{C}(\text{CH}_3)_2\text{COO}^-$. It was also found that the density axis of the unpaired electron orbital consisted mainly of the $2p_y$ orbitals of the skeleton atoms of the radical, is on the molecular plane, and is directed along the molecular axis, and that its g anisotropy is as small as those of hydrocarbon radicals.

Theoretical calculations for electronic features, including the g tensor, were examined for the deprotonated cation radical and its precursor, the cation radical of α -AIBA in a single crystal, using Pople's SCF MO INDO^{13,14} and by Stone's equation.¹⁵ These calculated results seem to support our experimental facts. The calculated direction cosines of the density axis of the unpaired electron orbital of the deprotonated cation radical agree with experiment.

Furthermore, an investigation was made using the same procedure for L- α -alanine and glycine which had a similar molecular conformation in their single crystals as that of α -AIBA, and the satellite line signals in the ESR spectra of γ -irradiated single crystals at 77 K were also assigned as deprotonated cation radicals similar to the case for α -AIBA.

2. Experimental Section

α -Aminoisobutyric acid, L- α -alanine, and glycine were used after recrystallization and their deuterated compounds, in which polar protons were replaced by deuterons, were prepared by repeated crystallization from heavy water solutions. Single crystals of these purified compounds were grown in desiccators containing P_2O_5 by the slow evaporation of the saturated aqueous or heavy water solutions at room temperature. α -Aminoisobutyric acid was supplied by Wako-Junyaku Co. Ltd., and L- α -alanine and glycine were supplied by Ajinomoto Co. Ltd., and Yukigose-Kogyo Co. Ltd., respectively.

The single crystal of α -aminoisobutyric acid,¹⁶ $^+\text{NH}_3\text{C}(\text{CH}_3)_2\text{COO}^-$, is rhombic and belongs to the space group $C_{2h}^6-C_{2/c}$ with unit cell constants $a = 10.59$ kX,¹⁷ $b = 8.97$ kX, $c = 11.34$ kX, and $\beta = 94 \pm 0.5^\circ$. There are eight molecules in the unit cell.

The single crystal of L- α -alanine,¹⁸ $^+\text{NH}_3\text{CHCH}_3\text{COO}^-$, is orthorhombic and the space group is $P_{2_1,2_1}$. The unit cell constants are $a = 6.032$ Å, $b = 12.343$ Å, and $c = 5.784$ Å. The number of molecules in the unit cell is four.

The single crystal of glycine,¹⁹ $^+\text{NH}_3\text{CH}_2\text{COO}^-$, is monoclinic and the space group is $C_{2h}^5-C_{2_1/n}$. The unit cell constants are $a = 5.1020$ Å, $b = 11.9709$ Å, $c = 5.4575$ Å, and $\beta = 111^\circ 42.3'$. The number of molecules in the unit cell is four.

In this paper, the c' axis is defined as perpendicular to the a and b axes for α -aminoisobutyric acid and glycine.

Since accurate crystal structures of these partially deuterated amino acids, $^+\text{ND}_3\text{CR}_1\text{R}_2\text{COO}^-$, were not available, they were treated the same as the crystal structures for normal α -amino acids in this paper.

The single crystals were irradiated at 77 K by ^{60}Co γ -rays. The dose rate was 4×10^5 rd/h and the total doses were $1 \sim 7 \times 10^6$ rd.

The X-band ESR spectra were measured at 77 K with a JEOL Model JVR-3 spectrometer operated at 9.2 GHz. The ESR spectra were recorded mainly as a second-derivative representation with 80-Hz and 100-kHz double modulation. For Q-band ESR spectrometry, a JEOL Model JES-3BS spectrometer was operated at 35 GHz. Microwave frequencies were estimated for the X-band by using a resonant-cavity wavemeter attached to the wave guide between the klystron and the magic T, and for the Q-band by using a calibrated dial scale of the frequency changer attached to the cavity resonator of the reflection-type klystron.

The angular dependence of the ESR spectra were measured at 2.5 – 10° intervals by rotating the crystals around the a , b , and c axes perpendicular to the external magnetic field.

A Toshiba-Daylight 500-W tungsten lamp was used for photobleaching of the γ -irradiated samples.

3. α -Aminoisobutyric Acid

3.1. Experimental Results. (I) Spectral Change due to Proton-Deuteron Exchange of Amino Protons. Single crystals of α -aminoisobutyric acid (α -AIBA) and its partially deuterated compound (part-d- α -AIBA) were γ -irradiated at 77 K. In their ESR spectra, a satellite line signal was superposed on a broad singlet absorption of the anion radical^{7,8} as shown in Figure 1.

For α -AIBA and part-d- α -AIBA, the satellite line signals indicate the same g values at the a , b , and c axes (Table I). The exchange of amino protons by deuterons does not alter the overall total widths of these satellite line signals remarkably (within 5 G) but induces a slight difference in the spectral shapes between them.

These facts suggest that the paramagnetic species giving rise to the satellite line signals of α -AIBA and part-d- α -AIBA have almost the same chemical structure, in which an unpaired electron is not localized remarkably on the amino protons. The slight difference in the spectral shapes may be attributed to the difference of the nuclear spins of the amino protons and deuterons and to the difference of the restricted positions of the rotated methyl groups concerning the hyperfine interaction.

(II) Disappearance of the Cation Radical by Irradiation with the Visible Light. The ESR signals of the anion radical and the satellite lines disappear simultaneously by irradiation with a 500-W tungsten visible light without producing any new signal. The spectra, before and after photobleaching, are shown in Figure 2a,b. Photobleaching by visible light suggests a charge neutralization reaction between a cationic radical and an electron reejected from the anion radical by the visible light, and indicates that the satellite line species should be a cationic radical.

Figure 2c is a magnified spectrum of Figure 2b with sufficient gain to show the signal of a radical produced by prolonged γ irradiation and barely surviving after photobleaching. Seven lines observed in these spectra are similar to the spectra of the deamino radical, $\text{C}(\text{CH}_3)_2\text{COO}^-$, which was observed at 165 K and identified by Box and Freund.^{8,20}

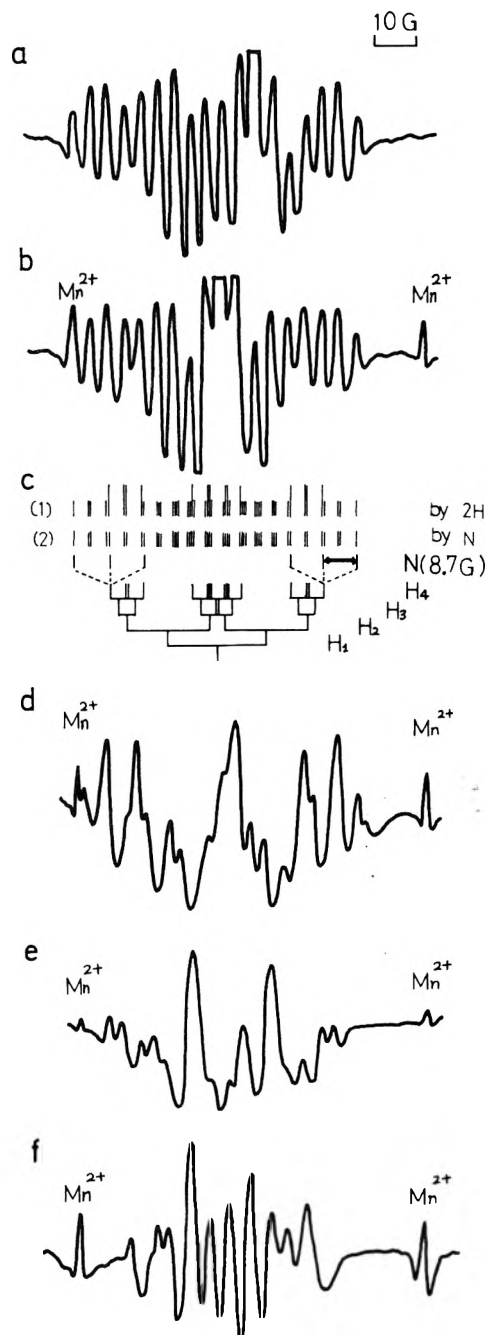


Figure 1. Second derivative ESR spectra of γ -irradiated single crystals of α -aminoisobutyric acid, L- α -alanine, and glycine at 77 K. The external field is applied along the c' (or c for L- α -alanine) axis. (a) Q-band ESR spectrum for partially deuterated α -aminoisobutyric acid. (b) X-band ESR spectrum for partially deuterated α -aminoisobutyric acid. (c) Assignment of hyperfine splittings for the satellite line signals of partially deuterated α -aminoisobutyric acid: (1) by four H determined by Box et al.¹² and two equivalent H; (2) by four H and N. The author concluded that the hyperfine splitting in question is due to N (see section 3.1.IV). (d) X-band ESR spectrum for normal α -aminoisobutyric acid. (e) X-band ESR spectrum for partially deuterated L- α -alanine. (f) X-band ESR spectrum for partially deuterated glycine.

(III) *Determination of the g tensor.* For an accurate determination of the angular dependence of the g values by one of the X-band or Q-band ESR spectroscopies, it is necessary to distinguish the superposed signals of the two sites.

For the satellite line species of part-d- α -AIBA, however, the superposed signals of the two sites with an external field perpendicular to the a and c axes present broad, complex, and undistinguishable appearances in almost all directions, and thus the determination of the g values

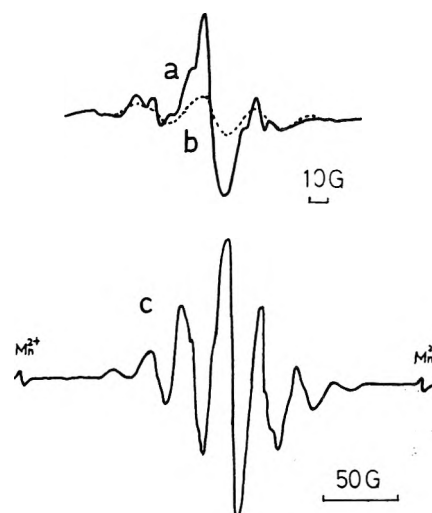


Figure 2. ESR spectra of the γ -irradiated single crystal of α -aminoisobutyric acid (a) before and (b) after photobleaching with a 500-W tungsten light at 77 K: (c) magnified spectrum of (b).

TABLE I: g Values and Hyperfine Couplings (A) of the Satellite Line Signal in the ESR Spectra of γ -Irradiated Single Crystals of Partially Deuterated α -Aminoisobutyric Acid at 77 K^a

	g	$A_{H_1},^b$ G	$A_{H_2},^b$ G	$A_{H_3},^b$ G	$A_{H_4},^b$ G	$A_N,^{c,f}$ G
$a \parallel H$	2.0041	22.7	21.3	6.9	6.5	$\geq 1.7^d$
$b \parallel H$	2.0024	24.0	19.6	5.4	4.2	$\gg 4.3^{d,f}$
$c' \parallel H$	2.0019	24.5	20.9	4.5	3.9	8.7 ^e

^a The external field (H) is applied parallel to the a , b , and c' axes, in which the c' axis is perpendicular to the a and b axes. ^b A_{H_1} , A_{H_2} , A_{H_3} , and A_{H_4} show the hyperfine couplings of the four protons determined by Box et al.¹² ^c A_N shows the hyperfine coupling by a nitrogen. The explanation for this splitting by the two equivalent protons (1:2:1 splitting) was eliminated by the reason described in section 3.1.IV. ^d These values are derived from the spectral width of the broader signal by eliminating the contribution of A_{H_1} , A_{H_2} , A_{H_3} , and A_{H_4} . ^e This value is obtained exactly from the distance between the two neighboring peaks as shown in Figure 1c. ^f The angular variation of A_N around the c axis shows an anomalous curve compared with those around a and b axes, where A_N around the a axis decreases from c' parallel to H to b parallel to H and A_N around b axis varies roughly by the relation, $A_N(\theta) = 8.7(\text{G}) \cos^2 \theta + 1.7(\text{G}) \sin^2 \theta$. The larger value of A_N in b parallel to H , 4.3 G, compared with that in a parallel to H , 1.7 G, may be explained by the contribution of the other nucleus, such as the remaining two protons, and the net value of A_N may be nearly equal to A_N in a parallel to H . Then, it may be expected that the hyperfine coupling of A_N is axially symmetric and its maximum is directed along the c' axis.

becomes rather difficult and remains uncertain.

However, when both the X- and Q-band spectra are obtained under suitable conditions to hold the same shape of each site at both bands, it is possible to estimate the g difference between the two sites from the difference of the overall total widths of X-band and Q-band spectra as described in the following. Combining this method with the usual g determination from known peaks, determination of g angular dependence becomes possible.

(a) *Estimation of g Difference of the two Sites, $\Delta g = g_1 - g_2$, from the Overall Total Widths of Superposed Signal of the Two Sites.* (a-1). The overall total widths of the partially superposed signal of the two sites, having g values of g_1 and g_2 , respectively, are assumed to be l_X and l_Q corresponding to X-band and Q-band ESR, respectively. The magnetic field at the center of the signal of each site

is represented as $H(X_1)$ and $H(X_2)$ for X-band, and $H(Q_1)$ and $H(Q_2)$ for Q-band, respectively. When the signal of the two sites partially overlapped each other at X-band and Q-band, the difference of overall total widths Δl between the X- and Q-band spectra is

$$\Delta l = l_Q - l_X = [H(Q_2) - H(Q_1)] - [H(X_2) - H(X_1)] \quad (1)$$

At each Q- and X-band frequency, ν_Q and ν_X , the resonance condition

$$h\nu = g\beta H \quad (2)$$

holds for the centers $H(Q_1)$, $H(Q_2)$, $H(X_1)$, and $H(X_2)$, where β is Bohr magneton, and h is Planck's constant. Equation 1 is further expressed as follows

$$\begin{aligned} \Delta l &= \frac{h}{\beta} \left[\nu_Q \left(\frac{1}{g_2} - \frac{1}{g_1} \right) - \nu_X \left(\frac{1}{g_2} - \frac{1}{g_1} \right) \right] \\ &= \frac{h}{\beta} \frac{g_1 - g_2}{g_1 g_2} (\nu_Q - \nu_X) \end{aligned} \quad (3)$$

and thus

$$\Delta g = g_1 - g_2 = \Delta l \frac{g_1 g_2}{\nu_Q - \nu_X} \frac{\beta}{h} \quad (4)$$

The difference in g values of the two sites, both near $g_e = 2.0023$, is given by eq 5, at $\nu_X = 9.2$ GHz and $\nu_Q = 35$ GHz.

$$\Delta g = g_1 - g_2 = \Delta l (\text{Gauss}) \times 2.2 \times 10^{-4} (\text{Gauss}^{-1}) \quad (5)$$

(a-2). When the overall total widths of the X-band and Q-band spectra are identical, it means that the narrower signal in one of the two sites is included in the broader signal of the other site observed in both bands and that the g value of the broader site is determined accurately from the value of the spectral center.

(a-3). When the broader signal includes the narrower one at X-band and partially overlaps the latter at Q-band, the true Δg should be greater than the g value calculated from eq 4.

(b) *Determination of the g tensor of the Satellite Line Species.* For an external field (H) rotated around the a axis, satellite line signals having the characteristics discussed in (a-2) were obtained in many directions, and for H rotated around the b axis, the signals of one site were obtained. When H was rotated around the c axis, signals corresponding to (a-1) were obtained. For example, Δg values evaluated from eq 5 for H rotated around the c axis are shown in Figure 3. The determined g angular dependence is illustrated in Figure 4.

The determined g tensor is shown in Table II. The g tensor shows relatively small anisotropy, and the direction of the unpaired electron orbital is estimated to be an eigenvector belonging to the g_{int} closest to g_e .

As shown in Figure 5-1, molecules in a single crystal of α -AIBA exist in a zwitterion form and the parent molecule A is linked to the neighboring molecules with four hydrogen bonds as follows: O(1)(molecule A)---N(molecule E), O(2)(molecule A)---N(molecule G'), N(molecule A)---O(1)(molecule E), and N(molecule A)---O(2)(molecule G), where the second and the fourth hydrogen bonds are parallel to the molecular axis defined as the bisector of O(1)-C-C-O(2).¹⁶ In these rigid hydrogen-bonded lattices, it may be assumed that the orientation of the initially produced cationic radical and its surrounding molecules is scarcely affected, and takes the same configuration as the molecules before γ irradiation at 77 K.

Then, the eigenvectors of the obtained g tensor are

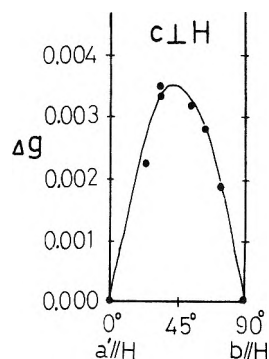


Figure 3. The difference of g values between two sites, $\Delta g = g_1 - g_2$, of the satellite line signals for a single crystal of deuterated α -aminoisobutyric acid γ irradiated and measured at 77 K. The external field is perpendicular to the c axis.

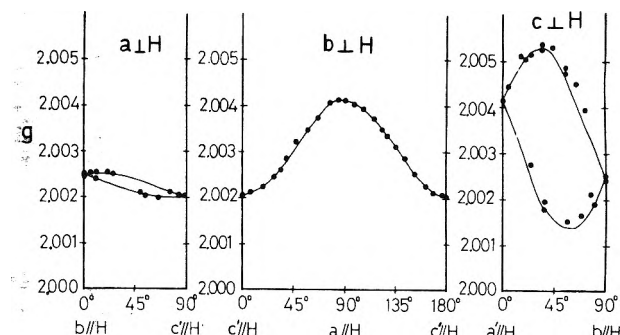


Figure 4. Angular dependence of the g values for the satellite line species (assigned as the deprotonated cation radical) in a single crystal of partially deuterated α -aminoisobutyric acid γ -irradiated and measured at 77 K: (●) observed value; (—) theoretical curve.

TABLE II: Eigenvalues and Eigenvectors of the g Tensor for the Satellite Line Species (Assigned as the Deprotonated Cation Radical, $\text{ND}_2\text{C}(\text{CH}_2)_2\text{COO}$) in γ -Irradiated Single Crystals of Deuterated α -Aminoisobutyric Acid^a

Eigenvalues	Direction cosines		
	l_X	m_Y	n_Z
2.0052	1.000	-0.026	0.018
2.0021	0.027	0.999	0.019
2.0013	-0.018	0.034	0.999
a axis	-0.832	0.100	-0.545
b axis	-0.553	-0.072	0.831
c' axis ^b	0.044	0.992	0.115

^a Direction cosines are given with respect to the X , Y , and Z axes. The X axis is normal to the COO plane. The Y axis is the bisector of O(1)-C-C-O(2), and the Z axis is perpendicular to the X and Y axes. ^b The c' axis is perpendicular to the a and b axes.

compared with the several chemical bonds, lone pairs, molecular axes, and the molecular plane (COO plane) of the parent molecule A. The density axis of the unpaired electron orbital, i.e., the eigenvector of g_{int} is parallel to the molecular axis. The eigenvector of g_{max} is perpendicular to the molecular plane, and the eigenvector of g_{min} lies in the molecular plane and perpendicular to the molecular axis.

These facts are recognized as the characteristic orientation of the unpaired electron orbital which contributes to the composite direction of the related chemical bonds and the lone pair orbitals in the cationic radical.

A detailed discussion concerning the unpaired electron orbital and the small g anisotropy of the cationic radical will be discussed in section 3.1.V.

(IV) *Hyperfine Splittings of part-d- α -AIBA.* As reported recently by the author and co-workers,¹¹ the hy-

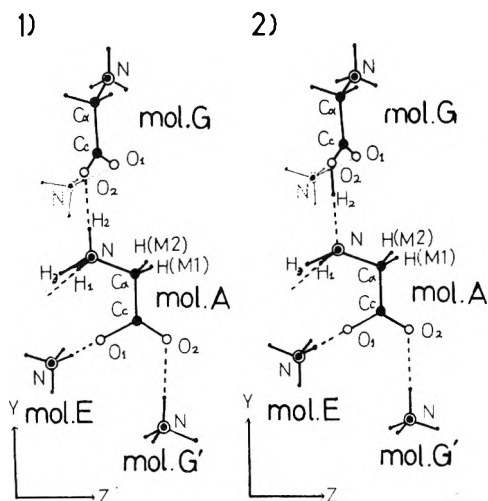


Figure 5. The projection of the molecular arrangement of α -aminoisobutyric acid to the YZ plane. The two CH $_3$ molecules are replaced by two H, and molecule E, molecule G', and molecule C are altered by NH $_4^+$, for simple treatment. (1) Molecules A and G take the zwitterion form as usual. (2) H $_2$ of molecule A transfers to O(2) of molecule G. Then, the deprotonated molecule A and protonated molecule G are formed.

perfine splittings of the satellite line species were estimated from the ESR spectra in the orientations, a parallel to H , b parallel to H , c' parallel to H , and some in b perpendicular to H , by the six protons in the neighboring molecules.

Very recently, however, Box et al.¹² studied the satellite line species by ENDOR measurement at 4.2 K, and determined the hyperfine tensors of four protons, which were considered to be four of the six inner protons of the radical. In the note to their Table I, it was also reported that two other weak proton couplings could not be completely characterized.

Looking at the results of the ENDOR study, this author felt it necessary to reexamine the hyperfine splittings of the ESR spectra by using the four hyperfine tensors determined by Box et al., and the following results were obtained other than those four hyperfine couplings. The hyperfine structure of the spectra can be explained either by a N nucleus (1:1:1 splitting) or by two equivalent protons (1:2:1 splitting), as well as by four protons, as shown in Table I. The hyperfine coupling in question had an average value of about 5 G and a larger anisotropy than those of the aforementioned four protons. If the hyperfine splitting was caused by two equivalent protons, their signals should be observed in the same region as those of the two weakly coupled protons determined by Box et al., A_{H_2} and A_{H_4} in Table I, in the ENDOR spectra. However, Box et al. reported that they did not observe such signals as described above. Therefore, it is concluded that the hyperfine splitting in question is due to a N nucleus. This conclusion was also supported by the fact that the spectral shape at c' parallel to H (as shown in Figure 1) is more suitably explained by considering a 1:1:1 splitting than by a 1:2:1 splitting. It is thought that the hyperfine couplings of the remaining two protons may be so minor as to contribute to the line width of the ESR signal and that their ENDOR signal may be in the region near the free proton frequency, where complex signals of uncertain couplings may mask the two signals.

The anisotropy of the hyperfine coupling by the N nucleus maintains axial symmetry and its maximum is directed along the molecular axis (nearly parallel to the c' axis). Then, it may be possible to consider that the hyperfine splitting by the N nucleus is caused by an

unpaired electron distribution extending to N-H(2)...O(2)(molecule G), which is parallel to the molecular axis of molecule A. The unpaired electron density on the N is estimated to be 0.01 for 2s and 0.1 for 2p $_y$, respectively²¹⁻²⁴ (see Appendix I).

In the present case, since the unpaired electron density on the amino protons is negligible (section 3.1.I), it is presumed that the H(2)⁺ of the N-H(2) bond of molecule G transfers to its hydrogen bonded O(2) in molecule A, leaving the deprotonated cation radical, NH $_2$ C(CH $_3$) $_2$ COO.

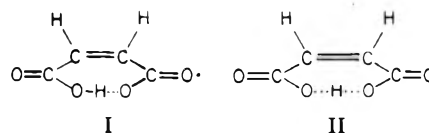
(V) *Discussion of the Experimental Results.* From the results of these ESR studies concerning the satellite line species of γ -irradiated single crystals of α -aminoisobutyric acid at 77 K, the following has been ascertained, and the deprotonated cation radical, NH $_2$ C(CH $_3$) $_2$ COO, was assigned.

1. Simultaneous bleaching of the satellite line signal and the broad singlet of an anionic radical of α -aminoisobutyric acid by visible tungsten light can be well explained if the satellite line signal is attributed to the cationic radical.

2. The satellite line signal also shows that the hyperfine splittings are produced by the four protons, which indicates a small anisotropy, and by a N atom, which shows axially symmetric anisotropy and A_{max}^N directed along the molecular axis. The N should belong to the N⁺-H(2) bond in molecule A.

3. The small deuteration effect on the spectral features suggests that the unpaired electron density is not remarkably localized on the amino protons of the satellite line species. Accordingly, it is presumed that the H(2)⁺ of the N⁺-H(2) bond transfers to the O(2) of -COO⁻ in molecule G.

4. The g tensor of the satellite line species (2.0054, 2.0022, and 2.0013) indicates small anisotropy compared with those of usual oxygen predominant radicals (OH: 2.013, 2.008, and 2.008;²⁵ HOOC(CH $_2$) $_2$ COO⁻: 2.019, 2.006, and 2.003;²⁶ I: 2.0261, 2.0061, and 2.0035;²⁷ II: 2.0303,



2.0071, and 2.0047;²⁸ and two carboxyl radicals of potassium deuterium fumarate: 2.0273, 2.0074, and 2.0033, and 2.0224, 2.0067, and 2.0023, respectively²⁹), but slightly larger anisotropy than those of carbon predominant radicals (HC(COOH) $_2$: 2.0038, 2.0033, and 2.0020;³⁰ H $_2$ C(COOH): 2.0042, 2.0034, and 2.0020³¹).

5. The density axis of the unpaired electron, defined from the eigenvector of g_{int} , is parallel to the molecular axis and the eigenvector of g_{max} is perpendicular to the molecular plane (COO plane). The eigenvector of g_{min} is on the molecular plane and parallel to the O(1)...O(2) line.

These facts suggest that the satellite line species is the deprotonated cation radical and that the unpaired electron orbital is distributed over the whole radical along the molecular axis and not localized extremely on the two oxygen atoms which have a large spin-orbit coupling constant with 2p orbital ($\zeta_0 = 151 \text{ cm}^{-1}$).

Debies and Rabalais³² observed, very recently, the ionization energies of vapor-phase glycine (130 °C) and alanine (145 °C), (undissociated and plane-formed amino acid, NH $_2$ CR $_1$ R $_2$ COOH), and compared with those of the related carboxylic acid and amines. The order of the electronic levels of NH $_2$ CR $_1$ R $_2$ COOH was found to be as follows: N nonbonding (perpendicular to the molecular plane) > carboxyl O nonbonding (lying on the molecular plane) > hydroxyl O nonbonding (perpendicular to the

molecular plane) > carboxyl π and σ core.

Correlating this information with the zwitterion-formed amino acid, $^+\text{NH}_3\text{CR}_1\text{R}_2\text{COO}^-$, it is expected that the highest occupied molecular orbital should be mainly attributed to the O-nonbonding orbitals of the COO^- group and that the unpaired electron orbital of the cation radical, $^+\text{NH}_3\text{CR}_1\text{R}_2\text{COO}$, is thus located on two oxygen atoms resulting in a large g anisotropy as the oxygen predominant radicals. From the small unpaired electron density on N, 0.1 for 2p and 0.01 for 2s, of the deprotonated cation radical, it is expected that the unpaired electron orbital would be similar to that of the cation radical. However, our experimental results are evidently in conflict with the expected large g anisotropy as described above.

In order to elucidate these problems, the electronic state of the cation radical and the deprotonated cation radical of α -aminoisobutyric acid in an irradiated single crystal will be calculated in the next section.

3.2. *Calculations of the Electronic State and g Tensor on the Cationic Radical Produced in a Single Crystal of α -Aminoisobutyric Acid γ Irradiated at 77 K.* (I) *Procedure.* Theoretical calculations of the electronic state and g tensor on the cationic radical of α -aminoisobutyric acid (α -AIBA) have been carried out. Pople's restricted SCF MO INDO (intermediate neglect of differential overlap) program^{13,14} has been used. The unpaired electron orbital of the ground state of the cationic radical is presumed to be the SOMO (semioccupied MO), which is equal to the HOMO (highest occupied MO) calculated on the ground state of the original parent molecular system. Since the wavefunction derived from the restricted SCF MO procedure is an eigenfunction of both S^2 and S_z ,¹⁴ the resultant MO can be applied to calculate the theoretical g value using Stone's equation.³²

The calculations by Pople's unrestricted SCF MO INDO program for the open-shell were also carried out for all cases treated in this paper. It was expected that the general relation would hold for all cases treated, namely, that the HOMO of α spin is similar to the LUMO (lowest occupied MO) of β spin and different from the HOMO of β spin for a radical.³³ Unexpectedly, however, the calculated results by the unrestricted SCF MO INDO program indicate that the HOMO of α spin was not similar to the LUMO of β spin but similar to the HOMO of β spin, and that the MO energy of each HOMO was very close to each other.^{34,35} Furthermore, the MO derived from the unrestricted SCF MO procedure cannot be applied to Stone's equation because the MO is an eigenfunction of S_z but not of S^2 .¹⁴ Because of these problems, the results of the unrestricted SCF MO INDO were omitted in this paper.

For the ground state of the cationic radical system, the resultant MO ψ_i is represented as

$$\psi_i = \sum_u (C_{i\text{us}}\phi_{\text{us}} + C_{i\text{ux}}\phi_{\text{ux}} + C_{i\text{uy}}\phi_{\text{uy}} + C_{i\text{uz}}\phi_{\text{uz}}) \quad (6)$$

where ϕ_{us} , ϕ_{ux} , ϕ_{uy} , and ϕ_{uz} are 2s, 2p_x, 2p_y, and 2p_z atomic orbitals of atom u (only for the H atom, ϕ_{is} is 1s) and $C_{i\text{us}}$, $C_{i\text{ux}}$, $C_{i\text{uy}}$, and $C_{i\text{uz}}$ are corresponding normalized coefficients.

Especially at $i = \text{S}$, i.e. in the SOMO, ψ_{S} , it is considered approximately that C_{Ss}^2 , C_{Sx}^2 , C_{Sy}^2 , and C_{Sz}^2 correspond to the unpaired electron densities for the respective atomic orbital of atom u and that the summation of these values on u ($C_{\text{Ss}}^2 + C_{\text{Sx}}^2 + C_{\text{Sy}}^2 + C_{\text{Sz}}^2$) indicates the unpaired electron density on atom u. $\sum_u C_{\text{Ss}}^2$, $\sum_u C_{\text{Sx}}^2$, $\sum_u C_{\text{Sy}}^2$, and $\sum_u C_{\text{Sz}}^2$ are the overall s, x, y, and z component of the unpaired electron distribution. Then, $\sum_u C_{\text{Sx}}^2/W$, $\sum_u C_{\text{Sy}}^2/W$, and $\sum_u C_{\text{Sz}}^2/W$ indicate the direction cosines

of the density axis of the unpaired electron orbital, where W is $\sum_u (C_{\text{Sx}}^2 + C_{\text{Sy}}^2 + C_{\text{Sz}}^2)$.

The g values were estimated by using the results of the above calculations. The g values of the radical (doublet state) are given by Stone's approximation¹⁵ as

$$g_{\text{rt}} = g_e \delta_{\text{rt}} - 2 \sum_{i \neq \text{S}} \frac{\langle \psi_{\text{S}} | \sum_k \zeta_k L_{\text{rk}} \delta_k | \psi_i \rangle \langle \psi_i | \sum_j L_{\text{tj}} \delta_j | \psi_{\text{S}} \rangle}{E_i - E_0} \quad (7)$$

(r = X, Y, or Z, and t = X, Y, or Z)

where δ_{rt} in the first term is 1 for $r = t$ and 0 for $r \neq t$. In the second term, ζ_k is the spin-orbit coupling constant for the 2p orbital of atom k, and $\delta_k = 1$ for the orbitals of atom k and 0 for those of the other atoms when L_{rk} , the orbital angular momentum operator about the center of atom k, acts on the atomic orbitals. Similarly, $\delta_j = 1$ for the orbitals of atom j and 0 for those of the others. In the second term of eq 7, $E_i - E_0$ is the energy difference between the i th excited state and the ground state and approximated by the MO energy difference, $\epsilon_i - \epsilon_{\text{S}}$, between the MO ψ_i and SOMO ψ_{S} of the ground state.

Finally, the G matrix, in which G_{rt} is $\sum_{m=\text{X,Y,Z}} g_{\text{rm}} g_{\text{mt}}$, is diagonalized in order to find the direction cosines and eigenvalues.

The equations derived from eq 7 are shown in Appendix II. The calculations were carried out by the following two computer systems: HITAC 8800/8700 and FACOM 230/50.

The analytical crystal data are used for the atomic positions and the coordinates adopted are as follows: the X axis, the normal of COO plane in molecule A (designated as the molecular plane); the Y axis, the bisector of O-(1)-C-C-O(2) in molecule A (designated as the molecular axis); the Z axis, the normal to the X and Y axes. The N-H bond length is assumed to be 0.95 Å as found in L- α -alanine.¹⁸ The two hydrogen bonded amino protons are regarded as lying on the two correspondent N...O lines and the remaining one is assumed to be located in the pyramidally equiangular direction of these N...O lines. It is assumed that the C-H bond length is 1 Å, and that the rotation of the two methyl groups is hindered.

(II) *Results and Discussion.* Calculations of the electronic states for the cation radical, $(^+\text{NH}_3\text{C}(\text{CH}_3)_2\text{COO})^+$, and the deprotonated cation radical, $\text{---NH}_2\text{C}(\text{CH}_3)_2\text{COO}^-$, have been carried out for the following systems. To simplify the treatment, both CH_3 groups of α -AIBA are replaced by two H, H(M1) and H(M2), respectively. The whole molecular arrangement is illustrated in Figure 5.

(1) The single molecular system concerning the isolated molecule (molecule A) in a single crystal.

(2) The hydrogen bonded system, which consists of molecule A and its hydrogen bonded neighboring molecules, molecules E, G', and G. Molecules E and G' are alternated with NH_4^+ (I) and NH_4^+ (II), respectively. NH_4^+ (I) is hydrogen bonded with O(1) of molecule A and the bonding direction is out of the molecular plane. NH_4^+ (II) is hydrogen bonded with O(2) in molecule A and the bonding direction is parallel to the molecular axis on the molecular plane. Molecule G is hydrogen bonded with the N-H(2) of molecule A, parallel to the molecular axis, and O(1) of molecule G is further hydrogen bonded with N-H(1) of molecule C. Molecule C is alternated with NH_4^+ (III). The hydrogen bonding between N(molecule A) and O(1) (molecule E) with an expected small contribution is neglected for simplicity. In the calculation of the deprotonated cation radical, O(2) of molecule G is protonated by H(2)⁺ of molecule A.

The unpaired electron orbital, i.e., SOMO, of the cation

TABLE III: Coefficients for Atomic Orbitals of Atom u Concerning SOMO, ψ_S , of Cationic Radicals in a Single Crystal of α -Aminoisobutyric Acid^a

$$\psi_S = \sum_u (C_{Sus} \phi_{us} + C_{Sux} \phi_{ux} + C_{Suy} \phi_{uy} + C_{Suz} \phi_{uz})$$

(a) Cation Radical in Single Molecular System^a (⁺NH₃CH₂COO⁻)⁺

u ^b	Molecule A										s, x, y, z ^c density component	
	O(1)	O(2)	Cc	C α	N	H ₁	H ₂	H ₃	H(M1)	H(M2)		
s	0.00	0.00	0.00	0.00	0.00	0.00	0.00	0.00	0.01	0.01	-0.01	0.00
p _x	-0.73	0.68	0.02	-0.01	0.02							0.99
p _y	-0.03	0.05	0.00	0.01	-0.00							0.00
p _z	-0.04	-0.04	0.00	0.00	0.00							0.00

(b) Cation Radical in Hydrogen Bonded System^{a,d,e} 2NH₄⁺ + (⁺NH₃CH₂COO⁻)⁺ + ⁺NH₃CH₂COO⁻ + NH₄⁺

u ^b	Molecule A										Mole- cule G	Molecule G'		s, x, y, z ^c density component
	O(1)	O(2)	Cc	C α	N	H ₁	H ₂	H ₃	H(M1)	H(M2)		O(2)	N	
s	0.03	0.01	-0.04	0.18	0.00	-0.02	0.07	-0.07	-0.06	-0.05	-0.01	-0.06	0.06	0.08
p _x	0.13	0.06	-0.01	0.01	-0.00						-0.05	0.01		0.02
p _y	-0.49	-0.64	0.18	-0.39	0.07						0.15	-0.10		0.88
p _z	0.08	0.12	-0.02	0.02	0.06						0.02	0.00		0.02

(c) Deprotonated Cation Radical in Single Molecular System^a (NH₃CH₂COO⁻)⁺

u ^b	Molecule A										s, x, y, z ^c density component
	O(1)	O(2)	Cc	C α	N	H ₁	H ₃	H(M1)	H(M2)		
s	0.04	0.02	-0.03	0.18	0.08	-0.01	-0.01	-0.07	-0.08	0.06	
p _x	0.01	0.05	-0.01	0.01	-0.01					0.00	
p _y	-0.56	-0.60	0.20	-0.42	0.18					0.93	
p _z	0.01	0.04	-0.01	0.03	0.07					0.01	

(d) Deprotonated Cation Radical in Single Molecular System^{a,e} 2NH₄⁺ + (NH₃CH₂COO⁻) + ⁺NH₃CH₂COOH + NH₄⁺

u ^b	Molecule A										Molecule G	Molecule G'		s, x, y, z ^c density component
	O(1)	O(2)	Cc	C α	N	H ₁	H ₃	H(M1)	H(M2)	O(2)		H ₂	N	
s	0.02	0.01	0.00	0.16	0.08	-0.02	-0.10	-0.08	-0.08	-0.02	0.03	-0.07	0.08	0.07
p _x	0.06	0.01	-0.01	0.02	-0.01					-0.01		0.01		0.00
p _y	-0.48	-0.62	0.23	-0.41	0.23					0.04		-0.10		0.91
p _z	0.06	0.08	-0.01	-0.02	0.07					0.00		-0.00		0.02

^a To simplify the treatment, two CH₃s of α -aminoisobutyric acid are replaced by two H, H(M1) and H(M2), respectively.^b Atoms with the unpaired electron density less than 0.01 are eliminated. ^c Overall s, x, y, and z component of unpaired electron density are denoted by $\sum_u C_{Sus}^2$, $\sum_u C_{Sux}^2$, $\sum_u C_{Suy}^2$, and $\sum_u C_{Suz}^2$, respectively. ^d This MO indicates the HOMO of the parent molecular system in a single crystal. ^e The secondary highest MO is $(0.7_{O(1)x} - 0.7_{O(2)x} + \dots)$, and the MO energy difference from the SOMO is -0.204 eV for (b) and -0.645 eV for (d), respectively.

radical and the deprotonated cation radical in these systems are summarized in Table III.

(1) *The Simple Molecular System of the Cation Radical.* As is clear from Table IIIa, the unpaired electron densities on O(1) and O(2) are 0.53 and 0.46, respectively, and the overall x component value of the unpaired electron density, $\sum_u C_{Sux}^2 = 0.99$, is most predominant compared with the overall y and z components. This result means that an unpaired electron is almost localized, 99%, on the two oxygen atoms and that the density axis of the unpaired electron orbital is perpendicular to the molecular plane.

These features, however, do not accord with the ESR experimental results that the g anisotropy is small and that the unpaired electron orbital is nearly along the molecular axis and not localized extremely on the two oxygen atoms nor on the carbon atoms (section 3).

(2) *The Hydrogen Bonded System of the Cation Radical* (see Figure 6-1). As shown in Table IIIb, the overall y component of the unpaired electron density, $\sum_u C_{Suy}^2$, is 0.88. This means that the density axis of the resultant unpaired electron orbital lies almost on the molecular plane and is nearly parallel to the molecular axis. Furthermore, an unpaired electron distributes over the p_y orbitals of atoms O(1), O(2), Cc, and C α (skeleton atoms except for N) of molecule A, and their unpaired electron densities are $C_{S,O(1),y}^2 = 0.24$, $C_{S,O(2),y}^2 = 0.41$, $C_{S,Cc,y}^2 = 0.03$, and $C_{S,C\alpha,y}^2$ = 0.15, respectively. It should be noted that the unpaired electron is localized first in the y components of the nonbonding orbitals of O(1) and O(2) and secondly in the Cc-C α bonding orbital.

In contrast with the simple molecular system, these results are in good accord with the nature of the experimentally obtained unpaired electron orbital, except for the unpaired electron density on N of molecule A.

(3) *The Simple Molecular System and (4) the Hydrogen-Bonded System of the Deprotonated Cation Radical* (see Figure 6-2). As shown in Table IIIc,d, the unpaired electron orbitals of these systems are very similar to one another. The overall y component of the unpaired electron density, $\sum_u C_{Suy}^2$, is 0.93 for the former and 0.91 for the latter, respectively. Namely, 90% of the unpaired electron orbital consists of p_y orbitals of the atoms forming a molecular skeleton of molecule A, that is, $C_{S,O(1),y}^2 = 0.31$, $C_{S,O(2),y}^2 = 0.36$, $C_{S,Cc,y}^2 = 0.04$, $C_{S,C\alpha,y}^2 = 0.18$, and $C_{S,N,y}^2 = 0.03$, for the simple molecular system and $C_{S,O(1),y}^2 = 0.23$, $C_{S,O(2),y}^2 = 0.39$, $C_{S,Cc,y}^2 = 0.05$, $C_{S,C\alpha,y}^2 = 0.17$, and $C_{S,N,y}^2 = 0.05$ for the hydrogen-bonded system of the deprotonate cation radical, respectively.

These features accord with the ESR experimental results that the unpaired electron orbital is parallel to the molecular axis and distributed over the whole radical, not localized extremely on the two oxygen atoms nor on the

TABLE IV: Calculated g Tensors using Stone's Equation^{a,b} for the Cation Radical and the Deprotonated Cation Radical in Single Crystals of α -Aminoisobutyric Acid^c

Δg_{kk}	l	m	n
Cation Radical in the Simple Molecular System			
0.0180	-0.03	-0.09	0.99 ₅
0.0024	0.07	0.99	0.09
0.0002	0.99 ₇	-0.08	0.02
Cation Radical in the Hydrogen Bonded System			
0.0172	0.99 ₅	0.08	-0.06
0.0001	-0.09	0.98	-0.16
0.0023	0.05	0.17	0.99
Deprotonated Cation Radical in the Simple Molecular System			
0.0139	0.99 ₈	0.06	-0.01
0.0000	-0.06	0.99 ₈	0.01
0.0006	0.01	-0.01	0.99 ₈
Deprotonated Cation Radical in the Hydrogen Bonded System			
0.0123	0.99 ₈	0.06	-0.01
0.0000	-0.06	0.99	-0.14
0.0004	0.01	0.14	0.99

^a MO_s and MO energies calculated by SCF MO INDO are used to obtain the g tensors, and $E_1 - E_0$ is approximated by the difference of MO energies, $\epsilon_1 - \epsilon_S$. ^b Reference 32. ^c To simplify the treatment, two CH₃ of α -aminoisobutyric acid are replaced by two H in this series. Eigenvalues are given by $g_{kk} = g_e + \Delta g_{kk}$ (see Table III and Figure 6). Direction cosines are given with respect to the X, Y and Z axes.

carbon atoms. Furthermore, the experimentally estimated unpaired electron densities on s and p_y of N in molecule A, 0.01 and 0.1, are confirmed by the calculated values as $C_{S,N,s}^2 = 0.01$ and $C_{S,N,y}^2 = 0.05$ or 0.04. The transfer of H(2) is also supported by the calculated unpaired electron density of 0.00 on H(2) of the H(2)-O(2) bond of molecule G.

These results for SOMO indicate that the deprotonated cation radical in the hydrogen bonded system is closer to the satellite line species. In addition it is interesting that the unpaired electron orbitals of the deprotonated cation radical and the cation radical, both in the hydrogen bonded system, resemble each other except for their N atomic orbitals.

In the next section, the g tensors have been calculated as shown in Table IV. In both radicals, except for the single molecular system of the cation radical, the eigenvector of g_{\max} is perpendicular to the molecular plane and the eigenvector of the g , being closest to g_e , is directed along the molecular axis as expected from the SOMO. The eigenvector of the remaining one is perpendicular to the molecular axis and to the normal of the molecular plane. These are in good accord with the experimentally obtained g tensor as shown in Table II.

On the other hand, the fact that the calculated g anisotropy of the deprotonated cation radical is smaller than that of the cation radical may explain the characteristically small g anisotropy of the satellite line species. The experimentally obtained $g_{\min} = 2.0013$, being lower than g_e , and the experimentally obtained g anisotropy, being still smaller than the calculated value, were not supported by the results of the calculation of the g tensors of the aforementioned deprotonated cation radical. The reason may be due to the fact that the actual C α -C β bond length and O(1)-C α -O(2) bond angle of the radical are significantly looser than those of the parent molecule because of the unpaired electron existing in the C α -C β bond as seen in Figure 6.³⁶

Therefore, it is concluded that the satellite line species

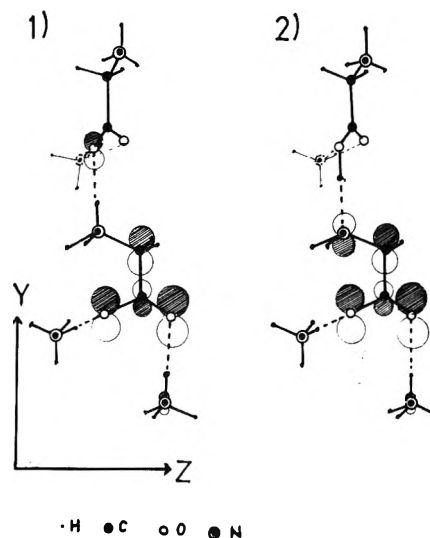


Figure 6. Unpaired electron orbitals of the cation radical and the deprotonated cation radical in the hydrogen bonded system: (1) the cation radical; (2) the deprotonated cation radical. These are calculated as HOMOs of the molecular states in Figure 5, and it is assumed that the unpaired electron orbital is equal to them. Each 2p orbital is indicated by a pair of two lobes, in which the volume is proportional to the unpaired electron density on the 2p orbital, and a shaded lobe shows the negatively signed part.

TABLE V: g Values of the Satellite Line Species (Assigned as the Deprotonated Cation Radicals, ND₂CR₂COO)^a of γ -Irradiated Single Crystals of Deuterated α -Aminoisobutyric Acid, Deuterated L- α -Alanine, and Deuterated Glycine at 77 K

	Deuterated α -aminoisobutyric acid	Deuterated L- α -alanine	Deuterated glycine
$a \parallel H$	2.0041	2.0028	2.003
$b \parallel H$	2.0024	2.0034	2.003
c (or c') $\parallel H$	2.0019	2.0016	2.0017

^a R₁ and R₂ represent CH₃ or H. The external field (H) is parallel to the a , b , or c (or c') axes, respectively. The c' axis is perpendicular to the a and b axes for α -aminoisobutyric acid and glycine.

must be the deprotonated cation radical.

4. Other α -Amino Acids

4.1. *Similarities of Experimental Results.* As it is known that the molecular conformations of L- α -alanine and glycine are similar with that of α -aminoisobutyric acid (α -AIBA), the satellite line species observed in the ESR spectra of γ -irradiated single crystals of L- α -alanine and glycine at 77 K would be assigned to the deprotonated cation radicals as we have done in the case of α -AIBA.

Because of the interference by the superposed signals of the anionic radicals,¹⁻⁵ the angular dependence of the g values for the satellite line signals could be determined only from the well-resolved spectra with an external magnetic field parallel to a , b , and c (or c' for glycine) axes, respectively. The spectra along the c (or c') axis are shown in Figure 1e,f. The g values are shown in Table V, which indicate the small g anisotropy, both for L- α -alanine and glycine, similar to the case in α -AIBA.

When the amino protons in L- α -alanine and glycine were replaced by deuterons, the overall total width of the satellite line signals were not altered markedly as well as in α -AIBA. These facts suggest that the unpaired electron densities on the amino protons are minor in the satellite line species.

Upon irradiation with 500-W tungsten visible light, the

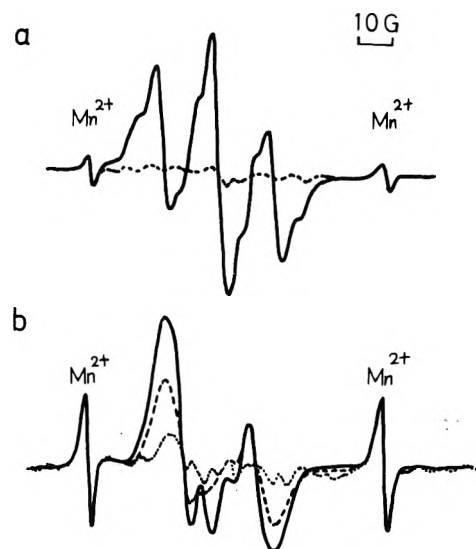


Figure 7. X-band ESR spectra of γ -irradiated single crystals of L- α -alanine and glycine at 77 K and their spectra after photobleaching with 500-W tungsten visible light: (1) L- α -alanine (—) before photobleaching, (---) after photobleaching (40-min exposure); (2) glycine (—) before photobleaching, (---) after photobleaching (3-min exposure), (····) after photobleaching (13-min exposure).

satellite line signals disappeared simultaneously with the signals of the anionic radicals as shown in Figure 7-1 and 7-2, where Figure 7-2 shows that the satellite line signals for glycine are somewhat partially converted into the other radical.

From the similar behavior of the satellite line species with that of α -AIBA, it is concluded that the satellite line species should be the deprotonated cation radicals, even though the glycine species is significantly labile.

4.2. Results of Calculations. The theoretical calculations on the unpaired electron orbital and the g tensor for

TABLE VI: Coefficients for Atomic Orbitals of Atom u Concerning SOMO, ψ_S , of Deprotonated Cation Radicals in Single Crystals of L- α -Alanine, Glycine, and α -Aminoisobutyric Acid

$$\psi_S = \sum_u (C_{S_{us}} \phi_{us} + C_{S_{ux}} \phi_{ux} + C_{S_{uy}} \phi_{uy} + C_{S_{uz}} \phi_{uz})$$

(a) L- α -Alanine: $3\text{NH}_4^+ + (\text{NH}_2\text{CHCH}_3\text{COO}) + \text{HCOOH}$

u^a	O(1)	O(2)	Cc	C_α	N	C_m	H_a	H_s	$\text{NH}_4^+(\text{III})^c$		s, x, y, z^b density component
									N	H_3	
s	0.01	0.00	0.06	0.12	0.11	-0.03	-0.10	0.13	-0.06	0.07	0.09
p_x	0.00	0.01	0.00	-0.01	-0.02	0.06			0.00		0.00
p_y	0.48	0.51	-0.27	0.42	-0.37	-0.09			0.08		0.90
p_z	0.01	-0.01	-0.00	0.02	0.02	-0.02			0.00		0.00

(b) Glycine: $3\text{NH}_4^+ + (\text{NH}_2\text{CH}_2\text{COO}) + \text{HCOOH}$

u^a	O(1)	O(2)	Cc	C_α	N	H_a	H_s	$\text{NH}_4^+(\text{I})^c$		s, x, y, z^b density component
								N	H_1	
s	-0.01	-0.00	-0.07	-0.12	-0.12	0.09	0.10	0.06	-0.09	0.07
p_x	-0.01	-0.00	0.00	0.03	-0.00			0.00		0.00
p_y	0.50	0.49	-0.28	0.41	-0.43			0.10		0.92
p_z	0.01	0.03	-0.00	-0.02	0.02			-0.01		0.00

(c) α -Aminoisobutyric Acid: $2\text{NH}_4^+ + (\text{NH}_2\text{C}(\text{CH}_3)_2\text{COO}) + \text{HCOOH}$

u^a	O(1)	O(2)	Cc	C_α	N	C_1	C_2	H_1	H_a	H_s	H_2	$\text{NH}_4^+(\text{II})^c$		s, x, y, z^b density component
												N	H_1	
s	-0.01	0.00	0.06	-0.11	-0.10	0.03	0.03	0.14	0.10	-0.10	-0.14	0.08	-0.02	0.12
p_x	-0.04	-0.02	0.02	-0.00	-0.00	0.05	-0.07					-0.00		0.01
p_y	0.44	0.53	-0.27	0.43	-0.30	-0.08	-0.10					0.10		0.84
p_z	-0.05	-0.04	0.01	0.02	-0.08	0.03	0.03					0.00		0.01

^a Atoms with an unpaired electron density less than 0.01 are eliminated. ^b Overall $s, x, y,$ and z component of unpaired electron density are denoted by $\sum_u C_{S_{us}}^2, \sum_u C_{S_{ux}}^2, \sum_u C_{S_{uy}}^2, \sum_u C_{S_{uz}}^2$, respectively. ^c The N-H...O lies along the molecular axis.

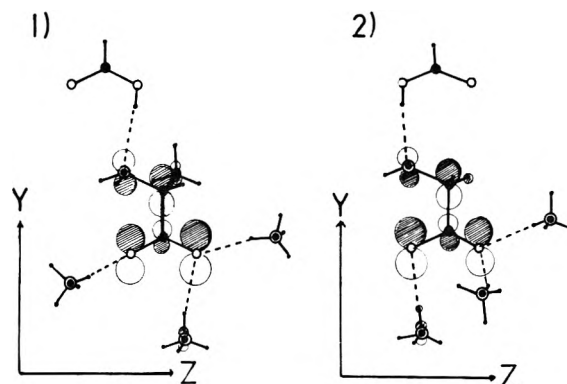


Figure 8. Molecular arrangements and unpaired electron orbitals. These are projected to the YZ plane: (1) L- α -alanine; (2) glycine. Each 2p orbital is indicated by a pair of two lobes, in which the volume is proportional to the unpaired electron density on the 2p orbital, and a shaded lobe shows the negatively signed part. The Y axis is the bisector of O-C-O and the z axis is perpendicular to the normal of COO plane (the X axis) and to the Y axis.

these deprotonated cation radicals have been carried out by the same procedure as described in the previous section.

The calculation was carried out for the following simplified hydrogen bonded systems: deprotonated L- α -alanine + $3\text{NH}_4^+ + \text{HCOOH}$ and deprotonated glycine + $3\text{NH}_4^+ + \text{HCOOH}$, where 3NH_4^+ s are used instead of the three neighboring amino groups and HCOOH is used instead of the neighboring COOH group, the O-H bond of which is hydrogen bonded (parallel to the molecular axis) with the N of the parent molecule. These molecular arrangements are shown in Figure 8. For comparison deprotonated α -AIBA + $2\text{NH}_4^+ + \text{HCOOH}$ was also calculated. The analytical crystal data^{18,19} were used for the atomic positions and the X, Y, and Z axes were chosen in a way similar to those of α -AIBA.

The calculated results for the unpaired electron orbital,

Radiation Biochemistry", headed by Dr. H. Hatano (Kyoto University)).

Appendix I

When the unpaired electron orbital of the N atom is expressed by

$$\psi = \dots + C_{2s}\phi_{2s} + C_{2p}\phi_{2p} + \dots$$

and the axially symmetric hyperfine couplings of N are

$$A_{\max}^N = A_{yy}^N \quad \text{and} \quad A_{\min}^N = A_{xx}^N \doteq A_{zz}^N$$

the unpaired electron density on N is given by the following equations:²¹⁻²³

$$C_{2s}^2 = (A_{\max}^N + 2A_{\min}^N)/3a_s$$

$$C_{2p_y}^2 = (A_{\max}^N - A_{\min}^N)/3a_p'$$

where a_s and a_p' are 550 and 17.0 G, respectively.²⁴

Appendix II

When the orbital angular momentum operators, L_{xu} , L_{yu} , and L_{zu} , act on the atomic orbitals of atom u, ϕ_{ux} , ϕ_{uy} , and ϕ_{uz} as defined in section 3.2.I, the relations shown in Chart I are derived.

Chart I

$$\begin{array}{lll} L_{xu}\phi_{ux} = 0 & L_{yu}\phi_{ux} = 0 & L_{zu}\phi_{ux} = 0 \\ L_{xu}\phi_{uy} = i\phi_{uz} & L_{yu}\phi_{uy} = 0 & L_{zu}\phi_{uy} = -i\phi_{ux} \\ L_{xu}\phi_{uz} = -i\phi_{uy} & L_{yu}\phi_{uz} = i\phi_{ux} & L_{zu}\phi_{uz} = 0 \end{array}$$

Based on these relations, the normalization condition and the orthogonality of the atomic orbitals on atom u, eq 7, substituted by MOs, eq 6, are then easily transformed to

$$g_{XX} = g_e + 2 \sum_{i \neq s} \frac{\sum_u \zeta_u A_{ux} \sum_u (-A_{ux})}{E_i - E_0}$$

$$g_{YY} = g_e + 2 \sum_{i \neq s} \frac{\sum_u \zeta_u A_{uy} \sum_u (-A_{uy})}{E_i - E_0}$$

$$g_{ZZ} = g_e + 2 \sum_{i \neq s} \frac{\sum_u \zeta_u A_{uz} \sum_u (-A_{uz})}{E_i - E_0}$$

and also under the assumption, $g_{rt} = g_{tr}$

$$g_{XY} = \frac{1}{2} \left[2 \sum_{i \neq s} \frac{\sum_u \zeta_u A_{ux} \sum_u (-A_{uy})}{E_i - E_0} + 2 \sum_{i \neq s} \frac{\sum_u \zeta_u A_{uy} \sum_u (-A_{ux})}{E_i - E_0} \right]$$

$$g_{YZ} = \frac{1}{2} \left[2 \sum_{i \neq s} \frac{\sum_u \zeta_u A_{uy} \sum_u (-A_{uz})}{E_i - E_0} + 2 \sum_{i \neq s} \frac{\sum_u \zeta_u A_{uz} \sum_u (-A_{uy})}{E_i - E_0} \right]$$

$$g_{ZX} = \frac{1}{2} \left[2 \sum_{i \neq s} \frac{\sum_u \zeta_u A_{uz} \sum_u (-A_{ux})}{E_i - E_0} + 2 \sum_{i \neq s} \frac{\sum_u \zeta_u A_{ux} \sum_u (-A_{uz})}{E_i - E_0} \right]$$

where

$$A_{ux} = C_{Suy}(-C_{iuz}) + C_{Suz}C_{iuy}$$

$$A_{uy} = C_{Suz}(-C_{iux}) + C_{Sux}C_{iuz}$$

$$A_{uz} = C_{Sux}(-C_{iuy}) + C_{Suy}C_{iux}$$

References and Notes

- (1) A. Minegishi, Y. Shinozaki, and G. Meshitsuka, *Bull. Chem. Soc. Jpn.*, **40**, 1271 (1967).
- (2) A. Minegishi, Y. Shinozaki, and G. Meshitsuka, *Bull. Chem. Soc. Jpn.*, **40**, 1549 (1967).
- (3) J. W. Sinclair and M. W. Hanna, *J. Phys. Chem.*, **71**, 84 (1967).
- (4) J. Sinclair and M. W. Hanna, *J. Chem. Phys.*, **50**, 2125 (1969).
- (5) I. Miyagawa, N. Tamura, and J. W. Cook, *J. Chem. Phys.*, **51**, 3520 (1969).
- (6) H. Muto and M. Iwasaki, *J. Chem. Phys.*, **59**, 4821 (1973).
- (7) H. Muto and M. Iwasaki, *J. Chem. Phys.*, **61**, 5315 (1974).
- (8) H. C. Box and H. G. Freund, *J. Chem. Phys.*, **44**, 2345 (1966).
- (9) M. Fujimoto, W. A. Seddon, and D. R. Smith, *J. Chem. Phys.*, **48**, 3345 (1968).
- (10) D. G. Cadena, Jr., R. E. Linder, and J. R. Rowlands, *Can. J. Chem.*, **47**, 3429 (1969).
- (11) A. Minegishi, Y. Shinozaki, and G. Meshitsuka, *J. Chem. Phys.*, **56**, 2481 (1972).
- (12) H. C. Box, H. G. Freund, K. T. Lilga, and E. B. Budzinski, *J. Chem. Phys.*, **63**, 2059 (1975).
- (13) J. A. Pople, D. L. Beveridge, and P. A. Dobosh, *J. Chem. Phys.*, **47**, 2026 (1967).
- (14) J. A. Pople and D. L. Beveridge, "Approximate Molecular Orbital Theory", McGraw-Hill, New York, N.Y., 1970.
- (15) A. J. Stone, *Proc. R. Soc. London Ser. A*, **271**, 424 (1963).
- (16) S. Hirokawa, S. Kuribayashi, and I. Nitta, *Bull. Chem. Soc. Jpn.*, **25**, 192 (1952).
- (17) kX was used in its original paper,¹⁶ where 1 Å = 1.00202 kX.
- (18) H. J. Simpson and R. E. Marsh, *Acta Crystallogr.*, **20**, 550 (1966).
- (19) R. E. Marsh, *Acta Crystallogr.*, **654** (1958).
- (20) J. W. Wells and H. C. Box, *J. Chem. Phys.*, **46**, 2935 (1967).
- (21) K. Kurita, M. Kashiwagi, and H. Nishikatsu, *Nippon Kagaku Zasshi*, **86**, 578 (1965).
- (22) K. Kurita, "Introduction to Electron Spin Resonance", Kodansha Ltd., 1975.
- (23) I. Miyagawa and W. Gordy, *J. Chem. Phys.*, **30**, 1590 (1959).
- (24) J. R. Morton, J. R. Rowlands, and D. H. Whiffen, *Natl. Phys. Lab. (U.K.)*, BPR 13 (1962); M. C. R. Symons, *Adv. Phys. Org. Chem.*, **1**, 332 (1963).
- (25) J. A. McMillan, M. S. Matheson, and B. Smaller, *J. Chem. Phys.*, **33**, 609 (1960).
- (26) H. C. Box, H. G. Freund, K. T. Lilga, and E. E. Budzinski, *J. Phys. Chem.*, **74**, 40 (1970).
- (27) M. Iwasaki, B. Eda, and K. Toriyama, *J. Am. Chem. Soc.*, **92**, 3211 (1970).
- (28) K. Toriyama, H. Muto, and M. Iwasaki, *J. Chem. Phys.*, **55**, 1885 (1971).
- (29) M. Iwasaki, K. Minakata, and K. Toriyama, *J. Am. Chem. Soc.*, **93**, 3533 (1971).
- (30) H. M. McConnell, C. Heller, T. Cole, and R. W. Fessenden, *J. Am. Chem. Soc.*, **82**, 766 (1960).
- (31) A. Forsfield, J. R. Morton, and D. H. Whiffen, *Mol. Phys.*, **4**, 327 (1961).
- (32) T. P. Debies and J. W. Rabalais, *J. Electron Spectrosc. Relat. Phenomena*, **3**, 315 (1974).
- (33) For an example of usual cases, the calculated result for HCO, with the coordinates H ($x = -0.940$ Å, $y = -0.532$ Å, $z = 0.000$ Å), C (0.000, 0.000, 0.000), and O (1.198, 0.000, 0.000), by the unrestricted SCF MO INDO program is as follows:
HOMO for α spin: $\epsilon_6^\alpha = -0.375$ au, $\varphi_6^\alpha = -0.34\phi_H + 0.33\phi_{Cs} - 0.15\phi_{Cx} + 0.66\phi_{Cy} - 0.04\phi_{Os} + 0.15\phi_{Ox} - 0.54\phi_{Cy}$
LUMO for β spin: $\epsilon_6^\beta = 0.172$ au, $\varphi_6^\beta = 0.39\phi_H - 0.44\phi_{Cs} + 0.22\phi_{Cx} - 0.60\phi_{Cy} + 0.05\phi_{Os} - 0.18\phi_{Ox} + 0.47\phi_{Oy}$
HOMO for β spin: $\epsilon_5^\beta = -0.655$ au, $\varphi_5^\beta = 0.18\phi_H + 0.16\phi_{Cs} - 0.26\phi_{Cx} + 0.45\phi_{Cy} + 0.10\phi_{Os} + 0.27\phi_{Ox} + 0.77\phi_{Oy}$
- (34) For example, the calculated result by the unrestricted SCF MO INDO program for the deprotonated cation radical of α -AIBA (two CH_3 s are replaced by H(M1) and H(M2)) in the single molecular system, $\text{NH}_2\text{CH}_2\text{COO}^-$, is as follows:
HOMO for α spin: $\epsilon_{15}^\alpha = -0.452$ au, $\varphi_{15}^\alpha = -0.23\phi_{H_1} + 0.23\phi_{N_5} + 0.57\phi_{N_y} + 0.12\phi_{C_{6s}} + 0.26\phi_{C_{6y}} - 0.38\phi_{C_{\alpha y}} - 0.46\phi_{O_{1y}} - 0.28\phi_{O_2} - 0.11\phi_{O_{2z}} - 0.13\phi_{H(M2)} + \dots$

$$\begin{aligned} \text{LUMO for } \beta \text{ spin: } \epsilon_{15}^{\beta} &= 0.056 \text{ au}, \varphi_{15}^{\beta} = 0.11\phi_{N_y} \\ &+ 0.19\phi_{C_{\alpha}S} - 0.29\phi_{C_{\alpha}y} - 0.12\phi_{O_1y} + 0.23\phi_{O_1z} \\ &- 0.80\phi_{O_2y} + 0.36\phi_{O_2z} + \dots \end{aligned}$$

$$\begin{aligned} \text{HOMO for } \beta \text{ spin: } \epsilon_{14}^{\beta} &= -0.465 \text{ au}, \varphi_{14}^{\beta} = -0.21\phi_{H_2} \\ &+ 0.23\phi_{N_s} + 0.55\phi_{N_y} + 0.13\phi_{C_{\alpha}S} + 0.23\phi_{C_{\alpha}y} \\ &- 0.28\phi_{C_{\alpha}y} - 0.48\phi_{O_1y} - 0.28\phi_{O_1z} - 0.32\phi_{O_2z} \\ &- 0.12\phi_{H(M2)} + \dots \end{aligned}$$

(35) Pointed out privately by Dr. O. Kikuchi (Tsukuba University).

- (36) In the preliminary calculation for the deprotonated cation radical in the single molecular system, $\text{NH}_2\text{CH(M1)H(M2)COO}$, a remarkable decrease of g anisotropy and lowering of g_{zz} below g_e were observed by the loosening of the $\text{C}_c\text{-C}_\alpha$ bond length and the $\text{O-C}_c\text{-O}$ bond angle, as follows: ($g_{xx} = 2.0152$, $g_{yy} = 2.0023$, $g_{zz} = 2.0030$) for 1.51 Å (125°); ($g_{xx} = 2.0056$, $g_{yy} = 2.0025$, $g_{zz} = 2.0024$) for 1.80 Å (134°); and ($g_{xx} = 2.0034$, $g_{yy} = 2.0025$, $g_{zz} = 2.0020$) for 2.09 Å (180°).
- (37) E. A. Friday and I. Miyagawa, *J. Chem. Phys.*, **55**, 3589 (1971).
- (38) J. Sinclair, *J. Chem. Phys.*, **55**, 245 (1971).
- (39) M. V. Serdobov and M. C. R. Symons, *J. Chem. Soc., Perkin Trans. 2*, 1808 (1973).
- (40) G. Meshitsuka, K. Shindo, A. Minegishi, H. Suguro, and Y. Shinozaki, *Bull. Chem. Soc. Jpn.*, **37**, 928 (1964).

Charge Transfer and 5d States of the Trivalent Rare Earths

R. C. Ropp* and B. Carroll

Chemistry Department, Rutgers, The State University, Newark, New Jersey 07102 (Received March 2, 1977)

The overlap, or separation, of intershell (4f-5d) and charge transfer (CT) spectra of trivalent rare earths depend upon properties of the host, not upon the rare earths themselves.

In a prior paper,¹ three types of experimental diffuse reflectance bands from trivalent rare earths in oxygen-dominated hosts were identified. These arose from either intrashell (4f-4f), intershell (4f-5d), or charge transfer (CT) states of the rare earth in the crystal. The experimental energy positions of these bands were compared to those predicted by Jørgensen,² who derived curves as a function of q in $4f^q$, for both 5d and CT states. One point has been implicit but not widely recognized in these calculations. For a given host, the 5d and CT curves may overlap rather closely, as shown in Figure 1, or they may be separated by a large energy gap, as will become apparent from the following discussion.

The 5d states are subject to splitting by the crystal field of the host ($3t_{2g}$ and $2e_g$ components for octahedral or tetrahedral symmetry). The higher the crystal field strength, the lower is their energy positions. A good example of this is the Ce^{3+} ion. The ground state is a doublet ($^2F_{5/2}$ and $^2F_{7/2}$). The field components are derived from the $^2D_{5/2}$ and $^2D_{3/2}$ free ion state. Deductions concerning excitation and emission spectra can approximate the energy separation of the lowest energy field component and the ground state. In a crystal with a weak field, such as $\text{YPO}_4\text{:Ce}$, the separation³ is about 30000 cm^{-1} . In a strong field crystal such as $\text{Y}_3\text{Al}_5\text{O}_{12}\text{:Ce}$, the energy separation⁴ is only 16500 cm^{-1} .

On the other hand, CT bands are not related to crystal field strength at all. Their energy positions can be related⁵ to (a) symmetry of neighboring atoms around the central rare earth, (b) degree of polarizability of these neighboring atoms, and (c) the amount of covalency/ionicity (the nephelauxetic effect) in the structural bonding. Eu^{3+} can be used as an example since it exhibits CT bands in a wide variety of oxygen-dominated hosts. In Y_2O_3 , the Eu^{3+} CT band is centered⁶ at about 40000 cm^{-1} for a composition of $0.975\text{Y}_2\text{O}_3 \cdot 0.025\text{Eu}_2\text{O}_3$. If about 3.0 mol % of sulfur is added to form:

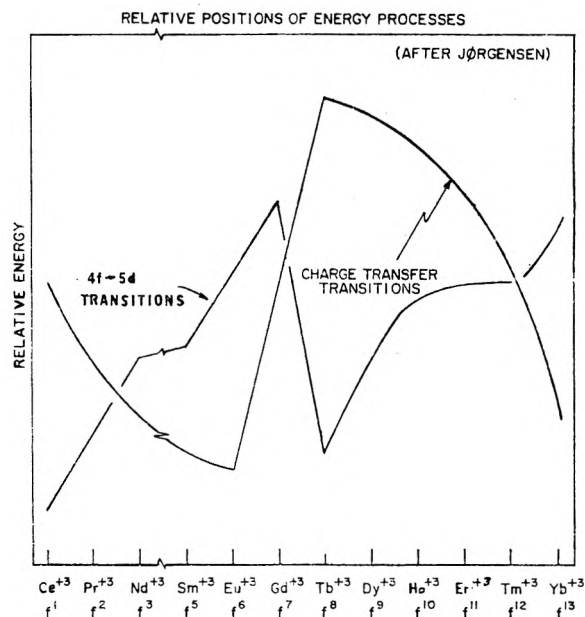
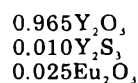


Figure 1.

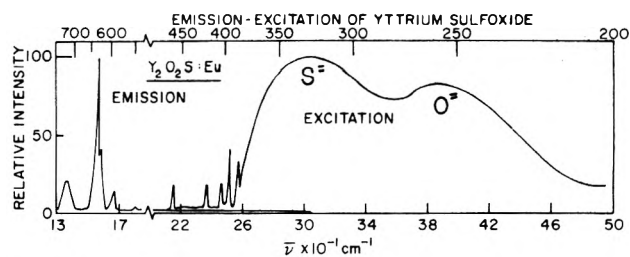


Figure 2.

then a new CT band appears at lower energy due to the higher polarizability of sulfide atoms, compared to the oxide CT band, as shown in Figure 2. (Therein, excitation is equivalent to absorption.) Note that the oxide CT band

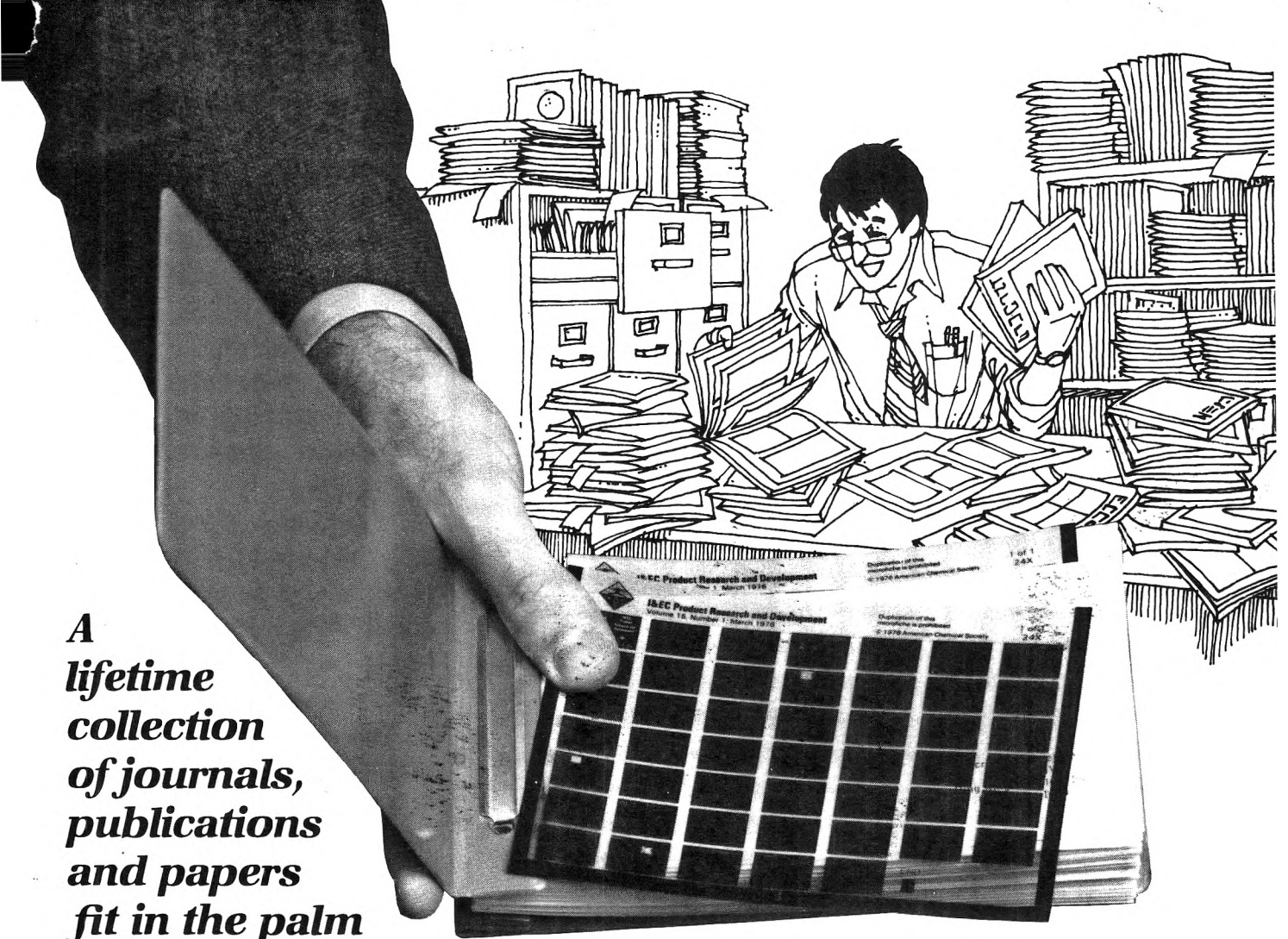
of europium remains at about the same energy in both yttrium oxide and yttrium sulfoxide.

Thus, in CaF_2 , or other hosts where the anion exhibits low polarizability, the 5d bands lie, on an average, near to $45\,000\text{ cm}^{-1}$ whereas the CT bands lie at $80\,000\text{ cm}^{-1}$, or above.⁷ The separation between the two is at least $35\,000\text{ cm}^{-1}$. However in an oxygen-dominated crystal, the two curves may overlap within the same energy range, e.g., LnPO_4 compositions.¹ Indeed, it is entirely possible that for more polarizable hosts such as sulfoxides, the CT bands could lie at energies lower than the 5d states. Thus ions such as Ce^{3+} and Tb^{3+} could exhibit CT bands rather than

the expected 5d states normally observed.

References and Notes

- (1) R. C. Ropp and B. Carroll, *J. Phys. Chem.*, **81**, 746 (1977).
- (2) C. K. Jørgensen, *Proc. Rare Earth Res. Conf.*, 5th (1965); *Mol. Phys.*, **5**, 271 (1962); *Solid State Phys.*, **13**, 375 (1962); *Mol. Phys.*, **7**, 417 (1964).
- (3) R. C. Ropp, *J. Luminen.*, **3**, 152 (1970).
- (4) M. J. Weber, *Solid State Commun.*, **12**, 741 (1973).
- (5) C. K. Jørgensen, "Orbitals in Atoms and Molecules", Academic Press, New York, N.Y., 1962.
- (6) R. C. Ropp, *J. Electrochem. Soc.*, **112**, 181 (1965).
- (7) E. Loh, *Phys. Rev.*, **147**, 332 (1966).



**A
lifetime
collection
of journals,
publications
and papers
fit in the palm
of your hand with**

Microfiche

A MONEY SAVING, TIME-SAVING, SPACE-SAVING AID FOR YOUR HOME, OFFICE, WORKSHOP OR LAB

It started when big organizations found microfiche an efficient, low cost space-saver. Now many individual scientists, information managers, teachers, researchers and executives recognize that the same benefits apply in their own homes and offices.

Consider: you can store three file cases of materials in one small album you can carry in your hand. Yet, you can buy a microfiche reader for less than the cost of a single good file cabinet.

Not only is a large portion of current reference material (including all ACS journals) now available in microfiche, you can even arrange to have your own material put in microfiche form! And subscriptions to many journals and other publications cost the same in microfiche or printed edition.

If space is important where you work or live; if you like to refer to back issues of ACS journals and other periodicals; if you like material that is easily mailed and distributed — turn to microfiche. Not only is it easy to file and retrieve, ACS Microfiche is archival quality so your material will be in good shape for a lifetime.

Surprisingly, it's not only scholarly material that is available on microfiche, you'll find everything from catalogs to magazines, from news weeklies to computer information can be ordered on microfiche. Imagine the advantages of doing away with cumbersome computer readouts and using a tiny film to replace pounds and pounds of paper!

Cut down on wasted space, time and money — turn to the modern method of storing readily available information... turn to microfiche!

Call or write to us for more information on this important aid.

THIS PUBLICATION IS AVAILABLE ON MICROFICHE

**ACS Microforms Program, Room 606
American Chemical Society,
1155 Sixteenth Street, N.W., Washington, D. C. 20036**

(202) 872-4554

When it comes to authoritative, in-depth coverage of the fundamental aspects of polymer chemistry . . .

here's the good word:

Macromolecules

Since its founding in 1968, MACROMOLECULES has become a favored research tool for practitioners in the field of polymer chemistry. For good reason:

Each bimonthly issue is crammed with papers prepared by recognized authorities, that provide definitive information for the field—complete with clear graphs, formulas, spectra, projections, and charts.

All of the reports are thoroughly reviewed and published promptly to provide you with a firm framework upon which to build tomorrow's polymer research and development.

Specifically, MACROMOLECULES provides pertinent polymer information in these fundamental areas:

- synthesis
- chemical reactions
- polymerization mechanisms and kinetics
- solution characteristics
- bulk properties of organic, inorganic, and biopolymers

So—how can you keep right on top of the ever-increasing activity in the area of polymer chemistry?

In a word: **MACROMOLECULES.**



Another service of ACS

Get started today. Mail this coupon.

Macromolecules 1977
American Chemical Society
1155 Sixteenth Street, N.W.
Washington, D.C. 20036

Yes, I would like to receive MACROMOLECULES at the one-year rate checked below:

	U.S.	Foreign and Canada	Latin America
ACS Member* <input type="checkbox"/>	<input type="checkbox"/> \$16.00	<input type="checkbox"/> \$20.00	<input type="checkbox"/> \$19.50
Nonmember <input type="checkbox"/>	<input type="checkbox"/> \$64.00	<input type="checkbox"/> \$68.00	<input type="checkbox"/> \$67.50
Bill me <input type="checkbox"/>	Bill company <input type="checkbox"/>	Payment enclosed <input type="checkbox"/>	

Air freight rates available on request.

Name _____

Street _____ Home
Business

City _____ State _____ Zip _____

Journal subscriptions start in January '77.

Allow 90 days for your first copy to be mailed.

*NOTE: Subscriptions at ACS member rates are for personal use only.

